Charles University in Prague
Faculty of Mathematics and Physics
Institute of Physics of Charles University

PhD Thesis

Diffraction on laterally structured anisotropic periodic systems

Roman Antoš

Supervisor: Prof. Ing. Štefan Višňovský, DrSc.
Advisor: RNDr. Dalibor Ciprian, PhD.

Study Program: Physics
Study Branch: F6 — Quantum optics and optoelectronics

Praha 2006

I declare that my PhD Thesis has been elaborated personally and that I have used only the literature listed. I agree with loaning out my work.

Praha, 21 September 2006

To my family
and friends

First of all, I would like to express a great deal of appreciation to Professor Stefan Visnovsky who was my leading supervisor already since 1997, the year of assigning my Master diploma thesis in Charles University. After finishing the Master Course studies in 2000, he continued leading me during the Doctor Course, giving me most of the knowledge of theoretical optics and magneto-optics. I also thank him for introducing me to Professor Tomuo Yamaguchi and for helping me to realize the invaluable study stay in Prof. Yamaguchi's laboratory in Japan.

Then, I would like to express my great thanks to Prof. Yamaguchi for enabling my study stay and research work in the Research Institute of Electronics of Shizuoka University in Japan and who gave me the background of experimental optical measurement and analysis.

Then I would like to thank Professor Jaromir Pistora who gratefully helped me in the troublesome beginning of my research on diffraction and who was consulting with me many details of the thesis. Similarly I would like to thank Professor Ivan Ohlidal for alike help with my research work.

I would like to give a special thank to Dr. Jan Mistrik, my long-time friend since the Master Course studies in Charles University, who terrifically helped me with my experimental and theoretical research work and with the style and quality of my publications and who also worked during my study stay in Japan in the laboratory of Prof. Yamaguchi.

I also thank my other colleagues and good friends from the Charles University, namely Jaroslav Hamrle, Jana Hamrlova, Jiri Franta, Martin Veis, Eva Liskova, Vratislav Kolinsky, Miroslav Nyvlt, and Radek Lopusnik.

Similarly, I thank to the colleagues and friends from VSB—Technical University of Ostrava, namely Kamil Postava, Dalibor Ciprian, and Martin Foldyna. Each of them discussed with me many details of optical simulation, leading to considerable improvement of my theoretical knowledge and experiences.

Next, my thanks belong to Dr. Daniel Franta and Dr. Petr Klapetek for making some additional measurements and analyses whose results are included in the thesis. I gratefully thank to Dr. Masahiro Horie for providing most of the samples analyzed in the thesis as well as for nice discussions related to experimental and modeling details of scatterometry. I also thank to Professor Burkard Hillebrands, Dr. S.O. Demokritov, Dr. Pavol Gustafik, Dr. Takashi Kimura, and Professor Yoshichika Otani for providing some additional samples.

Finally, I specially thank to Mr. Mitsuru Aoyama who helped me with many technical problems in the Japanese laboratory and who was a good companion during many conference journeys among Japan, Europe, China, and U.S.

Contents

Chapter 1

Introduction

Diffraction of light in periodically arranged inhomogeneous media, traditionally referred to as *gratings*, has been the subject of considerable scientific interest for more than one century. The general problem of their response to impinging electromagnetic waves is of great importance from both fundamental and application points of view.

Extensive investigations of advanced optical properties of gratings, which cannot be explained by Fraunhofer's grating equation, has been initiated by Wood's experimental discovery of grating diffraction anomalies in 1902 [1]. Since then many scientists were developing various theories of diffraction by gratings, accounting for many particular optical features and leading to remarkable advances in electromagnetic science from a more general point of view, e. g., wave propagation in uniform media, reflection and refraction on interfaces, optics of thin films and multilayers [2, 3], slab dielectric waveguides [4, 5, 6], crystal optics [7], ellipsometry [8], acousto-, electro-, and magneto-optics [9, 10], etc.

The development of theoretical approaches describing the diffraction response of various grating systems has been presently continuing with respect to the enhancement of numerical efficiency, complexity of geometrical and material properties of grating patterns, as well as new points of view such as creating metamaterials based on photonic band-gap structures. In this thesis we focus our attention to the *coupled-wave theory*, which is a very general and perhaps the most used approach treating optical diffraction by gratings and band structures in photonic cystals. We describe this approach in a very general way, capable of simulating one- or two-dimensional, multilayered, and anisotropic gratings.

Recent developments in various fundamental and applied fields concerned with periodically inhomogeneous media have revealed that the formalism treating coupled electromagnetic waves is more universal than originally proposed. In particular, there are no practical limitations on the periodicity of the permittivity tensor, and even no limitations how the periodic inhomogeneities and/or anisotropies are induced, including lithographic patterning, special crystal growth, externally applied fields, acoustical vibrations, or just the native, energetically favored ordering of geometrically confined crystalline configura-

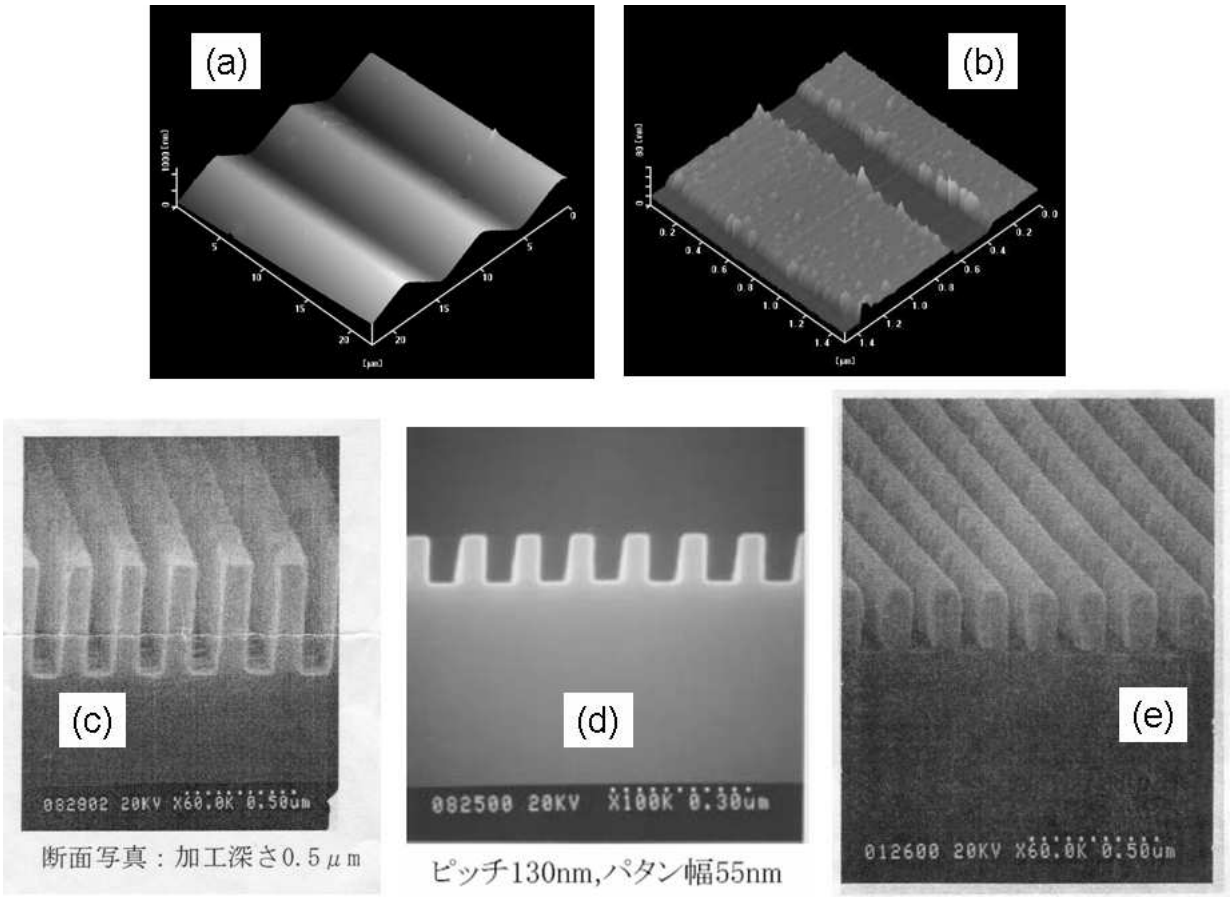

Figure 1.1 Examples of AFM **(a, b)** and SEM **(c, d, e)** pictures of various gratings whose optical response is analyzed in Chapters 7 and 8.

tions (e. g., vortex spin structures in laterally confined ferromagnetic elements), etc.

One of the most important applications of diffraction analysis is *optical scatterometry*, i. e., a technique of characterizing the geometrical and/or material properties of patterned structures by solving the inverse problem to the optical diffraction response. The application of our diffraction approach to scatterometry is the subject of this thesis. A brief review of characterization techniques with respect to recent developments in lithographic production, including optical scatterometry and its advantages over the conventional ones, is provided in Chap. 2. Then we demonstrate the theoretical basis (Chap. 4), methodology (Chaps. 5 and 6) and results of analyses using both purely optical specular spectroscopic scatterometry (Chap. 7) and magneto-optic spectroscopic scatterometry (Chaps. 8 and 9). Examples of atomic force micrographs and scanning electron micrographs of selected studied samples are displayed in Fig. 1.1.

In Chap. 4 we present the principles of coupled wave theory together with our original (Airy-like series) implementation. In Chap. 5 we introduce measurement techniques applied in the thesis. The data obtained by these experimental arrangements are analyzed by the implementation of novel processing whose details are specified in Chap. 6.

In Chap. 7, spectroscopic ellipsometry is applied to gratings prepared from various

materials and with various profiles. A new technical solution for gratings located on transparent plates is presented in Sec. 7.1. Then the analyses of special grating profiles are demonstrated including imperfectly shaped lamellar-like, sine-like, and binary gratings. In Fig. 1.1 (a), an AFM picture of a sine-like grating is shown, whose relief is textured on the top of an optically thick epoxy-polymer film by means of interference lithography. Figs. 1.1 (c, d) display SEM cross sections of lamellar relief gratings made on the top of quartz and silicon substrates, respectively. Fig. 1.1 (e) shows a cross section of imperfectly shaped periodic tantalum wires.

In Chap. 8, the evaluation of the quality of shallow magnetically anisotropic gratings with respect to native oxides and sharpness of patterning is performed using magneto-optic Kerr effect spectroscopy. Fig. 1.1 (b) presents an AFM picture of shallow periodic Permalloy wires covered by ultrathin chromium capping, the sample chosen for the analyses.

In Chap. 9, we provide a demonstration of further magneto-optic analyses. In Secs. 9.1 and 9.2, we show numerical analyses of the spectroscopic response of one- and two-dimensional magnetic gratings, respectively. In Sec. 9.3, we present experimental MO spectroscopic analyses of two special kinds of gratings.

Finally, Chapter 10 summarizes the main conclusions of the thesis and suggests future areas of research.

Chapter 2

Techniques of characterizing laterally structured periodic systems— topical review

Many kinds of laterally patterned periodic nanostructures (conventionally called *diffraction gratings*) are realized for various application purposes in optics, electronics, spintronics, magnetic and magneto-optical recording, biophysics, lithography, etc. For the sake of their preparation, a lot of techniques have been developed based on electron-beam [11, 12, 13, 14, 15, 16], x-ray [17], nanoimprint [18, 19], or laser-interference [20, 21] lithography combined with electroplating [17, 22], wet [22, 23] or dry [18, 19, 20] etching, lift-off [13, 14], direct writing [15, 16], etc. Recent advances in micro- and nano-scaled lithography yielded periodic lateral patterning with features of shapes with unlimited complexity, ultrahigh lateral resolution of elements with the size of a few nanometers, high aspect ratios (in-depth to lateral dimension relationships), and various materials compositions including dielectrics, semiconductors, metals, polymers, etc.

The conventional surface-monitoring techniques such as atomic force microscopy (AFM), scanning electron microscopy (SEM), scanning tunneling microscopy (STM), or (in the case of the presence of magnetically ordered materials) magnetic force microscopy (MFM), provide the shape of the surface directly, but each of them has its limitations.

The scanning probe methods, STM and AFM, measure the surface topography by detecting interactions between the tip (the part of the probe that approaches the sample's surface) and the sample. Samples measured by means of STM must either have conductive surface or be further coated by an ultrathin metallic layer, which is a destructive operation disabling the sample's later application [24]. Moreover, some fine details of the patterning can be lost. On the other hand, AFM [25] is a non-destructive versatile probe method usable to any kind of solid materials forming the surface. Nevertheless, the accuracy and reliability of this technique are reduced due to the limitations of the tip–sample scanning operation.

Unlike the probe methods, SEM is a non-contact method based on detecting secondary electrons emitted via interaction between a fine focused electron beam and the atoms forming the sample's surface. Although the spot size of the beam can presently become 1 nm, the technique also has limitations. Linewidths detected by SEM can be changed due to contamination; moreover, measurements on dielectric surfaces are unstable due to charging. In addition, to detect the in-depth profile of the patterning with appropriate precision, the sample must be cut for the cross-sectional measurement.

All the mentioned conventional surface measurement techniques are presently being developed to achieve higher capabilities, mainly with respect to monitoring critical dimensions and subtle features of patterning with high resolution and complexity. New kinds of materials for tips are searched for such as carbon nanotube tips for STM probes [26]. To use AFM for measuring the surface topography of complex structures with curved edges of lines of pattern trenches, advanced wear-resistant designs and complex probe tip shapes are utilized [27, 28]. After receiving the sub-100-nm resolution, not only the critical dimensions receive attention in AFM and SEM measurements, but also the line-edge roughness (LER, deviations from the linearity of the edges of patterned lines) and the linewidth roughness (LWR, deviations from the uniformity of linewidths). To evaluate those characteristics, the resolution of the both techniques had to be improved and an appropriate postprocessing analysis of the obtained images had to be performed [29, 30].

Despite the advances in the discussed techniques, the fundamental physics barriers (conductive surface for STM, tip–sample contacts in the case of AFM, linewidth modulation by contamination for SEM, etc.) limit the application of the mentioned approaches. For these reasons, optical-diagnostic techniques have been developed to study the quality of patterning as well as lateral non-uniformity of surfaces and thin films. Besides the near-filed optical topographic techniques based on scanning optical microscopic imaging (which can also be considered as a type of scanning probe method), most of attention has been devoted to the "optical scatterometry"—a method of inspecting the periodic structures by optical diffraction.

Broadly speaking, the optical scatterometry is a set of measurement techniques originally developed for the nondestructive optics-based quality control of the integrated circuit production. Every instance of scatterometry comprises an experimental technique, a theoretical model, and a method of processing the experimental and theoretical diffraction-response data. Accordingly, various scatterometric techniques can be classified and recent advances of those can be more easily reviewed.

Before applying sensitively arranged specular-mode optics to gratings, scatterometry mostly referred to analyses of off-specular intensity distribution of light reflected from non-planar structures. From that distribution the characteristics such as surface roughness or microstructure could be determined [31]. After that McNeil and co-workers developed the angular scatterometry (alternatively called "2-Θ scatterometry")—a technique involving single wavelength measurement of diffraction on laterally periodic structures carried

out at many incidence angles. It enables to deduce the geometric parameters of gratings [32, 33, 34]. During establishing the 2-Θ scatterometry, numerous other optical critical dimension (OCD) measurement techniques appeared based on intensity measurements, phase-difference experimental approaches, polarization-conversion arrangements, and ellipsometry. For the purpose of real-time etching-process monitoring, single-wavelength (or several-wavelength) incidence-angle-fixed measurements of the time dependence (usually) of a single geometrical parameter (e. g., the etch depth) was performed [35, 36, 37, 38]. On the other hand, for the objective of detailed *ex situ* evaluation of patterns identified by many parameters including OCDs, subtle features, LER, and LWR, the single-wavelength measurement becomes insufficient, even if it is carried out at many angles of incidence.

Therefore recently, since advanced spectroscopic apparatuses such as spectroscopic ellipsometers and spectrophotometers have widely spread among industrial and research areas, rather dependence on the wavelength of light is analyzed at one or several fixed angles of incidence, mostly in the 0th diffraction order of reflection. This method is more specifically called *specular spectroscopic scatterometry* [39, 40, 41, 42], frequently based on spectroscopic ellipsometry (SE) and/or reflectometry.

For various purposes of metrology, inspection, testing, and process control for lithography, remarkable advances of the scatterometric techniques have been achieved regarding all the three aspects mentioned above: experimental configurations, modeling approaches, and data processing. Special experimental arrangements were implemented. For instance, transverse electric and transverse magnetic spectra were simultaneously detected, combining the speed of photometric measurement and the SE precision [40]. Higher diffraction orders were also sometimes sensed for rapid real-time evaluation of the lithographic process to determine its optimal conditions, but usually for a single wavelength [43].

According to Moore's law, the patterning resolution capabilities systematically improve every year [44]. To keep the acceptable sensitivity and precision of scatterometry, measurements in new photon-energy ranges were performed such as ultraviolet (UV) [45], extreme ultraviolet (EUV) [46], and X-ray band [47]. However, such improvement is obviously coupled with higher cost and new difficulties; therefore, new ideas have been employed to enhance the optical measurement while keeping the visible/near-UV spectral range. For instance, the "interfero-scatterometry" combines the amplitudes of the primary specular beam with a higher-order retro-reflected beam (light reflected by a mirror, again diffracted, and interfering with the primary specular beam) [48]. Similarly, Mueller polarimetry was applied to gratings in conical-diffraction mountings [49] and to two-dimensional gratings [50], proven to be sensitive to additional features nondetectable by the standard SE arrangement. The immersion scatterometry, another method to detect shorter periods of gratings sensitively, is based on exchanging the usual ambient medium (air or vacuum) by a medium with a higher refractive index [51]. In this case, all the optical-spectroscopic characteristics containing the essential information on the grating geometries are simply shifted to larger wavelengths. Analogously, a similar effect can be

achieved by approaching a prism to the grating surface, the technique called the total internal reflection scatterometry [52].

There are many papers on detailed error analyses and evaluation of limitations of the most widely used scatterometric technique—the specular-mode SE (alternatively combined with reflectometry) in the visible/near-UV spectral range. As the fundamental conclusion we can state that this technique has been proven to be highly sensitive not only to standard OCDs, but also to subtle phenomena such as line and line-edge rounding, T-topping, or groove footing with the degree of correlation mostly depending on the range of wavelengths. The method has also been successfully used to extract parameters of very deep trench etches [53] as well as three-dimensional-geometry parameters of hole matrices patterned in thin films [54]. On the other hand, there still remain parameters whose appropriate specification requires further research in the frame of scatterometry, such as LER and LWR detection; it is not possible without special optical Fourier transform arrangement. As another examples, the optical-spectroscopic response of gratings with shallow trenches or with subwavelengh periodicity does not contain sufficient interference-resonation effects to observe the real periodicity. Finally, there are still aspects in scatterometry which essentially need improvement such as the techniques of optical simulation. Although time-effective library analyses [39] have been successfully employed in *in situ* metrology (based on comparing measurement with a set of pre-calculated spectra), the method was only usable to a set of standard structures corresponding to the generated library. Such a standard library must obviously be updated with new types of studied structures or if some of the parameters exceeds the range of the library. Therefore, general modeling approaches based on the rigorous coupled wave analysis or analytical approximations of sufficient precision are worth developing.

According to the demanding tasks of the above paragraph, in this thesis we focus our effort to the development of some fundamental physical background of scatterometry and to the solution of selected scatterometric problems which have rarely been handled in literature but are of high importance with respect to modern trends of analyses. Briefly summarizing our results, we have successfully applied scatterometry to the precise and sensitive specification of geometric and material properties of one-dimensional, two-dimensional, and more-complex-pattern structures made of various materials [55, 56, 57, 58, 59, 60, 61]. We report our original results acquired for dielectric, semiconductor, metallic, and polymer structures transformed to the perfect lamellar-relief gratings, imperfectly shaped lamellar-like and sinusoidal-like relief ones, two-dimensional periodical structures, and shallow trench gratings. We studied both high-resolution patterns and longer-period gratings. We focus our report to the detailed analysis of the diffraction response with particular stress on spectroscopic features related to the optogeometric parameters of interest, including utilization of diffraction anomalies to increase the sensitivity and accuracy of the technique, as well as detailed description of the convergence properties of the extracted OCDs. Among our important fundamental-physics results, the

solution to the scatterometric problem for gratings fabricated on thick transparent plates suggests advantageous utilization to measure both the reflection and transmission modes, each of which is sensitive to different parameters. While the reflection mode of metallic structures is highly affected by the surface properties of the metals (surface roughness or top native oxides), the transmission mode spectrum is mostly sensitive to the bulk-like extinction coefficient. Correspondingly, a three-parameter line-edge fit of the specular-mode SE was performed on a metallic wire-grid polarizer (WGP) with a native oxide layer on the top of each wire, while the transmission-mode SE was analyzed to determine the attenuation ratio and phase-difference of the WGP—the two main characteristics of its practical application. The edges of the lines were approximated by a parabolic function. The reliability of that fit as well as the reliability and accuracy of the method in general was evidenced by comparing the fitted result with both top-view and cross-sectional SEM sample pictures.

As mentioned in the above discussion, the 0th diffraction order measured on particular structures, e. g., shallow gratings patterned from ultrathin films or shallow relief gratings, is not sufficiently sensitive to all the geometric features of patterning. Such an obstacle can naturally be overcome by including an analysis of higher diffraction orders or with a complementary technique. If the sample is prepared of a material with a slight anisotropy, e. g., a magnetically ordered material, then generalized ellipsometry can be chosen as such a complementary approach, utilizing a configuration sensitive to the material anisotropy. To detect the anisotropy of ordered magnetic structures, magneto-optic (MO) effect measurement has been realized as the preferred technique, being generally more sensitive to ultrathin features than the purely optical spectroscopy.

The MO diffraction techniques applied to arrays of submicron magnetic elements have provided valuable information on their fundamental micromagnetic properties [62, 63]. It has been the main application of MO diffraction measurements, almost entirely restricted to single-wavelength measurements with coherent wave sources. Nevertheless, those techniques are also promising for contactless, nondestructive, and low-cost metrology of magnetic nanostructures such as magnetic and MO recording disks and magnetic random access memory (MRAM) chips. Arrays of magnetic wires [64, 65, 66], dots [67], and antidots [68] have been investigated in the reflection mode by measuring the magneto-optical Kerr effect (MOKE) at polar, longitudinal, and transverse magnetization achieved by properly oriented external magnetic filed. Further data were acquired by the extension of experiments to multiple incidence angles and to changing the orientation of the magnetization vector. It was found that lateral magnetization distribution can be deduced from the diffracted MOKE, which makes it an important technique complementary to MFM, Brillouin light scattering [69], etc. The extension of the single-wavelength MOKE to the multiple-wavelength version, i. e., "diffracted MOKE spectroscopy," should in principle deliver larger volume of information on the optical and MO characteristics of magnetic gratings, which is the aim of our original technique, the *magneto-optic spectroscopic scat-*

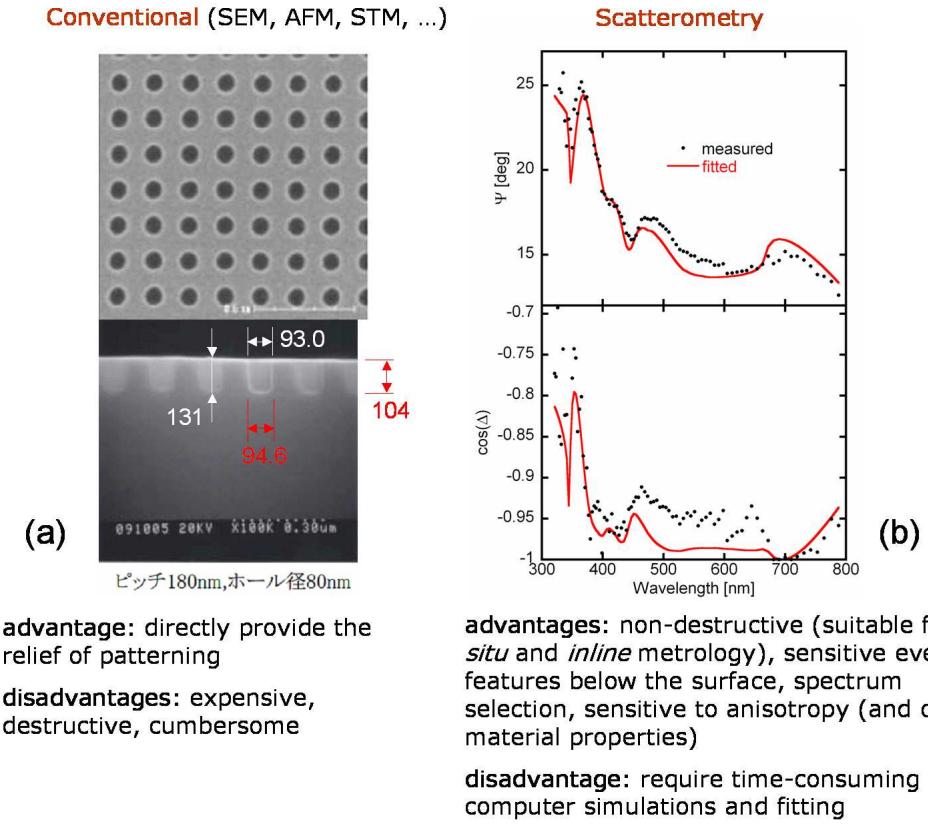

Figure 2.1 Classical **(a)** and scatterometric **(b)** analysis of a laterally patterned structure. In the scanning electron micrograph (SEM), the white-drawn dimensions are directly measured on the picture, corresponding to SEM's critical dimensions, whereas the red-drawn dimensions are obtained from the ellipsometric spectrum by fitting the Ψ and Δ parameters (by minimizing the difference between the red-plotted simulation and black-dotted measurement).

terometry [70, 71, 72, 73, 74]. We demonstrate that the MO scatterometric analysis combining the specular and a higher-order diffracted beam is capable to extract features of shallow gratings with a very low degree of correlation. Moreover, the technique successfully provides a highly sensitive quantitative characteristic of LER without any special optical Fourier transform component.

Theoretical and experimental results of the thesis declare new quality of nondestructive diagnostics which cannot be achieved by SEM, AFM, STM, etc. The main advantages and disadvantages are summarized and the comparison with the conventional approaches is depicted in Fig. 2.1.

Chapter 3

Description of light states and optical systems

Before an appropriate formulation of the theory of optical diffraction by gratings, it is necessary to introduce quantities describing the light optically interacting with the studied structures, as well as quantities describing the diffraction response. This chapter is devoted to the definition of these quantities and to the explanation of how they refer to the light interaction with linear media described by Maxwell's equations.

Section 3.1 states Maxwell's electromagnetic wave equations from which the ideas of light behavior in space and of the optical response follow, including elementary examples of optical systems. In Sec. 3.2 the idea of light behavior is formulated in the form of abstract light states, which are mathematically identified with elements of a linear space of all the possible states. In this manner states of polarization and states of space modulation are described. Then in Sec. 3.3 the transformation of the light states via propagation through linear optical systems is formulated by means of linear operators and their appropriate representations. These linear transforms are applied to define the optical response of planar structures in Sec. 3.4 and diffraction gratings in Sec. 3.5.

3.1 Electromagnetic waves and their interaction with a linear medium

The idea of studying the optical response is depicted in Fig. 3.1. The studied system, consisting of inhomogeneous, linear, and generally anisotropic media, responses to waves emitted from a distant light source. For simplicity it is assumed that the whole space surrounding both the light source and the structure is entirely filled with a linear, homogenous, and isotropic ambient medium; in reality it is usually air or vacuum. For practical purposes, since the optical response must be theoretically determined by solving differential equations governing propagation of waves, instead of studying the response to the light source, we usually study the transformation of electromagnetic fields from one

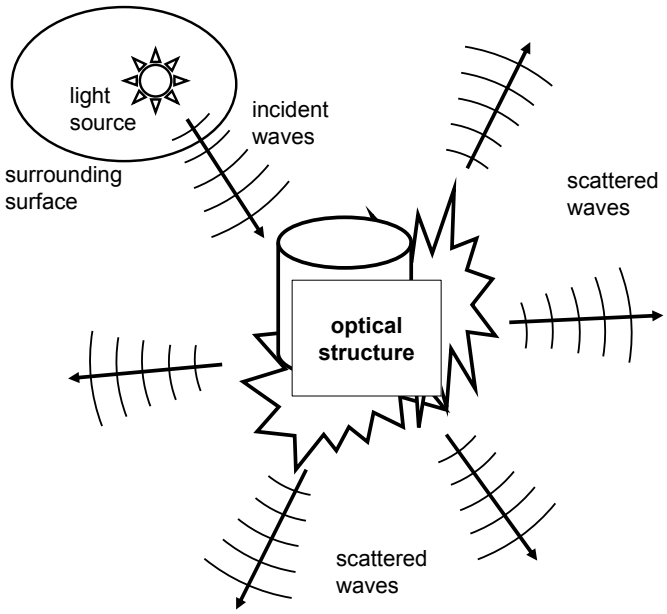

Figure 3.1 Cartoon depicting the scattering of light waves by an optical structure. The waves are emitted from a distant light source, then they are optically interacting with the structure consisting of linear media, which results in secondary light waves scattered by the structure. The full process, referred to as the optical response, can be determined via the transformation of electromagnetic fields from one surface surrounding the light source into another one surrounding the studied optical structure.

surface surrounding the light source into another one surrounding the optical structure.

3.1.1 Electromagnetic field equations and elementary assumptions

The propagation of light in a linear anisotropic nonmagnetic medium is governed by Maxwell's partial differential equations (with the constitutive material equations inhered)

$$\nabla \times \boldsymbol{E} = -\mu_0 \frac{\partial \boldsymbol{H}}{\partial t}, \tag{3.1}$$

$$\nabla \times \boldsymbol{H} = \varepsilon_0 \, \boldsymbol{\varepsilon}(\boldsymbol{r}) \cdot \frac{\partial \boldsymbol{E}}{\partial t}, \tag{3.2}$$

$$\nabla \cdot [\boldsymbol{\varepsilon}(\boldsymbol{r}) \cdot \boldsymbol{E}] = 0, \tag{3.3}$$

$$\nabla \cdot \boldsymbol{H} = 0, \tag{3.4}$$

in which $\boldsymbol{E}(\boldsymbol{r}, t)$, $\boldsymbol{H}(\boldsymbol{r}, t)$ are vectors of complex electric and magnetic fields, respectively, ε_0, μ_0 denote the electric permittivity and magnetic permeability in vacuum, and $\boldsymbol{\varepsilon}(\boldsymbol{r})$ the relative electric permittivity (generally tensorial) function of the medium, also called the *dielectric function*.

What we usually mean when talking about states of light are solutions of Eqs. (3.1–3.4) in a given space-time area with appropriate initial and/or boundary conditions. What we usually mean by an optical system is a transformation from one state of light into another. Thus, for instance, if we know the electric and magnetic fields at an initial

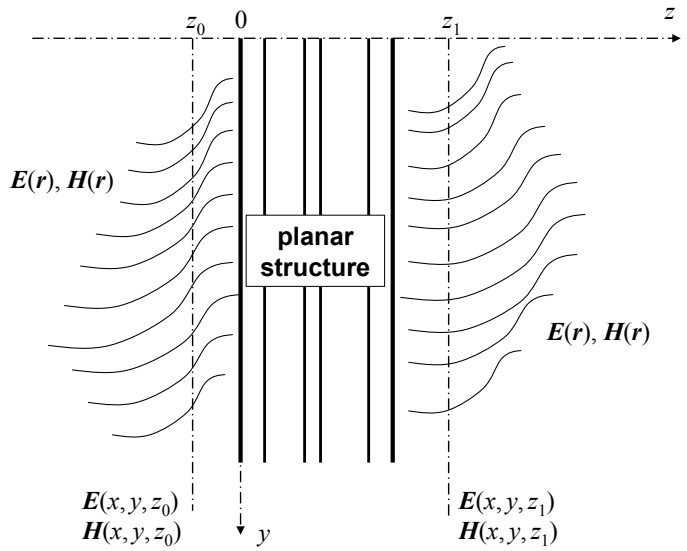

Figure 3.2 Transfer of electromagnetic fields through a planar optical structure. If we know the spatial dependence of the electric and magnetic field vectors in one chosen plane, say $z = z_0$, than we can determine the fields $\boldsymbol{E}(\boldsymbol{r})$, $\boldsymbol{H}(\boldsymbol{r})$ in the whole space. This determination can be realized via the linear transform describing the transfer from the plane $z = z_0$ into another plane, say $z = z_1$.

point in the whole space, i. e., $\boldsymbol{E}(\boldsymbol{r}, t_0) = \boldsymbol{E}_0(\boldsymbol{r})$ and $\boldsymbol{H}(\boldsymbol{r}, t_0) = \boldsymbol{H}_0(\boldsymbol{r})$, we should also be capable to use Maxwell's equations to evaluate the field functions with respect to the time variable—also in the whole space. In other words, to solve Maxwell's equations means to describe the optical system of transformation from the time $t = t_0$ to the time $t = t_1$. In this thesis, however, we will only consider stationary monochromatic (or sometimes quasi-monochromatic) light sources and hence such a transformation becomes trivial; all the fields take on the time-harmonic dependence

$$\boldsymbol{E}(\boldsymbol{r}, t) = \boldsymbol{E}(\boldsymbol{r}, 0)\, e^{i\omega t} \cong \boldsymbol{E}(\boldsymbol{r})\, e^{i\omega t}, \tag{3.5}$$

$$\boldsymbol{H}(\boldsymbol{r}, t) = \boldsymbol{H}(\boldsymbol{r}, 0)\, e^{i\omega t} \cong \boldsymbol{H}(\boldsymbol{r})\, e^{i\omega t}, \tag{3.6}$$

where ω is the angular frequency of the fields. Consequently, all the time derivatives can simply be replaced by the $i\omega$ factor, which leads to the time-harmonic version of Maxwell's equations

$$\nabla \times \boldsymbol{E} = -i\omega\mu_0 \boldsymbol{H}, \tag{3.7}$$

$$\nabla \times \boldsymbol{H} = i\omega\varepsilon_0\, \boldsymbol{\varepsilon}(\boldsymbol{r}) \cdot \boldsymbol{E}, \tag{3.8}$$

$$\nabla \cdot [\boldsymbol{\varepsilon}(\boldsymbol{r}) \cdot \boldsymbol{E}] = 0, \tag{3.9}$$

$$\nabla \cdot \boldsymbol{H} = 0. \tag{3.10}$$

Now, instead of looking for time-dependent solutions of Maxwell's equations, we encounter a different problem—to find values of the field in space according to values given on an appropriately chosen surface. In the case of a homogenous isotropic medium, for instance, such a solution is given by Kirchhoff's integral theorem, which provides values

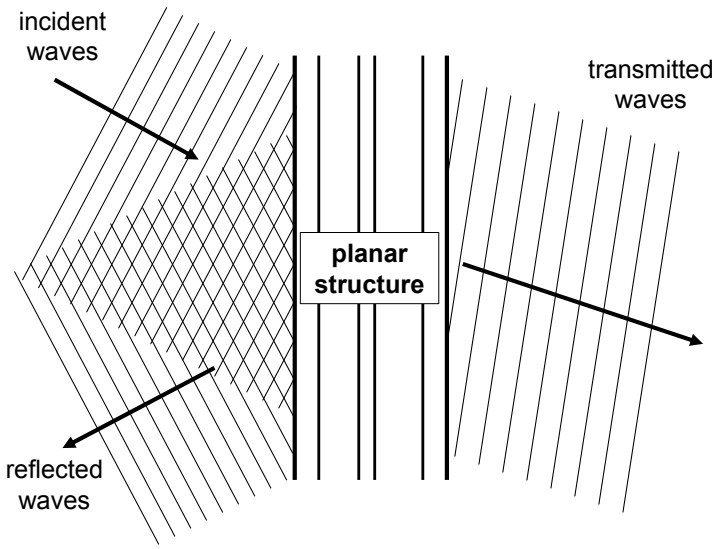

Figure 3.3 Simplified notion of scattering of electromagnetic waves by a planar optical structure. The scattered waves are conventionally called reflected and transmitted waves.

of fields in or outside a volume surrounded by a closed surface on which the field is known. In this thesis, however, we will restrict our analyses to planar and planar-like structures, so instead of closed surfaces we will work with planes, as depicted in Fig. 3.2. Hereafter, a state of light will be defined within a single plane, e. g., in the plane $z = z_0$, and its determination will be identified with the determination of the functions $\boldsymbol{E}(x, y, z_0)$, $\boldsymbol{H}(x, y, z_0)$. The optical system will then be identified with an operator $\hat{\mathbf{M}}$, mapping this state of light into a state in another plane, e. g., the plane $z = z_1$, which can be symbolically written

$$\vec{\boldsymbol{F}}(z_1) = \hat{\mathbf{M}}\,\vec{\boldsymbol{F}}(z_0), \tag{3.11}$$

where

$$\vec{\boldsymbol{F}}(z_j) = \begin{bmatrix} \boldsymbol{E}(x, y, z_j) \\ \boldsymbol{H}(x, y, z_j) \end{bmatrix}, \tag{3.12}$$

is an element of a linear space of all the possible states of light regarded with the plane $z = z_j$. We refer to $\hat{\mathbf{M}}$ as the *transfer operator*.

After determining the direction of propagation, i. e., after splitting

$$\boldsymbol{E}(x, y, z_j) = \boldsymbol{E}^{(+)}(x, y, z_j) + \boldsymbol{E}^{(-)}(x, y, z_j), \tag{3.13}$$

where $\boldsymbol{E}^{(+)}$ is the electric field propagating in the $+z$ direction and $\boldsymbol{E}^{(-)}$ in the $-z$ direction, we can define the second kind of light states corresponding to waves propagating in a single direction. The optical system is then defined by another operator $\hat{\mathbf{S}}$, mapping generally two input states of light incident from both sides of the structure into two output states which are said to be scattered, i. e.,

$$\begin{bmatrix} \boldsymbol{E}^{(-)}(x, y, z_0) \\ \boldsymbol{E}^{(+)}(x, y, z_1) \end{bmatrix} = \hat{\mathbf{S}} \begin{bmatrix} \boldsymbol{E}^{(+)}(x, y, z_0) \\ \boldsymbol{E}^{(-)}(x, y, z_1) \end{bmatrix}, \tag{3.14}$$

where the structure is located between the two planes $z = z_0$ and $z = z_1$, provided $z_0 < z_1$. We refer to $\hat{\mathbf{S}}$ as the *scattering operator*. The simplified notion of the scattering process by a planat structure is described in Fig. 3.3.

Usually the light source is only present on one side of the structure, say, $\boldsymbol{E}^{(-)}(x, y, z_1) = 0$; therefore, we define an incident wave $\boldsymbol{E}^{(i)}(\boldsymbol{r}) = \boldsymbol{E}^{(+)}(\boldsymbol{r})$ $(z \leq z_0)$ and accordingly evaluate the simplified system

$$\boldsymbol{E}^{(r)}(x, y, z_0) = \hat{\mathbf{R}}\, \boldsymbol{E}^{(i)}(x, y, z_0), \tag{3.15}$$

$$\boldsymbol{E}^{(t)}(x, y, z_1) = \hat{\mathbf{T}}\, \boldsymbol{E}^{(i)}(x, y, z_0), \tag{3.16}$$

where $\boldsymbol{E}^{(r)}(\boldsymbol{r}) = \boldsymbol{E}^{(-)}(\boldsymbol{r})$ $(z \leq z_0)$ and $\boldsymbol{E}^{(t)}(\boldsymbol{r}) = \boldsymbol{E}^{(+)}(\boldsymbol{r})$ $(z \geq z_1)$ denote the reflected and transmitted waves, respectively, and where $\hat{\mathbf{R}} = \hat{\mathbf{S}}_{11}$ is the operator of reflection by the structure and $\hat{\mathbf{T}} = \hat{\mathbf{S}}_{21}$ the operator of transmission through it, both determined as subblock operators of the operator $\hat{\mathbf{S}}$. The detailed derivation of the transmission and reflection operators will be performed in Chap. 4.

According to the nature of the media assumed in this thesis, all the optical systems will be considered linear, described by linear operators.

3.1.2 Light propagation in a homogenous isotropic medium

The interaction of light with inhomogeneous (generally anisotropic) media are governed by quite complicated ways and are the subject of many large-scale numerical models such as the coupled wave theory which will be demonstrated in Chap. 4. Generally it is even not easy to split the field into the directions of propagation such as in Eq. (3.13). On the other hand, the propagation through a homogenous medium as the simplest example of an optical system is perfectly known and its rules can provide a detailed notion of the properties of light states and optical systems. Moreover, the simplified light behavior in such a medium is of great importance since the incident and scattered waves and the corresponding optical-response quantities are determined in ambient media, which are—according to the above assumption—both isotropic and homogenous.

In the case of a medium with homogenous isotropic permittivity described by a scalar constant ε, we can simplify Maxwell's equations by eliminating the magnetic field $\boldsymbol{H}$. Applying "$\nabla\times$" to Eq. (3.7), using Eq. (3.9), and substituting Eq. (3.8) into it yields Helmholtz's equation

$$\left[\frac{\omega^2}{c^2}\varepsilon + \nabla^2\right]\boldsymbol{E} = 0, \tag{3.17}$$

where $c = 1/\sqrt{\varepsilon_0\mu_0}$ denotes the velocity of light in vacuum.

The basic solution of Eq. (3.17) in the Cartesian coordinates is a plane wave

$$\boldsymbol{E}(\boldsymbol{r}) = A\hat{\boldsymbol{e}}\exp(-i\boldsymbol{k}\cdot\boldsymbol{r}), \tag{3.18}$$

where A is the homogenous complex amplitude of the wave, $\boldsymbol{k}$ its wave vector, and $\hat{\boldsymbol{e}}$ a unit vector perpendicular to $\boldsymbol{k}$, denoting its polarization state. Moreover, Eq. (3.17) also

determines the square power of the wave vector

$$\boldsymbol{k}^2 = \boldsymbol{k} \cdot \boldsymbol{k} = \frac{\omega^2}{c^2}\varepsilon = \left(\frac{2\pi}{\lambda}\right)^2 \varepsilon, \tag{3.19}$$

where λ is the wavelength of the wave in vacuum.

Owing to Eq. (3.19) and the transversal behavior of electromagnetic waves, the field propagating in a single direction is uniquely determined in the whole space if its two components are known in one chosen plane, e. g., in the plane $z = 0$. Suppose that the x and y components of the electric field in this plane are

$$E_x(x, y, 0) = A_x \exp[-i(k_x x + k_y y)], \tag{3.20}$$
$$E_y(x, y, 0) = A_y \exp[-i(k_x x + k_y y)], \tag{3.21}$$

where A_x, A_y are components of the amplitude vector $\boldsymbol{A} = A\hat{\boldsymbol{e}}$, the components tangential with respect to the plane $z = 0$. Then we can determine the remaining properties of the plane wave, i. e., the normal component of its wave vector and the normal component of its amplitude vector, respectively,

$$k_z = \pm\sqrt{\varepsilon k_0^2 - k_x^2 - k_y^2}, \tag{3.22}$$
$$A_z = -\frac{1}{k_z}(A_x k_x + A_y k_y), \tag{3.23}$$

where the latter follows from the transversality condition $\boldsymbol{A} \cdot \boldsymbol{k} = 0$ and where $k_0 = 2\pi/\lambda$ is the wave number in vacuum. The plus and minus sign in Eq. (3.22) corresponds to a wave propagating in the $+z$ and in the $-z$ direction, respectively.

More generally, suppose that the tangential components of the electric field in the plane $z = 0$ are arbitrary elements from the space of integrable functions $L^2(\mathbb{R}^2)$. Then they can be expanded into two-dimensional Fourier transforms

$$E_x(x, y, 0) = \int_{-\infty}^{+\infty}\int_{-\infty}^{+\infty} f_x(p, q) e^{-ik_0(px+qy)} \mathrm{d}p\, \mathrm{d}q, \tag{3.24}$$
$$E_y(x, y, 0) = \int_{-\infty}^{+\infty}\int_{-\infty}^{+\infty} f_y(p, q) e^{-ik_0(px+qy)} \mathrm{d}p\, \mathrm{d}q \tag{3.25}$$

with the solution of propagation based on plane-wave solutions (3.22, 3.23),

$$\boldsymbol{E}(x, y, z) = \int_{-\infty}^{+\infty}\int_{-\infty}^{+\infty} \boldsymbol{f}(p, q) e^{-ik_0[px+qy+s(p,q)z]} \mathrm{d}p\, \mathrm{d}q, \tag{3.26}$$
$$s(p, q) = \sqrt{\varepsilon - p^2 - q^2}, \tag{3.27}$$
$$f_z(p, q) = -\frac{1}{s(p, q)}\left[f_x(p, q)p + f_y(p, q)q\right] \tag{3.28}$$

assuming propagation in the $+z$ direction.

We can conclude this subsection by the statement that the propagation in a uniform isotropic medium is governed by a linear transform which does not change the polarization state and is "diagonal" in the basis of Fourier modes.

3.1.3 Reflection and transmission by a boundary

As a second simple example of a linear optical system we can examine the interaction of electromagnetic waves with the simplest inhomogeneity—a plain boundary between two different homogenous isotropic media described by permittivity constants $\varepsilon^{(0)}$ and $\varepsilon^{(1)}$.

Suppose that a general wave $\boldsymbol{E}^{(i)}(\boldsymbol{r})$ defined by Eq. (3.26) impinges onto a boundary located at $z = 0$. As the result we assume the formation of a reflected wave $\boldsymbol{E}^{(r)}(\boldsymbol{r})$ defined within the half-space $z < 0$ and a transmitted wave $\boldsymbol{E}^{(t)}(\boldsymbol{r})$ defined within $z > 0$. We can summarize the general dependences of all the three waves as

$$\boldsymbol{E}^{(i)}(x,y,z) = \int_{-\infty}^{+\infty}\int_{-\infty}^{+\infty} \boldsymbol{f}^{(i)}(p,q) e^{-ik_0\left[px+qy+s^{(i)}(p,q)z\right]} \mathrm{d}p\,\mathrm{d}q, \tag{3.29}$$

$$\boldsymbol{E}^{(r)}(x,y,z) = \int_{-\infty}^{+\infty}\int_{-\infty}^{+\infty} \boldsymbol{f}^{(r)}(p,q) e^{-ik_0\left[px+qy+s^{(r)}(p,q)z\right]} \mathrm{d}p\,\mathrm{d}q, \tag{3.30}$$

$$\boldsymbol{E}^{(t)}(x,y,z) = \int_{-\infty}^{+\infty}\int_{-\infty}^{+\infty} \boldsymbol{f}^{(t)}(p,q) e^{-ik_0\left[px+qy+s^{(t)}(p,q)z\right]} \mathrm{d}p\,\mathrm{d}q, \tag{3.31}$$

with

$$s^{(i)}(p,q) = s^{(0)}(p,q) = \sqrt{\varepsilon^{(0)} - p^2 - q^2}, \tag{3.32}$$

$$s^{(r)}(p,q) = -s^{(0)}(p,q) = -\sqrt{\varepsilon^{(0)} - p^2 - q^2}, \tag{3.33}$$

$$s^{(t)}(p,q) = s^{(1)}(p,q) = \sqrt{\varepsilon^{(1)} - p^2 - q^2}, \tag{3.34}$$

where $s^{(J)}$ denotes the propagation numbers in the Jth medium, analogous to Eq. (3.27).

Our aim is to calculate the reflected and transmitted mode amplitudes, $\boldsymbol{f}^{(r)}(p,q)$, $\boldsymbol{f}^{(t)}(p,q)$ as the response to the incident ones, $\boldsymbol{f}^{(i)}(p,q)$. For this purpose we must also evaluate the magnetic field, because the response of the boundary is determined via the requirement for the continuity of the tangential components of the electric and magnetic fields. Thus, Eq. (3.7) applied to the incident wave yields

$$\omega\mu_0 \boldsymbol{H}^{(i)}(\boldsymbol{r}) = k_0 \int_{-\infty}^{+\infty}\int_{-\infty}^{+\infty} \boldsymbol{h}^{(i)}(p,q) e^{-ik_0\left[px+qy+s^{(i)}(p,q)z\right]} \mathrm{d}p\,\mathrm{d}q, \tag{3.35}$$

where $\boldsymbol{h}^{(i)} = \boldsymbol{N}^{(i)} \times \boldsymbol{f}^{(i)}$ with $\boldsymbol{N}^{(i)}(p,q) = [p, q, s^{(i)}]^{\mathrm{T}}$. Since the requirement for the continuity employs only the tangential components, we can reduce the dimension of the above

vectorial equations by dropping their normal components and by substituting Eq. (3.28) into the normal field components where they appear in the tangential equations. We obtain the formula

$$\omega\mu_0 \begin{bmatrix} H_x^{(i)} \\ H_y^{(i)} \end{bmatrix} = k_0 \int_{-\infty}^{+\infty}\int_{-\infty}^{+\infty} \mathbf{D}^{(i)} \begin{bmatrix} f_x^{(i)} \\ f_y^{(i)} \end{bmatrix} e^{-ik_0\left[px+qy+s^{(i)}(p,q)z\right]} \mathrm{d}p\,\mathrm{d}q, \tag{3.36}$$

where

$$\mathbf{D}^{(i)}(p,q) = \frac{1}{s}\begin{bmatrix} -pq & -(s^2+q^2) \\ s^2+p^2 & pq \end{bmatrix} \tag{3.37}$$

is the derived matrix transform from tangential electric to tangential magnetic field components, and where $s = s^{(i)}(p,q)$ is the corresponding propagation number. Similarly, we can determine analogous equations for reflected and transmitted waves, which we use in the desired continuity requirements

$$\boldsymbol{f}_{\hat{t}}^{(i)} + \boldsymbol{f}_{\hat{t}}^{(r)} = \boldsymbol{f}_{\hat{t}}^{(t)}, \tag{3.38}$$

$$\mathbf{D}^{(i)}\boldsymbol{f}_{\hat{t}}^{(i)} + \mathbf{D}^{(r)}\boldsymbol{f}_{\hat{t}}^{(r)} = \mathbf{D}^{(t)}\boldsymbol{f}_{\hat{t}}^{(t)}, \tag{3.39}$$

corresponding to electric and magnetic fields, respectively, for each pair of p, q mode numbers, because the total continuity can only be satisfied if it is valid for each harmonic mode $e^{-ik_0(px+qy)}$ independently. In the above equations we used the subscript $\hat{t}$ to denote the tangential (two-dimensional) parts of the vectorial amplitudes. After realizing that $\mathbf{D}^{(r)} = -\mathbf{D}^{(i)}$, following from Eq. (3.33), the reflected and transmitted mode amplitudes easily follow,

$$\boldsymbol{f}_{\hat{t}}^{(r)} = \mathbf{R}\boldsymbol{f}_{\hat{t}}^{(i)}, \tag{3.40}$$

$$\boldsymbol{f}_{\hat{t}}^{(t)} = \mathbf{T}\boldsymbol{f}_{\hat{t}}^{(i)}, \tag{3.41}$$

with the reflection and transmission matrix transforms defined as

$$\mathbf{R} = -\left(1+\mathbf{D}^{(t)^{-1}}\mathbf{D}^{(i)}\right)^{-1}\left(1-\mathbf{D}^{(t)^{-1}}\mathbf{D}^{(i)}\right), \tag{3.42}$$

$$\mathbf{T} = 1-\left(1+\mathbf{D}^{(t)^{-1}}\mathbf{D}^{(i)}\right)^{-1}\left(1-\mathbf{D}^{(t)^{-1}}\mathbf{D}^{(i)}\right). \tag{3.43}$$

Clearly, if we choose the Cartesian coordinates so that either p or q of a particular $[p,q]$-mode vanishes, then two elements of the matrix (3.37) become zero and the reflection and transmission matrices (3.42, 3.43) become diagonal. Let us choose the coordinates with $p = 0$; then the diagonal elements of the reflection and transmission matrices

$$\mathbf{R} = \begin{bmatrix} r_x & 0 \\ 0 & r_y \end{bmatrix}, \quad \mathbf{T} = \begin{bmatrix} t_x & 0 \\ 0 & t_y \end{bmatrix}, \tag{3.44}$$

easily follow:

$$r_x = \frac{s^{(0)} - s^{(1)}}{s^{(0)} + s^{(1)}}, \tag{3.45}$$

$$r_y = \frac{\varepsilon^{(0)} s^{(1)} - \varepsilon^{(1)} s^{(0)}}{\varepsilon^{(0)} s^{(1)} + \varepsilon^{(1)} s^{(0)}}, \tag{3.46}$$

$$t_x = \frac{2s^{(0)}}{s^{(0)} + s^{(1)}}, \tag{3.47}$$

$$t_y = \frac{2\varepsilon^{(0)} s^{(1)}}{\varepsilon^{(0)} s^{(1)} - \varepsilon^{(1)} s^{(0)}}. \tag{3.48}$$

We can conclude this section by the statement, that like in the case of the propagation through a homogenous medium, the reflection and transmission by a boundary between two uniform media is governed by a linear transform which is "diagonal" in the basis of Fourier modes. However, contrary to the propagation, the boundary changes the polarization state unless the wave is polarized in one of the Cartesian directions just determined above. In the following section we will refer to these states as the `s` and `p` polarizations, the former of which denotes the electric field *perpendicular* to the plane of incidence (`s` from German *senkrecht*) and the latter the electric field *parallel*. Thus, the above derived modal reflection and transmission eigenvalues denote Fresnel's amplitude reflection coefficients $r_{\mathtt{s}} = r_x$, $r_{\mathtt{p}} = r_y$ $t_{\mathtt{s}} = t_x$, and $t_{\mathtt{p}} = t_y$.

3.2 Description of light states

3.2.1 Polarization of light

We will distinguish between two Cartesian coordinate systems, one linked with a wave and one linked with the optical system the wave interacts with. The z coordinate of the former system will always be coincident with the direction of the wave vector. Thus the plane wave propagation can be written

$$\boldsymbol{E}(\boldsymbol{r}) = \begin{bmatrix} A_x \\ A_y \\ 0 \end{bmatrix} \exp(-ik_z z) \tag{3.49}$$

and hence the z component of the wave can be omitted. The complex two-dimensional vector

$$\boldsymbol{J} = \begin{bmatrix} j_x \\ j_y \end{bmatrix} = \begin{bmatrix} A_x \\ A_y \end{bmatrix} \tag{3.50}$$

is called Jones'es vector of the polarization of the electromagnetic wave. We can demonstrate how the polarization behaves by restoring the time dependence in Eq. (3.49) at a chosen point, e. g., at $z = 0$,

$$\boldsymbol{E}(t) = \begin{bmatrix} A_x \\ A_y \end{bmatrix} e^{i\omega t} = \begin{bmatrix} a_x e^{i\delta_x} \\ a_y e^{i\delta_y} \end{bmatrix} e^{i\omega t} \tag{3.51}$$

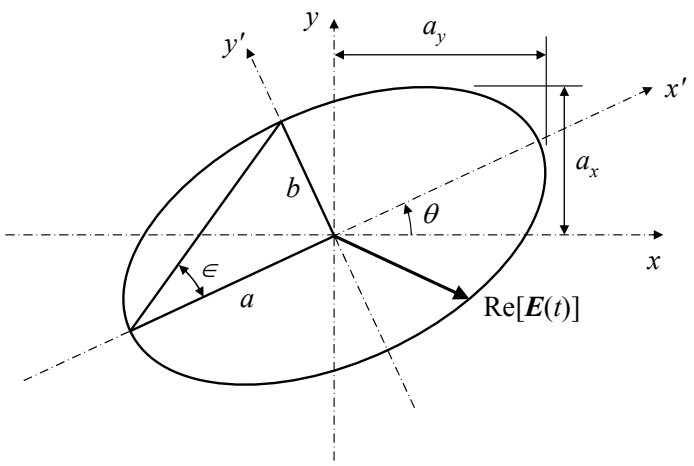

Figure 3.4 Polarization ellipse defined as the time trajectory of the real electric filed. The parameters describing the ellipse are its azimuth θ and ellipticity angle $\epsilon = \arctan(b/a)$, where a and b are the semimajor and semiminor axes of the ellipse, respectively.

where a_x, a_y are the real amplitudes and δ_x, δ_y the real phases of the Cartesian components of the field. Only the real part of the field

$$\mathrm{Re}[\boldsymbol{E}(t)] = a_x \cos\delta_x \begin{bmatrix} a_x \cos(\omega t) \\ a_y \cos(\omega t + \delta) \end{bmatrix} \tag{3.52}$$

has physical meaning, with $\delta = \delta_y - \delta_x$ denoting the phase difference between the two components. Now we see that the real electric field harmonically varies in time, describing a line, a circle, or an ellipse according to the values of a_x, a_y, and δ. Correspondingly we distinguish three kinds of polarization: linear, circular, and elliptic. In Fig. 3.4 an elliptical trajectory of the real electric field is displayed; the linear and circular polarizations can be regarded as limits of the elliptic one.

The Jones vector of the linear polarization can generally be written as $\boldsymbol{J} = a[\cos\theta, \sin\theta]^{\mathrm{T}}$ where a is an arbitrary complex number and θ is the azimuthal angle of the polarization line. The Jones vector of the left-hand and right-hand circular polarization is $\boldsymbol{J} = a[1, \mp i]^{\mathrm{T}}$ where a is again a complex number. All the other cases correspond to elliptic polarizations. We can define unit basis vectors $\hat{\boldsymbol{x}} = [1, 0]^{\mathrm{T}}$ and $\hat{\boldsymbol{y}} = [0, 1]^{\mathrm{T}}$ corresponding to the Cartesian coordinates, or other bases, e. g., the basis of circular polarizations $\hat{\boldsymbol{c}}_{\mathtt{l}} = [1, -i]^{\mathrm{T}}/\sqrt{2}$ and $\hat{\boldsymbol{c}}_{\mathtt{r}} = [1, i]^{\mathrm{T}}/\sqrt{2}$. A general polarization state is a linear combination

$$\boldsymbol{J} = j_1 \hat{\boldsymbol{j}}_1 + j_2 \hat{\boldsymbol{j}}_2 \tag{3.53}$$

of two basis vectors $\hat{\boldsymbol{j}}_1$, $\hat{\boldsymbol{j}}_2$. Bases are usually chosen obeying the orthonormality condition

$$\left\langle \hat{\boldsymbol{j}}_j, \hat{\boldsymbol{j}}_k \right\rangle = \hat{\boldsymbol{j}}_j^{\dagger} \hat{\boldsymbol{j}}_k = \delta_{jk}. \tag{3.54}$$

The simplest examples of linear and circular polarization bases are displayed in Fig. 3.5.

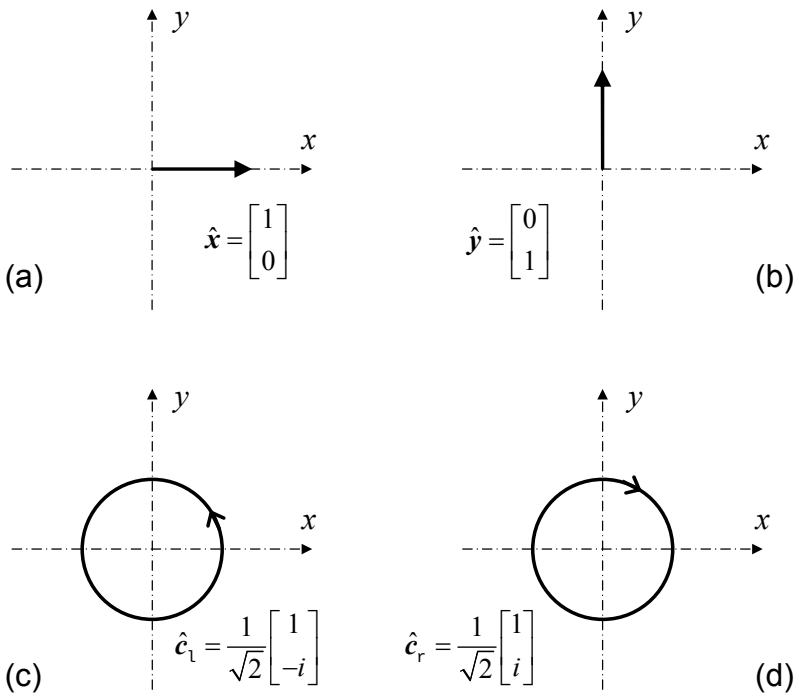

Figure 3.5 Two elementary examples of polarization bases, the basis of linear polarizations (a, b) and the basis of circular polarizations (c, d). The figures are completed by the corresponding Jones vectors evaluated in the representation of linear polarizations.

Although the Jones vector consists of two complex numbers, the polarization state can be represented by fewer parameters because two different vectors $a[j_x, j_y]^{\mathrm{T}}$ and $b[j_x, j_y]^{\mathrm{T}}$ with a and b being different complex numbers correspond to the same state. A way of expressing the polarization by the minimum number of parameters is the representation by a complex number

$$\chi = \frac{j_y}{j_x}, \tag{3.55}$$

where j_x and j_y are the Cartesian components of the Jones vector. Similarly, we can define the complex number $\chi_c = j_{\mathtt{r}}/j_{\mathtt{l}}$ where $j_{\mathtt{l}}$, $j_{\mathtt{r}}$ are the elements of the Jones vector in the circular-polarization basis, or we can use some other basis of two orthogonal elliptic states.

The third way of expressing polarization states which provides a vivid imagination is the representation by ellipsometric parameters, the azimuth θ and the ellipticity angle ϵ of the polarization ellipse. The ellipticity angle $\epsilon = \arctan(b/a)$, where a, b denote the ellipse's semimajor and semiminor axes, is zero for a linear polarization, $\pi/2$ for a circular polarization, and has values between the two limits for elliptic polarizations. By reasoning similar to that leading to Eq. (3.52), we obtain the Jones vector dependence on the ellipsometric parameters

$$\boldsymbol{J} = \mathbf{R}(-\theta) \begin{bmatrix} \cos\epsilon \\ \pm i \sin\epsilon \end{bmatrix} = \begin{bmatrix} \cos\theta\cos\epsilon \mp i \sin\theta\sin\epsilon \\ \sin\theta\cos\epsilon \pm i \cos\theta\sin\epsilon \end{bmatrix}, \tag{3.56}$$

where $\mathbf{R}(-\theta)$ denotes the rotation by the angle $-\theta$. The corresponding dependence of the χ-number on the ellipsometric parameters is

$$\chi = \frac{\tan\theta \pm i\tan\epsilon}{1 \mp i\tan\theta\tan\epsilon}. \tag{3.57}$$

To avoid the ambiguity in choosing the plus or minus sign in the above expressions, we also define the negative ellipticity for the case of counter clockwise polarization. The bottom minus sign is then inhered within the ellipticity angle, which leads to the general formulae

$$\boldsymbol{J} = \begin{bmatrix} \cos\theta\cos\epsilon - i\sin\theta\sin\epsilon \\ \sin\theta\cos\epsilon + i\cos\theta\sin\epsilon \end{bmatrix}, \tag{3.58}$$

$$\chi = \frac{\tan\theta + i\tan\epsilon}{1 - i\tan\theta\tan\epsilon}. \tag{3.59}$$

Similarly, we can derive different dependences of the Jones vector and χ-number on the ellipsometric parameters in other polarization bases.

3.2.2 Space modulation and scalar modes

As we have seen in Eqs. (3.24–3.25), the complete information on a field consists of the information on its polarization and information on its space modulation. Thus the general field can be decomposed into two polarization modes and into modes of different space modulations. Since the propagation in uniform isotropic medium does not change the state of polarization, only the space modulation modes are sometimes studied, referred to as scalar modes.

The decomposition into polarization and scalar modes in a chosen plane $z = 0$ can be written

$$\boldsymbol{E}(x, y, 0) = \sum_{j=1}^{2} \sum_{\mu} f_{j,\mu}\, \hat{\boldsymbol{j}}_j\, \psi_\mu(x, y) \tag{3.60}$$

where $\hat{\boldsymbol{j}}_j$ denotes the jth basis Jones vector, $\psi_\mu(x, y)$ represents the μth scalar mode of propagation, and $f_{j,\mu}$ is the amplitude of the mode characterized by the j and μ mode numbers. According to the type of decomposition, μ can represent either a discrete or a continuous set of values. In the latter case, an integral "$\int \mathrm{d}\mu$" would be used instead of summation.

The simplest basis of scalar modes is the basis of Fourier modes as already seen in Eqs. (3.24–3.25), where the mode identification μ was represented by two real values p, q. Since the propagation of one mode is independent on each other, i. e., the $[p, q]$-mode

$$\psi_{p,q}(x, y) = e^{-ik_0(px+qy)} \tag{3.61}$$

propagates as

$$E_{p,q}(x, y, z) = \psi_{p,q}(x, y) e^{-ik_0\sqrt{\varepsilon - p^2 - q^2}\, z}, \tag{3.62}$$

the modes are called eigenmodes of propagation.

When we look for a solution of the Helmholtz equation in the cylindrical coordinates $[\rho, \phi, z]$, we find other eigenmodes of propagation

$$\psi_{n,\kappa}(\rho, \phi) = B_n(k_0\kappa\rho)e^{-in\phi}, \tag{3.63}$$

where $B_n(k_0\kappa\rho)$ denotes any of the Bessel, Neumann, or Hankel functions. The propagation is then governed by the $e^{-ik_0\sqrt{\varepsilon-\kappa^2}\,z}$ factor, and the scalar modes are represented by a set of one discrete (n) and one continuous (κ) mode numbers.

3.2.3 Symbolic notation of general states of light

So far we were only describing scalar modes using the coordinate and Fourier representations, analogous to the "$\boldsymbol{R}$" and "$\boldsymbol{P}$" representations in quantum physics. For the purpose of later application of linear-algebraic expressions with operators, it will be useful to rewrite the mode decomposition and the requirements of the orthogonality and completeness of modes into a symbolic vectorial form. For the scalar electric field $E(x, y, 0)$ in the chosen plane $z = 0$, we define a vector $\vec{E}$ which can be decomposed

$$\vec{E} = \sum_{\mu} f_\mu \hat{\psi}_\mu, \tag{3.64}$$

with the space propagation symbolically written $\vec{E}(z) = \sum_\mu f_\mu \hat{\psi}_\mu e^{-ik_0 s_\mu z}$ in the case that $\hat{\psi}_\mu$ denote eigenmodes of propagation. The requirements for the orthogonality and completeness of the modes, respectively, can be symbolically written

$$\left\langle \hat{\psi}_\mu, \hat{\psi}_\nu \right\rangle = \delta_{\mu\nu}, \tag{3.65}$$

$$\sum_{\mu} \hat{\psi}_\mu \hat{\psi}_\mu^\dagger = \mathbf{1}, \tag{3.66}$$

where on the left-hand side of the former "$\langle \cdot, \cdot \rangle$" denotes the scalar product defined within the elements of the Hilbert space $L^2(\mathbb{R}^2)$ of all the possible modes. In the latter, $\mathbf{1}$ denotes the identity on the space $L^2(\mathbb{R}^2)$.

Finally, we can combine both the polarization and space-modulation modes to define general modes $\hat{\boldsymbol{\psi}}_{j,\mu} = \hat{\boldsymbol{j}}_j \hat{\psi}_\mu$ with the polarization $\hat{\boldsymbol{j}}_j \in \mathbb{C}^2$ and with the space modulation $\hat{\psi}_\mu \in L^2(\mathbb{R}^2)$. The Hilbert space of general modes is the direct product of the two-dimensional space of Jones vectors and multidimensional space of scalar modes, i. e., $\mathcal{H} = \mathbb{C}^2 \otimes L^2(\mathbb{R}^2)$. Now the requirements for the orthogonality and completeness of the general modes can be written, respectively,

$$\left\langle \hat{\boldsymbol{\psi}}_{j,\mu}, \hat{\boldsymbol{\psi}}_{k,\nu} \right\rangle = \delta_{jk}\delta_{\mu\nu}, \tag{3.67}$$

$$\sum_j \sum_\mu \hat{\boldsymbol{\psi}}_{j,\mu} \hat{\boldsymbol{\psi}}_{j,\mu}^\dagger = \mathbf{1}_{\mathcal{H}} = \mathbf{1}_{\mathbb{C}^2} \otimes \mathbf{1}_{L^2(\mathbb{R}^2)}, \tag{3.68}$$

where on the right-hand side of the latter the identity on the space $\mathcal{H}$ is the tensor product of identities on the $\mathbb{C}^2$ and $L^2(\mathbb{R}^2)$ spaces.

3.3 Propagation through linear optical systems

3.3.1 Definition and symbolic notation of linear optical systems

In Sec. 3.1.2 we demonstrate propagation in a homogenous medium which can be regarded as a linear optical system of transform from one chosen plane $z = z_0$ to another plane $z = z_1$. With the symbolic notation of general states of light, we can define a general linear optical system as a linear operator $\hat{\mathbf{P}}$ operating on the Hilbert space $\mathcal{H}$ of general modes, i. e.,

$$\begin{aligned} \hat{\mathbf{P}} &= \sum_{A,B} \mathbf{P}_A \otimes \hat{\mathsf{P}}_B, \\ \hat{\mathbf{P}} &: \ \mathcal{H} \to \mathcal{H}, \\ \mathbf{P}_A &: \ \mathbb{C}^2 \to \mathbb{C}^2, \\ \hat{\mathsf{P}}_B &: \ L^2(\mathbb{R}^2) \to L^2(\mathbb{R}^2), \end{aligned} \tag{3.69}$$

where $\mathbf{P}_A$ are operators of change of polarization and $\hat{\mathsf{P}}_B$ denote operators of linear transform from one space-modulation mode to another one.

As an illustrative example, suppose a simple dyadic form $\hat{\mathbf{P}} = \mathbf{P} \otimes \hat{\mathsf{P}}$. Thus, if we have a state of an incident wave given by an expansion

$$\vec{\boldsymbol{E}}^{(i)} = \sum_{j=1}^{2} \sum_{\mu} f_{j,\mu}^{(i)} \hat{\boldsymbol{j}}_j \hat{\psi}_\mu \tag{3.70}$$

then the output state is determined as

$$\vec{\boldsymbol{E}}^{(o)} = \hat{\mathbf{P}} \vec{\boldsymbol{E}}^{(i)} = \sum_{j=1}^{2} \sum_{\mu} f_{j,\mu}^{(i)} (\mathbf{P} \hat{\boldsymbol{j}}_j)(\hat{\mathsf{P}} \hat{\psi}_\mu) \tag{3.71}$$

or, after expansion of the output state

$$\vec{\boldsymbol{E}}^{(o)} = \sum_{j=1}^{2} \sum_{\mu} f_{j,\mu}^{(o)} \hat{\boldsymbol{j}}_j \hat{\psi}_\mu, \tag{3.72}$$

we can write the transformation between the components of the both states, i. e.,

$$f_{j,\mu}^{(o)} = \sum_{k=1}^{2} \sum_{\nu} p_{jk} P_{\mu\nu} f_{k,\nu}^{(i)}, \tag{3.73}$$

where $p_{jk} = \langle \hat{\boldsymbol{j}}_j, \mathbf{P} \hat{\boldsymbol{j}}_k \rangle$ and $P_{\mu\nu} = \langle \hat{\psi}_\mu, \hat{\mathsf{P}} \hat{\psi}_\nu \rangle$ are matrix elements of the operators $\mathbf{P}$ and $\hat{\mathsf{P}}$. More symbolically, the above formula can be written

$$f_\alpha^{(o)} = \sum_{\beta} \hat{\mathbf{P}}_{\alpha\beta} f_\beta^{(i)}, \tag{3.74}$$

where α represents the pair of indices j, μ and β represents the pair k, ν.

More specially, if the incident state can be resolved into a dyadic product $\vec{\boldsymbol{E}}^{(i)} = \boldsymbol{J}^{(i)} \vec{E}^{(i)}$, then the transformation can be symbolically written without expansion, i. e., $\vec{\boldsymbol{E}}^{(o)} = (\mathbf{P} \boldsymbol{J}^{(i)})(\hat{\mathsf{P}} \vec{E}^{(i)}) = \boldsymbol{J}^{(o)} \vec{E}^{(o)}$, which means that both the polarization and the space-modulation modes are treated independently.

3.3.2 Transformation of polarization—Jones matrices and ellipsometry

In a chosen basis of two orthogonal states of polarization, the operator $\mathbf{P}$ becomes a Jones matrix. For instance, the Jones matrix in the Cartesian coordinates is

$$\mathbf{P} = \begin{bmatrix} p_{xx} & p_{xy} \\ p_{yx} & p_{yy} \end{bmatrix}, \tag{3.75}$$

where p_{ij} are the amplitude coefficients of the linear transform from one state of polarization into another.

Clearly, the Jones matrix does not only describe the transformation of the polarization ellipse, but also the change of the amplitude of the wave propagating through the optical system. Sometimes it is useful to determine only the former, i. e., the transformation between the complex number $\chi^{(i)}$ of the input polarization and the complex number $\chi^{(o)}$ of the output polarization. Straightforwardly this transform is

$$\chi^{(o)} = \frac{j_y^{(o)}}{j_x^{(o)}} = \frac{p_{yx} j_x^{(i)} + p_{yy} j_y^{(i)}}{p_{xx} j_x^{(i)} + p_{xy} j_y^{(i)}} = \frac{p_{yy}\chi^{(i)} + p_{yx}}{p_{xy}\chi^{(i)} + p_{xx}}, \tag{3.76}$$

where $j_k^{(i)}$, $j_k^{(o)}$ $(k = x, y)$ are the Cartesian components of the input and output Jones vectors, respectively. It is very important to notice that the change of the polarization ellipse is governed by a bilinear transformation of the χ-number and that the output polarization does not depend on the amplitude of the incident light.

Suppose that both the input and the output χ-numbers are evaluated in the basis of the eigenmodes of the matrix $\hat{\mathbf{P}}$. In this basis

$$\hat{\mathbf{P}} = \begin{bmatrix} p_1 & 0 \\ 0 & p_2 \end{bmatrix}, \tag{3.77}$$

$$\chi^{(o)} = \frac{p_2}{p_1}\chi^{(i)}. \tag{3.78}$$

and hence the transformation of the polarization ellipse is governed by a linear transform between the χ-numbers. We define a complex quantity

$$\varrho = \frac{p_2}{p_1} = \tan\Psi \exp i\Delta, \tag{3.79}$$

where the real angles Ψ, Δ are called the ellipsometric parameters of the linear optical system. The parameter Ψ describes the difference in the amplitude changes between the two eigenmodes, whereas Δ the difference in the phase changes.

In more general cases, e. g., when using anisotropic media, the eigenmodes are generally elliptic. Then it is useful to describe the transformation of polarization from an input linear state into an output, generally elliptic state. First, suppose that an x-polarized wave is incident onto the optical system, i. e., $\boldsymbol{J}^{(i)} = \hat{\boldsymbol{x}}$ $(j_x^{(i)} = 1,\ j_y^{(i)} = 0)$. Then, according to

Eq. (3.76), $\chi^{(o)} = p_{yx}/p_{xx}$ describes the output polarization state. On the other hand, if a y-polarized wave is incident, it is better to imagine the whole optical system as rotated by 90° and hence to adopt the coordinates $x' = y$, $y' = -x$. In the rotated coordinates we can apply the same formula, leading to the expression $\chi^{(o)} = -p_{xy}/p_{yy}$ assuming the former coordinates.

Summarizing the above results, we define two complex effects of the polarization-changing system P (described by the Jones matrix $\mathbf{P}$) as

$$\Phi_x^{(P)} = \frac{p_{yx}}{p_{xx}} = \frac{\tan\theta_x^{(P)} + i\tan\epsilon_x^{(P)}}{1 - i\tan\theta_x^{(P)}\tan\epsilon_x^{(P)}}, \tag{3.80}$$

$$\Phi_y^{(P)} = -\frac{p_{xy}}{p_{yy}} = \frac{\tan\theta_y^{(P)} + i\tan\epsilon_y^{(P)}}{1 - i\tan\theta_y^{(P)}\tan\epsilon_y^{(P)}}, \tag{3.81}$$

where the second equalities describe the output polarization states in terms of the azimuth and ellipticity angles, using Eq. (3.59). We refer to $\theta_{x(y)}^{(P)}$ and $\epsilon_{x(y)}^{(P)}$ as the azimuth rotation and ellipticity of the optical system P for incident $x(y)$-polarization.

Besides the trivial example of propagation through a homogenous isotropic medium, we can also write the two Jones matrices describing the reflection and transmission of a plane wave by a boundary between two uniform isotropic media with permittivities $\varepsilon^{(0)}$ and $\varepsilon^{(1)}$, as treated in Sec. 3.1.3. Suppose that a generally polarized plane wave is incident from medium 0 with its angle of incidence (i. e., the angle between the direction of propagation and the normal to the boundary) $\vartheta^{(i)}$. After decomposing the Jones vector into the eigenmodes of reflection and transmission, i. e.,

$$\boldsymbol{J}^{(i)} = j_{\mathtt{s}}^{(i)}\hat{\boldsymbol{s}} + j_{\mathtt{p}}^{(i)}\hat{\boldsymbol{p}}, \tag{3.82}$$

we again obtain

$$\mathbf{R} = \begin{bmatrix} r_{\mathtt{s}} & 0 \\ 0 & r_{\mathtt{p}} \end{bmatrix}, \tag{3.83}$$

$$\mathbf{T} = \begin{bmatrix} t_{\mathtt{s}} & 0 \\ 0 & t_{\mathtt{p}} \end{bmatrix}, \tag{3.84}$$

where the quantities of the diagonals, defined by Eqs. (3.45–3.48), denote the Fresnel reflection and transmission amplitude coefficients of an `s`- or `p`-polarized plane wave, respectively. In Eqs. (3.45–3.48)

$$s^{(J)} = \frac{k_z^{(J)}}{k_0} = N^{(J)}\cos\vartheta^{(J)} \tag{3.85}$$

denotes the normal component of the normalized wave vector $\boldsymbol{k}^{(J)}/k_0$ in the Jth medium with its complex refractive index $N^{(J)} = n^{(J)} - ik^{(J)} = \sqrt{\varepsilon^{(J)}}$.

3.3.3 Transformation of scalar modes

Analogous to the s- and p-eigenmodes of the polarization transforms, the eigenmodes of the reflection and transmission of scalar waves are Fourier modes, owing to the requirement for the continuity of the tangential fields on the boundary. To evaluate the matrix components of the reflection and transmission operators $\hat{\mathsf{R}}$ and $\hat{\mathsf{T}}$, however, each of the s- and p-polarizations must be treated separately, i. e.,

$$\vec{E}^{(r)}_{\mathtt{s}} = \hat{\mathsf{R}}_{\mathtt{s}}\, \vec{E}^{(i)}_{\mathtt{s}}, \tag{3.86}$$
$$\vec{E}^{(r)}_{\mathtt{p}} = \hat{\mathsf{R}}_{\mathtt{p}}\, \vec{E}^{(i)}_{\mathtt{p}}, \tag{3.87}$$
$$\vec{E}^{(t)}_{\mathtt{s}} = \hat{\mathsf{T}}_{\mathtt{s}}\, \vec{E}^{(i)}_{\mathtt{s}}, \tag{3.88}$$
$$\vec{E}^{(t)}_{\mathtt{p}} = \hat{\mathsf{T}}_{\mathtt{p}}\, \vec{E}^{(i)}_{\mathtt{p}}, \tag{3.89}$$

which, after expansion into Fourier modes

$$\vec{E}^{(i)}_{\mathtt{s(p)}} = \int_{-\infty}^{+\infty}\int_{-\infty}^{+\infty} f^{(i)}_{\mathtt{s(p)}}\hat{\psi}(p,q)\,\mathrm{d}p\,\mathrm{d}q, \tag{3.90}$$
$$\vec{E}^{(r)}_{\mathtt{s(p)}} = \int_{-\infty}^{+\infty}\int_{-\infty}^{+\infty} f^{(r)}_{\mathtt{s(p)}}\hat{\psi}(p,q)\,\mathrm{d}p\,\mathrm{d}q, \tag{3.91}$$
$$\vec{E}^{(t)}_{\mathtt{s(p)}} = \int_{-\infty}^{+\infty}\int_{-\infty}^{+\infty} f^{(t)}_{\mathtt{s(p)}}\hat{\psi}(p,q)\,\mathrm{d}p\,\mathrm{d}q, \tag{3.92}$$

with the basis vectors in the Cartesian coordinates being $\hat{\psi}(p,q) = e^{-ik_0(px+qy)}$, become

$$f^{(r)}_{\mathtt{s}} = r_{\mathtt{s}}(p,q) f^{(i)}_{\mathtt{s}}(p,q), \tag{3.93}$$
$$f^{(r)}_{\mathtt{p}} = r_{\mathtt{p}}(p,q) f^{(i)}_{\mathtt{p}}(p,q), \tag{3.94}$$
$$f^{(t)}_{\mathtt{s}} = t_{\mathtt{s}}(p,q) f^{(i)}_{\mathtt{s}}(p,q), \tag{3.95}$$
$$f^{(t)}_{\mathtt{p}} = t_{\mathtt{p}}(p,q) f^{(i)}_{\mathtt{p}}(p,q), \tag{3.96}$$

where $r_{\mathtt{s(p)}}(p,q)$, $t_{\mathtt{s(p)}}(p,q)$ are the Fresnel reflection and transmission amplitude coefficients of s(p)-modes taking the same values as in Eq. (3.45–3.48) but with

$$s^{(J)}(p,q) = \sqrt{\varepsilon^{(J)} - p^2 - q^2}, \tag{3.97}$$

like in Eq. (3.27).

3.4 Optical response of planar structures

So far we have shown two types of linear optical systems, a homogenous medium between two plan-parallel planes and an interface between two homogenous media with different

permittivities. In general, we will refer to a *planar structure* as a set of one or more plan-parallel interfaces between homogenous media indexed by integers $J \in \{0, 1, 2, \ldots, N{+}1\}$ with permittivities $\varepsilon^{(J)}$. The top medium, a half-space indexed $J = 0$, is called *superstrate*, the bottom medium, a half-space indexed $J = N + 1$, is called *substrate*, and the media sandwiched between the two ambient half-spaces are called *thin films* or *layers* when their thicknesses are smaller than the coherence length of light or *thick layers* when their thicknesses are higher. In the former case the interference effects in the optical response appear, whereas in the latter case only the intensities are superposed.

3.4.1 Fraunhofer approximation

A traditional notion of the optical response of planar structures is that light is generated by a point source located in a sufficient distance from the structure, a distance much higher than the structure's dimensions. Thus, instead of a spherical wave whose interaction with a planar structure is governed by quite a complicated way, Fraunhofer's plane-wave approximation of the spherical wave can be used. As we have seen in Sec. 3.3, this method is very advantageous since the plane waves are eigenmodes of reflection and transmission on plane boundaries.

To avoid enormous waste of energy in directions beyond the structure, particular arrangements are used in practice to achieve high intensity of illumination. In spectroscopic ellipsometers, usually the light generated by a lamp is reflected by a spherical mirror to obtain a beam of parallel rays from which the main part is selected by a pinhole and then collimated, so that the pinhole's image is focused on the top surface of the structure. Thus, only a small area of interest is measured on the sample, but still this area is bigger by several orders than the wavelength of light, so that the Fraunhofer approximation by a single plane wave can be applied if the position of the detector is adjusted to the maximum intensity to choose the major plane-wave mode from the beam reflected or transmitted by the structure.

3.4.2 Fresnel formulae for an interface

Applying the Fraunhofer approximation, we only work with one chosen $[p, q]$-mode. For simplicity we choose the Cartesian coordinates $[x^{(i)}, y^{(i)}, z^{(i)}]$ linked with the incident plane wave so that the $x^{(i)}$-coordinate is coincident with the `s`-eigenmode of polarization, the $y^{(i)}$-coordinate with the `p`-eigenmode of polarization, and the $z^{(i)}$-coordinate with the direction of propagation. On the other hand, the coordinates $[x, y, z]$ linked with the planar structure are chosen so that the x-coordinate is equal to the $x^{(i)}$-coordinate, the z-coordinate is normal to the interfaces and points to the direction of the increasing index of media J, and the y-coordinate uniquely completes the clockwise coordinate system.

With the above definition of the coordinates, the x-component of the wave vector of the incident plane wave is reduced, so that only a planar problem is to be solved, characterized

by two coordinates $[y, z]$. Now the propagation (3.62) of the space-modulation mode characterized by the q-number is in medium J governed by the relation

$$E^{(J)}(y,z) = E^{(J)}(y,z_{J-1}) \exp\left[-ik_0\sqrt{\varepsilon^{(J)}-q^2}(z-z_{J-1})\right], \tag{3.98}$$

where $z = z_{J-1}$ is the plane of interface between media $J-1$ and J (except medium 0 for which $z = z_0$ is chosen) while the reflection and transmission (3.93)–(3.96) of the mode on the interface between medium J and medium $J+1$ can be written as

$$f_{\mathtt{s}}^{(r)} = r_{\mathtt{s}}^{J,J+1} f_{\mathtt{s}}^{(i)}, \tag{3.99}$$
$$f_{\mathtt{p}}^{(r)} = r_{\mathtt{p}}^{J,J+1} f_{\mathtt{p}}^{(i)}, \tag{3.100}$$
$$f_{\mathtt{s}}^{(t)} = t_{\mathtt{s}}^{J,J+1} f_{\mathtt{s}}^{(i)}, \tag{3.101}$$
$$f_{\mathtt{p}}^{(t)} = t_{\mathtt{p}}^{J,J+1} f_{\mathtt{p}}^{(i)}, \tag{3.102}$$

where

$$r_{\mathtt{s}}^{J,J+1} = \frac{s^{(J)} - s^{(J+1)}}{s^{(J)} + s^{(J+1)}}, \tag{3.103}$$
$$t_{\mathtt{s}}^{J,J+1} = \frac{2s^{(J)}}{s^{(J)} + s^{(J+1)}}, \tag{3.104}$$
$$r_{\mathtt{p}}^{J,J+1} = \frac{\varepsilon^{(J)}s^{(J+1)} - \varepsilon^{(J+1)}s^{(J)}}{\varepsilon^{(J)}s^{(J+1)} + \varepsilon^{(J+1)}s^{(J)}}, \tag{3.105}$$
$$t_{\mathtt{p}}^{J,J+1} = \frac{2\varepsilon^{(J)}s^{(J+1)}}{\varepsilon^{(J)}s^{(J+1)} - \varepsilon^{(J+1)}s^{(J)}}, \tag{3.106}$$

with

$$s^{(J)} = \sqrt{\varepsilon^{(J)} - q^2}. \tag{3.107}$$

3.4.3 Airy formulae for a thin film

As a little more complicated example, we will evaluate the amplitude reflection and transmission coefficients of a plane wave incident to a single thin film with permittivity $\varepsilon^{(1)}$ sandwiched between a superstrate with permittivity $\varepsilon^{(0)}$ and substrate with permittivity $\varepsilon^{(2)}$ under the angle of incidence $\vartheta^{(i)}$.

Besides the Fresnel coefficients $r_{\mathtt{s(p)}}^{01}$, $t_{\mathtt{s(p)}}^{01}$, $r_{\mathtt{s(p)}}^{10}$, $r_{\mathtt{s(p)}}^{10}$, $r_{\mathtt{s(p)}}^{12}$, $t_{\mathtt{s(p)}}^{12}$, governing the interaction of light with the two boundaries, we apply Eq. (3.98) to define an amplitude coefficient governing the propagation of the mode between the two interfaces of the thin film with the ambient media. The propagation coefficient is simply

$$p = \frac{E(y,z_1)}{E(y,z_0)} = e^{-ik_0 s^{(1)}(z_1-z_0)} \tag{3.108}$$

for both s- and p-polarizations, with $s^{(1)} = +\sqrt{\varepsilon^{(1)} - q^2}$ and $q = \sqrt{\varepsilon^{(0)}}\sin\vartheta^{(i)}$. Analogously we can calculate the propagation coefficient for the corresponding upward mode

$$p' = \frac{E'(y,z_0)}{E'(y,z_1)} = e^{-ik_0 s'^{(1)}(z_0-z_1)} \tag{3.109}$$

with $s'^{(1)} = -\sqrt{\varepsilon^{(1)} - q^2}$, and hence $p' = p$.

The optical response of the thin film for one chosen polarization can be evaluated as the superposition of wave contributions resulting from multiple internal reflections

$$\begin{aligned} r^{02} &= r^{01} + t^{10} p\, r^{12} p\, t^{01} + t^{10} p\, r^{12} \left(p\, r^{10} p\, r^{12}\right) p\, t^{01} + \ldots \\ &= r^{01} + t^{10} p\, r^{12} \left(1 + Q + Q^2 + \ldots\right) p\, t^{01} \\ &= r^{01} + \frac{t^{10} p\, r^{12} p\, t^{01}}{1 - Q}, \end{aligned} \tag{3.110}$$

$$\begin{aligned} t^{02} &= t^{12} p\, t^{01} + t^{12} \left(p\, r^{10} p\, r^{12}\right) p\, t^{01} + \ldots \\ &= t^{12} \left(1 + Q + Q^2 + \ldots\right) p\, t^{01} \\ &= \frac{t^{12} p\, t^{01}}{1 - Q}, \end{aligned} \tag{3.111}$$

where $Q = p\, r^{10} p\, r^{12}$ is the coefficient of the geometric series. The resulting formulae

$$r^{02} = \frac{r^{01} + r^{12} p^2}{1 + r^{01} r^{12} p^2}, \tag{3.112}$$

$$t^{02} = \frac{t^{01} t^{12} p}{1 + r^{01} r^{12} p^2}, \tag{3.113}$$

are Airy's formulae for the amplitude reflection and transmission coefficients of a thin film.

3.4.4 Recursive formulae for multilayers

The optical response of a system of more than one thin film, called a *multilayer*, can easily be calculated by the recursive relations

$$r^{0,J+1} = r^{0J} + \frac{t^{J0} p^{(J)}\, r^{J,J+1} p^{(J)} t^{0J}}{1 - Q^{(J)}}, \tag{3.114}$$

$$t^{0,J+1} = \frac{t^{J,J+1} p^{(J)} t^{0J}}{1 - Q^{(J)}}, \tag{3.115}$$

obtained directly from Eqs. (3.110–3.111) recursively for $J = 1, 2, \ldots, N$, where the quantities $p^{(J)}$ and $Q^{(J)}$ belong to the Jth layer and where the quantities with the "$0J$" and "$J0$" superscripts are regarded as quantities belonging to a pseudointerface consisting of the first $J - 1$ layers.

3.4.5 Optical response of planar anisotropic structures

Propagation through a uniform anisotropic medium, defined by a tensorial permittivity constant

$$\boldsymbol{\varepsilon} = \begin{bmatrix} \varepsilon_{xx} & \varepsilon_{xy} & \varepsilon_{xz} \\ \varepsilon_{yx} & \varepsilon_{yy} & \varepsilon_{yz} \\ \varepsilon_{zx} & \varepsilon_{zy} & \varepsilon_{zz} \end{bmatrix}, \tag{3.116}$$

and reflection/transmission on interfaces between such media are governed by more general relations than derived above, where we assumed for simplicity the optical isotropy. Analytical solution corresponding to either general or particular cases (such as *uniaxial anisotropy*) are beyond the scope of this thesis. However, the numerical solution is inhered within the general case of optical theory for anisotropic inhomogeneous media treated in Chap 4. The formally written optical response of planar anisotropic structures in the form of Jones matrices is of high importance since in this thesis we work with anisotropic media.

We assume a multilayer structure consisting of N thin films, where at least one of those is anisotropic and described by the permittivity tensor (3.116). The the reflection and transmission by such a structure is described by generally nondiagnonal Jones matrices

$$\mathbf{R}^{0,N+1} = \begin{bmatrix} r_{\mathtt{ss}}^{0,N+1} & r_{\mathtt{sp}}^{0,N+1} \\ r_{\mathtt{ps}}^{0,N+1} & r_{\mathtt{pp}}^{0,N+1} \end{bmatrix}, \tag{3.117}$$

$$\mathbf{T}^{0,N+1} = \begin{bmatrix} t_{\mathtt{ss}}^{0,N+1} & t_{\mathtt{sp}}^{0,N+1} \\ t_{\mathtt{ps}}^{0,N+1} & t_{\mathtt{pp}}^{0,N+1} \end{bmatrix}, \tag{3.118}$$

where the matrix elements are proper generalized versions of the reflection and transmission coefficients (3.114, 3.115), respectively.

Because in this thesis we will focus on uniaxial anisotropies induced by external magnetic fields, i. e., magneto-optic anisotropies, particularly studied in the reflection mode, we will here briefly describe how a uniaxial anisotropy determines the Jones reflection matrix. Suppose that the the above defined structure is optically isotropic but one of the layers is ferromagnetic and that its magnetization, described by a constant vector $\boldsymbol{M} = [m_x, m_y, m_z]$, is saturated everywhere within the ferromagnetic medium by an external magnetic field of sufficient magnitude. Then the Jones reflection matrix of the whole structure can be written as

$$\mathbf{R}^{0,N+1} = \begin{bmatrix} r_{\mathtt{ss}}^{(0)} & P(m_z) - L(m_y) \\ P(m_z) + L(m_y) & r_{\mathtt{pp}}^{(0)} + T(m_x) \end{bmatrix}, \tag{3.119}$$

where $r_{\mathtt{ss}}^{(0)}$ and $r_{\mathtt{pp}}^{(0)}$ are reflection coefficients with the absence of magnetization (corresponding to an entirely isotropic structure) and where $P(m_z)$, $L(m_y)$, and $T(m_x)$ describe the polar, longitudinal, and transverse magneto-optic effects, referred to as *Kerr's magneto-optic effects* in the particular geometries. In other words, the dependence of the reflection coefficients is only via these three quantities, each of which only depends on a single component of the magnetization vector. In most materials (and in all the materials used in this thesis) the Kerr magneto-optic effects are small so that they can be described as linear effects, i. e.,

$$P(m_z) \approx P_0 m_z, \tag{3.120}$$

$$L(m_y) \approx L_0 m_y, \tag{3.121}$$

$$T(m_x) \approx T_0 m_x. \tag{3.122}$$

Similarly, we can describe the transmission through an anisotropic structure by analogous reasoning. We refer to the transmission effect of a change of polarization as Faraday's (magneto-optic) effect.

3.4.6 Quantities characterizing planar structures—photometric and ellipsometric parameters

A simple and straightforward characterization which provides the complete information on a planar structure is using the Jones reflection and transmission matrices. In practice, however, such complete information is not usually measurable. Instead, the transformation of only the intensity or only the polarization ellipse are measured. For this purpose, assuming an isotropic structure, we define photometric parameters

$$R_{\mathtt{s(p)}} = \left|r_{\mathtt{s(p)}}\right|^2, \tag{3.123}$$

$$T_{\mathtt{s(p)}} = \left|t_{\mathtt{s(p)}}\right|^2, \tag{3.124}$$

called the energy reflectance and transmittance of an $\mathtt{s(p)}$-polarized wave, and ellipsometric parameters by the formulae

$$\varrho^{(r)} = \frac{r_{\mathtt{p}}}{r_{\mathtt{s}}} = \tan\Psi^{(r)} \exp i\Delta^{(r)}, \tag{3.125}$$

$$\varrho^{(t)} = \frac{t_{\mathtt{p}}}{t_{\mathtt{s}}} = \tan\Psi^{(t)} \exp i\Delta^{(t)}, \tag{3.126}$$

for the reflected and transmitted waves, respectively.

Then, assuming an anisotropic structure we formulate the above mentioned Kerr (K) and Faraday (F) effects as

$$\Phi_{\mathtt{s}}^{(K)} = -\frac{r_{\mathtt{ps}}}{r_{\mathtt{ss}}} = \frac{\tan\theta_{\mathtt{s}}^{(K)} + i\tan\epsilon_{\mathtt{s}}^{(K)}}{1 - i\tan\theta_{\mathtt{s}}^{(K)}\tan\epsilon_{\mathtt{s}}^{(K)}}, \tag{3.127}$$

$$\Phi_{\mathtt{p}}^{(K)} = \frac{r_{\mathtt{sp}}}{r_{\mathtt{pp}}} = \frac{\tan\theta_{\mathtt{p}}^{(K)} + i\tan\epsilon_{\mathtt{p}}^{(K)}}{1 - i\tan\theta_{\mathtt{p}}^{(K)}\tan\epsilon_{\mathtt{p}}^{(K)}}, \tag{3.128}$$

$$\Phi_{\mathtt{s}}^{(F)} = \frac{t_{\mathtt{ps}}}{t_{\mathtt{ss}}} = \frac{\tan\theta_{\mathtt{s}}^{(F)} + i\tan\epsilon_{\mathtt{s}}^{(F)}}{1 - i\tan\theta_{\mathtt{s}}^{(F)}\tan\epsilon_{\mathtt{s}}^{(F)}}, \tag{3.129}$$

$$\Phi_{\mathtt{p}}^{(F)} = -\frac{t_{\mathtt{sp}}}{t_{\mathtt{pp}}} = \frac{\tan\theta_{\mathtt{p}}^{(F)} + i\tan\epsilon_{\mathtt{p}}^{(F)}}{1 - i\tan\theta_{\mathtt{p}}^{(F)}\tan\epsilon_{\mathtt{p}}^{(F)}}, \tag{3.130}$$

for the both cases of an incident $\mathtt{s}$- and $\mathtt{p}$-polarized wave, respectively. The angular parameters $\theta_{s(p)}^{(K,F)}$, $\epsilon_{s(p)}^{(K,F)}$ are called the Kerr and Faraday azimuth rotation and ellipticity angle for the incident $\mathtt{s(p)}$-polarization.

3.5 Optical response of diffraction gratings

Unlike the planar structures, the eigenmodes of a structure with periodic lateral patterning, called a *grating*, are more complicated modes, generally composed of many Fourier

modes which are themselves said to be coupled by the grating's periodicity. Therefore, if the illumination in the Fraunhofer approximation is described by an incident plane wave

$$\boldsymbol{E}^{(i)}(\boldsymbol{r}) = A^{(i)}\boldsymbol{j}^{(i)} \exp\left[-ik_0(p^{(i)}x + q^{(i)}y + s^{(i)}z)\right], \tag{3.131}$$

with an amplitude $A^{(i)}$, polarization $\boldsymbol{j}^{(i)}$, and wave vector $\boldsymbol{k}^{(i)} = k_0[p^{(i)}, q^{(i)}, s^{(i)}]^{\mathrm{T}}$, the reflected and transmitted waves will generally be consisting of many $[p, q]$-modes. We refer to this phenomenon as *diffraction* by non-planar structures.

3.5.1 Rayleigh expansion

The translational symmetry induced by the periodicity of the grating implies a highly appreciable reduction of the dimension of the diffraction problem. In the case of a general two-dimensional grating with periodicities Λ_x, and Λ_y in the directions of the x- and y-axes, respectively, the symmetry can be mathematically stated as

$$\begin{aligned}
\boldsymbol{E}^{(i)}(x + m\Lambda_x, y + n\Lambda_y, 0) &= \boldsymbol{E}^{(i)}(x, y, 0)\, e^{-ik_0(p^{(i)}m\Lambda_x + q^{(i)}n\Lambda_y)}, && (3.132)\\
\boldsymbol{E}^{(r)}(x + m\Lambda_x, y + n\Lambda_y, 0) &= \boldsymbol{E}^{(r)}(x, y, 0)\, e^{-ik_0(p^{(i)}m\Lambda_x + q^{(i)}n\Lambda_y)}, && (3.133)\\
\boldsymbol{E}^{(t)}(x + m\Lambda_x, y + n\Lambda_y, d) &= \boldsymbol{E}^{(t)}(x, y, d)\, e^{-ik_0(p^{(i)}m\Lambda_x + q^{(i)}n\Lambda_y)}, && (3.134)
\end{aligned}$$

where d is the thickness of the grating and m, n denote arbitrary integers. Then the reflected and transmitted waves can be written as a periodic vectorial function $\boldsymbol{f}^{(r,t)}(x, y)$ factorized by the $e^{-ik_0\left(p^{(i)}x + q^{(i)}y\right)}$ factor, i. e.,

$$\begin{aligned}
\boldsymbol{E}^{(r)}(x, y, 0) &= \boldsymbol{f}^{(r)}(x, y)\, e^{-ik_0(p^{(i)}x + q^{(i)}y)} = \sum_{m,n=-\infty}^{+\infty} \boldsymbol{f}_{mn}^{(r)}\, e^{-ik_0(p_m x + q_n y)}, && (3.135)\\
\boldsymbol{E}^{(t)}(x, y, d) &= \boldsymbol{f}^{(t)}(x, y)\, e^{-ik_0(p^{(i)}x + q^{(i)}y)} = \sum_{m,n=-\infty}^{+\infty} \boldsymbol{f}_{mn}^{(t)}\, e^{-ik_0(p_m x + q_n y)}, && (3.136)
\end{aligned}$$

where $\boldsymbol{f}_{mn}^{(r,t)}$ denote the components of the Fourier series of the function $\boldsymbol{f}^{(r,t)}(x, y)$ and where

$$\begin{aligned}
p_m &= p^{(i)} + m\frac{\lambda}{\Lambda_x}, && (3.137)\\
q_n &= q^{(i)} + n\frac{\lambda}{\Lambda_y}. && (3.138)
\end{aligned}$$

Hence, only a discrete set of plane waves in both the reflection and transmission modes appears, referred to as *diffraction orders*, each of which is identified by the m, n numbers. The resulting propagation of diffracted waves is governed by the formulae

$$\begin{aligned}
\boldsymbol{E}^{(r)}(\boldsymbol{r}) &= \sum_{m,n=-\infty}^{+\infty} \boldsymbol{f}_{mn}^{(r)} \exp\left[-ik_0(p_m x + q_n y + s_{mn}^{(r)} z)\right], && (3.139)\\
\boldsymbol{E}^{(t)}(\boldsymbol{r}) &= \sum_{m,n=-\infty}^{+\infty} \boldsymbol{f}_{mn}^{(t)} \exp\left\{-ik_0\left[p_m x + q_n y + s_{mn}^{(t)}(z - d)\right]\right\}, && (3.140)
\end{aligned}$$

where the normal components of the wave vectors are

$$s_{mn}^{(r)} = -\sqrt{\varepsilon^{(0)} - p_m^2 - q_n^2}, \tag{3.141}$$

$$s_{mn}^{(t)} = \sqrt{\varepsilon^{(2)} - p_m^2 - q_n^2}, \tag{3.142}$$

$$\tag{3.143}$$

with $\varepsilon^{(0)}$ and $\varepsilon^{(2)}$ denoting the permittivities of the superstrate and substrate media, respectively, sandwiching a generally unspecified grating medium 1. The series in Eqs. (3.139–3.140) are called Rayleigh's expansion of reflected and transmitted waves.

3.5.2 Planar diffraction mounting

Let $[x^{(i)}, y^{(i)}, z^{(i)}]$ and $[x, y, z]$ be two Cartesian coordinate systems linked with an incident plane wave and with a one-dimensional grating, respectively, defined so that the $x \equiv x^{(i)}$-axis coincides with the s-polarization, $y^{(i)}$-axis with the p-polarization, $z^{(i)}$-axis with the incident wave's propagation, and z-axis with a vector normal to the grating's interfaces; the $+z$ direction points to the substrate. Essentially this arrangement is identical with the case of a planar structure described in Sec. 3.4.2; this time, however, the structure exhibits different optical responses when it is rotated around the z-axis.

The most simple configuration is such that the grating's periodicity coincides with the y-axis, because then both the permittivity function $\varepsilon(y, z)$ defined in the whole space and the electric and magnetic fields $\boldsymbol{E}(y, z)$, $\boldsymbol{H}(y, z)$ including the fields in the superstrate, in the substrate, and inside the grating are functions of only two Cartesian coordinates, and hence the entire problem of diffraction can be described in the y—z plane. This is the reason for referring this arrangement as the *planar diffraction* mounting.

3.5.3 Planar diffraction on one-dimensional isotropic gratings

Assuming a one-dimensional grating mounted for planar diffraction, the time-harmonic Maxwell equations

$$\nabla \times \boldsymbol{E} = -i\omega\mu_0 \boldsymbol{H}, \tag{3.144}$$

$$\nabla \times \boldsymbol{H} = i\omega\varepsilon_0 \varepsilon(y, z)\boldsymbol{E}, \tag{3.145}$$

$$\nabla \cdot [\varepsilon(y, z)\boldsymbol{E}] = 0, \tag{3.146}$$

$$\nabla \cdot \boldsymbol{H} = 0, \tag{3.147}$$

can be separated into two independent sets of equations, one for the transverse electric field $\boldsymbol{E}_{\mathrm{TE}} = [E_x, 0, 0]^{\mathrm{T}}$,

$$\begin{aligned}
\partial_z E_x &= -i\omega\mu_0 H_y, && (3.148)\\
-\partial_y E_x &= -i\omega\mu_0 H_z, && (3.149)\\
\partial_y H_z - \partial_z H_y &= i\omega\varepsilon_0\varepsilon(y,z) E_x && (3.150)\\
\partial_y H_y + \partial_z H_z &= 0, && (3.151)
\end{aligned}$$

and one for the transverse magnetic field $\boldsymbol{H}_{\mathrm{TM}} = [H_x, 0, 0]^{\mathrm{T}}$,

$$\begin{aligned}
\partial_z H_x &= i\omega\mu_0 E_y, && (3.152)\\
-\partial_y H_x &= i\omega\mu_0 E_z, && (3.153)\\
\partial_y E_z - \partial_z E_y &= -i\omega\mu_0 H_x && (3.154)\\
\partial_y \left[\varepsilon(y,z) E_y\right] + \partial_z \left[\varepsilon(y,z) E_z\right] &= 0, && (3.155)
\end{aligned}$$

and, of course, the trivial equations $\partial_x E_j = 0$ and $\partial_x H_j = 0$, $j = x, y, z$.

As a result we can write a statement that the s- and p-polarization modes are preserved in the planar diffraction mounting, which reduces the problem into *scalar diffraction*, i. e., diffraction of scalar waves. The incident, reflected, and transmitted waves are then

$$\begin{aligned}
\boldsymbol{E}^{(i)}(\boldsymbol{r}) &= A^{(i)}\hat{\boldsymbol{x}} \exp\left[-ik_0(q^{(i)}y + s^{(i)}z)\right], && (3.156)\\
\boldsymbol{E}^{(r)}(\boldsymbol{r}) &= \hat{\boldsymbol{x}} \sum_{n=-\infty}^{+\infty} f_n^{(r)} \exp\left[-ik_0(q_n y + s_n^{(r)} z)\right], && (3.157)\\
\boldsymbol{E}^{(t)}(\boldsymbol{r}) &= \hat{\boldsymbol{x}} \sum_{n=-\infty}^{+\infty} f_n^{(t)} \exp\left\{-ik_0\left[q_n y + s_n^{(t)}(z-d)\right]\right\} && (3.158)
\end{aligned}$$

for the case of s-polarization and

$$\begin{aligned}
\boldsymbol{H}^{(i)}(\boldsymbol{r}) &= B^{(i)}\hat{\boldsymbol{x}} \exp\left[-ik_0(q^{(i)}y + s^{(i)}z)\right], && (3.159)\\
\boldsymbol{H}^{(r)}(\boldsymbol{r}) &= \hat{\boldsymbol{x}} \sum_{n=-\infty}^{+\infty} h_n^{(r)} \exp\left[-ik_0(q_n y + s_n^{(r)} z)\right], && (3.160)\\
\boldsymbol{H}^{(t)}(\boldsymbol{r}) &= \hat{\boldsymbol{x}} \sum_{n=-\infty}^{+\infty} h_n^{(t)} \exp\left\{-ik_0\left[q_n y + s_n^{(t)}(z-d)\right]\right\} && (3.161)
\end{aligned}$$

for the case of p-polarization. The optical response can be divided into the diffraction orders by defining generalized amplitude reflection and transmission coefficients

$$\begin{aligned}
r_{\mathtt{s}}^{(n)} &= \frac{f_n^{(r)}}{A^{(i)}}, && (3.162)\\
t_{\mathtt{s}}^{(n)} &= \frac{f_n^{(t)}}{A^{(i)}}, && (3.163)\\
r_{\mathtt{p}}^{(n)} &= \frac{f_n^{(r)}}{B^{(i)}}, && (3.164)\\
t_{\mathtt{p}}^{(n)} &= \frac{h_n^{(t)}}{B^{(i)}} && (3.165)
\end{aligned}$$

for both polarizations, respectively, from which we obtain the Jones reflection and transmission matrices

$$\mathbf{R}^{(n)} = \begin{bmatrix} r_{\mathtt{s}}^{(n)} & 0 \\ 0 & r_{\mathtt{p}}^{(n)} \end{bmatrix}, \tag{3.166}$$

$$\mathbf{T}^{(n)} = \begin{bmatrix} t_{\mathtt{s}}^{(n)} & 0 \\ 0 & t_{\mathtt{p}}^{(n)} \end{bmatrix} \tag{3.167}$$

and the corresponding photometric and ellipsometric parameters

$$R_{\mathtt{s(p)}}^{(n)} = \left| r_{\mathtt{s(p)}}^{(n)} \right|^2, \tag{3.168}$$

$$T_{\mathtt{s(p)}}^{(n)} = \left| t_{\mathtt{s(p)}}^{(n)} \right|^2, \tag{3.169}$$

$$\varrho_r^{(n)} = \frac{r_{\mathtt{p}}^{(n)}}{r_{\mathtt{s}}^{(n)}} = \tan \Psi_r^{(n)} \exp i\Delta_r^{(n)}, \tag{3.170}$$

$$\varrho_t^{(n)} = \frac{t_{\mathtt{p}}^{(n)}}{t_{\mathtt{s}}^{(n)}} = \tan \Psi_t^{(n)} \exp i\Delta_t^{(n)}. \tag{3.171}$$

3.5.4 Planar diffraction on one-dimensional magnetic gratings

In a more general case of a magneto-optically anisotropic grating, which partially mixes s- and p-polarizations due to magnetic ordering described above, we write the incident, reflected, and transmitted electric fields as

$$\boldsymbol{E}^{(i)}(\boldsymbol{r}) = A^{(i)} \hat{\boldsymbol{s}} \exp\left[-ik_0(q^{(i)}y + s^{(i)}z)\right], \tag{3.172}$$

$$\boldsymbol{E}^{(r)}(\boldsymbol{r}) = \sum_{n=-\infty}^{+\infty} (f_{\mathtt{s},n}^{(r)} \hat{\boldsymbol{s}} + f_{\mathtt{p},n}^{(r)} \hat{\boldsymbol{p}}_n^{(r)}) \exp\left[-ik_0(q_n y + s_n^{(r)} z)\right], \tag{3.173}$$

$$\boldsymbol{E}^{(t)}(\boldsymbol{r}) = \sum_{n=-\infty}^{+\infty} (f_{\mathtt{s},n}^{(t)} \hat{\boldsymbol{s}} + f_{\mathtt{p},n}^{(t)} \hat{\boldsymbol{p}}_n^{(t)}) \exp\left[-ik_0(q_n y + s_n^{(r)}(z-d))\right], \tag{3.174}$$

(where $\hat{\boldsymbol{s}}$, $\hat{\boldsymbol{p}}_n^{(r,t)}$ are unit polarization vectors for each diffraction order) provided that an s-polarized wave is incident upon the grating. The generalized amplitude reflection and transmission coefficients then become

$$r_{\mathtt{ss}}^{(n)} = \frac{f_{\mathtt{s},n}^{(r)}}{A^{(i)}}, \tag{3.175}$$

$$r_{\mathtt{ps}}^{(n)} = \frac{f_{\mathtt{p},n}^{(r)}}{A^{(i)}}, \tag{3.176}$$

$$t_{\mathtt{ss}}^{(n)} = \frac{f_{\mathtt{s},n}^{(t)}}{A^{(i)}}, \tag{3.177}$$

$$t_{\mathtt{ps}}^{(n)} = \frac{f_{\mathtt{p},n}^{(t)}}{A^{(i)}}, \tag{3.178}$$

respectively, where the offdiagonal coefficients can be separated into the polar and longitudinal Kerr or Faraday effects, like in the above case of a planar magnetic structure.

Analogously we can assume a p-polarized incident wave

$$\boldsymbol{E}^{(i)}(\boldsymbol{r}) = B^{(i)}\hat{\boldsymbol{p}}^{(i)} \exp\left[-ik_0(q^{(i)}y + s^{(i)}z)\right], \tag{3.179}$$

and keep the diffracted fields in the forms (3.173, 3.174). Then we obtain

$$r_{\mathtt{sp}}^{(n)} = \frac{f_{\mathtt{s},n}^{(r)}}{B^{(i)}}, \tag{3.180}$$

$$r_{\mathtt{pp}}^{(n)} = \frac{f_{\mathtt{p},n}^{(r)}}{B^{(i)}}, \tag{3.181}$$

$$t_{\mathtt{sp}}^{(n)} = \frac{f_{\mathtt{s},n}^{(t)}}{B^{(i)}}, \tag{3.182}$$

$$t_{\mathtt{pp}}^{(n)} = \frac{f_{\mathtt{p},n}^{(t)}}{B^{(i)}}, \tag{3.183}$$

determining the amplitude reflection and transmission coefficients.

Finally we will write the Jones reflection and transmission matrices

$$\mathbf{R}^{(n)} = \begin{bmatrix} r_{\mathtt{ss}}^{(n)} & r_{\mathtt{sp}}^{(n)} \\ r_{\mathtt{ps}}^{(n)} & r_{\mathtt{pp}}^{(n)} \end{bmatrix}, \tag{3.184}$$

$$\mathbf{T}^{(n)} = \begin{bmatrix} t_{\mathtt{ss}}^{(n)} & t_{\mathtt{sp}}^{(n)} \\ t_{\mathtt{ps}}^{(n)} & t_{\mathtt{pp}}^{(n)} \end{bmatrix} \tag{3.185}$$

and the corresponding generalized complex Kerr and Faraday effects

$$\Phi_{K\mathtt{s}}^{(n)} = -\frac{r_{\mathtt{ps}}^{(n)}}{r_{\mathtt{ss}}^{(n)}} = \frac{\tan\theta_{K\mathtt{s}}^{(n)} + i\tan\epsilon_{K\mathtt{s}}^{(n)}}{1 - i\tan\theta_{K\mathtt{s}}^{(n)}\tan\epsilon_{K\mathtt{s}}^{(n)}}, \tag{3.186}$$

$$\Phi_{K\mathtt{p}}^{(n)} = \frac{r_{\mathtt{sp}}^{(n)}}{r_{\mathtt{pp}}^{(n)}} = \frac{\tan\theta_{K\mathtt{p}}^{(n)} + i\tan\epsilon_{K\mathtt{p}}^{(n)}}{1 - i\tan\theta_{K\mathtt{p}}^{(n)}\tan\epsilon_{K\mathtt{p}}^{(n)}}, \tag{3.187}$$

$$\Phi_{F\mathtt{s}}^{(n)} = \frac{t_{\mathtt{ps}}^{(n)}}{t_{\mathtt{ss}}^{(n)}} = \frac{\tan\theta_{F\mathtt{s}}^{(n)} + i\tan\epsilon_{F\mathtt{s}}^{(n)}}{1 - i\tan\theta_{F\mathtt{s}}^{(n)}\tan\epsilon_{F\mathtt{s}}^{(n)}}, \tag{3.188}$$

$$\Phi_{F\mathtt{p}}^{(n)} = -\frac{t_{\mathtt{sp}}^{(n)}}{t_{\mathtt{pp}}^{(n)}} = \frac{\tan\theta_{F\mathtt{p}}^{(n)} + i\tan\epsilon_{F\mathtt{p}}^{(n)}}{1 - i\tan\theta_{F\mathtt{p}}^{(n)}\tan\epsilon_{F\mathtt{p}}^{(n)}}, \tag{3.189}$$

describing the change of polarization for each nth diffraction order.

3.5.5 General optical response in conical mountings and response of two-dimensional gratings

The general case of a one-dimensional anisotropic grating in a non-planar diffraction mounting (referred to as *conical mounting*) comprises the purely optical cross-polarization effect and the magneto-optical mixing effect. The same statement can be written for the case of a two-dimensional anisotropic grating. Therefore, if we discuss the Kerr or Faraday

effect, we mean only the magneto-optical effect, which is the perturbation from the state without magnetization. However, in this thesis we only apply the planar diffraction mounting in the case of one-dimensional gratings, and a mounting of two-dimensional ones where purely optical cross-polarization does not occur (the case when the plane of incidence is parallel to one direction of periodicity).

Chapter 4

Coupled wave theory of diffraction by gratings

After defining the quantities describing the optical response of planar and planar-like periodic structures we are free to derive the algorithm of their calculation. Unlike the planar structures whose response can be easily formulated by means of analytical equations, the diffraction response of nonplanar structures is governed by complicated diffraction laws. The particular problem of diffraction by periodic structures is therefore transformed from the partial differential equations describing light propagation through inhomogeneous media into linear-algebraic equations treating coupled plane waves. After formulating general linear operation equations describing the response of general anisotropic gratings, we reformulate a particular problem of a one-dimensional isotropic grating in the planar diffraction mounting into matrix equations in the Fourier representation. The Fourier-basis equations can also be straightforwardly formulated for any type of general structures.

4.1 Description of the modeled structure

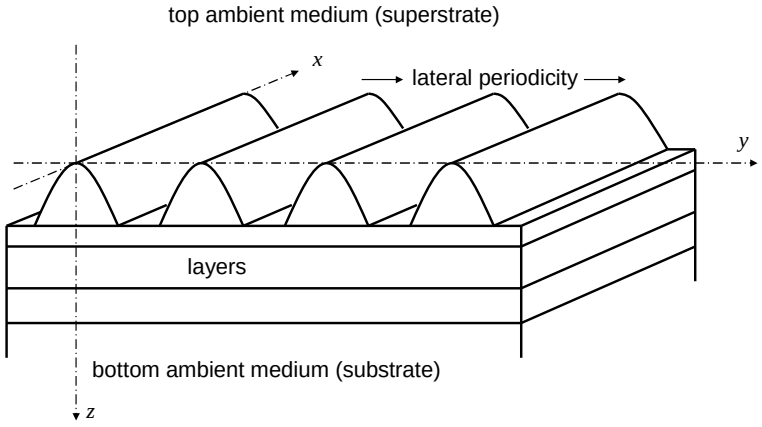

Figure 4.1 Geometrical configuration of the modeled structure.

We will provide a detailed description of the coupled wave theory of the optical response of a structure with periodic lateral texturing, generally located on the top of a multilayer system sandwiched between top and bottom ambient media (superstrate and substrate). The general structure is displayed in Fig. 4.1, including the configuration of the Cartesian coordinates.

4.2 Transfer of electromagnetic waves in symbolic notation

Defining new Cartesian coordinates scaled by the wave number in vacuum $k_0 = 2\pi/\lambda$, i. e.,

$$\bar{\boldsymbol{r}} = k_0 \boldsymbol{r}, \tag{4.1}$$

$$\bar{\nabla} = \frac{1}{k_0} \nabla, \tag{4.2}$$

and a scaled magnetic field

$$\tilde{\boldsymbol{H}} = \mu_0 c \boldsymbol{H} \tag{4.3}$$

yields the time-harmonic Maxwell equations in a brief form

$$\bar{\nabla} \times \boldsymbol{E} = -i\tilde{\boldsymbol{H}}, \tag{4.4}$$

$$\bar{\nabla} \times \tilde{\boldsymbol{H}} = i\boldsymbol{\varepsilon}(\bar{\boldsymbol{r}}) \cdot \boldsymbol{E}, \tag{4.5}$$

$$\bar{\nabla} \cdot [\boldsymbol{\varepsilon}(\bar{\boldsymbol{r}}) \cdot \boldsymbol{E}] = 0, \tag{4.6}$$

$$\bar{\nabla} \cdot \tilde{\boldsymbol{H}} = 0, \tag{4.7}$$

where

$$\boldsymbol{\varepsilon}(\bar{\boldsymbol{r}}) = \begin{bmatrix} \varepsilon_{xx} & \varepsilon_{xy} & \varepsilon_{xz} \\ \varepsilon_{yx} & \varepsilon_{yy} & \varepsilon_{yz} \\ \varepsilon_{zx} & \varepsilon_{zy} & \varepsilon_{zz} \end{bmatrix} \tag{4.8}$$

is the permittivity tensorial function of an inhomogeneous anisotropic medium. Hereafter throughout this chapter, we will assume the scaled coordinates and scaled magnetic field but omit the top bars and tildes for simplicity.

Expressing the normal (∂_z) derivatives of the fields, we obtain a set of partial differ-

ential equations for their tangential components

$$\partial_z E_x = -\partial_x \frac{\varepsilon_{zx}}{\varepsilon_{zz}} E_x - \partial_x \frac{\varepsilon_{zy}}{\varepsilon_{zz}} E_y + \partial_x \frac{i}{\varepsilon_{zz}} \partial_y H_x - i \left(1 + \partial_x \frac{1}{\varepsilon_{zz}} \partial_x\right) H_y, \tag{4.9}$$

$$\partial_z E_y = -\partial_y \frac{\varepsilon_{zx}}{\varepsilon_{zz}} E_x - \partial_y \frac{\varepsilon_{zy}}{\varepsilon_{zz}} E_y + i \left(1 + \partial_y \frac{1}{\varepsilon_{zz}} \partial_y\right) H_x - \partial_y \frac{i}{\varepsilon_{zz}} \partial_x H_y, \tag{4.10}$$

$$\partial_z H_x = i \left(\varepsilon_{yx} - \frac{\varepsilon_{yz}\varepsilon_{zx}}{\varepsilon_{zz}} - \partial_x \partial_y\right) E_x + i \left(\varepsilon_{yy} - \frac{\varepsilon_{yz}\varepsilon_{zx}}{\varepsilon_{zz}} + \partial_x^2\right) E_y - \frac{\varepsilon_{yz}}{\varepsilon_{zz}} \partial_y H_x + \frac{\varepsilon_{yz}}{\varepsilon_{zz}} \partial_x H_y, \tag{4.11}$$

$$\partial_z H_y = -i \left(\varepsilon_{xx} - \frac{\varepsilon_{xz}\varepsilon_{zx}}{\varepsilon_{zz}} - \partial_y^2\right) E_x - i \left(\varepsilon_{xy} - \frac{\varepsilon_{xz}\varepsilon_{zy}}{\varepsilon_{zz}} - \partial_y \partial_x\right) E_y + \frac{\varepsilon_{xz}}{\varepsilon_{zz}} \partial_y H_x - \frac{\varepsilon_{xz}}{\varepsilon_{zz}} \partial_x H_y, \tag{4.12}$$

and a set for the normal components

$$E_z = -\frac{\varepsilon_{zx}}{\varepsilon_{zz}} E_x - \frac{\varepsilon_{zy}}{\varepsilon_{zz}} E_y + \frac{i}{\varepsilon_{zz}} \partial_y H_x - \frac{i}{\varepsilon_{zz}} \partial_x H_y, \tag{4.13}$$

$$H_z = -i\partial_y E_x + i\partial_x E_y. \tag{4.14}$$

We regard the field components $E_j(x, y, z_0)$, $H_j(x, y, z_0)$ $(j = x, y, z)$ in a chosen plane $z = z_0$ as elements of the Hilbert space $\vec{E}_j(z_0), \vec{H}_j(z_0) \in L^2(\mathbb{R}^2)$ describing altogether the state of light in that plane, like in the case of a homogenous medium. Thus the partial differential equations can be regarded as linear operator equations describing an infinitesimal change of the light state in the normal direction [Eqs. (4.9–4.12)] and that the tangential components are sufficient to describe the state uniquely [Eqs. (4.13–4.14)]. The operator equations are expressed in the Cartesian-coordinate representation; in this case, two types of operators are present: the operator of a partial derivative $\hat{\partial}_j$ and the operator of multiplication by a function $\hat{\varepsilon}_{jk} = \varepsilon_{jk}$ or $\hat{\varepsilon}_{jk}^{-1} = 1/\varepsilon_{jk}$.

Applying the above reasoning, we may express the both sets of operator equations as matrix formulae

$$\partial_z \vec{\boldsymbol{F}}_{\hat{t}} = -i\hat{\boldsymbol{\Omega}} \vec{\boldsymbol{F}}_{\hat{t}} \tag{4.15}$$

$$\vec{\boldsymbol{F}}_{\hat{n}} = \hat{\mathbf{N}} \vec{\boldsymbol{F}}_{\hat{t}} \tag{4.16}$$

where the tangential and normal fields are now vector fields

$$\vec{\boldsymbol{F}}_{\hat{t}}(z) = \begin{bmatrix} \vec{E}_x(z) \\ \vec{E}_y(z) \\ \vec{H}_x(z) \\ \vec{H}_y(z) \end{bmatrix}, \tag{4.17}$$

$$\vec{\boldsymbol{F}}_{\hat{n}}(z) = \begin{bmatrix} \vec{E}_z(z) \\ \vec{H}_z(z) \end{bmatrix}, \tag{4.18}$$

respectively, and where the tangential and normal operators are defined as

$$\hat{\mathbf{\Omega}} = \begin{bmatrix} -i\partial_x \frac{\varepsilon_{zx}}{\varepsilon_{zz}} & -i\partial_x \frac{\varepsilon_{zy}}{\varepsilon_{zz}} & -\partial_x \frac{1}{\varepsilon_{zz}} \partial_y & 1 + \partial_x \frac{1}{\varepsilon_{zz}} \partial_x \\ -i\partial_y \frac{\varepsilon_{zx}}{\varepsilon_{zz}} & -i\partial_y \frac{\varepsilon_{zy}}{\varepsilon_{zz}} & -(1 + \partial_y \frac{1}{\varepsilon_{zz}} \partial_y) & \partial_y \frac{1}{\varepsilon_{zz}} \partial_x \\ -(\varepsilon_{yx} - \frac{\varepsilon_{yz}\varepsilon_{zx}}{\varepsilon_{zz}} - \partial_x \partial_y) & -(\varepsilon_{yy} - \frac{\varepsilon_{yz}\varepsilon_{zy}}{\varepsilon_{zz}} + \partial_x^2) & -i\frac{\varepsilon_{yz}}{\varepsilon_{zz}} \partial_y & i\frac{\varepsilon_{yz}}{\varepsilon_{zz}} \partial_x \\ \varepsilon_{xx} - \frac{\varepsilon_{xz}\varepsilon_{zx}}{\varepsilon_{zz}} + \partial_y^2 & \varepsilon_{xy} - \frac{\varepsilon_{xz}\varepsilon_{zy}}{\varepsilon_{zz}} - \partial_y \partial_x & i\frac{\varepsilon_{xz}}{\varepsilon_{zz}} \partial_y & -i\frac{\varepsilon_{xz}}{\varepsilon_{zz}} \partial_x \end{bmatrix}, \tag{4.19}$$

$$\hat{\mathbf{N}} = \begin{bmatrix} -\frac{\varepsilon_{zx}}{\varepsilon_{zz}} & -\frac{\varepsilon_{zy}}{\varepsilon_{zz}} & \frac{i}{\varepsilon_{zz}} \partial_y & -\frac{i}{\varepsilon_{zz}} \partial_x \\ -i\partial_y & i\partial_x & 0 & 0 \end{bmatrix}. \tag{4.20}$$

Now we can easily formulate a boundary value problem and solve it in the symbolic vectorial notation as follows. Suppose that the tangential components of the fields are known in one chosen plane, e. g.,

$$\vec{\boldsymbol{F}}_{\hat{t}}(0) = \vec{\boldsymbol{A}}. \tag{4.21}$$

To evaluate the fields $\vec{\boldsymbol{F}}_{\hat{t}}(z)$, $\vec{\boldsymbol{F}}_{\hat{n}}(z)$ in the space, we first look for eigenmodes, i. e., modes with the z-dependence

$$\vec{\boldsymbol{F}}_{\hat{t}}^{(\mu)}(z) = \vec{\boldsymbol{\psi}}_{\mu}\, e^{-is_\mu z}, \tag{4.22}$$

with μ formally distinguishing between different eigenmodes, which, after substituting into Eq. (4.15), yields

$$\hat{\mathbf{\Omega}} \vec{\boldsymbol{\psi}}_{\mu} = s_\mu \vec{\boldsymbol{\psi}}_{\mu}, \tag{4.23}$$

which is an equation for eigenvalues s_μ and eigenvectors $\vec{\boldsymbol{\psi}}_{\mu}$ of the operator $\hat{\mathbf{\Omega}}$.

Next, suppose that the medium is uniform in the direction of the z-coordinate. Then the solution of Eq. (4.23) does not depend on z and hence the same basis of eigenmodes can be chosen everywhere. In this representation, the operator describing transferring from the plane $z = z_0$ to the plane $z = z_1$ takes on a diagonal form with values on the diagonal being $e^{-is_\mu(z_1 - z_0)}$. Therefore, the transfer operator can be written

$$\hat{\mathbf{M}}(z_1 - z_0) = \mathbf{G}\, e^{-i\mathbf{S}(z_1 - z_0)}\, \mathbf{G}^{-1}, \tag{4.24}$$

where $\mathbf{S}$ is a diagonal matrix composed of values s_μ and $\mathbf{G}$ is a "diagonalizer," i. e., the matrix of transformation between the initial basis of the stated problem and the basis in which

$$\hat{\mathbf{\Omega}} = \mathbf{G}\mathbf{S}\mathbf{G}^{-1} \tag{4.25}$$

becomes diagonal. The state of light in any plane can then be determined by the linear transformation

$$\vec{\boldsymbol{F}}_{\hat{t}}(z) = \hat{\mathbf{M}}(z) \vec{\boldsymbol{F}}_{\hat{t}}(0) = \mathbf{G}\, e^{-i\mathbf{S}z}\, \mathbf{G}^{-1} \vec{\boldsymbol{A}}, \tag{4.26}$$

where $\hat{\mathbf{M}}(z)$ only depends on the distance of propagation z but does not depend on the initial and final points. Note that we can symbolically write $\hat{\mathbf{M}}(z) = e^{-i\hat{\mathbf{\Omega}}z}$ without solving the eigenvalue problem explicitly (which would now become inhered in the numerical evaluation of the matrix exponential function).

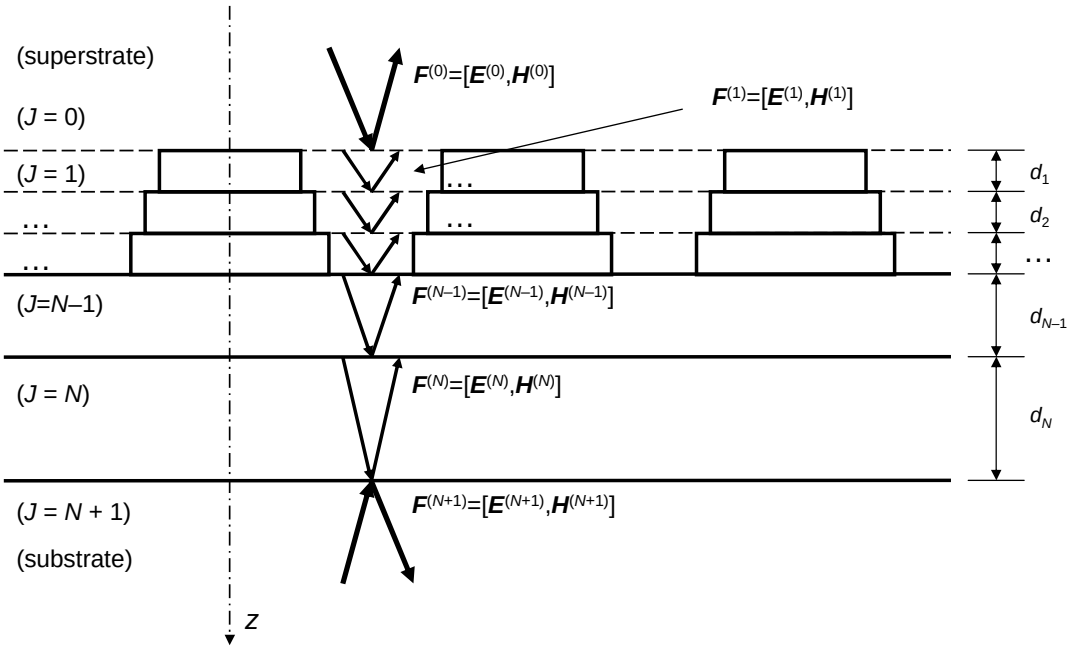

Figure 4.2 The geometry of the transferring problem. The structure including the top periodic relief is sliced into N layers, each of which is treated by the transfer operator.

More generally, suppose that the problem is not uniform in the normal direction. We have defined an initial state by the same condition (4.21) and want to determine the state in another plane $z = d$. We can approximately solve this problem by dividing the interval $\langle 0, d\rangle$ into N slices, i. e., by defining numbers $0 = z_0 < z_1 < z_2 < \ldots < z_N = d$, so that all the distances $d_J = z_J - z_{J-1}$ are small enough to assume the uniformity of the operator describing transferring from z_{J-1} to z_J, i. e., $\hat{\mathbf{M}}_{z_{J-1},z_J} \approx \hat{\mathbf{M}}_J(z_J - z_{J-1}) = \hat{\mathbf{M}}_J(d_J)$. The geometry of the transferring problem is displayed in Fig. 4.2. Since the tangential components of the fields in a boundary $z = z_J$ are continuous, i. e.,

$$\vec{\boldsymbol{F}}_{\hat{t}}(z_J - 0) = \vec{\boldsymbol{F}}_{\hat{t}}(z_J + 0), \tag{4.27}$$

the total transfer operator can simply be calculated as

$$\hat{\mathbf{M}}_{0,d} = \hat{\mathbf{M}}_N(d_N)\,\hat{\mathbf{M}}_{N-1}(d_{N-1})\ldots\hat{\mathbf{M}}_2(d_2)\,\hat{\mathbf{M}}_1(d_1). \tag{4.28}$$

In practice, however, we usually state a different boundary condition corresponding to a wave incident from one chosen direction, cf. Eqs. (3.15–3.16). For this purpose, we have interest to split the state $\vec{\boldsymbol{F}}_{\hat{t}}(z_0)$ into the directions of propagation and to solve the problem by means of scattering.

4.3 Formulation of the scattering problem

Before formulation the scattering problem, it is important to make an assumption that the both top and bottom ambient media are isotropic. While the superstrate is usually air

or vacuum, the substrate can be made of a more general material. The only requirement important for the later derivation is the substrate's isotropy or polar symmetry which simplifies the form of Eq. (4.15). This simplification enables us to reformulate the coupled wave equations as follows.

In the both superstrate and substrate we will treat the tangential electric and magnetic fields separately by defining

$$\vec{\boldsymbol{f}}(z) = \begin{bmatrix} \vec{E}_x(z) \\ \vec{E}_y(z) \end{bmatrix}, \tag{4.29}$$

$$\vec{\boldsymbol{h}}(z) = \begin{bmatrix} \vec{H}_x(z) \\ \vec{H}_y(z) \end{bmatrix}. \tag{4.30}$$

The above assumption of isotropy permits us to rewrite Eq. (4.15) as

$$\partial_z \vec{\boldsymbol{f}} = -i\hat{\boldsymbol{\Omega}}_{12}\vec{\boldsymbol{h}}, \tag{4.31}$$

$$\partial_z \vec{\boldsymbol{h}} = -i\hat{\boldsymbol{\Omega}}_{21}\vec{\boldsymbol{f}}, \tag{4.32}$$

where $\hat{\boldsymbol{\Omega}}_{12}$, $\hat{\boldsymbol{\Omega}}_{21}$ denote the nonzero subblocks of $\hat{\boldsymbol{\Omega}}$, and correspondingly

$$\hat{\boldsymbol{\Omega}}_{12}\hat{\boldsymbol{\Omega}}_{21}\vec{\boldsymbol{f}} = -\partial_z^2\vec{\boldsymbol{f}}. \tag{4.33}$$

Looking again for eigenmodes $\vec{\boldsymbol{f}}^{(\mu)}(z) = \hat{\boldsymbol{\psi}}_\mu e^{-is_\mu z}$ formally distinguished by μ, we obtain an equation for eigenvalues μ,

$$\hat{\mathbf{C}}\hat{\boldsymbol{\psi}}_\mu = \mu\hat{\boldsymbol{\psi}}_\mu, \tag{4.34}$$

$$\hat{\mathbf{C}} = \hat{\boldsymbol{\Omega}}_{12}\hat{\boldsymbol{\Omega}}_{21},$$

each of which corresponds to two different propagation numbers

$$s_\mu^{(+)} = +\sqrt{\mu}, \tag{4.35}$$

$$s_\mu^{(-)} = -\sqrt{\mu}, \tag{4.36}$$

the first of which corresponds to propagation in the $+z$ direction and the second in the $-z$ direction. This means that the vector $\vec{\boldsymbol{f}}$ itself does not contain information on the direction of propagation; therefore, the complete state of light in a chosen plane can be determined by the pair $\vec{\boldsymbol{f}}^{(+)}$, $\vec{\boldsymbol{f}}^{(-)}$ of vectors corresponding to the either directions or, as before, by the pair $\vec{\boldsymbol{f}}$, $\vec{\boldsymbol{h}}$.

We can determine the magnetic field from the electric field in each separate direction of propagation

$$\vec{\boldsymbol{h}}^{(+)} = \hat{\mathbf{D}}^{(+)}\,\vec{\boldsymbol{f}}^{(+)}, \tag{4.37}$$

$$\vec{\boldsymbol{h}}^{(-)} = \hat{\mathbf{D}}^{(-)}\,\vec{\boldsymbol{f}}^{(-)}, \tag{4.38}$$

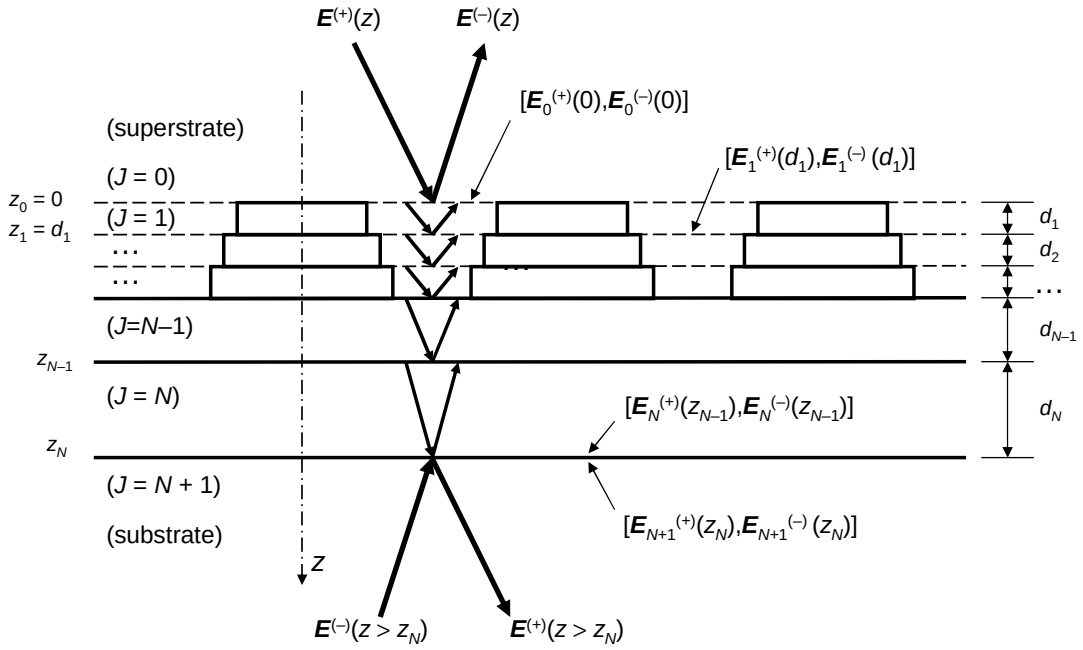

Figure 4.3 The geometry of the scattering problem. The structure is illuminated from the top and/or bottom half-space, and the scattered (reflected and transmitted) waves are searched for.

where $\hat{\mathbf{D}}^{(\pm)}$ can be determined from Eq. (4.32) after solving Eq. (4.34) as

$$\hat{\mathbf{D}}^{(+)} = \mathbf{G}\mathbf{S}^{-1}\mathbf{G}^{-1}\hat{\mathbf{\Omega}}_{21}, \tag{4.39}$$

$$\hat{\mathbf{D}}^{(-)} = -\hat{\mathbf{D}}^{(+)}, \tag{4.40}$$

where $\mathbf{S}$ is a diagonal matrix composed of the eigenvalues $s_\mu^{(+)}$ and $\mathbf{G}$ is a diagonalizer corresponding to Eq. (4.34). We refer to $\hat{\mathbf{D}} = \hat{\mathbf{D}}^{(+)} = -\hat{\mathbf{D}}^{(-)}$ as the dynamical operator. Note that Eq. (4.39) can be symbolically written $\hat{\mathbf{D}} = (\sqrt{\hat{\mathbf{C}}})^{-1}\,\hat{\mathbf{\Omega}}_{21}$.

The splitting $\vec{\boldsymbol{F}} = \vec{\boldsymbol{F}}^{(+)} + \vec{\boldsymbol{F}}^{(-)}$ can now be written

$$\begin{aligned}\begin{bmatrix} \vec{\boldsymbol{f}} \\ \vec{\boldsymbol{h}} \end{bmatrix} &= \begin{bmatrix} \vec{\boldsymbol{f}}^{(+)} \\ \hat{\mathbf{D}}\vec{\boldsymbol{f}}^{(+)} \end{bmatrix} + \begin{bmatrix} \vec{\boldsymbol{f}}^{(-)} \\ -\hat{\mathbf{D}}\vec{\boldsymbol{f}}^{(-)} \end{bmatrix} \\ &= \begin{bmatrix} \mathbf{1} & \mathbf{1} \\ \hat{\mathbf{D}} & -\hat{\mathbf{D}} \end{bmatrix} \begin{bmatrix} \vec{\boldsymbol{f}}^{(+)} \\ \vec{\boldsymbol{f}}^{(-)} \end{bmatrix}\end{aligned} \tag{4.41}$$

and hence

$$\begin{bmatrix} \vec{\boldsymbol{f}}^{(+)} \\ \vec{\boldsymbol{f}}^{(-)} \end{bmatrix} = \begin{bmatrix} \mathbf{1} & \mathbf{1} \\ \hat{\mathbf{D}} & -\hat{\mathbf{D}} \end{bmatrix}^{-1} \begin{bmatrix} \vec{\boldsymbol{f}} \\ \vec{\boldsymbol{h}} \end{bmatrix} = \frac{1}{2}\begin{bmatrix} \mathbf{1} & \hat{\mathbf{D}}^{-1} \\ \mathbf{1} & -\hat{\mathbf{D}}^{-1} \end{bmatrix} \begin{bmatrix} \vec{\boldsymbol{f}} \\ \vec{\boldsymbol{h}} \end{bmatrix}. \tag{4.42}$$

Finally, all the derived quantities can be applied to solve the scattering problem, which is depicted in Fig. 4.3. Suppose that a general structure is contained between the planes $z = 0$ and $z = d$ and that its optics is solved by means of the transfer operator $\hat{\mathbf{M}}$ [Eq. (4.28)]. Next, suppose that the structure is illuminated by a wave incident from the

half-space $z < 0$, i. e., $\vec{\boldsymbol{f}}^{(+)}(0) = \vec{\boldsymbol{f}}^{(i)}$, $\vec{\boldsymbol{f}}^{(-)}(d) = 0$. Then combining Eqs. (4.26, 4.41–4.42) yields

$$\vec{\boldsymbol{f}}^{(r)} = \hat{\mathbf{R}}\vec{\boldsymbol{f}}^{(i)}, \tag{4.43}$$

$$\vec{\boldsymbol{f}}^{(t)} = \hat{\mathbf{T}}\vec{\boldsymbol{f}}^{(i)}, \tag{4.44}$$

where $\vec{\boldsymbol{f}}^{(r)} = \vec{\boldsymbol{f}}^{(-)}(0)$ and $\vec{\boldsymbol{f}}^{(t)} = \vec{\boldsymbol{f}}^{(+)}(d)$ are waves reflected and transmitted by the structure, respectively, and where the reflection and transmission operators are

$$\begin{aligned}\hat{\mathbf{R}} &= -\left[\hat{\mathbf{M}}_{11} - \hat{\mathbf{M}}_{12}\hat{\mathbf{D}}_0 - \hat{\mathbf{D}}_{N+1}^{-1}\left(\hat{\mathbf{M}}_{21} - \hat{\mathbf{M}}_{22}\hat{\mathbf{D}}_0\right)\right]^{-1} \\ &\quad \times \left[\hat{\mathbf{M}}_{11} + \hat{\mathbf{M}}_{12}\hat{\mathbf{D}}_0 - \hat{\mathbf{D}}_{N+1}^{-1}\left(\hat{\mathbf{M}}_{21} + \hat{\mathbf{M}}_{22}\hat{\mathbf{D}}_0\right)\right], \qquad (4.45) \\ \hat{\mathbf{T}} &= \frac{1}{2}\left[\hat{\mathbf{M}}_{11} + \hat{\mathbf{M}}_{12}\hat{\mathbf{D}}_0 + \hat{\mathbf{D}}_{N+1}^{-1}\left(\hat{\mathbf{M}}_{21} + \hat{\mathbf{M}}_{22}\hat{\mathbf{D}}_0\right)\right] \\ &\quad + \frac{1}{2}\left[\hat{\mathbf{M}}_{11} - \hat{\mathbf{M}}_{12}\hat{\mathbf{D}}_0 + \hat{\mathbf{D}}_{N+1}^{-1}\left(\hat{\mathbf{M}}_{21} - \hat{\mathbf{M}}_{22}\hat{\mathbf{D}}_0\right)\right]\hat{\mathbf{R}}, \qquad (4.46)\end{aligned}$$

where $\hat{\mathbf{M}}_{jk}$ $(j, k = 1, 2)$ are the subblocks of the transfer operator $\hat{\mathbf{M}}$ with respect to the symbolic basis $[\vec{\boldsymbol{f}}, \vec{\boldsymbol{h}}]$ and where $\hat{\mathbf{D}}_0$, $\hat{\mathbf{D}}_{N+1}$ are the dynamical operators of the superstrate and substrate, respectively.

4.4 Basic propagation algorithms

Above we have demonstrated a symbolic solution of the scattering problem by means of the transfer operator. In this section we will repeat it in detail for the case of a multilayered grating with polar anisotropy, which not only simplifies the determination of the transfer operator, but also enables us to apply improved propagation algorithms. The polar anisotropy, which assumes $\varepsilon_{xz} = \varepsilon_{zy} = \varepsilon_{yz} = \varepsilon_{zy} = 0$, is the only case studied in this thesis.

4.4.1 Transfer-matrix approach

Suppose that a grating is located between the planes $z = 0$ and $z = d$, with d denoting its thickness. The incident wave $\vec{\boldsymbol{f}}^{(i)}$ propagates from the superstrate $z < 0$ and is scattered by the grating into the reflection mode, $\vec{\boldsymbol{f}}^{(r)} = \hat{\mathbf{R}}\vec{\boldsymbol{f}}^{(i)}$, and the transmission mode, $\vec{\boldsymbol{f}}^{(t)} = \hat{\mathbf{T}}\vec{\boldsymbol{f}}^{(i)}$. Our aim is to determine the reflection and transmission matrices $\hat{\mathbf{R}}$, $\hat{\mathbf{T}}$ in the Fourier representation.

First we will determine the transfer operator $\hat{\mathbf{M}}_{0,\,d}$ of the structure, i. e., the operator describing the transfer of electromagnetic field between the two planes sandwiching the structure. For this purpose, we slice the structure into N layers that are or can be considered uniform in the normal direction. Thus the total transfer

$$\begin{bmatrix} \vec{\boldsymbol{f}}(d) \\ \vec{\boldsymbol{h}}(d) \end{bmatrix} = \hat{\mathbf{M}}_{0,\,d} \begin{bmatrix} \vec{\boldsymbol{f}}(0) \\ \vec{\boldsymbol{h}}(0) \end{bmatrix} \tag{4.47}$$

can be divided into transfers within sub-layers

$$\begin{bmatrix} \vec{f}(z_J) \\ \vec{h}(z_J) \end{bmatrix} = \hat{\mathbf{M}}_{z_{J-1},\, z_J} \begin{bmatrix} \vec{f}(z_{J-1}) \\ \vec{h}(z_{J-1}) \end{bmatrix}, \tag{4.48}$$

with

$$\hat{\mathbf{M}}_{z_{J-1},\, z_J} = \hat{\mathbf{M}}_J(d_J) = e^{-i\,\hat{\mathbf{\Omega}}_J\, d_J}, \tag{4.49}$$

where $d_J = z_J - z_{J-1}$ denotes the thickness of the Jth layer and where

$$\hat{\mathbf{\Omega}}_J = \begin{bmatrix} 0 & 0 & -\partial_x \frac{1}{\varepsilon_{zz}^{(J)}} \partial_y & 1 + \partial_x \frac{1}{\varepsilon_{zz}^{(J)}} \partial_x \\ 0 & 0 & -(1 + \partial_y \frac{1}{\varepsilon_{zz}^{(J)}} \partial_y) & \partial_y \frac{1}{\varepsilon_{zz}^{(J)}} \partial_x \\ -(\varepsilon_{yx}^{(J)} - \partial_x \partial_y) & -(\varepsilon_{yy}^{(J)} + \partial_x^2) & 0 & 0 \\ \varepsilon_{xx}^{(J)} + \partial_y^2 & \varepsilon_{xy}^{(J)} - \partial_y \partial_x & 0 & 0 \end{bmatrix} \tag{4.50}$$

where $\varepsilon_{jk}^{(J)}$ denote the elements of the permittivity tensorial function of the Jth layer. The resulting transfer matrix is then

$$\hat{\mathbf{M}}_{0,\, d} = e^{-i\,\hat{\mathbf{\Omega}}_N\, d_N} e^{-i\,\hat{\mathbf{\Omega}}_{N-1}\, d_{N-1}} \ldots e^{-i\,\hat{\mathbf{\Omega}}_2\, d_2} e^{-i\,\hat{\mathbf{\Omega}}_1\, d_1}, \tag{4.51}$$

where the exponents do not generally commute and therefore cannot be summed as a single exponent.

Instead of determining the reflection and transmission of a wave incident from a single direction, we will evaluate the scattering matrix

$$\hat{\mathbf{S}} = \begin{bmatrix} \hat{\mathbf{R}}^{0,\, N+1} & \hat{\mathbf{T}}^{N+1,\, 0} \\ \hat{\mathbf{T}}^{0,\, N+1} & \hat{\mathbf{R}}^{N+1,\, 0} \end{bmatrix} \tag{4.52}$$

describing a more general scattering problem

$$\begin{bmatrix} \vec{f}_0^{\,(-)} \\ \vec{f}_{N+1}^{\,(+)} \end{bmatrix} = \hat{\mathbf{S}} \begin{bmatrix} \vec{f}_0^{\,(+)} \\ \vec{f}_{N+1}^{\,(-)} \end{bmatrix}, \tag{4.53}$$

where $\vec{f}_0^{\,(+)}$ denotes a wave incident from the superstrate medium 0, $\vec{f}_{N+1}^{\,(-)}$ a wave incident from the substrate medium $N+1$, $\vec{f}_0^{\,(-)}$ a wave scattered to the superstrate, and $\vec{f}_{N+1}^{\,(+)}$ a wave scattered to the substrate. Accordingly, the subblock matrices $\hat{\mathbf{R}}^{0,\, N+1}$, $\hat{\mathbf{T}}^{0,\, N+1}$ denote the reflection and transmission of a wave incident from the superstrate, while $\hat{\mathbf{R}}^{N+1,\, 0}$, $\hat{\mathbf{T}}^{N+1,\, 0}$ denote the reflection and transmission of a wave incident from the substrate.

Rewriting Eq. (4.47) into the symbolic basis $[\vec{f}^{\,(+)}, \vec{f}^{\,(-)}]$, i. e.,

$$\hat{\mathbf{U}}_{N+1} \begin{bmatrix} \vec{f}_{N+1}^{\,(+)} \\ \vec{f}_{N+1}^{\,(-)} \end{bmatrix} = \hat{\mathbf{M}}_{0,\, d} \hat{\mathbf{U}}_0 \begin{bmatrix} \vec{f}_0^{\,(+)} \\ \vec{f}_0^{\,(-)} \end{bmatrix}, \tag{4.54}$$

where, according to Eq. (4.41),

$$\hat{\mathbf{U}}_J = \begin{bmatrix} \mathbf{1} & \mathbf{1} \\ \hat{\mathbf{D}}_J & -\hat{\mathbf{D}}_J \end{bmatrix} \tag{4.55}$$

is the transformation between the two symbolic bases in the Jth medium provided that

$$\hat{\mathbf{D}}_J = \left(\sqrt{\hat{\mathbf{\Omega}}_{12}\hat{\mathbf{\Omega}}_{21}}\right)^{-1}\hat{\mathbf{\Omega}}_{21}, \tag{4.56}$$

we can define a modified transfer matrix

$$\hat{\mathbf{W}}^{0,\,N+1} = \hat{\mathbf{U}}_{N+1}^{-1}\hat{\mathbf{M}}_{0,\,d}\hat{\mathbf{U}}_0, \tag{4.57}$$

whose subblocks $\hat{\mathbf{W}}_{jk}$ can be calculated from the subblocks $\hat{\mathbf{M}}_{jk}$ $(j,k=1,2)$ of the original transfer matrix $\hat{\mathbf{M}}_{0,\,d}$, i. e.,

$$\begin{aligned}
\hat{\mathbf{W}}_{11} &= \tfrac{1}{2}\left[\hat{\mathbf{M}}_{11} + \hat{\mathbf{M}}_{12}\hat{\mathbf{D}}_0 + \hat{\mathbf{D}}_{N+1}^{-1}\left(\hat{\mathbf{M}}_{21} + \hat{\mathbf{M}}_{22}\hat{\mathbf{D}}_0\right)\right],\\
\hat{\mathbf{W}}_{12} &= \tfrac{1}{2}\left[\hat{\mathbf{M}}_{11} - \hat{\mathbf{M}}_{12}\hat{\mathbf{D}}_0 + \hat{\mathbf{D}}_{N+1}^{-1}\left(\hat{\mathbf{M}}_{21} - \hat{\mathbf{M}}_{22}\hat{\mathbf{D}}_0\right)\right],\\
\hat{\mathbf{W}}_{21} &= \tfrac{1}{2}\left[\hat{\mathbf{M}}_{11} + \hat{\mathbf{M}}_{12}\hat{\mathbf{D}}_0 - \hat{\mathbf{D}}_{N+1}^{-1}\left(\hat{\mathbf{M}}_{21} + \hat{\mathbf{M}}_{22}\hat{\mathbf{D}}_0\right)\right],\\
\hat{\mathbf{W}}_{22} &= \tfrac{1}{2}\left[\hat{\mathbf{M}}_{11} - \hat{\mathbf{M}}_{12}\hat{\mathbf{D}}_0 - \hat{\mathbf{D}}_{N+1}^{-1}\left(\hat{\mathbf{M}}_{21} - \hat{\mathbf{M}}_{22}\hat{\mathbf{D}}_0\right)\right].
\end{aligned} \tag{4.58}$$

After rearranging the elements in Eq. (4.54), we obtain the resulting formula for the scattering matrix

$$\hat{\mathbf{S}} = \begin{bmatrix} -\hat{\mathbf{W}}_{22}^{-1}\hat{\mathbf{W}}_{21}, & \hat{\mathbf{W}}_{22}^{-1} \\ \hat{\mathbf{W}}_{11} - \hat{\mathbf{W}}_{12}\hat{\mathbf{W}}_{22}^{-1}\hat{\mathbf{W}}_{21}, & \hat{\mathbf{W}}_{12}\hat{\mathbf{W}}_{22}^{-1} \end{bmatrix}, \tag{4.59}$$

whose subblocks are the reflection and transmission matrices being searched for.

We refer to the method of obtaining $\hat{\mathbf{S}}$ from the subblocks of $\hat{\mathbf{M}}_{0,\,d}$ as the *transfer-matrix (T-matrix) approach*, since the diffraction problem is solved via the general transfer from the superstrate to the substrate. Unfortunately, this method becomes numerically unstable when the thickness becomes higher so that one of the transmitted modes tends to zero. From the mathematical point of view, the subblock matrix $\hat{\mathbf{S}}_{12} = \hat{\mathbf{T}}^{N+1,\,0} = \hat{\mathbf{W}}_{22}^{-1}$ describing transmission from the substrate to the superstrate becomes singular and hence $\hat{\mathbf{W}}_{22}$ is not possible to evaluate [this singularity arises from $\hat{\mathbf{D}}_{N+1}^{-1}$ in Eq. (4.58)]. For this reason, various improved propagation algorithms has been derived, the most used of which is the *scattering-matrix (S-matrix) approach*.

4.4.2 Scattering-matrix approach

The improvement is based on evaluating the scattering matrix only from quantities corresponding to individual layers whose thicknesses are assumed sufficiently small to avoid the instability. Thus, instead of deriving the matrix $\hat{\mathbf{S}}^{0,\,N+1}$ from the total transfer matrix $\hat{\mathbf{M}}_{0,\,d}$, we first evaluate the matrix $\hat{\mathbf{S}}^{0,\,1}$ describing the scattering by the first interface, and then we recursively evaluate matrices $\hat{\mathbf{S}}^{0,\,J}$ $(J = 2,\,3,\,\ldots,\,N+1)$ of the sub-systems consisting of the first J layers.

According to Eqs. (4.58, 4.59), the scattering matrix of the first interface (the interface between the superstrate and the first layer) becomes

$$\hat{\mathbf{S}}^{0,\,1} = \begin{bmatrix} -\hat{\mathbf{w}}_1^{-1}\hat{\mathbf{w}}_2, & \hat{\mathbf{w}}_1^{-1} \\ \hat{\mathbf{w}}_1 - \hat{\mathbf{w}}_2\hat{\mathbf{w}}_1^{-1}\hat{\mathbf{w}}_2, & \hat{\mathbf{w}}_2\hat{\mathbf{w}}_1^{-1} \end{bmatrix}, \tag{4.60}$$

with

$$\hat{\mathbf{w}}_{1,\,2} = \tfrac{1}{2}\left(\mathbf{1} \pm \hat{\mathbf{D}}_1^{-1}\hat{\mathbf{D}}_0\right). \tag{4.61}$$

Then we assume we have evaluated the scattering matrix $\hat{\mathbf{S}}^{0,\,J}$ corresponding to the subsystem of the first J layers and want to evaluate $\hat{\mathbf{S}}^{0,\,J+1}$. For this purpose we evaluate the transfer from the $J+1$st layer to the Jth layer

$$\hat{\mathbf{L}}_J = \hat{\mathbf{W}}_J^{-1} = \hat{\mathbf{U}}_J^{-1}\hat{\mathbf{M}}_J^{-1}\hat{\mathbf{U}}_{J+1} = \hat{\mathbf{U}}_J^{-1}e^{i\hat{\mathbf{\Omega}}_J\,d_J}\hat{\mathbf{U}}_{J+1}, \tag{4.62}$$

and then, from the two conditions

$$\begin{bmatrix} \vec{f}_0^{\,(-)} \\ \vec{f}_J^{\,(+)} \end{bmatrix} = \hat{\mathbf{S}}^{0,\,J}\begin{bmatrix} \vec{f}_0^{\,(+)} \\ \vec{f}_J^{\,(-)} \end{bmatrix}, \tag{4.63}$$

$$\begin{bmatrix} \vec{f}_J^{\,(+)} \\ \vec{f}_J^{\,(-)} \end{bmatrix} = \hat{\mathbf{L}}_J\begin{bmatrix} \vec{f}_{J+1}^{\,(+)} \\ \vec{f}_{J+1}^{\,(-)} \end{bmatrix}, \tag{4.64}$$

we obtain

$$\begin{bmatrix} \vec{f}_0^{\,(-)} \\ \vec{f}_{J+1}^{\,(+)} \end{bmatrix} = \hat{\mathbf{S}}^{0,\,J+1}\begin{bmatrix} \vec{f}_0^{\,(+)} \\ \vec{f}_{J+1}^{\,(-)} \end{bmatrix}, \tag{4.65}$$

where the subblocks of

$$\hat{\mathbf{S}}^{0,\,J+1} = \begin{bmatrix} \hat{\mathbf{R}}^{0,\,J+1} & \hat{\mathbf{T}}^{J+1,\,0} \\ \hat{\mathbf{T}}^{0,\,J+1} & \hat{\mathbf{R}}^{J+1,\,0} \end{bmatrix} \tag{4.66}$$

become

$$\hat{\mathbf{R}}^{0,\,J+1} = \hat{\mathbf{R}}^{0,\,J} + \hat{\mathbf{T}}^{J,\,0}\hat{\mathbf{L}}_{21}\left(\hat{\mathbf{L}}_{11} - \hat{\mathbf{R}}^{J,\,0}\,\hat{\mathbf{L}}_{21}\right)^{-1}\hat{\mathbf{T}}^{0,\,J}, \tag{4.67}$$

$$\hat{\mathbf{T}}^{0,\,J+1} = \left(\hat{\mathbf{L}}_{11} - \hat{\mathbf{R}}^{J,\,0}\hat{\mathbf{L}}_{21}\right)^{-1}\hat{\mathbf{T}}^{0,\,J}, \tag{4.68}$$

$$\hat{\mathbf{T}}^{J+1,\,0} = \hat{\mathbf{T}}^{J,\,0}\hat{\mathbf{L}}_{22} + \hat{\mathbf{T}}^{J,\,0}\hat{\mathbf{L}}_{21}\left(\hat{\mathbf{L}}_{11} - \hat{\mathbf{R}}^{J,\,0}\,\hat{\mathbf{L}}_{21}\right)^{-1}\left(\hat{\mathbf{R}}^{J,\,0}\hat{\mathbf{L}}_{22} - \hat{\mathbf{L}}_{12}\right), \tag{4.69}$$

$$\hat{\mathbf{R}}^{J+1,\,0} = \left(\hat{\mathbf{L}}_{11} - \hat{\mathbf{R}}^{J,\,0}\,\hat{\mathbf{L}}_{21}\right)^{-1}\left(\hat{\mathbf{R}}^{J,\,0}\hat{\mathbf{L}}_{22} - \hat{\mathbf{L}}_{12}\right), \tag{4.70}$$

where $\hat{\mathbf{L}}_{jk}$ $(j,k=1,2)$ are the subblocks of $\hat{\mathbf{L}}_J$.

4.4.3 Airy-like series

The above iteration method is simple, straightforward, and numerically stable. However, a similar result can be obtained by physically more transparent reasoning, analogous to the method of calculating the Airy reflection and transmission coefficients in Sec. 3.4.3.

Instead of the matrix $\hat{\mathbf{L}}_J$, we will evaluate matrices governing the propagation in the single directions

$$\vec{f}_J^{(+)}(z_{J+1}) = \hat{\mathbf{P}}_J^{(+)} \vec{f}_J^{(+)}(z_J), \tag{4.71}$$
$$\vec{f}_J^{(-)}(z_{J+1}) = \hat{\mathbf{P}}_J^{(-)} \vec{f}_J^{(-)}(z_J), \tag{4.72}$$

related to propagation through the Jth layer. Here it is assumed that the modes $(+)$ and $(-)$ are not coupled within a layer homogenous in the direction of the z-coordinate, which will become clear in the following.

Looking for eigenmodes in the Jth layer (with "J" omitted for brevity) $\vec{f}^{(j)} = \hat{\boldsymbol{\varphi}}_j \, e^{-is_j z}$ distinguished by the mode number j, we obtain, like in the case of Eq. (4.34),

$$\hat{\mathbf{C}}_J \hat{\boldsymbol{\varphi}}_j = \mu_j \hat{\boldsymbol{\varphi}}_j, \tag{4.73}$$
$$\hat{\mathbf{C}}_J = \hat{\boldsymbol{\Omega}}_{12} \hat{\boldsymbol{\Omega}}_{21}, \tag{4.74}$$

with

$$s_j^{(+)} = +\sqrt{\mu_j}, \tag{4.75}$$
$$s_j^{(-)} = -\sqrt{\mu_j} \tag{4.76}$$

being the propagation numbers in the $+z$ and $-z$ directions, respectively. Accordingly we can simply evaluate the matrix describing propagation through the Jth layer corresponding to the $\vec{f}^{(+)}$ mode, i. e.,

$$\hat{\mathbf{P}}_J^{(+)} = \hat{\mathbf{G}}_J \, e^{-i \hat{\mathbf{s}}_J d_J} \, \hat{\mathbf{G}}_J^{-1} \tag{4.77}$$

where $\hat{\mathbf{G}}_J$ is the diagonalizer of $\hat{\mathbf{C}}_J$ corresponding to the Jth medium, whose columns are the eigenvectors $\hat{\boldsymbol{\varphi}}_j$, and

$$\hat{\mathbf{s}}_J = \begin{bmatrix} s_1^{(+)} & 0 & 0 & \cdots \\ 0 & s_2^{(+)} & 0 & \cdots \\ 0 & 0 & s_3^{(+)} & \cdots \\ \vdots & \vdots & \vdots & \ddots \end{bmatrix}, \tag{4.78}$$

is a diagonal matrix with the $(+)$ propagation numbers [Eq. (4.75)] on the diagonal. Similarly we obtain

$$\hat{\mathbf{P}}_J^{(-)} = \hat{\mathbf{G}}_J \, e^{+i \hat{\mathbf{s}}_J d_J} \, \hat{\mathbf{G}}_J^{-1} = \left[\hat{\mathbf{P}}_J^{(+)} \right]^{-1}, \tag{4.79}$$

and therefore we define the matrix

$$\hat{\mathbf{P}}_J = \hat{\mathbf{P}}_J^{(+)} = \left[\hat{\mathbf{P}}_J^{(-)} \right]^{-1}, \tag{4.80}$$

which governs propagation in both $(+)$ and $(-)$ directions, the latter of which is described by the inverted version of Eq. (4.72).

Finally, suppose that we have calculated the reflection and transmission matrices $\hat{\mathbf{R}}^{0,J}$, $\hat{\mathbf{T}}^{0,J}$, $\hat{\mathbf{R}}^{J,0}$, and $\hat{\mathbf{T}}^{J,0}$ corresponding to the sub-system (alternatively called a pseudointerface) of the first J layers. For the case of $J = 1$ (the first interface) these matrices are mathematically equal to the subblocks of Eq. (4.60). Like in the case of the S-matrix approach, the matrices indexed by $J+1$ are calculated recursively from the matrices indexed by J. This time, instead of evaluating the transfer matrix and stating the boundary conditions, the propagation matrix $\hat{\mathbf{P}}_J$ of the Jth layer enters into the calculation together with the reflection and transmission matrices $\hat{\mathbf{R}}^{J,J+1}$, $\hat{\mathbf{T}}^{J,J+1}$, $\hat{\mathbf{R}}^{J+1,J}$, and $\hat{\mathbf{T}}^{J+1,J}$ corresponding to the next interface. Thus, analogously to deriving the Airy formulae (3.110, 3.111) for a thin film, we superpose the contributions from multiple internal reflections and propagations inside the Jth layer, i. e.,

$$\begin{aligned}
\hat{\mathbf{R}}^{0,J+1} &= \hat{\mathbf{R}}^{0J} + \hat{\mathbf{T}}^{J0}\hat{\mathbf{P}}_J\hat{\mathbf{R}}^{J,J+1}\hat{\mathbf{P}}_J\hat{\mathbf{T}}^{0J} + \hat{\mathbf{T}}^{J0}\hat{\mathbf{P}}_J\hat{\mathbf{R}}^{J,J+1}\left(\hat{\mathbf{P}}_J\hat{\mathbf{R}}^{J0}\hat{\mathbf{P}}_J\hat{\mathbf{R}}^{J,J+1}\right)\hat{\mathbf{P}}_J\hat{\mathbf{T}}^{0J} + \dots \\
&= \hat{\mathbf{R}}^{0J} + \hat{\mathbf{T}}^{J0}\hat{\mathbf{P}}_J\hat{\mathbf{R}}^{J,J+1}\left(\mathbf{1} + \hat{\mathbf{Q}}_J + \hat{\mathbf{Q}}_J^2 + \dots\right)\hat{\mathbf{P}}_J\hat{\mathbf{T}}^{0J} \\
&= \hat{\mathbf{R}}^{0J} + \hat{\mathbf{T}}^{J0}\hat{\mathbf{P}}_J\hat{\mathbf{R}}^{J,J+1}\left(\mathbf{1} - \hat{\mathbf{Q}}_J\right)^{-1}\hat{\mathbf{P}}_J\hat{\mathbf{T}}^{0J}, \qquad (4.81) \\
\hat{\mathbf{T}}^{0,J+1} &= \hat{\mathbf{T}}^{J,J+1}\hat{\mathbf{P}}_J\hat{\mathbf{T}}^{0J} + \hat{\mathbf{T}}^{J,J+1}\left(\hat{\mathbf{P}}_J\hat{\mathbf{R}}^{J0}\hat{\mathbf{P}}_J\hat{\mathbf{R}}^{J,J+1}\right)\hat{\mathbf{P}}_J\hat{\mathbf{T}}^{0J} + \dots \\
&= \hat{\mathbf{T}}^{J,J+1}\left(\mathbf{1} + \hat{\mathbf{Q}}_J + \hat{\mathbf{Q}}_J^2 + \dots\right)\hat{\mathbf{P}}_J\hat{\mathbf{T}}^{0J} \\
&= \hat{\mathbf{T}}^{J,J+1}\left(\mathbf{1} - \hat{\mathbf{Q}}_J\right)^{-1}\hat{\mathbf{P}}_J\hat{\mathbf{T}}^{0J}, \qquad (4.82)
\end{aligned}$$

with the matrix coefficient of the generalized geometric series being

$$\hat{\mathbf{Q}}_J = \hat{\mathbf{P}}_J\hat{\mathbf{R}}^{J0}\hat{\mathbf{P}}_J\hat{\mathbf{R}}^{J,J+1}, \qquad (4.83)$$

and similarly for $\hat{\mathbf{R}}^{J+1,0}$ and $\hat{\mathbf{T}}^{J+1,0}$.

We refer to the method just described as the Airy-like series. At first glance it seems that the difference between the S-matrix approach and the Airy-like series is just the physical point of view. In fact, however, the latter method is numerically more efficient. For this reason we use it universally in later chapters.

4.5 Periodicity and the Floquet theorem

In Sec. 3.5.1 we demonstrated reduction of the diffraction problem induced by the translational symmetry coupled with the periodicity of a grating without an explicit treatment of the field inside the periodic medium the grating consists of. However, for solving the diffraction problem we need to evaluate this field, at least as a middle step before evaluating the scattered fields.

In the Cartesian-coordinate representation, the tangential electric field (4.29) in a chosen plane $z = z_0$ of a periodic medium is a function of two variables, i. e., $\vec{f} =$

$\boldsymbol{f}(x, y)$. Like in the case of deriving the Rayleigh expansion, we suppose illumination in the Fraunhofer approximation described by an incident plane wave

$$\boldsymbol{E}^{(i)}(\boldsymbol{r}) = A^{(i)}\boldsymbol{j}^{(i)} \exp\left[-i(p^{(i)}x + q^{(i)}y + s^{(i)}z)\right], \tag{4.84}$$

with an amplitude $A^{(i)}$, polarization $\boldsymbol{j}^{(i)}$, and wave vector $\boldsymbol{k}^{(i)} = [p^{(i)}, q^{(i)}, s^{(i)}]^{\mathrm{T}}$ (recall that we work with the coordinates scaled by the vacuum wave number). Then the field in the periodic medium has the following translation properties:

$$\boldsymbol{f}(x + m\Lambda_x, y + n\Lambda_y, z_0) = \boldsymbol{f}(x, y, z_0)\, e^{-i(p^{(i)}m\Lambda_x + q^{(i)}n\Lambda_y)}, \tag{4.85}$$

where Λ_x, Λ_y are periods of the permittivity function $\varepsilon(x, y)$ in the directions of the corresponding coordinates. According to Floquet's theorem, the field can then be evaluated as

$$\boldsymbol{f}(x, y, z_0) = \boldsymbol{u}(x, y, z_0)\, e^{-i(p^{(i)}x + q^{(i)}y)}, \tag{4.86}$$

where $\boldsymbol{u}(x, y, z_0)$ is a periodic function with the same periods Λ_x, Λ_y as the permittivity function. The equal statement, of course, can be written about all the other fields such as magnetic fields, normal components of the fields, or fields split into the directions of propagation.

4.6 Coordinate representation

In the Cartesian-coordinate representation, the operator equations contain partial derivatives $\hat{\partial}_j$ ($j = x, y$) and multiplication by a function $\hat{\varepsilon} = \varepsilon(x, y)$. These two kinds of operators do not commute; indeed

$$[\hat{\partial}_j, \hat{\varepsilon}] = \hat{\varepsilon}_j + \hat{\varepsilon}\hat{\partial}_j \tag{4.87}$$

where $\hat{\varepsilon}_j = \partial_j\varepsilon(x, y)$ is the operator of multiplication by the function's derivative $\partial_j\varepsilon(x, y)$. Applying this rule, we can evaluate the operators (4.19, 4.20) and all the other operators (including the infinitesimal version of $\hat{\mathbf{M}}$) in normal ordering, i. e., as matrices of the type $\hat{\alpha} + \hat{\beta}\hat{\partial}_j + \hat{\gamma}\hat{\partial}_k\hat{\partial}_l$, where $\hat{\alpha}$, $\hat{\beta}$, and $\hat{\gamma}$ are operators of multiplication by some functions $\alpha(x, y)$, $\beta(x, y)$, and $\gamma(x, y)$.

For shallow gratings, i. e., for gratings with horizontal features much larger than vertical ones, the problem can be solved just locally—by applying the approximation of constant values α, β, and γ; then the partial derivatives only apply to the incident wave. Without such an approximation, however, the problem of solving a set of partial differential equations remains. Therefore, for a rigorous analysis of a deeper grating it is more convenient to use the Fourier representation which utilizes both the Fraunhofer approximation and the periodicity of the grating. However, before proceeding to the Fourier representation we will simplify the diffraction problem to the case mostly used in practice.

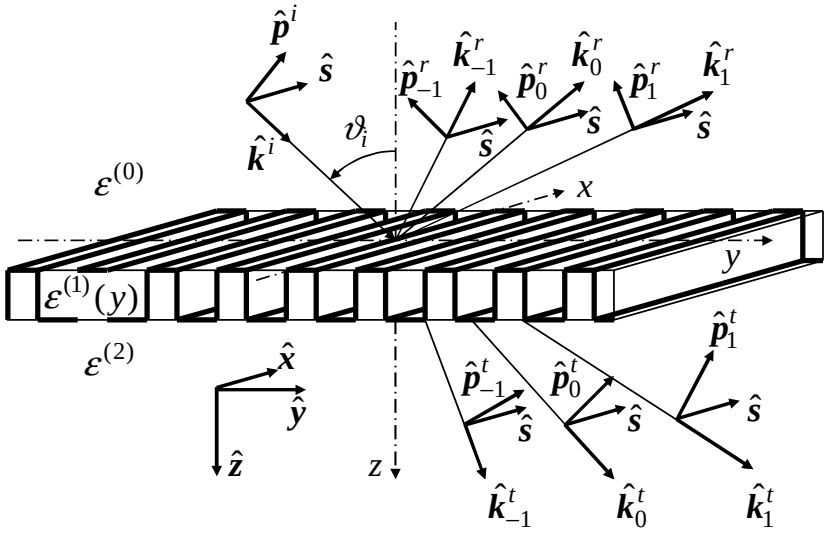

Figure 4.4 The geometry of the planar diffraction mounting.

4.7 Field formulae for a one-dimensional isotropic grating in planar-diffraction mounting

The problem will be significantly simplified when we study a one-dimensional isotropic grating in the planar diffraction mounting, which is displayed in Fig. 4.4. In this case, all the fields do not depend on the x-coordinate, and hence $\hat{\partial}_x \cong 0$. Therefore, Eq. (4.19) becomes

$$\hat{\boldsymbol{\Omega}} = \begin{bmatrix} 0 & 0 & 0 & 1 \\ 0 & 0 & -(1+\partial_y \frac{1}{\varepsilon}\partial_y) & 0 \\ 0 & -\varepsilon & 0 & 0 \\ \varepsilon+\partial_y^2 & 0 & 0 & 0 \end{bmatrix}. \tag{4.88}$$

and the problem of Eq. (4.31) is reduced into scalar-field equations

$$\partial_z \vec{f}^{(\mathtt{s},\mathtt{p})} = -i\,\hat{\Omega}_{12}^{(\mathtt{s},\mathtt{p})} \vec{h}^{(\mathtt{s},\mathtt{p})}, \tag{4.89}$$

$$\partial_z \vec{h}^{(\mathtt{s},\mathtt{p})} = -i\,\hat{\Omega}_{21}^{(\mathtt{s},\mathtt{p})} \vec{f}^{(\mathtt{s},\mathtt{p})}, \tag{4.90}$$

where we have defined, independently for the case of $\mathtt{s}$-polarization,

$$\vec{f}^{(\mathtt{s})}(z_0) = E_x(y, z_0), \tag{4.91}$$

$$\vec{h}^{(\mathtt{s})}(z_0) = H_y(y, z_0), \tag{4.92}$$

$$\hat{\Omega}_{12}^{(\mathtt{s})} = \mathbf{1}, \tag{4.93}$$

$$\hat{\Omega}_{21}^{(\mathtt{s})} = \hat{\varepsilon} + \hat{\partial}_y^2, \tag{4.94}$$

$$\tag{4.95}$$

and independently for the case of p-polarization,

$$\vec{f}^{(\mathtt{p})}(z_0) = H_x(y, z_0), \tag{4.96}$$
$$\vec{h}^{(\mathtt{p})}(z_0) = E_y(y, z_0), \tag{4.97}$$
$$\hat{\Omega}_{12}^{(\mathtt{p})} = -\hat{\varepsilon}, \tag{4.98}$$
$$\hat{\Omega}_{21}^{(\mathtt{p})} = -\left(\mathbf{1} + \hat{\partial}_y \hat{\varepsilon}^{-1} \hat{\partial}_y\right), \tag{4.99}$$

respectively. Notice that although we have identified $\vec{f}$ with the electric field in the case of s-polarization, we are now changing its meaning in the case of p-polarization. In the latter we choose $\vec{f}$ to be the magnetic field because now, independently on polarization, $\vec{f}$ will always be the transverse (x) component of the electromagnetic field while $\vec{h}$ will always be the tangential part of the in-plane field (the field lying within the y—z plane).

Since Eqs. (4.89, 4.90) are formally equal for the both polarizations, we will mostly omit the s(p) index for simplicity, treating only a single polarization in the same time. It is worth pointing out that $L^2(\mathbb{R})$ is now the Hilbert space of states of light in a plane $z = z_0$ corresponding to a single polarization, because the x-coordinate looses its importance in the planar-diffraction mounting.

4.8 Fourier representation

For the numerical solution of diffraction by general periodic structures the Cartesian-coordinate representation becomes inappropriate. The periodicity suggests obvious advantages of using the representation of Fourier series. The general operator equations then become matrix equations based on the Fourier components of the electromagnetic fields and their corresponding linear transforms.

Each jth Cartesian component of the periodic vectorial function from Eq. (4.86) can be expanded into Fourier series

$$u_j(x, y, z) = \sum_{m,\, n=-\infty}^{+\infty} f_{j,\, mn}(z)\, e^{-i(mpx+nqy)}, \tag{4.100}$$
$$p = \frac{\lambda}{\Lambda_x},$$
$$q = \frac{\lambda}{\Lambda_y},$$

where the Fourier components $f_{j,\, mn}$ are functions of only the normal coordinate. Accord-

ingly, the expansion of $\vec{\boldsymbol{f}}(z)$ can be symbolically written as a pseudo-Fourier series

$$\begin{aligned} \vec{\boldsymbol{f}}(z) &= \sum_{m,\,n=-\infty}^{+\infty} f_{j,\,mn}(z)\,\hat{\boldsymbol{\psi}}_{j,\,mn}, \\ \hat{\boldsymbol{\psi}}_{j,\,mn} &= \hat{\boldsymbol{j}}_j\, e^{-i(p_m x + q_n y)},\ j = x,\, y, \\ p_m &= p^{(i)} + mp, \\ q_n &= q^{(i)} + nq. \end{aligned} \tag{4.101}$$

Hereafter, we will omit the qualifier "pseudo" for simplicity.

4.8.1 Matrix notation applied to one-dimensional isotropic grating

Applying the results obtained for one-dimensional isotropic gratings with the planar-diffraction mounting, we can rewrite Eq. (4.101) to the scalar-field form

$$\begin{aligned} \vec{f}(z) &= \sum_{n=-\infty}^{+\infty} f_n(z)\,\hat{\psi}_n, \\ \hat{\psi}_n &= e^{-iq_n y}, \end{aligned} \tag{4.102}$$

which corresponds to any of the s- or p-polarization.

As the next step, we will evaluate the matrix elements of the operators in the Fourier representation. The symbolic vector (4.102) gets a column-vector form

$$\vec{f} = \begin{bmatrix} \vdots \\ f_{-2} \\ f_{-1} \\ f_0 \\ f_1 \\ f_2 \\ \vdots \end{bmatrix}, \tag{4.103}$$

where f_n denote the Fourier components of the function $u(y, z_0) = f(y, z_0)e^{iq^{(i)}y}$ in a fixed plane $z = z_0$, which is a scalar and planar version of $\boldsymbol{u}(x, y, z_0)$ from Eq. (4.86).

The matrix elements of a general operator $\hat{\mathsf{P}}$ in the Fourier representation are simply defined as

$$p_{mn} = \left\langle \hat{\psi}_m, \hat{\mathsf{P}}\hat{\psi}_n \right\rangle, \tag{4.104}$$

where "$\langle \cdot, \cdot \rangle$" denotes the scalar product defined within the Hilbert space $L^2(\mathbb{R})$. Accord-

ingly, we can identify $\hat{\mathsf{P}}$ with a matrix

$$\hat{\mathsf{P}} = \begin{bmatrix} \ddots & & & & & & \ddots \\ & p_{-2,-2} & p_{-2,-1} & p_{-2,0} & p_{-2,1} & p_{-2,2} & \\ & p_{-1,-2} & p_{-1,-1} & p_{-1,0} & p_{-1,1} & p_{-1,2} & \\ & p_{0,-2} & p_{0,-1} & p_{0,0} & p_{0,1} & p_{0,2} & \\ & p_{1,-2} & p_{1,-1} & p_{1,0} & p_{1,1} & p_{1,2} & \\ & p_{2,-2} & p_{2,-1} & p_{2,0} & p_{2,1} & p_{2,2} & \\ \ddots & & & & & & \ddots \end{bmatrix}, \tag{4.105}$$

owing to the following discussion. Suppose that a general operator $\hat{\mathsf{P}}$ acting on $\vec{f}$ produces another vector $\vec{g} = \hat{\mathsf{P}}\vec{f}$ which has its column vector $[\ldots, g_{-2}, g_{-1}, g_0, g_1, g_2, \ldots]^{\mathrm{T}}$ defined analogously as $\vec{f}$, i. e., $\vec{g} = \sum_n g_n \hat{\psi}_n$. Then

$$g_m = \left\langle \hat{\psi}_m, \vec{g} \right\rangle = \left\langle \hat{\psi}_m, \hat{\mathsf{P}}\vec{f} \right\rangle = \sum_n \left\langle \hat{\psi}_m, \hat{\mathsf{P}} f_n \hat{\psi}_n \right\rangle = \sum_n p_{mn} f_n.$$

As the first example, we will find matrix elements of the operator which was defined in the Cartesian coordinate representation as the partial derivative $\hat{\partial}_y = \partial_y$. Applying to Eq. (4.102), we obtain

$$\begin{aligned} \hat{\partial}_y \vec{f} &= \sum_{n=-\infty}^{+\infty} f_n(z)\, \hat{\partial}_y \hat{\psi}_n = \sum_{n=-\infty}^{+\infty} f_n\, \partial_y \left(e^{-iq_n y}\right) \\ &= -i \sum_{n=-\infty}^{+\infty} q_n f_n\, e^{-iq_n y} = -i \sum_{n=-\infty}^{+\infty} q_n f_n\, \hat{\psi}_n, \end{aligned} \tag{4.106}$$

and hence

$$\hat{\partial}_y = -i\, \hat{\mathsf{q}}, \tag{4.107}$$

with

$$\hat{\mathsf{q}} = \begin{bmatrix} \ddots & & & & & & \\ & q_{-2} & & & & & \\ & & q_{-1} & & & & \\ & & & q_0 & & & \\ & & & & q_1 & & \\ & & & & & q_2 & \\ & & & & & & \ddots \end{bmatrix} \tag{4.108}$$

being a diagonal matrix composed of the wave numbers of the Fourier series.

Analogously, we will evaluate the matrix elements of the operator which was in the Cartesian coordinates represented as multiplication by a function such as the permittivity $\varepsilon(y)$, whose periodicity is depicted in Fig. 4.5.

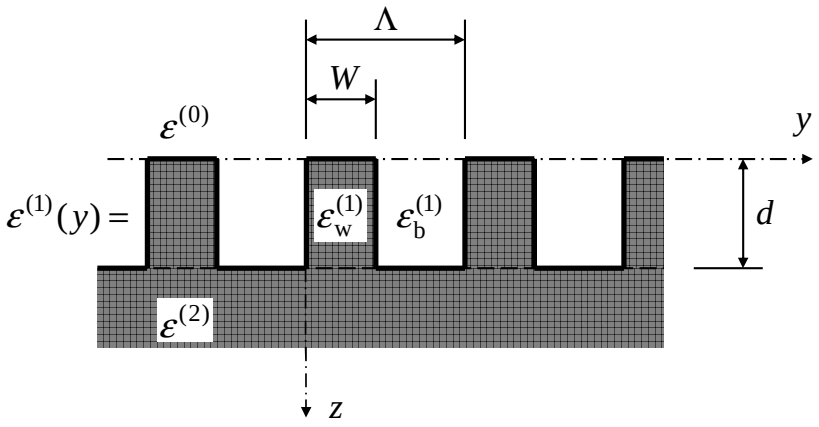

Figure 4.5 The lateral periodicity of the permittivity function $\varepsilon^{(1)}(y)$ which takes on only two values, the permittivity of the medium of "wires," $\varepsilon_{\rm w}^{(1)}$, and the permittivity of the medium "between wires," $\varepsilon_{\rm b}^{(1)}$.

Let $\hat{\alpha}$ be the operator of multiplication by a function $\alpha(y)$ with the periodicity Λ same as the periodicity of the permittivity function $\varepsilon(y)$ and let α_k be its Fourier components. Applying to Eq. (4.102), we obtain

$$\begin{aligned}\hat{\alpha}\vec{f} = \alpha(y)f(y) &= \left(\sum_{k=-\infty}^{+\infty}\alpha_k e^{-ikqy}\right)\left(\sum_{n=-\infty}^{+\infty} f_n e^{-iq_n y}\right), \\ &= \sum_{k,\,n=-\infty}^{+\infty}\alpha_k f_n\, e^{-iq_{n+k}y}, \end{aligned} \tag{4.109}$$

where we have utilized $q_{n+k} = q_n + kq$. Defining another summation index $m = n + k$, we obtain

$$\hat{\alpha}\vec{f} = \sum_{m,\,n=-\infty}^{+\infty}\alpha_{m-n} f_n\, e^{-iq_m y} = \sum_{m,\,n=-\infty}^{+\infty}\alpha_{m-n} f_n\,\hat{\psi}_m \tag{4.110}$$

or, if we define $\vec{g} = \hat{\alpha}\vec{f}$,

$$g_m = \alpha_{m-n} f_n, \tag{4.111}$$

which is referred to as Laurent's rule. Clearly, the matrix elements of the operator $\hat{\alpha}$ are the components of the Fourier series of $\alpha(y)$, each of which fills up one negative-sloping diagonal, and hence $\hat{\alpha}$ is represented by a Toeplitz matrix

$$\hat{\alpha} = [\![\alpha]\!] = \begin{bmatrix} \ddots & & & & & & \ddots \\ & \alpha_0 & \alpha_{-1} & \alpha_{-2} & \alpha_{-3} & \alpha_{-4} & \\ & \alpha_1 & \alpha_0 & \alpha_{-1} & \alpha_{-2} & \alpha_{-3} & \\ & \alpha_2 & \alpha_1 & \alpha_0 & \alpha_{-1} & \alpha_{-2} & \\ & \alpha_3 & \alpha_2 & \alpha_1 & \alpha_0 & \alpha_{-1} & \\ & \alpha_4 & \alpha_3 & \alpha_2 & \alpha_1 & \alpha_0 & \\ \ddots & & & & & & \ddots \end{bmatrix}, \tag{4.112}$$

where the brackets "$[\![\cdot]\!]$" symbolically denote the Toeplitz matrix composed by the Fourier components.

Now the operators in Eqs. (4.89, 4.90) can be written as

$$\hat{\Omega}_{12}^{(\mathrm{s})} = \mathbf{1}, \tag{4.113}$$
$$\hat{\Omega}_{21}^{(\mathrm{s})} = [\![\varepsilon]\!] - \hat{\mathsf{q}}^2, \tag{4.114}$$
$$\hat{\Omega}_{12}^{(\mathrm{p})} = -[\![\varepsilon]\!], \tag{4.115}$$
$$\hat{\Omega}_{21}^{(\mathrm{p})} = -\left(\mathbf{1} - \hat{\mathsf{q}}[\![\varepsilon]\!]^{-1}\hat{\mathsf{q}}\right), \tag{4.116}$$

the last of which can be alternatively rewritten as

$$\hat{\Omega}'^{(\mathrm{p})}_{21} = -\left(\mathbf{1} - \hat{\mathsf{q}}\left[\!\!\left[\frac{1}{\varepsilon}\right]\!\!\right]\hat{\mathsf{q}}\right). \tag{4.117}$$

The operator equations thus become simple matrix equations which, after appropriate truncation of high-order Fourier-series elements, can be easily solved with linear-algebraic techniques.

4.8.2 Fourier factorization

In Sec. (4.8) we have shown how the operator of multiplication by a function is represented by a Toeplitz matrix, referred to as the Laurent rule. For the purpose of numerical evaluation, the Fourier series and corresponding matrices must be truncated, which causes trouble with mathematical correctness of the Laurent rule when applied to periodic functions with discontinuities. Therefore, three theorems of the so-called *Fourier factorization* were derived by Li [75], which will be briefly described here and then applied to our diffraction problem.

For all the three theorems, let $f(y)$, $g(y)$, and $\alpha(y)$ be piecewise-continuous functions with the same periodicity related

$$g(y) = \alpha(y)f(y), \tag{4.118}$$

and let f_n, g_n, and α_n denote the coefficients of their Fourier series.

Theorem 1. If $\alpha(y)$ and $f(y)$ have no concurrent discontinuities, then the Laurent rule applied to Eq. (4.118) converges correctly, i. e.,

$$g_m = \lim_{n_{\max}\to\infty} \sum_{n=-n_{\max}}^{n_{\max}} \alpha_{m-n} f_n, \tag{4.119}$$

and hence

$$\vec{g} = [\![\alpha]\!]\vec{f} \tag{4.120}$$

can be applied.

Theorem 2. If $\alpha(y)$ and $f(y)$ have one or more concurrent discontinuities but $g(y)$ is continuous, then Eq. (4.118) can be transformed into the case of *Theorem 1*,

$$f(y) = \frac{1}{\alpha(y)} g(y), \tag{4.121}$$

and hence

$$f_m = \lim_{n_{\max}\to\infty} \sum_{n=-n_{\max}}^{n_{\max}} \beta_{m-n} g_n, \tag{4.122}$$

where β_n are the Fourier coefficients of the function $\beta(y) = 1/\alpha(y)$. Accordingly, we can state

$$\vec{g} = \left[\!\left[\frac{1}{\alpha}\right]\!\right]^{-1} \vec{f} \tag{4.123}$$

referred as the inverse rule. We say that the functions $\alpha(y)$ and $f(y)$ have complementary discontinuities.

Theorem 3. If none of the requirements of the first two theorems are satisfied, then none of the rules can be applied correctly because Eqs. (4.119, 4.122) are not valid. Therefore, we must carefully analyze the continuity of the functions and transform all the partial differential formulae to the first two cases.

To apply the Fourier factorization rules in our case of a one-dimensional grating with the planar diffraction mounting, we will analyze Eqs. (4.89, 4.90). First, for the case of s-polarization, the only partial differential equation containing $\varepsilon(y)$ is

$$\partial_z H_y = -i \left[\varepsilon(y) + \partial_y^2\right] E_x. \tag{4.124}$$

Here the Laurent rule can be applied because $E_x(y, z)$ is tangential to all the normal and lateral interfaces and hence continuous everywhere.

Second, for the case of p-polarization, we have two tangential equations containing $\varepsilon(y)$:

$$\partial_z H_x = i\varepsilon(y) E_y, \tag{4.125}$$

$$\partial_z E_y = i \left[\mathbf{1} + \partial_y \frac{1}{\varepsilon(y)} \partial_y\right] H_x. \tag{4.126}$$

In the former equation, H_x is tangential to all the interfaces and hence continuous everywhere. Since we analyze the equations in media with uniformity in the normal direction, also $\partial_z H_x$ is continuous, and hence we apply the inverse rule. To analyze the latter of the above equations, the simplified version of Eq. (4.13) will help us, i. e.,

$$E_z = \frac{i}{\varepsilon} \partial_y H_x, \tag{4.127}$$

from which the continuity of $(1/\varepsilon)\partial_y H_x$ is obvious, and hence the inverse rule

$$\frac{1}{\varepsilon} \partial_y H_x = [\![\varepsilon]\!]^{-1} (-i\hat{\mathsf{q}}) \vec{H}_x$$

can be applied.

As a summary, we will write the matrices $\hat{\Omega}_{12}$ and $\hat{\Omega}_{21}$ in the Fourier representation as follows:

$$\hat{\Omega}_{12}^{(\mathrm{s})} = \mathbf{1}, \tag{4.128}$$
$$\hat{\Omega}_{21}^{(\mathrm{s})} = [\![\varepsilon]\!] - \hat{\mathsf{q}}^2, \tag{4.129}$$
$$\hat{\Omega}_{12}^{(\mathrm{p})} = -\left[\!\left[\tfrac{1}{\varepsilon}\right]\!\right]^{-1}, \tag{4.130}$$
$$\hat{\Omega}_{21}^{(\mathrm{p})} = -\left(\mathbf{1} - \hat{\mathsf{q}}[\![\varepsilon]\!]^{-1}\hat{\mathsf{q}}\right), \tag{4.131}$$

from which all the other matrices are derived.

4.8.3 General binary and/or anisotropic gratings

Binary gratings, alternatively called two-dimensional, biperiodic, or crossed gratings, are structures with two-dimensional lateral patterning. The algorithm of rewriting their operator equations into the form of Fourier representation is formally almost identical with the approach described for the case of one-dimensional gratings, except that the vectors and matrices are derived on the basis of two-dimensional Fourier transform. Similarly, when we are treating generally anisotropic media, we must expand each element of the periodic permittivity tensorial function into the Fourier series and use it in the general coupled wave equations.

Chapter 5

Description of experimental techniques

There are many methods of measuring the optical response of planar and planar-like structures according to the type of light sources, detectors and other tools used, according to the quantities measured, and according to the type of the parameters the response is resolved into. For the purpose of scatterometry, the most powerful are spectroscopic techniques, i. e., techniques providing optical measurements in a broad range of wavelengths for which proper light sources, detectors, and polarizing tools operate. In our work we use spectroscopic techniques operating in the visible/near-UV spectral range which is provided by thermal sources of light such as a xenon or mercury-xenon lamp. Techniques other than spectroscopic mostly use coherent single-wavelength sources and provide, for instance, dependences on the angle of incidence or, in the presence of magnetic materials, dependences on the intensity and/or direction of an external magnetic field (hysteresis loops).

General arrangement of a spectroscopic measurement on a thin-film or grating sample is depicted in Fig. 5.1. Light flux is generated by a lamp, then undergoes input optics to become (in the Fraunhofer approximation) a plane wave with an amplitude $A^{(i)}$ and a polarization ellipse $\chi^{(i)}$ incident onto the sample. In the case of a planar structure, the flux is scattered into two independent modes, referred to as reflection and transmission, one of which only is usually measured the same time. The mode of interest subsequently undergoes output optics and finally its intensity is detected by a detector.

In the case of a grating, the flux is scattered into more modes, referred to as diffraction orders within both the reflection and the transmission modes. The most often mode analyzed is the specular mode, i. e., the 0th diffraction order of reflection. Sometimes the transmitted 0th diffraction order is also measured to obtain additional spectroscopic data which can help in scatterometric analyses. However, higher orders of diffraction are analyzed by spectroscopy very rarely, probably due to the spectral dependence of the directions of their wave vectors.

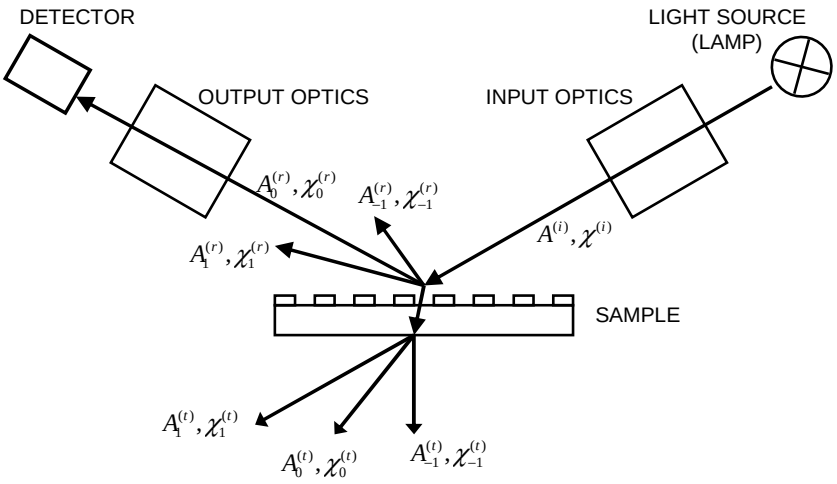

Figure 5.1 General arrangement of an experimental technique of measuring the optical response of a grating in a single diffraction order.

According to quantities measured, the spectroscopic techniques can generally be classified into two different groups. First, photometric techniques measure the amount of energy reflected or transmitted into the nth diffraction order, and hence provide the ratio $(A_n^{(r,t)}/A^{(i)})^2$ of output to incident intensities (Sec. 5.1). Second, ellipsometric techniques measure the change of the polarization of the incident light, and hence provide the ratio $\chi_n^{(r,t)}/\chi^{(i)}$ of the complex χ-numbers (Sec. 5.2). A technique combining both photometry and ellipsometry is sometimes referred to as polarimetry. We will also distinguish between purely optical techniques and magneto-optics, the latter of which corresponds to measurement on a structure with magnetic ordering which induces slight anisotropy in the magnetic material. The magnetic ordering is frequently induced by an external magnetic field (Sec. 5.3).

5.1 Spectrophotometry

Spectrophotometry refers to energy reflectance and/or transmittance measurement in spectral resolution. Light flux generated by a lamp is driven to the sample through input optics which usually consists of a set of mirrors, a monochromator, an entrance slit, and (optionally) a polarizer. The reflected or transmitted light flux is then driven directly to a detector (usually through a set of mirrors again) which detects the intensity $I_n^{(r,t)}$ of the diffracted flux via voltage. To obtain the reflectance R_n or transmittance T_n of the nth diffraction order in percentage, we first measure the reflected intensity $I_{\mathrm{ref}}^{(r)}$ or transmitted intensity $I_{\mathrm{ref}}^{(t)}$ of a well-known reference sample, and then we apply the both values in the

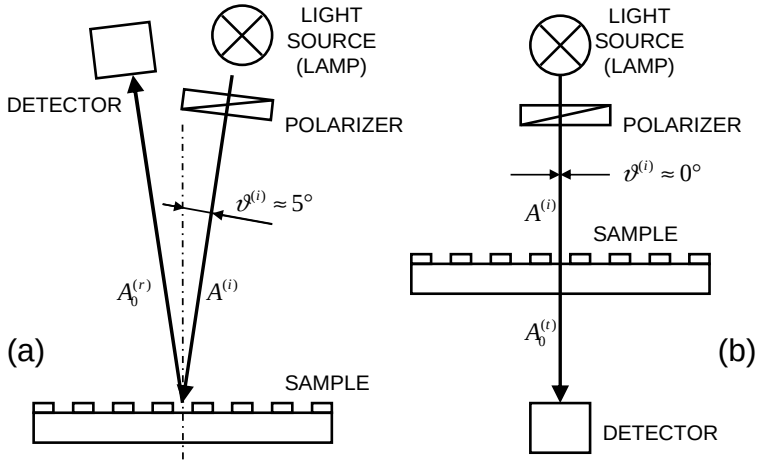

Figure 5.2 Usual arrangements for normal-incidence reflectance (a) and transmittance (b) measurements.

formulae

$$R_n = \frac{I_n^{(r)}}{I_{\mathrm{ref}}^{(r)}} R_{\mathrm{ref}}, \tag{5.1}$$

$$T_n = \frac{I_n^{(t)}}{I_{\mathrm{ref}}^{(t)}} T_{\mathrm{ref}}, \tag{5.2}$$

where R_{ref} and T_{ref} denote simulated reflectance and transmittance of the reference sample assumed perfectly known. In the case of measuring reflectance we often use a silicon wafer whose native SiO_2 overlayer is detected by another method. In the case of measuring transmittance, on the other hand, the reference sample is represented just by air with $T_{\mathrm{ref}} = 1$.

The most often configuration for measuring photometric quantities is with normal or nearly normal incidence, as shown in Fig. 5.2. In the case of reflectance, the incidence angle cannot be exactly zero; manufacturers usually choose approximately $\vartheta^{(i)} \approx 5°$. In the case of transmittance, the incidence angle is adjusted to zero. The purpose of choosing the normal incidence is independence of the optical response of planar structures on polarization; therefore, many apparatuses are constructed without polarizers. Normal-incidence response from gratings, however, strongly depends on the incident polarization except the response of very shallow gratings without internal-diffraction edge effects. Therefore, during measuring deeper gratings, a polarizer must be included within the input optics for both the sample and the reference to avoid an influence of the polarizer's transmittance.

The main disadvantage of spectrophotometric techniques is time instability of the intensity of the light flux generated by thermal sources. A time delay during achieving the whole spectrum is usually too large to keep the intensity constant, which causes a high inaccuracy of Eqs. (5.1, 5.2). Therefore, special configurations with double beams are arranged, one beam for the sample and second for the reference, which are produced

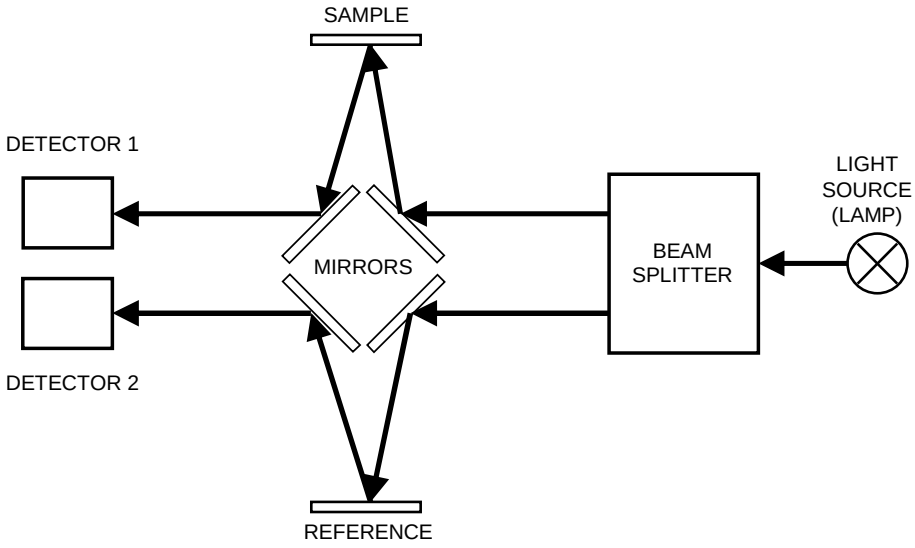

Figure 5.3 Arrangement for double-beam reflectance measurement. The same configuration is used for double-beam transmittance measurement when the mirrors are removed.

by a beam splitter from a single light flux, as schematically depicted in Fig. 5.3. Since the both beams are not perfectly equal, the measurement is carried twice; first time with the sample and the reference as shown on the scheme, second time with two (usually identical) references. The modified formulae for the photometric quantities are

$$R_n = \frac{I_n^{(r)}/I_{\mathrm{ref1}}^{(r)}}{\tilde{I}_{\mathrm{ref2}}^{(r)}/\tilde{I}_{\mathrm{ref1}}^{(r)}} R_{\mathrm{ref1}}, \tag{5.3}$$

$$T_n = \frac{I_n^{(t)}/I_{\mathrm{ref1}}^{(t)}}{\tilde{I}_{\mathrm{ref2}}^{(t)}/\tilde{I}_{\mathrm{ref1}}^{(t)}} T_{\mathrm{ref2}}, \tag{5.4}$$

where the non-tilded intensities $I_n^{(r,t)}$, $I_{\mathrm{ref1}}^{(r,t)}$ correspond to the first-time measurement on the sample and the reference, respectively, as precisely shown in Fig. 5.3, whereas the tilded intensities $\tilde{I}_{\mathrm{ref1}}^{(r,t)}$, $\tilde{I}_{\mathrm{ref2}}^{(r,t)}$ correspond to the second-time measurement on the two references. The subscript "ref1" corresponds to the reference which is always put to the reference position (the bottom part of Fig. 5.3), while the subscript "ref2" corresponds to the reference which is during the second-time measurement put instead of the sample (the top part of Fig. 5.3). If we want to measure polarized reflectance or transmittance, we have to put two identical polarizers into the spectrophotometer to polarize the light flux at both the sample and the reference positions, and keep them there during both the sample-reference and the double-reference measurements.

5.2 Spectroscopic ellipsometry

Unlike the photometric methods, ellipsometry is a way of measuring the change of the polarization ellipse without being concerned with light intensities. However, the detection

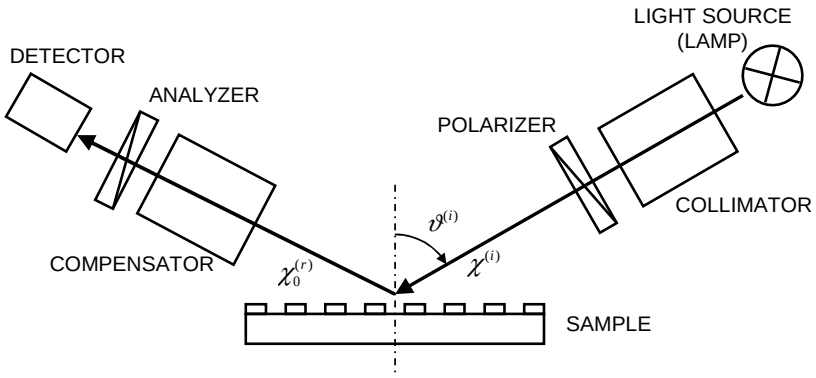

Figure 5.4 Usual arrangement of a spectroscopic ellipsometer with the polarizer-sample-compensator-analyzer configuration.

of the properties of the light flux scattered by the sample is achieved via the same detecting tools as in the case of photometry, and hence special configurations of the input and output optics must be arranged.

In Fig. 5.4, a standard arrangement of an ellipsometer is displayed with the polarizer-sample-compensator-analyzer (PSCA) configuration, in which the analyzer is another polarizer located within the output optics while the compensator is a phase-retarding tool, usually a quarter-wave retarder or a photoelastic modulator (PEM). There are also configurations with the compensator put before the sample (PCSA), configurations without compensator (PSA), etc.

Before demonstrating particular ellipsometric techniques, we will first derive general equations governing the propagation of polarized light through the PSCA system. For this purpose we make use of the Jones formalism.

Suppose that a light beam propagates through the set of optical components displayed in Fig. 5.4. For simplicity we only assume specular reflection described by the amplitude reflection coefficients $r_{\mathtt{s}}$, $r_{\mathtt{p}}$, though the same procedure can be applied to any diffracted order. The beam is polarized by the polarizer, then is reflected by the structure, undergoes phase retardation by the compensator, is re-polarized by the analyzer, and finally its intensity is detected by the detector. The propagation through each of the components is described by a Jones matrix. In the linear-polarization $[x, y]$ representation, the Jones matrix of a polarizer takes the form

$$\mathbf{P} = \begin{bmatrix} 1 & 0 \\ 0 & 0 \end{bmatrix}, \tag{5.5}$$

provided that the polarizer is oriented so that its transmission and extinction axes coincide with the x- and y-axes, respectively. The Jones matrix of a compensator in the same representation is

$$\mathbf{C}(\delta) = \begin{bmatrix} e^{i\frac{\delta}{2}} & 0 \\ 0 & e^{-i\frac{\delta}{2}} \end{bmatrix}, \tag{5.6}$$

provided that the fast and slow axes coincide with the x- and y-axes. Finally, the Jones matrix of the sample in the basis of its specular-reflection eigenmodes is

$$\mathbf{S} = \begin{bmatrix} r_{\mathtt{s}} & 0 \\ 0 & r_{\mathtt{p}} \end{bmatrix}. \tag{5.7}$$

We choose the `s`- and `p`-axes corresponding to the sample as the absolute coordinates of all the components, which will themselves be rotated relatively to the sample. We denote α, β, and γ the rotation angles of the polarizer, compensator, and analyzer, respectively. Accordingly, the Jones vector of the beam outgoing from the analyzer in the basis of the analyzer's eigenmodes can be written

$$\boldsymbol{J}^{(o)} = \mathbf{P}\,\mathbf{R}(\beta-\gamma)\,\mathbf{C}(\delta)\,\mathbf{R}(\gamma)\,\mathbf{S}\,\mathbf{R}(-\alpha)\,\boldsymbol{J}^{(i)}, \tag{5.8}$$

where

$$\mathbf{R}(\omega) = \begin{bmatrix} \cos\omega & \sin\omega \\ -\sin\omega & \cos\omega \end{bmatrix}, \tag{5.9}$$

denotes the matrix of rotation by an angle ω and where $\boldsymbol{J}^{(i)} = [1,0]^{\mathrm{T}}$ denotes the Jones vector of the polarized beam incident to the sample in the basis of the polarizer's eigenmodes. The intensity of the output beam detected by the detector is

$$I^{(o)} = I^{(i)} \left(\boldsymbol{J}^{(o)}\right)^{\dagger} \boldsymbol{J}^{(o)} = I^{(i)}|L|, \tag{5.10}$$

where $I^{(i)}$ denotes the intensity of the polarized beam incident to the sample, and with the complex quantity defined

$$\begin{aligned} L &= r_{\mathtt{s}} \cos\alpha \left[e^{i\delta}\cos\gamma\cos(\beta-\gamma) - \sin\gamma\sin(\beta-\gamma)\right] \\ &+ r_{\mathtt{p}} \sin\alpha \left[\cos\gamma\sin(\beta-\gamma) + e^{i\delta}\sin\gamma\cos(\beta-\gamma)\right]. \end{aligned} \tag{5.11}$$

Usually it is more convenient to work with translated angles $\bar{\alpha} = \alpha - \frac{\pi}{2}$ and $\bar{\beta} = \beta - \frac{\pi}{2}$, according to which Eq. (5.11) takes the form

$$\begin{aligned} L &= r_{\mathtt{s}} \sin\bar{\alpha} \left[e^{i\delta}\cos\gamma\sin(\bar{\beta}-\gamma) + \sin\gamma\cos(\beta-\gamma)\right] \\ &+ r_{\mathtt{p}} \cos\bar{\alpha} \left[\cos\gamma\cos(\bar{\beta}-\gamma) - e^{i\delta}\sin\gamma\sin(\beta-\gamma)\right], \end{aligned} \tag{5.12}$$

from which we will derive equations corresponding to special ellipsometric techniques which are mostly used in the scatterometric analyses presented in this thesis.

5.2.1 Four-zone null ellipsometry

Null ellipsometry is a measurement technique which provides the ellipsometric ratio $\varrho = r_{\mathtt{p}}/r_{\mathtt{s}}$ by searching null-intensity positions of the polarizer and analyzer according to fixed

Zone	Ψ	Δ
1	$\bar{\alpha}$	$2\bar{\beta}+\frac{\pi}{2}$
2	$-\bar{\alpha}$	$2\bar{\beta}-\frac{\pi}{2}$
3	$\bar{\alpha}$	$-2\bar{\beta}-\frac{\pi}{2}$
4	$-\bar{\alpha}$	$-2\bar{\beta}+\frac{\pi}{2}$

Table 5.1 Four zones of the null intensity in an ellipsometer with the PSCA configuration. Parameters $\bar{\alpha}$ and $\bar{\beta}$ denote the angles of the polarizer and analyzer, respectively, rotated relatively to the p axis of the sample.

positions of the compensator. Stating the null condition for L in Eq. (5.12), i. e., $L=0$, yields

$$\varrho = -\tan\bar{\alpha}\frac{\tan\gamma + e^{i\delta}\tan(\bar{\beta}-\gamma)}{1-e^{i\delta}\tan\gamma\tan(\bar{\beta}-\gamma)}. \tag{5.13}$$

In our ellipsometric system, the compensator is a quarter-wave retarder, i. e., $\delta=\frac{\pi}{2}$, which operates at two different positions $\gamma^{(\pm)}=\pm\frac{\pi}{4}$. Accordingly we rewrite Eq. (5.13) as

$$\varrho = -\tan\bar{\alpha}\frac{\pm 1 + i\tan(\bar{\beta}\mp\frac{\pi}{4})}{1\mp i\tan(\bar{\beta}\mp\frac{\pi}{4})} \tag{5.14}$$

or, after substituting $\varrho=\tan\Psi\, e^{i\Delta}$ and using the mathematical formula $e^{2i\omega}=(1+i\tan\omega)/(1-i\tan\omega)$,

$$\tan\Psi\, e^{i\Delta} = -\tan\bar{\alpha}\, e^{2i(\bar{\beta}-\frac{\pi}{4})}, \tag{5.15}$$

$$\tan\Psi\, e^{i\Delta} = \tan\bar{\alpha}\, e^{-2i(\bar{\beta}+\frac{\pi}{4})}, \tag{5.16}$$

the former of which corresponds to $\gamma^{(+)}$ while the latter to $\gamma^{(-)}$, respectively. Obviously, each of Eqs. (5.15, 5.16) has two solutions; therefore, we have four so-called null zones as written in Tab. 5.1. Each of the zones can provide the intended Ψ and Δ parameters. For the purpose of eliminating slight misalignment in the setup of the polarizing components, all the four zones are measured and the ellipsometric parameters are calculated as the averages

$$\Psi = \tfrac{1}{4}\left(\bar{\alpha_1}-\bar{\alpha_2}+\bar{\alpha_3}-\bar{\alpha_4}\right), \tag{5.17}$$

$$\Delta = \tfrac{1}{2}\left(\bar{\beta_1}+\bar{\beta_2}-\bar{\beta_3}-\bar{\beta_4}\right), \tag{5.18}$$

where $\bar{\alpha}_j$, $\bar{\beta}_j$ are the null positions of the polarizer and analyzer corresponding to the jth zone. It is worth noting that in the absence of the compensator the null positions of the polarizers and analyzer $[\alpha,\beta]$ are the trivial positions $[0,\pm\frac{\pi}{2}]$ and $[\pm\frac{\pi}{2},0]$ from which the ellipsometric parameters are not detectable.

The most of the experimental data analyzed in this thesis were obtained on a four-zone null ellipsometer whose detailed arrangement is displayed in Fig. 5.5.

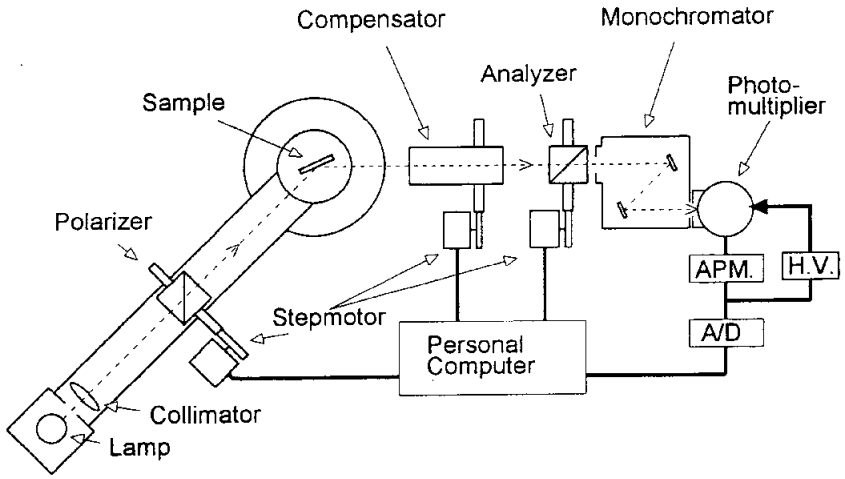

Figure 5.5 The computer-controlled four-zone null spectroscopic ellipsometer with the PSCA configuration which was used to measure most of the samples analyzed in this thesis.

5.2.2 Rotating analyzer ellipsometry

Besides null ellipsometric techniques, there are so-called photometric techniques which are based on analyzing the dependence of the detected intensity on one or more components of the ellipsometric system. The most simple of those is a technique at which one of the polarizers is fixed and the other one rotates while the intensity is recorded. The resulting record is then Fourier analyzed to determine the ellipsometric parameters. Since this technique does not need null positions, the compensator is not necessary to be included in the system. (However, it is frequently included to increase the sensitivity of measurement.) Therefore, for simplicity we will derive the formulae of ellipsometric system with the simple PSA configuration, i. e., with $\delta = 0$ and $\gamma = 0$ in Eq. (5.12)., according to which the intensity (5.10) becomes

$$I^{(o)} = I^{(i)} |r_{\mathrm{s}}|^2 \left(\sin\bar{\alpha}\sin\bar{\beta} + \varrho^* \cos\bar{\alpha}\cos\bar{\beta}\right)\left(\sin\bar{\alpha}\sin\bar{\beta} + \varrho\cos\bar{\alpha}\cos\bar{\beta}\right), \tag{5.19}$$

where $\varrho = \tan\Psi\, e^{i\Delta}$ again denotes the ellipsometric ratio $r_{\mathrm{p}}/r_{\mathrm{s}}$.

Obviously, Eq. (5.19) remains equal when $\bar{\alpha}$, $\bar{\beta}$ are changed; therefore, it is sufficient just to derive formulae corresponding to *rotation analyzer ellipsometry (RAE)* at which the analyzer is rotated while the polarizer is fixed.

Using $\sin^2\bar{\beta} = \frac{1}{2}(1 - \cos 2\bar{\beta})$, $\cos^2\bar{\beta} = \frac{1}{2}(1 + \cos 2\bar{\beta})$, and $\sin\bar{\beta}\cos\bar{\beta} = \frac{1}{2}\sin 2\bar{\beta}$ yields

$$I^{(o)} = \frac{1}{2} I^{(i)} |r_{\mathrm{s}}|^2 \left(1 + a\cos 2\bar{\beta} + b\cos 2\bar{\beta}\right), \tag{5.20}$$

where

$$a = \frac{|\varrho|^2 - \tan^2\bar{\alpha}}{|\varrho|^2 + \tan^2\bar{\alpha}}, \tag{5.21}$$

$$b = \frac{2\,\mathrm{Re}(\varrho)\tan\bar{\alpha}}{|\varrho|^2 + \tan^2\bar{\alpha}} \tag{5.22}$$

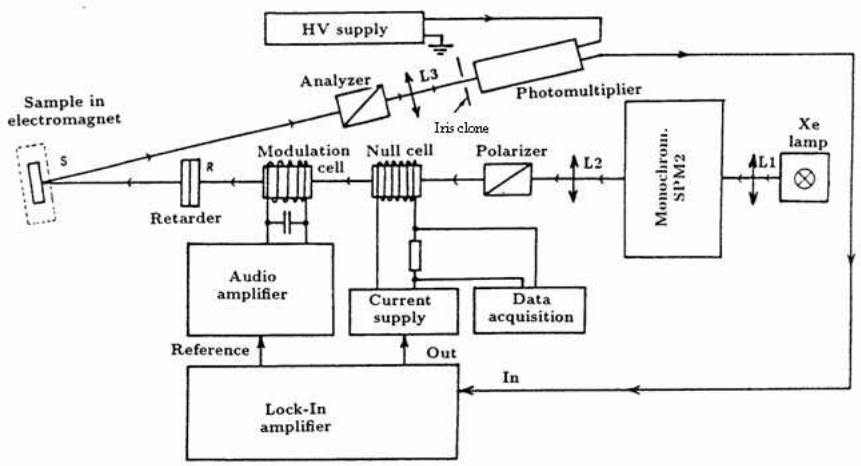

Figure 5.6 Magneto-optic spectrometer applied for measuring the polar magneto-optic Kerr effect.

are coefficients which can easily be determined by the Fourier analysis of the recorded intensity $I_{\bar{\alpha}}^{(o)}(\bar{\beta})$, which is a function of the angle $\bar{\beta}$ of the rotated analyzer for a single fixed angle $\bar{\alpha}$ of the polarizer. Solving Eqs. (5.21, 5.22) for $|\varrho|$ and $\mathrm{Re}(\varrho)$ yields

$$\tan\Psi = \sqrt{\frac{1+a}{1-a}}\,|\tan\bar{\alpha}| \tag{5.23}$$

$$\tan\Psi\,\cos\Delta = \frac{b}{1-a}\tan\bar{\alpha}. \tag{5.24}$$

Unfortunately, the RAE technique in the absence of a compensator does not directly provide the Δ parameter, but only its cosine. Therefore, authors presenting results obtained on such ellipsometers only demonstrate spectral dependences of $\tan\Psi$ and $\cos\Delta$, though the the unknown sign of $\sin\Delta = \pm\sqrt{1-\cos^2\Delta}$ could be determined by comparing with simulation.

5.3 Magneto-optic spectroscopy

Fig. 5.6 shows the arrangement of the magneto-optic spectrometer applied here for measuring polar magneto-optical Kerr effect in the visible and near-UV spectral range. The details of the techniques are described in Ref. [76].

Chapter 6

Data processing in optical scatterometry

Optical scatterometry is a measurement technique based on analyzing the experimental optical response of laterally patterned structures in order to determine their material and/or geometrical properties, particularly the dielectric functions and optical critical dimensions. In this chapter, a brief technical description of the least-square method applied in scatterometry based on specular-mode spectroscopic ellipsometry will be provided together with examples of parameterization of the dielectric function and topographic profiles of gratings. Hereafter in this chapter we assume that the experimental optical response consists of a measurement of specular-mode spectroscopic ellipsometry at one or more angles of incidence, optionally completed by energy reflectance and/or transmittance measurements.

6.1 Application of the least-square method in scatterometry

The principle of determining unknown parameters of an analyzed structure, known as the fitting, is minimizing the difference between simulated and measured values. This error is here evaluated as the angular distance between the measured and simulated points plotted on Poincaré's sphere, which is specified by the azimuthal angle 2Ψ and the polar angle Δ, i. e.,

$$\cos \mathcal{E}_j = \boldsymbol{S}_{\mathrm{e},\,j} \cdot \boldsymbol{S}_{\mathrm{m},\,j}, \tag{6.1}$$

where $\mathcal{E}_j$ represents the error of the jth value, while

$$\boldsymbol{S}_{\mathrm{e},\,j} = \begin{bmatrix} \sin 2\Psi_{\mathrm{e},\,j} \cos \Delta_{\mathrm{e},\,j} \\ \sin 2\Psi_{\mathrm{e},\,j} \sin \Delta_{\mathrm{e},\,j} \\ \cos 2\Psi_{\mathrm{e},\,j} \end{bmatrix}, \tag{6.2}$$

$$\boldsymbol{S}_{\mathrm{m},\,j} = \begin{bmatrix} \sin 2\Psi_{\mathrm{m},\,j} \cos \Delta_{\mathrm{m},\,j} \\ \sin 2\Psi_{\mathrm{m},\,j} \sin \Delta_{\mathrm{m},\,j} \\ \cos 2\Psi_{\mathrm{m},\,j} \end{bmatrix} \tag{6.3}$$

denote the three-dimensional normalized Stokes vectors of the jth experimental [Eq. (6.2)] and modeled [Eq. (6.3)] ellipsometric value, respectively, in an ideal nondepolarizing system. For the sake of fitting in this thesis, the sum of squares of differences

$$\mathcal{E}_{\mathrm{LS}}^2 = \sum_j \mathcal{E}_j^2 \tag{6.4}$$

will be minimized (LS = least squares). In tables, however, the averaged error over M experimental values

$$\mathcal{E} = \frac{1}{M} \sum_{j=1}^{M} \mathcal{E}_j \tag{6.5}$$

will be listed. To evaluate errors of values measured by RAE, which only provides $\mathrm{Re}(e^{i\Delta_{\mathrm{e},\,j}}) = \cos \Delta_{\mathrm{e},\,j}$ instead of the complete phase information $\Delta_{\mathrm{e},\,j}$, we will simply complete that information by defining

$$\sin \Delta_{\mathrm{e},\,j} = \sin \left[\arccos \left(\cos \Delta_{\mathrm{e},\,j} \right) \right], \tag{6.6}$$

$$\sin \Delta_{\mathrm{m},\,j} = \sin \left[\arccos \left(\cos \Delta_{\mathrm{m},\,j} \right) \right] \tag{6.7}$$

to substitute in Eqs. (6.2, 6.3).

6.2 Determination of material properties

Usually two different methods are used to perform the determination of unknown spectral dependences of materials present in the sample, a "point-by-point" analysis and using the *model dielectric function (MDF)*.

Fitting the measured optical spectrum point-by-point is convenient when just two real parameters are to be determined while all the others are known, because the ellipsometric ratio $\varrho = r_{\mathtt{p}}(\lambda)/r_{\mathtt{s}}(\lambda)$ also consists of two real values $\Psi(\lambda)$, $\Delta(\lambda)$ for each wavelength λ. In a special case of a *bulk sample*, i. e., an interface between two semi-infinite half-spaces, the point-by-point analysis is reduced to a simple bulk formula

$$N^{(1)} = N^{(0)} \tan \vartheta^{(i)} \sqrt{1 - \frac{4\varrho}{(1+\varrho)^2} \sin^2 \vartheta^{(i)}}, \tag{6.8}$$

No.	Name	Formula $\varepsilon(E) = \varepsilon_r - i\varepsilon_i$	Parameters	
1	vacuum	1	0	—
2	nondispersive	$\varepsilon_{r\infty}$	1	$\varepsilon_{r\infty}$
3	Sellmeier	$\frac{A\lambda^2}{\lambda^2 - B^2}$	2	A, B
4	Cauchy	$n(\lambda) = A + \frac{B}{\lambda^2} + \frac{C}{\lambda^4}$	3	A, B, C
5	Tauc-Lorentz	$\varepsilon_i = \frac{AE_0C(E-E_g)^2}{[(E^2-E_0^2)^2+C^2E^2]E}$ $\varepsilon_r = \varepsilon_{r\infty} + \mathrm{KK}^{a)}$ integr. of ε_i	5	$\varepsilon_{r\infty}$, E_g, A, E_0, C
6	DHO [b)]	$\frac{AE_0^2}{E_0^2 - E^2 + i\Gamma E E_0}$	3	A, E_0, Γ
7	Drude	$-\frac{E_1^2}{E^2 - iE_2E}$	3	E_1, E_2

[a)] KK = Krammers-Kroenig

[b)] DHO = damped harmonic oscillator

Table 6.1 Model dielectric functions of various materials. Some of them are defined as functions of the wavelength λ, and some as functions of the photon energy E.

where $\vartheta^{(i)}$ is the angle of incidence, $N^{(0)} = n^{(0)} - ik^{(0)}$ is the complex refractive index of the incidence medium (usually air or vacuum), and $N^{(1)} = n^{(1)} - ik^{(1)}$ is the complex refractive index of the bulk medium to be determined. For more complicated structures such as thin films and especially gratings, however, the analysis must be performed numerically by using the least-square method described in Sec. 6.1.

Sometimes more than two real parameters can be determined point-by-point, although the material parameters at a single wavelength are correlated with the third (usually geometrical) parameter. In such a case, usually a function of $2M + 1$ real variables

$$\mathcal{E}^2_{\mathrm{LS}}(n_1, k_1, n_2, k_2, \ldots, n_M, k_M, d) = \sum_{j=1}^{M} \mathcal{E}_j^2(n_j, k_j, d) \tag{6.9}$$

is minimized, in which n_j and k_j are unknown real optical parameters at the jth wavelength and d is the unknown geometrical parameter whose value, of course, is independent on the wavelength. Strictly speaking, this method is not exactly point-by-point, but is close to it since it provides a set of the optical parameters whose individual values are not related by any formula. The initial values for fitting are usually chosen point-by-point one from another provided that the spectral points are close to each other.

Much more powerful method is the application of an MDF provided that the spectral properties of the permittivity are known analytically. Examples of MDFs of different types of materials are summarized in Tab. 6.1. Generally, a realistic MDF is a superposition of several simple elements from Tab. 6.1. For instance, the dielectric function of a usual dielectric consists of the nondispersive term (No. 2) and the Sellmeier term (No. 3). Analogously, the dielectric function of a usual metal consists of the Drude term and (optionally) the nondispersive term. In the case of using an MDF, a function of MDF's

parameters

$$\mathcal{E}^2_{\mathrm{LS}}(p_1, p_2, \ldots, d_1, d_2, \ldots) = \sum_{j=1}^{M} \mathcal{E}^2_j[\varepsilon_j(p_1, p_2, \ldots), d_1, d_2, \ldots], \tag{6.10}$$

is minimized, in which p_j are fitted parameters from the last column of Tab. 6.1 and d_j are fitted geometrical parameters.

6.3 Parameterization of relief profiles and slicing

In order to perform a topographic analysis of an analyzed grating, we parameterize the geometric profile of its relief. In this thesis we will mostly analyze *lamellar* (one-dimensional rectangular-relief) profiles, but we will also demonstrate scatterometry on two examples of non-lamellar gratings—periodic wires with paraboloid edges and a sine-like relief grating.

As the first example of a non-lamellar grating, we expand the z-dependence of the filling factor, defined in each plane $z = \text{const}$ as the linewidth-to-period ratio $w(z) = W(z)/\Lambda$, into a Taylor series up to the 2nd order, i. e.,

$$w(z) = w_1 + w_2 \left(\frac{2z}{d} - 1\right) - w_3 \left(\frac{2z}{d} - 1\right)^2, \tag{6.11}$$

where d is the depth of the relief structure and w_j represent the parameters of the relief profile. The function $w(z)$ depends on the normal coordinate z and has its domain of definition between 0 and d. For lamellar gratings with a constant linewidth W, only $w_1 = W/\Lambda$ is nonzero. Trapezoidal-wire gratings are characterized by w_1 and w_2 that are related to the top linewidth by $W(0) = w_1 - w_2$ and to the average linewidth $W\left(\frac{d}{2}\right) = w_1$. In a special case of wires with paraboloid edges, the grating is characterized by w_1 and w_3 that are related to the top linewidth by $W(0) = w_1 - w_3$ and to the maximum linewidth $W\left(\frac{d}{2}\right) = w_1$. Finally, a general profile is characterized by all the three w_j parameters in Eq. (6.11), or more if we assume a polynomial approximation of a higher order. We will refer to this type of profiles as lamellar-like gratings, contrary to sine-like gratings.

For the purpose of the application of the Airy-like series algorithm, we slice the relief profile into N sub-layers, and correspondingly evaluate N discrete values of Eq. (6.11) as

$$w^{(J)} = w_1 + w_2 \left(\frac{2(J - \frac{1}{2})}{N} - 1\right) - w_3 \left(\frac{2(J - \frac{1}{2})}{N} - 1\right)^2, \tag{6.12}$$

for each Jth sub-layer.

Analogously, the z-dependence of the filling factor of a sinusoidal-relief profile defined

$$z(y) = \frac{d}{2}\left(1 - \cos\frac{2\pi y}{\Lambda}\right) \tag{6.13}$$

can be written as

$$w(z) = \frac{1}{z}\arccos\left(1 - \frac{2z}{d}\right), \tag{6.14}$$

so that an ideal sinusoidal relief profile is identified only by the depth d. More generally, we can assume sine-like profiles as a perturbed sinusoidal function, e. g., a linear combination of the sinusoidal and linear functions

$$z(y) = \begin{cases} (1-\sigma)\frac{d}{2}\left(1-\cos\frac{2\pi y}{\Lambda}\right) + \sigma\frac{2d}{\Lambda}y, & y \in \langle 0, \frac{\Lambda}{2}\rangle, \\ (1-\sigma)\frac{d}{2}\left(1-\cos\frac{2\pi y}{\Lambda}\right) - \sigma\frac{2d}{\Lambda}y, & y \in \langle -\frac{\Lambda}{2}, 0\rangle, \end{cases} \tag{6.15}$$

where σ is the weight parameter, referred to as *sharpness*. The function (6.15) corresponds to an ideal sinusoidal grating when $\sigma = 0$, whereas to a sharp triangular grating when $\sigma = 1$. The z-dependence can be determined by invertin Eq. (6.15) to obtain $y(z)$ and stating $w(z) = 2y(z)/\Lambda$. However, this problem contains solution of a transcendent equation which must be treated numerically. Finally, by slicing the relief profile into N sub-layers we would obtain a formula analogous to Eq. (6.12).

Chapter 7

Characterization of grating profiles by spectroscopic ellipsometry

This chapter is devoted to the demonstration of our original results of optical scatterometry based on spectroscopic ellipsometry. Each section provides a particular analysis consisting of the introduction, sample and experimental details, description of results, and conclusions. Section 7.1 specifies a special theoretical and experimental solution of the ellipsometric problem of gratings fabricated on thick transparent plates. Sec. 7.2 shows spectroscopic properties of lamellar gratings with respect to extracting the critical dimensions. In Sec. 7.3 the convergence of geometrical dimensions fitted from experimental data (optical critical dimensions) is analyzed in detail. The analysis consists of three kinds of gratings made of quartz, silicon, and tantalum. In the case of the quartz and silicon gratings, the lamellar profile fits the measurement perfectly. For the tantalum gratings which are fabricated on a quartz substrate, another profile with paraboloidally curved edges of Ta wires must be chosen to reflect the measurement correctly, as shown by various numerical simulations. Section 7.4 presents the ellipsometric analysis on transparent sinusoidal gratings prepared on a polymer/glass structure. Here imperfections of the sinusoidal profile, as well as the quality of the optical matching of the polymer to the glass are studied. Section 7.5 comprises a scatterometric analysis of binary arrays of holes in a silicon wafer. Finally, in Sec. 7.6 the results of the fitted geometrical dimensions are successfully compared with dimensions specified by SEM.

7.1 Spectroscopic ellipsometry on gratings fabricated on thick transparent plates

Introduction

Various kinds of periodic nanostructures are considered for the transmission mode, e.g., "moth eye" antireflection surfaces, wire grid polarizers, or photonic and magnetopho-

tonic crystals; therefore, many kinds of standard samples are fabricated on transparent substrates. Including the transmission configuration among the optical and/or magneto-optical techniques even enhances the sensitivity of the optical monitoring (e. g., determining the extinction coefficient of materials forming a grating or pseudodielectric constants of metamaterials) or is necessary to measure particular transmission-mode effects (e. g., the Faraday rotation of magnetic gratings or magnetophotonic crystals). The optical response of structures located on a thick transparent plate is affected by incoherent backreflections that complicate the optical characterization.

In simulations, the backreflections may sometimes be neglected; in particular arrangements, however, those contributions are of high importance. The optical and magneto-optical responses affected by the backreflections were therefore studied theoretically and experimentally, e. g., in specular-mode spectroscopic ellipsometry [77, 78, 79, 80, 81, 82] or in the configuration for measuring the Faraday effect [83, 84]. If a system is composed of so-called thin and thick layers only, the former of which is sufficiently thinner than the coherence length of the incident light and the latter sufficiently thicker, then a simple approach can be applied, dividing the optical interactions into two individual problems of the coherent and incoherent systems. If a system contains a dimension comparable with the coherence length or if the depolarization effects become significant, then a more general approach has to be applied such as the coherence-matrix or Mueller-matrix formalism.

The thicknesses of transparent plates are usually comparable with the light-beam diameters; therefore, the axes of backreflected beams are deflected from the primary specular beam axis in the usual oblique incidences of an ellipsometric system. This reduces the efficiencies of secondary contributions and thus complicates the optical characterization of such systems. Moreover, if the deflection of a backreflection reaches a sufficient value, then its influence can be eliminated. Gratings containing thick layers are affected by the "diminution effect" more generally, because different diffraction orders propagating in the transparent plate are deflected to different distances. The diminution effects of such waves therefore differ too.

Researchers usually avoid the backreflections by grinding the back surface or by covering it with a strongly absorbing paint, e. g., colloidal graphite. Grinding the back surface is a destructive operation, which disables using the sample later in the transmission mode; hence, other ways are worth searching for. In this section we report on two solutions in specular-mode ellipsometry. Instead of the colloidal graphite that does not banish the reflection perfectly, a liquid solution is applied made of its refractive index almost identical to the index of the plate. The *liquid solution procedure (LSP)* simulates the effect of grinding, with the samples remaining preserved.

Sometimes it is not easy to prepare a proper liquid according to the optical properties of a plate made of a special material, and LSP is evidently inapplicable for in situ. Moreover, there are systems with non-separable backreflections, e.g., polymer gratings situated on a glass plate [58]. For this purpose we developed the *incoherent backreflection method for*

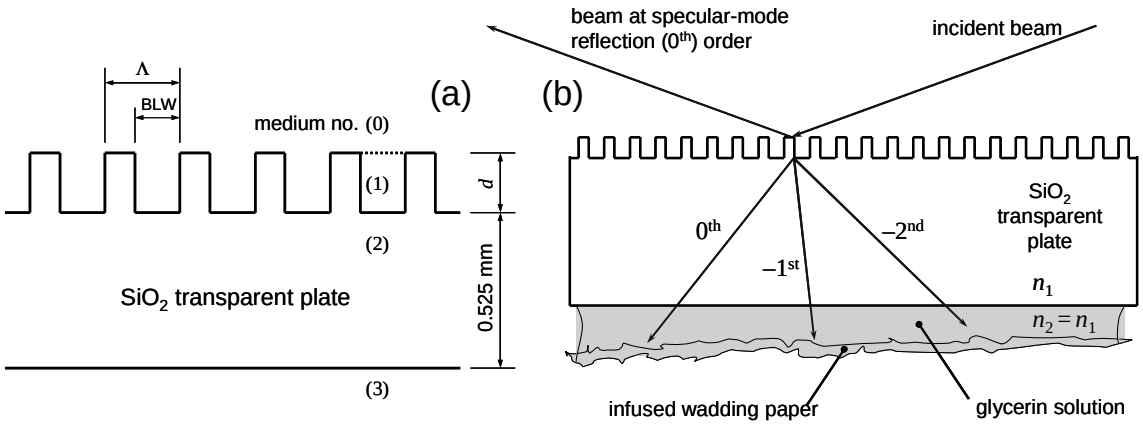

Figure 7.1 Definition of the geometrical parameters of a lamellar grating located on a transparent quartz plate (a) (BLW = bottom linewidth) and the liquid solution procedure using glycerin (b).

gratings (IBMG), similar to previous theoretical models of Chateau et al. [85] or Li. [86] Here the diminution effect is considered using a special "diminution function" obtained by direct measuring.

Samples and experiments

For our purposes, five rectangular relief gratings were chosen made by x-ray lithography on a 0.525 mm thick fused-quartz plate, as shown in Fig. 7.1 (a). The gratings were patterned with the period $\Lambda = 260$ nm same for all the samples. The valley depth d was in the range of 400–500 nm and the bottom linewidths (BLW) ranged between 80 and 180 nm. The area of each pattern on the plate on which lithography was applied was 5×5 mm^2. The ellipsometric measurements were performed on a four-zone null spectroscopic ellipsometer in the polarizer-sample-compensator-analyzer (PSCA) configuration covering the wavelength range of approx. 240–840 nm in the planar diffraction arrangement for both LSP and IBMG.

The arrangement for LSP is depicted in Fig. 7.1 (b). A liquid solution optically matched to quartz was prepared by mixing glycerin with a small amount of pure, deionized water. The optical matching between the quartz and the liquid was achieved with a standard quartz plate immersed into the solution by changing the concentration until the plate was not visible. A small amount of wadding paper was infused by the final solution and put on the back surface. All the transmitted diffraction orders were thus scattered and depolarized by the rough paper; hence no backreflections affected the specular ellipsometric response. The reliability of this method was verified on the non-patterned area of the plate with the known optical response. The method was applied at several angles of incidence (32, 45, 56, 70, 75, 80°) in order to optimize the reliability of the deduced grating parameters.

Applying IBMG, we mounted the sample with its back surface clean and untouched by the holder in the illumination area. The light beam was collimated to the middle

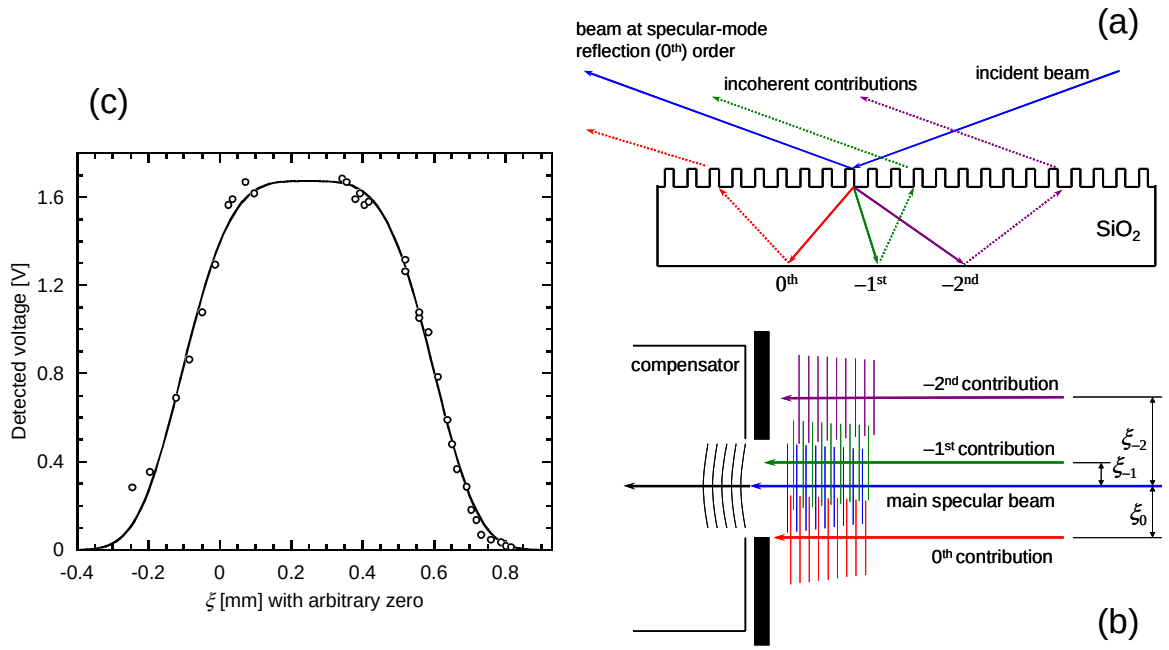

Figure 7.2 Experimental arrangement of the incoherent backreflection method for gratings. Incoherent contributions from backreflections (a) are deflected by the distances ξ_j (b) which cases a diminution effect in the detected voltage (c) (The circles mark the direct measurement of the intensity in the detector while manually deflecting a beam. The curve is an analytical approximation.).

of the patterned squares to receive the maximum number of backreflections, as shown in Fig. 7.2 (a). The axis of the first specular beam was adjusted to make maximal intensity in the detector while applying LSP. Evidently, the axis of the jth backreflection is deflected from the primary beam by a value of ξ_j, as depicted in Fig. 7.2 (b). The values of the backreflections are thus affected by the diminution effect. To evaluate it for the subsequent modeling, the dependence of the relative intensity on the parameter was measured using a standard silicon wafer, moved by ξ while recording the detected voltage readout, as displayed by marks in Fig. 7.2(c). The deviations from linearity in the photomultiplier response and its spectral dependence were not considered. The important advantage of this technique consists in eliminating the diffraction effects in the light traveling from the sample to the detector. The diminution effect depends on a particular ellipsometer configuration; this can be accounted for in other ellipsometers in a similar way, provided an appropriate adjustment of the procedure described here.

Modeling and fitting

We suppose the transparent substrate much thicker than the coherence length of the light source; therefore, the intensities of electromagnetic waves are treated without assuming interference. We use the reflection and transmission matrices evaluated in Chap. 4 in solving the general structure composed of the coherent and the incoherent system, i. e., the relief grating located on the thick plate. The reflection and transmission intensities of

the relief grating for the either s or p polarization with respect to the propagation angles can be determined by the formulae

$$R^{JK}_{\mathtt{s(p)},mn} = \left|r^{JK}_{\mathtt{s(p)},mn}\right|^2 \frac{\cos\vartheta^{(J)}_m}{\cos\vartheta^{(J)}_n}, \tag{7.1}$$

$$T^{JK}_{\mathtt{s(p)},mn} = \left|t^{JK}_{\mathtt{s(p)},mn}\right|^2 \frac{n^{(K)}\cos\vartheta^{(K)}_m}{n^{(J)}\cos\vartheta^{(J)}_n}, \tag{7.2}$$

where $r^{JK}_{\mathtt{s(p)},mn}$ and $t^{JK}_{\mathtt{s(p)},mn}$ denote the $[m,n]$th element of the amplitude reflection and transmission matrices corresponding to the s (p)-polarization, respectively, with J and K denoting the indices of the incidence and transmission media with the refractive indices $n^{(J)}$ and $n^{(J)}$ (cf. Fig. 7.1). The propagation angle of the nth diffraction order in the Jth medium, $\vartheta^{(J)}_n$, is determined by the standard grating formula

$$n_j \sin\vartheta^{(J)}_n = \sin\vartheta^{(i)} + n\frac{\lambda}{\Lambda}, \tag{7.3}$$

in which $\vartheta^{(i)}$ denotes the incidence angle. In the case of high n for which Eq. (7.3) has no real solution in our spectral range, the left hand sides of Eqs. (7.1, 7.2) are assumed zero since no energy is transferred along the normal direction. Introducing the phase compensator in the ellipsometric measurement system enables us to define the intensity-based quantities [77, 78]

$$R^{JK}_{\mathtt{ps},mn} = r^{JK}_{\mathtt{p},mn}\left(r^{JK}_{\mathtt{s},mn}\right)^* \frac{\cos\vartheta^{(J)}_m}{\cos\vartheta^{(J)}_n}, \tag{7.4}$$

$$T^{JK}_{\mathtt{ps},mn} = t^{JK}_{\mathtt{p},mn}\left(t^{JK}_{\mathtt{s},mn}\right)^* \frac{n^{(K)}\cos\vartheta^{(K)}_m}{n^{(J)}\cos\vartheta^{(J)}_n}, \tag{7.5}$$

with the full meaning of the energy reflectance/transmittance coefficients. These quantities help to complete the evaluation of the ellipsometric Δ-parameter.

In the case of highly transparent structures, only the contribution of the first backreflection is necessary to include, which can be written for both polarization states and for the "ps" pseudo-polarization as

$$R^{03}_{\mathtt{s},00} = R^{02}_{\mathtt{s},00} + \sum_n \kappa(\xi_n) T^{20}_{\mathtt{s},0n} R^{23}_{\mathtt{s},nn} T^{02}_{\mathtt{s},n0}, \tag{7.6}$$

$$R^{03}_{\mathtt{p},00} = R^{02}_{\mathtt{p},00} + \sum_n \kappa(\xi_n) T^{20}_{\mathtt{p},0n} R^{23}_{\mathtt{p},nn} T^{02}_{\mathtt{p},n0}, \tag{7.7}$$

$$R^{03}_{\mathtt{ps},00} = R^{02}_{\mathtt{ps},00} + \sum_n \kappa(\xi_n) T^{20}_{\mathtt{ps},0n} R^{23}_{\mathtt{ps},nn} T^{02}_{\mathtt{ps},n0}, \tag{7.8}$$

where the first term on the right hand sides corresponds to the first specular reflection determined by Eqs. (7.1, 7.4). The term with the summation over n represents the contribution of the first backreflection, with $\kappa(\xi_n)$ denoting the diminution of the nth-diffracted and backreflected order, caused by its deflection from the primary beam axis, as depicted

in Fig. 7.2(a, b). Eqs. (7.6–7.8) can easily be generalized by including other backreflections branched out by the relief grating; our modeling experiences, however, manifest the first backreflection sufficient. The diminution function $\kappa(\xi)$ could be theoretically derived by considering the diffraction effects in the light traveling through the ellipsometric components. Here this function is determined empirically, i. e., by measuring on the standard sample as described above. The analytical function representing $\kappa(\xi)$ in treating our experimental data was found

$$\kappa(\xi) = \exp\left[-\left(\frac{\xi}{\sigma}\right)^{\nu}\right], \tag{7.9}$$

with two parameters fitted, $\nu = 3.9$ and $\sigma = 0.38$ mm. This function is plotted in Fig. 7.2(c). The amplitude of the detected voltage and the relative position of zero were fitted altogether, but are not important in analyzing. In Eq. (7.9) the maximum value is unit in the case of $\xi_n = 0$, i. e., if the nth contribution is not deflected from the primary beam axis. All the deflection parameters are determined by the formula [cf. Fig. 7.2 (a)]

$$\xi_n = 2d_{\text{sub}}\frac{q_n}{s_n}\cos\vartheta^{(i)}, \tag{7.10}$$

in which d_{sub} denotes the substrate's finite thickness while $q_n = \sin\vartheta^{(i)} + n\frac{\lambda}{\Lambda}$ and $s_n = \sqrt{n_{\text{sub}}^2 - q_n^2}$ represent the components of the wave vector of the nth diffraction order normalized to the substrate's refractive index n_{sub}.

Using the intensity-based quantities, we can easily calculate the specular ellipsometric parameters by the formulae [77, 78]

$$\Psi = \arctan\sqrt{\frac{R^{03}_{\mathtt{p},00}}{R^{03}_{\mathtt{s},00}}}, \tag{7.11}$$

$$\Delta = \arg R^{03}_{\mathtt{ps},00}, \tag{7.12}$$

in which we have not taken into account the depolarization effects caused by the incoherent superpositions [79].

Results and discussion

The results of fitting are summarized in Tab. 7.1; the details about the ellipsometric response of the lamellar gratings are described in Sec. 7.2. The comparison of both methods is shown for Sample A at two different angles of incidence and for Sample D at a single angle of incidence. The comparison of the errors corresponding to both methods in the chosen configurations is summarized in Tab. 7.2, where the errors are averaged over the spectrum of a single angle of incidence. The simulations are based on the parameters listed in Tab. 7.1.

The ellipsometric response of Sample D at the angle of incidence of 70° is displayed in Fig. 7.3. The left hand part of the figure corresponds to LSP, which exhibits deep spectral

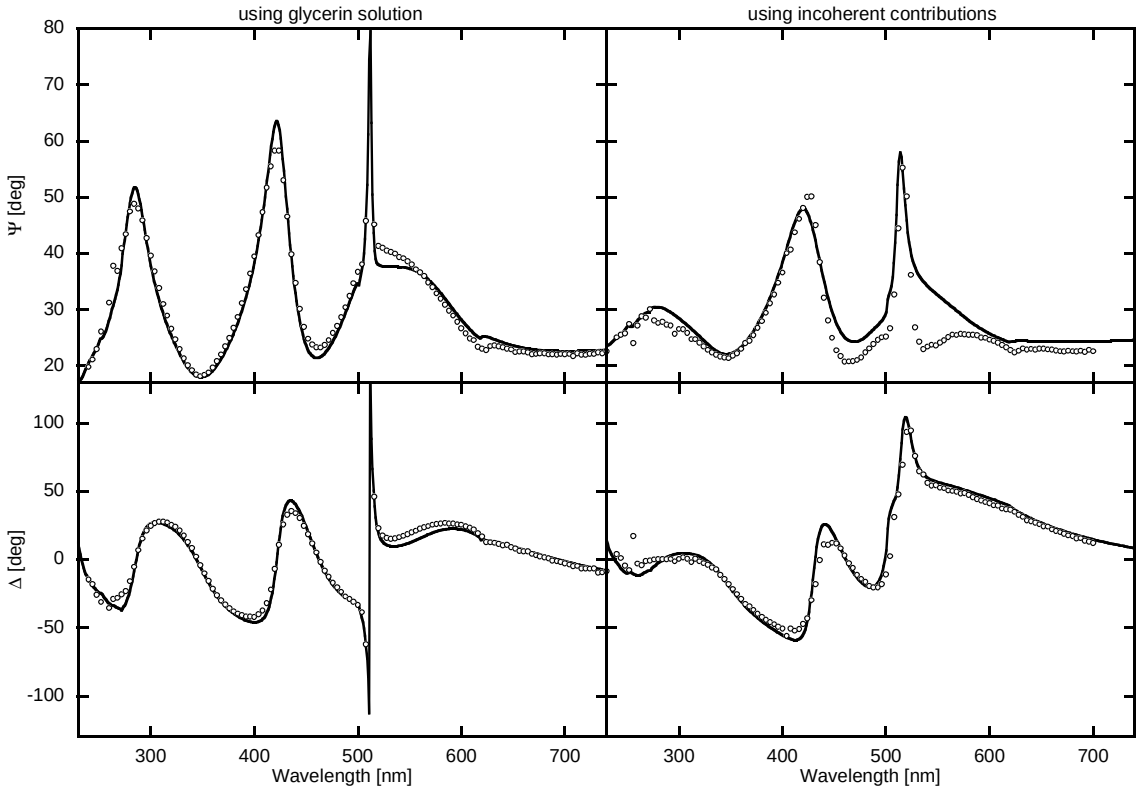

Figure 7.3 Comparison of both methods on sample D at 70° of incidence. The circles mark measurement, while the curves correspond to modeling.

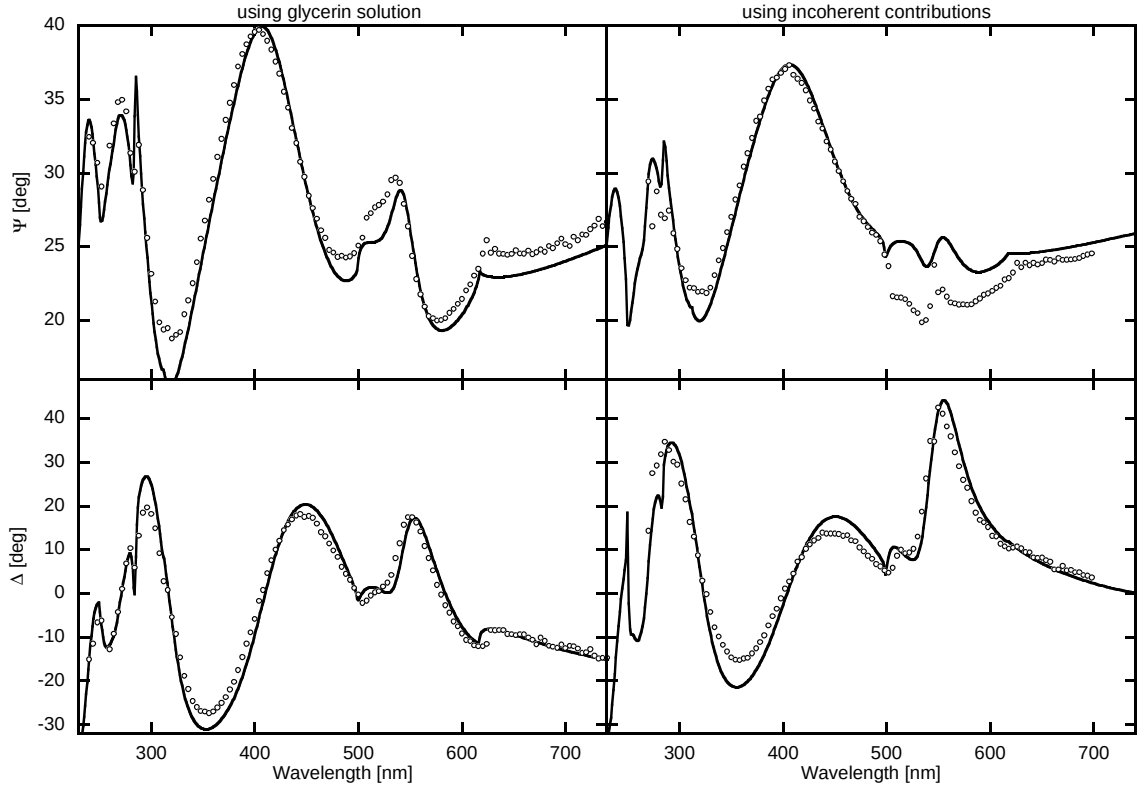

Figure 7.4 Comparison of both methods on sample A at 70° of incidence. The circles mark measurement, while the curves correspond to modeling.

Sample	Period [nm]	Depth [nm]	BLW [nm]	Error [deg]
A	257.3	364.2	87.8	4.0
B	257.1	396.6	105.7	3.4
C	257.3	401.7	117.0	3.8
D	258.2	512.7	160.2	5.9
E	259.4	501.4	173.5	7.4
F	199.5	126.4	177.3	7.2

Table 7.1 Fitted grating parameters.

oscillations due to interference effects in the periodic medium, a sharp Wood anomaly at the spectral point of the −1st diffraction order passing off (the Rayleigh wavelength of 504 nm), and a monotonous dependence at large wavelengths. The spectral properties of the Wood anomalies will be in detail shown in Sec. 7.2. The effect of backreflections can be observed in the right hand part of Fig. 7.3. The amplitudes of the deep interference effects are reduced—especially in the small wavelength part of the spectrum. The Wood anomaly at 504 nm is preserved; its line width is increased and its peak amplitude reduced. No remarkable effects are observed in the large wavelength range, since all the higher backreflected diffraction orders are already too far from the axis of the primary specular beam.

The response of Sample A with a small BLW or, in other words, with a high filling factor is displayed in Fig. 7.4. The explanation of the ellipsometric results follows that given above except a difference in the manifestation of the Wood anomalies. The sharp beat expected at 504 nm is almost invisible; several more intricate anomalies appear in the short wavelength range instead, non-dissipated by the backreflections.

At the angle of incidence of 32°, the propagation directions of the diffracted waves are markedly different, which makes the optical response to vary in a large scale, as visible

Sample	Incidence [deg]	Error 1[a)] [deg]	Error 2[b)] [deg]
D	70	3.9	7.4
A	70	3.7	4.1
A	32	4.9	9

[a)]Error 1 stands for the liquid solution method.

[b)]Error 2 stands for the incoherent backreflection method for gratings.

Table 7.2 Comparison of the errors of both methods.

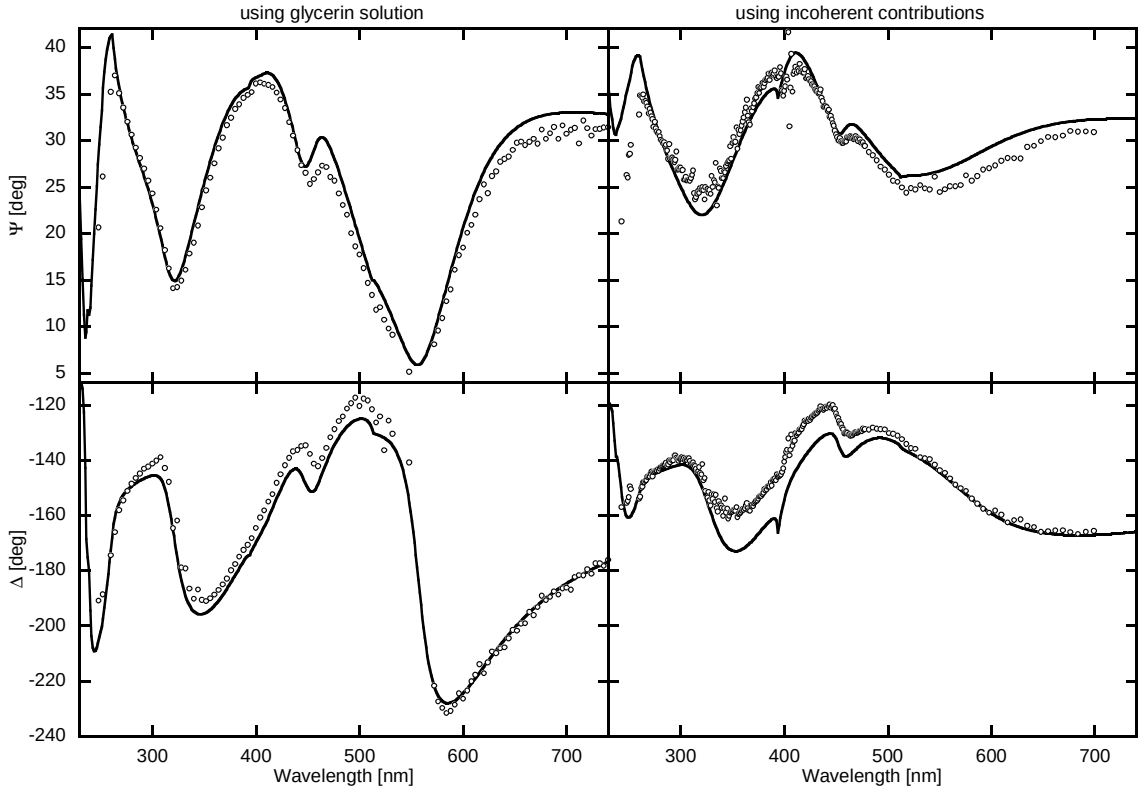

Figure 7.5 Comparison of both methods on sample A at 32° of incidence. The circles mark measurement, while the curves correspond to modeling.

in Fig. 7.5 for Sample A. Here the 0th diffraction order backreflected has almost the normal direction, while the higher orders in both directions rapidly become leaky. Except the short wavelength range, the backreflection effects are observed exclusively due to the 0th diffraction order with its direction spectrally independent. The strong interference minimum in the Ψ-parameter together with the rapid change in Δ, observed above the wavelength of 517 nm where no higher propagating diffraction orders contribute (left hand part of Fig. 7.5), almost vanishes due to the effect of the backreflected 0th order (right hand part of Fig. 7.5).

The agreement between the modeled and measured spectral dependences is achieved with remarkable precision. Minor discrepancies are visible at interference extremes and in the range of Wood anomalies; these effects represent the main sources for the errors listed in Tab. 7.2. It is not easy to distinguish between the influence of an imperfect optical matching (of the glycerin solution to the quartz) and the influence of imperfections in the rectangular shape of the gratings. Further improvement of the preparation of a liquid solution with enhanced or better-defined optical properties can help to perform more reliable extraction of the grating profile identified by more topographic parameters. All the modeling discrepancies in LSP naturally occur in the simulations including backreflections. Moreover, the backreflections themselves cause other discrepancies coupled with small errors in the parameters describing the overall situation. These include the effect of the

finite thickness of the substrate medium, an error in the aperture in the lamp housing, and, in particular, the finite size of the grating patterns limited to 5×5 mm^2 in the present study. The critical spectral range occurs if a higher transmitted diffraction order is backreflected out of the patterning, which is observed near the most visible Wood anomaly, which is at 504 nm for 70° of incidence and at 398 nm for 32° of incidence. Around these wavelengths, the -1st backreflected wave is partially incident upon the nonpatterned area which causes the main deviations in the measured ellipsometric values. Nevertheless, with the correctly determined diminution function, the theoretical model employing backreflections evidently yields valuable information on the gratings.

Conclusions

We can close this section with the following conclusion. Using a glycerin solution to remove backreflections helps to perform a reliable three-parameter fit of the grating's optical critical dimensions. The comparison between the simulated and experimental ellipsometric curves in the three chosen configurations suggests the high usability of the optical-monitoring techniques also for gratings located on a thick transparent plate. Considering a more accurate and more complex system of parameters identifying gratings and ellipsometric arrangements may enhance the accuracy of this method to be applied as a tool for the commercial lithography.

7.2 Analysis of spectral properties of lamellar gratings

Introduction

Various authors have successfully demonstrated high-accuracy extraction of linewidths, feature heights, sidewall angles, or cross-sectional curvatures from ellipsometric measurements [39, 41, 42]. The *cross-sectional function* (CSF) is usually determined by a few parameters, and a small change of any of them affects the *spectro-ellipsometric function* (SEF) by a rather strong, non-linear variation. This leads to the unique solution important for scatterometry. If the number of the CSF parameters to be extracted becomes comparable with the dimension of the linear space of the SEFs measured, then the mutual correlation of the parameters raises uncertainty on their validity. This risk may be avoided by a detailed measurement of many spectral points, by measuring more angles of incidence, or by including complementary techniques such as measuring energy reflectance/transmittance spectra.

Another way to ensure the uniqueness of topographic extraction is performing a detailed study of the optical spectral dependences according to the geometrical properties of gratings. Especially, the resonation effects close to the spectral points of Rayleigh wave-

lengths (Wood anomalies) are very sensitive on all the CSF parameters. The spectral dependences of the energy reflectance in the range of the Wood anomalies have been investigated extensively [87, 88]. Since those anomalies strongly depend on polarization, the SEF contains breaks at the points of the Rayleigh wavelengths, or even more complicated oscillations if a diffracted order becoming evanescent causes a significant resonance.

The aim of this section is studying the influence of the CSF parameters over the SEF in the case of the simplest, rectangular profile, in order to demonstrate their uniqueness, and to suggest an improvement of a multi-parameter fitting by emphasizing the importance of the Wood anomalies.

Samples, experiment, and modeling

For the purposes of this section, the same experimental and simulation data obtained on the same samples as in Sec. 7.1 were analyzed, with the extracted geometrical parameters summarized in Tab. 7.1.

Results and discussion

From the theory of interference in thin films, the spectral dependences of the ellipsometric parameters are well known. Analytical formulae directly show a trace of a circle on the Poincaré sphere, or the sine-like curves of $\Psi(E)$ and $\Delta(E)$, E being the photon energy. Increasing the layer thickness raises the number of oscillations in the SEF while the amplitude stays same. On the other hand, increasing the refractive index also enlarges the optical thickness of the layer, but additionally it changes the amplitudes calculated by the Fresnel formulae on the boundaries. The amplitude of the SEF curve is thus affected independently on the geometrical thickness. Moreover, the material dispersion eliminates the correlation between the geometrical thickness and refractive index in the *optical thickness*, and thus increases the uniqueness of the inverse problem in which the material and geometrical parameters are determined from an optical measurement.

The idea described above can also be applied to gratings, although the optical interactions in a periodic medium are more complicated. Instead of one propagation mode, there are many harmonic waves, and hence the SEF is not formed by a sine-like curve. Nevertheless, as shown in Fig. 7.6, increasing the thickness of the periodic medium raises the number of oscillations in the SEF.

Figure 7.7 displays what happens when the depth remains same and BLW increases or, in other words, the grating's filling factor decreases. The shape of the SEF with its number of oscillations remains same, whereas the amplitude is raised. The analogy with varying the refractive index of a homogenous layer is obvious since the filling factor may be used to determine effective refractive indices using the effective medium theory for subwavelength gratings [89].

The spectral dependences of the Wood anomalies, which have no analogy in stratified

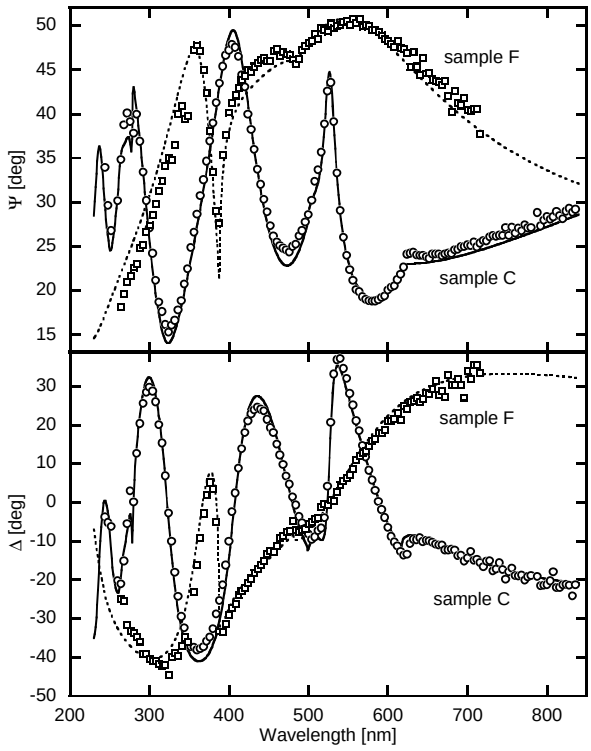

Figure 7.6 Optical responses corresponding to two samples with different depths in incidence of 70°. The periodic layer of Sample C is three times higher than the layer of Sample F. The circles and squares mark measurement while the solid and dotted curves correspond to simulations, respectively.

homogenous media, are displayed in Fig. 7.8 for two examples of incidence angles. The sharp breaks of the curves correspond to the spectral points of Rayleigh wavelengths in which the number of permitted reflected (up) or transmitted (down) Rayleigh waves is decreasing by one passing off. The position of the Rayleigh wavelength for the kth diffraction order to pass off is determined by the simple formulae

$$\lambda_k^{\mathrm{up}} = \frac{\Lambda}{|k|}\left(1 \mp \sin\vartheta^{(i)}\right), \tag{7.13}$$

$$\lambda_k^{\mathrm{down}} = \frac{\Lambda}{|k|}\left[n\left(\lambda_k^{\mathrm{down}}\right) \mp \sin\vartheta^{(i)}\right], \tag{7.14}$$

where $\vartheta^{(i)}$ is the incidence angle. The upper $(-)$ and lower $(+)$ signs correspond to positive and negative k, respectively. The possibility to determine accurately the period Λ from the values of λ_k^{up} is obvious. The values of $\lambda_k^{\mathrm{down}}$ are coupled with the values of the refractive-index dispersion function $n(\lambda_k^{\mathrm{down}})$, which helps to look for the correct values of $n_k^{\mathrm{down}} = n(\lambda_k^{\mathrm{down}})$. It is important to point out that the effective medium theory becomes accurate after the last higher diffraction order has passed off, i. e., in the region $\lambda > \lambda_{-1}^{\mathrm{down}}$. The optical response then becomes independent on the grating's period, which is another instrumental effect to increase the uniqueness of the inverse problem.

Sometimes a strong resonation effect appears in the spectral range of a Wood anomaly introduced by a Rayleigh wavelength, as depicted in the details of Fig. 7.8 in the case of

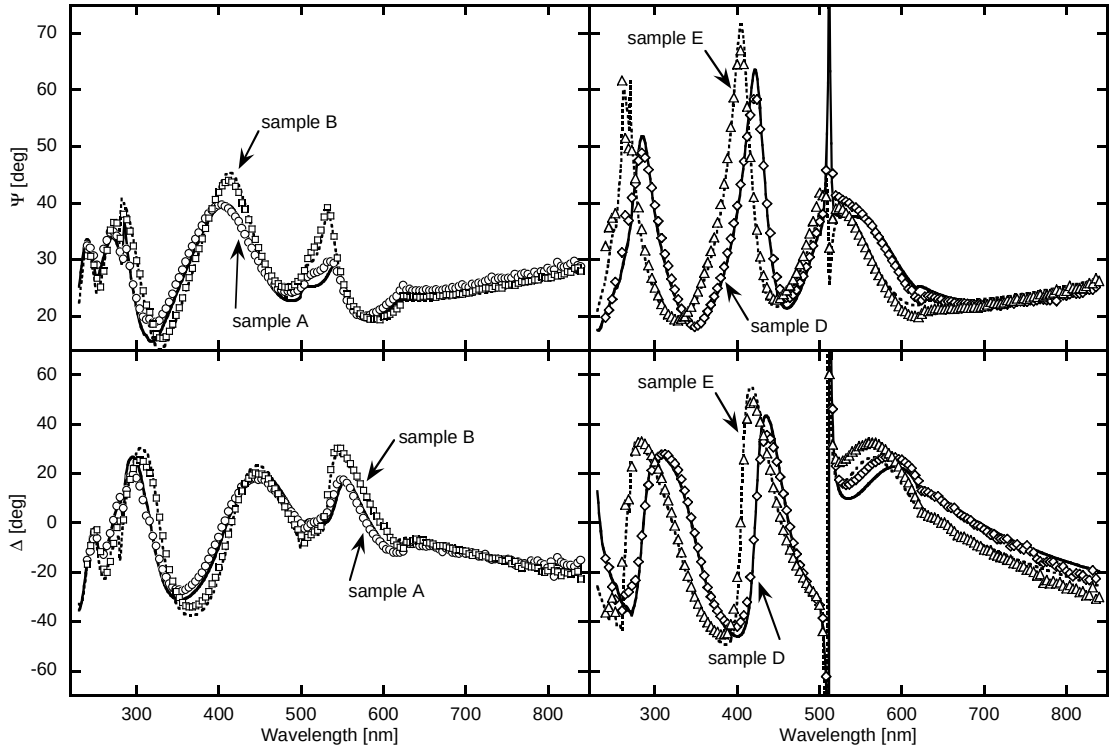

Figure 7.7 A tendency of increasing amplitude of the SEF generated by increasing the BLW in incidence of $70°$. Marks and curves have the same meaning as in Fig. 7.6.

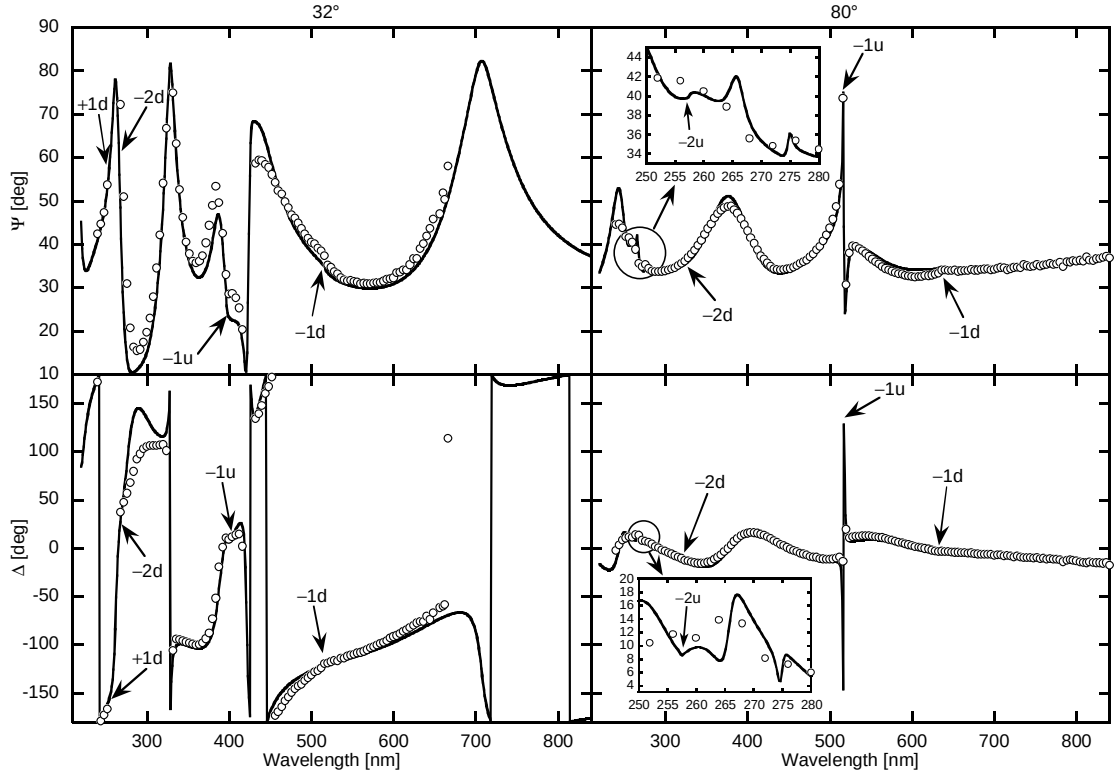

Figure 7.8 The Wood anomalies observed on Sample E in incidences of $32°$ and $80°$. The arrows indicate the Rayleigh wavelengths of diffraction orders $(+1, -1, -2)$ passing off up (u) and down (d) the grating.

the −2nd reflected diffraction order passing off (−2u). The shape of the Wood anomaly is then very sensitive on all the parameters describing the CSF. This may be effectively used to increase the dimension of the space of SEFs by the detailed measurement of the spectral dependences of Wood anomalies, which dissolves the uncertainty on the uniqueness of the multi-parameter fitting.

Conclusions

In summary, the three-parameter fit summarized in Sec. 7.1 is evidenced to be performed with high precision and reliability. Independent influences of the period, linewidth, and depth of the gratings on their optical response are demonstrated by using numerical analysis together with measurement. The Wood anomalies are shown highly sensitive on all the imperfections and inclinations of a rectangular profile, which may be used to increase the number of parameters extracted from ellipsometric measurements and to improve understanding the optical interactions in gratings.

7.3 Convergence analysis on lamellar-like gratings

Introduction

In recent years scatterometry of diffraction gratings based on spectroscopic ellipsometry has widely spread owing to considerable progress in computation scopes that are necessary for the effective analysis of experimental diffraction-response data, particularly for the real-time process monitoring [40]. Moreover, progress in theoretical algorithms with increasing convergence properties enabled researchers to improve the correspondence between surface-relief profiles monitored optically and profiles visible by SEM or AFM. Especially, the introduction of Li's Fourier factorization rules for electromagnetic fields propagating inside media with periodic discontinuous permittivity remarkably enhanced the convergence of the algorithms [75, 90].

Among many diffraction theories in the literature, the coupled-wave theory is the mostly used method for the purpose of scatterometry, widely referred to as the rigorous coupled-wave analysis (RCWA) [91]. Authors presenting various implementations of RCWA usually focus their numerical analyses to single-wavelength numerical experiments on hypothetical gratings that are considered perfectly known, and present convergence properties according to the number of Fourier harmonics assumed inside a periodic medium [92]. On the other hand, authors of scatterometric analyses on real samples do not provide details of algorithms they use, thereby not clarifying the effectiveness of their methods. For this reason, we devote this section to an analysis of the convergence properties with respect to extracting critical-dimension and topographic data and to a comparison of results obtained on gratings made of transparent quartz, semiconductive silicon, and metallic tantalum.

Sample	Structure [lamella/substrate]	Depth [nm]	Linewidth [nm]	Period [nm]
A	SiO_2/SiO_2	500	110	260
B	Si/Si	110	55	130
C	Ta/SiO_2	200	100	200

Table 7.3 Nominal grating parameters of the samples under measurement.

Samples and experiments

Three sets of samples were analyzed, made as (A) rectangular-relief quartz gratings studied in Sec. 7.1, (B) rectangular-relief gratings patterned on an Si substrate, and (C) rectangular-relief gratings patterned in a Ta thin film deposited on a fused-quartz substrate. For our purposes we have chosen one sample from each set, with their fabrication parameters summarized in Tab. 7.3. The Ta film of Sample C was deposited by means of RF sputtering. The patterning was made by means of x-ray lithography.

The ellipsometric measurements on Samples A and C were performed on a four-zone null spectroscopic ellipsometer in the polarizer-sample-compensator-analyzer (PSCA) configuration, covering the wavelength range of 230–840 nm and with the adjustable angle of incidence $\vartheta^{(i)}$. Here we report on measurements at $\vartheta^{(i)} = 70°$. To avoid the influence of incoherent backreflections in the case of the Samples A and C we have utilized the liquid solution procedure whose details are described in Sec. 7.1.

The ellipsometric measurements on Sample B were performed on a rotating-analyzer ellipsometer (RAE) in the polarizer-sample-analyzer (PSA) configuration with a measurement spot size down to 30 μm, covering the wavelength range of 300–800 nm, and with a fixed angle of incidence $\vartheta^{(i)} = 65.45°$. Since the measurement on RAE in the PSA configuration does not provide the imaginary component of $\tan\Psi\, e^{i\Delta}$, we present, in this case, the values of Ψ and $\cos\Delta$.

Modeling and fitting

The convergence properties are in this paper presented either according to the increasing number of slices N or according to the maximum diffraction order $n_{\max}$ assumed in the Rayleigh, Floquet, and Fourier expansions in Eqs. (3.157, 3.158, 4.102, 4.109), where each infinite sum is replaced with $\sum_{n=-n_{\max}}^{n_{\max}}$. This means that the field in the periodic medium as well as in the sandwiching media is being described by the so-called $2n_{\max}+1$-wave approximation, the value of which corresponds to the dimension of the column vectors and to the order of the matrices of the linear-algebraic equations in Chap. 4. The dependences of the optical critical dimensions on N and $n_{\max}$ are obtained by applying the fitting procedure described in Chap. 6 for each pair of N and $n_{\max}$ that are fixed during fitting.

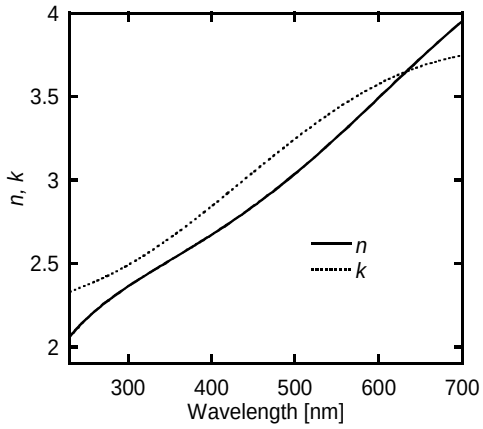

Figure 7.9 Refractive index n and extinction coefficient k yielded by an analysis of ellipsometric and energy transmittance measurements carried out on a nonpatterned reference Ta/quartz sample.

	Sample A				Sample B				Sample C			
$n_{\max}$	d [nm]	W [nm]	Λ [nm]	error [deg]	d [nm]	W [nm]	Λ [nm]	error [deg]	d [nm]	W [nm]	Λ [nm]	error [deg]
1	498.18	102.82	257.84	3.34	108.29	51.56	130.71	6.7	252.76	89.57	174.48	7.99
2	500.44	102.77	257.51	3.21	116	49.16	137.09	2.54	248.87	75.63	182.78	9.02
3	502.36	101.4	257.72	3.33	113.01	45.94	126.84	3.6	249.92	73.78	190.49	9.23
5	503.68	100.73	257.89	3.41	116.39	47.27	133.77	2.68	250.11	78.83	190.15	9.93
10	503.86	100.64	257.91	3.42	116.71	47.07	134.11	2.7	249.6	82.64	189.84	10.35
20	503.9	100.61	257.91	3.43	116.64	47.1	134.01	2.71	249.35	83.49	189.77	10.37
50	503.9	100.61	257.91	3.43	116.69	47.08	134.05	2.71	249.34	83.42	189.78	10.39

Table 7.4 Fitted critical dimensions (depth d, linewidth W, and period Λ) and errors of the fits of lamellar gratings according to increasing $n_{\max}$.

In the calculations we used the optical constants of SiO_2, Si, and Ta_2O_5 from literature [93, 94, 95]. To obtain the constants of Ta, however, we analyzed optical experiments carried out on a nonpatterned reference sample prepared with the same conditions as Sample C but with shorter deposition time to facilitate measurement in the transmission mode. A joint analysis of the ellipsometric and energy transmittance measurements yielded the refractive index and extinction coefficient of Ta (Fig. 7.9) as well as the thickness $t_{Ta_2O_5} = 4.5$ nm of a native oxide overlayer assumed present on the top of the Ta film.

Results and discussion

In the case of Samples A and B, the simulation corresponding to lamellar gratings, that assume $N = 1$, adequately interprets the experimental ellipsometric data. The dependences of the extracted critical dimensions on increasing $n_{\max}$ are summarized in Table 7.4, together with the dimensions obtained with assuming an ideal lamellar-grating profile of Sample C as well. The corresponding fitted ellipsometric parameters $\Psi(\lambda)$ and $\Delta(\lambda)$ are displayed for a few demonstrative examples of $n_{\max}$ in Fig. 7.10 (a) for Sample A, in Fig. 7.10 (b) for Sample B, and in Fig. 7.11 (a) for Sample C.

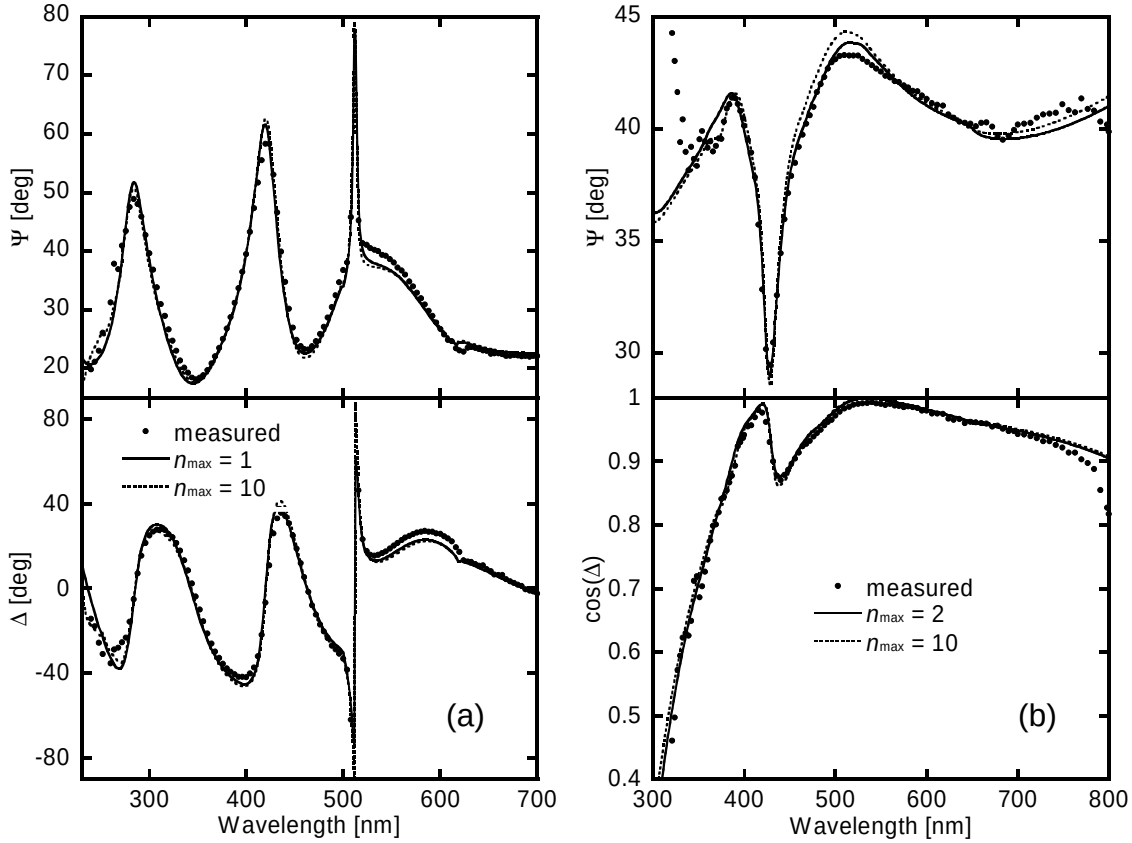

Figure 7.10 (a) Experimental (marks) and fitted 4-zone null ellipsometric parameters Ψ and Δ on a lamellar quartz grating (Sample A) in incidence of 70° for two examples of maximum Fourier harmonics, $n_{\max} = 1$ (solid curves) and $n_{\max} = 10$ (dotted curves). Obviously, the 3-wave approximation (corresponding to $n_{\max} = 1$) is sufficient to fit almost perfectly the measurement. **(b)** Experimental (marks) and fitted RAE parameters Ψ and $\cos\Delta$, on a lamellar Si grating (Sample B) in incidence of 65.45° for two examples of maximum Fourier harmonics, $n_{\max} = 2$ (solid curves) and $n_{\max} = 10$ (dotted curves). In this case the 5-wave approximation (corresponding to $n_{\max} = 2$) is sufficient to fit the measurement.

As clearly visible from Fig. 7.10 (a), the ellipsometric response of the transparent sample in the spectral range of interest is perfectly described by the 3-wave approximation since the curves corresponding to $n_{\max} = 1$ are almost overlapped with those of the 21-wave approximation (corresponding to $n_{\max} = 10$). It is nearly surprising that the 3-wave approximation is capable to simulate with high accuracy not only the two interference oscillations below 500 nm of wavelength but also Wood's anomaly appearing near Rayleigh's wavelength 504 nm at which the -1st diffraction order of reflection passes off.

What has been stated about Sample A can analogously be repeated for the case of Sample B except that instead of three waves we need the 5-wave approximation to interpret the ellipsometric measurement correctly, as visible from Fig. 7.10 (b) where we compare two fits with $n_{\max}$ equal to 2 and 10. Especially, the 3-wave approximation would be insufficient in the near-UV spectral range where Si is more absorbing. Slight discrepancies between the measured and fitted ellipsometric values in the peripheral parts of the spectral range can be explained by the presence of a TECH SPEC$^{\text{TM}}$ Heat Absorbing

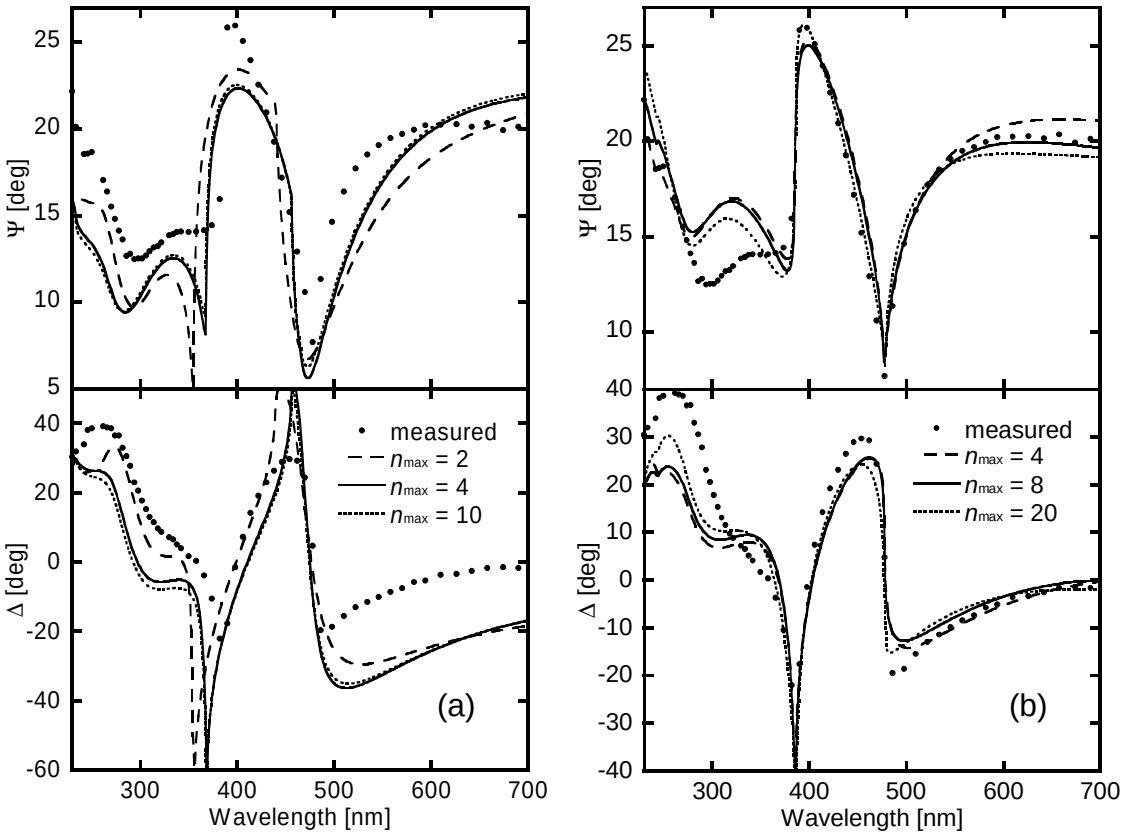

Figure 7.11 (a) Experimental (marks) and fitted 4-zone null ellipsometric parameters Ψ and Δ on a lamellar-assumed Ta grating (Sample C) in incidence of 70° for three examples of maximum Fourier harmonics, $n_{\max} = 2$ (dashed curves), $n_{\max} = 4$ (solid curves), and $n_{\max} = 10$ (dotted curves). Since the artificially assumed lamellar profile does not correspond to the reality, none of the approximations fits the measurement correctly. Nevertheless, the 9-wave approximation (corresponding to $n_{\max} = 4$) can obviously be considered sufficient to simulate a lamellar metallic grating with the same dimensions. **(b)** Experimental (marks) and fitted 4-zone null ellipsometric parameters Ψ and Δ on a paraboloidal-wire Ta grating (Sample C) in incidence of 70° for three examples of maximum Fourier harmonics, $n_{\max} = 4$ (dashed curves), $n_{\max} = 8$ (solid curves), and $n_{\max} = 20$ (dotted curves), sliced into $N = 20$ sublayers. In this case, higher-order approximations fit the measurement reasonably, especially in the longer-wavelength spectral range.

Glass filter within the RAE apparatus, which cuts off the intensity of light out of the range 300–800 nm and hence increases the noise and systematic errors of ellipsometric measurement near the limit points.

Contrary to Samples A and B, the ellipsometric response of Sample C in Fig. 7.11 (a) cannot be correctly interpreted as a response measured on an ideal rectangular-relief grating, as is obvious from the discrepancy between the experimental data and the fits using any value of $n_{\max}$. However, carrying out the same procedure is useful to find out that the 9-wave approximation (corresponding to $n_{\max} = 4$) is necessary in the case of a lamellar metallic grating.

Rather than a lamellar grating, we identify the geometrical profile of Sample C with a profile whose filling factor depends on the z-coordinate as described by Eq. (6.11). Ac-

$n_{\max}$	d [nm]	W_{top} [nm]	$W_{\max}$ [nm]	Λ [nm]	error [deg]
2	235.84	71.45	101.46	190.63	6.72
4	226.75	52.12	100.44	198.65	4.8
6	226.88	59.87	102.94	198.12	4.7
8	224.73	53.3	103.37	198.69	4.72
10	224.64	56.16	103.14	198.68	4.39
20	219.27	49.41	103.79	199.2	4.01
50	219.01	50.46	103.42	199.29	3.87

Table 7.5 Fitted critical dimensions (depth d, top linewidth W_{top}, maximum linewidth $W_{\max}$, and period Λ) and errors of the fits of Ta-paraboloidal-wire gratings according to increasing $n_{\max}$ with a fixed number of slices $N = 20$ (dimensions are in nanometers, errors in degrees).

N	d [nm]	W_{top} [nm]	$W_{\max}$ [nm]	Λ [nm]	error [deg]
3	231.6	60.85	96.48	194.63	8.33
5	226.29	55.81	99.06	197.63	5.19
7	225.03	55.98	99.49	197.93	4.52
10	222.37	53.2	101.37	198.41	4.07
20	219.27	49.41	103.79	199.2	4.01
50	219.63	53.97	104.17	199.58	4.2

Table 7.6 Fitted critical dimensions (depth d, top linewidth W_{top}, maximum linewidth $W_{\max}$, and period Λ) and errors of the fits of Ta-paraboloidal-wire gratings according to increasing number of slices N with fixed $n_{\max}$ (dimensions are in nanometers, errors in degrees).

cording to various numerical experiments performed, we consider the profile as symmetric wires with paraboloidal edges, i. e., with the linear element in Eq. (6.11) omitted. Thus four critical dimensions are used to identify the profile, i. e., the depth, top linewidth, maximum linewidth (at the half of the depth), and period. Two kinds of analyses on the convergence properties of the dimensions were carried out, according to increasing $n_{\max}$ while N was fixed to 20 (Tab. 7.5) and according to increasing N while $n_{\max}$ was fixed to 20 (Tab. 7.6).

The fitted ellipsometric parameters corresponding to the former case for three demonstrative examples of $n_{\max}$ are displayed in Fig. 7.11 (b). In most of the spectral range, the 17-wave approximation (corresponding to $n_{\max} = 8$) is sufficient to perform a reliable fit. A higher value of $n_{\max}$ can slightly improve the accuracy of simulation in the short wavelength range and at the extreme points near Rayleigh's wavelengths, one at 388 nm where the -1st diffraction order in reflection passes off and another one at 480 nm where

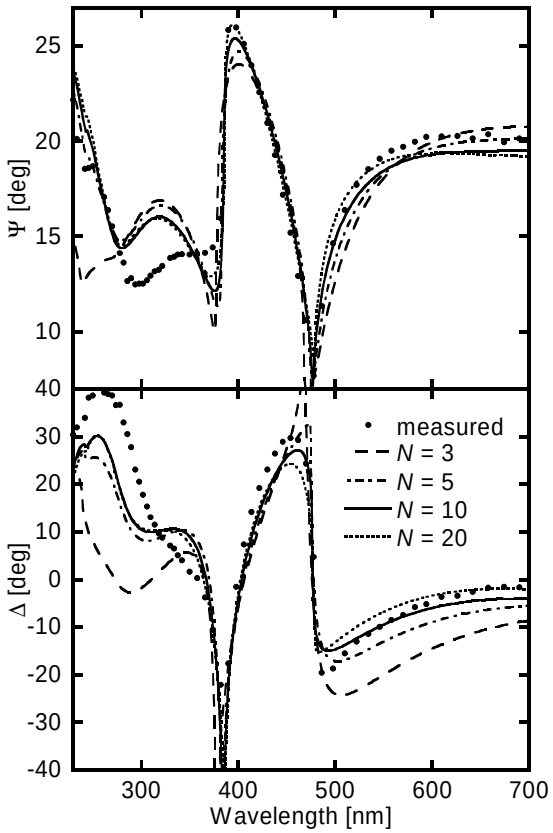

Figure 7.12 Experimental (marks) and fitted 4-zone null ellipsometric parameters Ψ and Δ on a paraboloidal-wire Ta grating (Sample C) in incidence of 70° for four examples of the number of slices, $N = 4$ (dashed curves), $N = 5$ (dash-dotted curves), $N = 10$ (solid curves), and $N = 20$ (dotted curves), in each case with the maximum Fourier harmonics $n_{\max} = 20$. Here the quality of the fit is monotonously improving by increasing N.

the -1st diffraction order in transmission passes off.

The fitted ellipsometric parameters with $n_{\max}$ fixed to 20 for four demonstrative examples of N are displayed in Fig. 7.12. Here the agreement between experiment and fitting is improved gradually while N is increasing. Again, the short spectral ranges near Rayleigh's wavelengths are most sensitive to insufficient slicing. We can conclude that the fit with $N = 10$ is satisfactory according to the error of the ellipsometric parameters.

Finally, in Fig. 7.13 we present the convergence dependences of relative critical dimensions, i. e., parameters defined as $p(n_{\max})p(n'_{\max})$ where $p(n_{\max})$ denotes a dimension whose convergence properties according to increasing $n_{\max}$ are studied, while $p(n'_{\max})$ represents a reference value obtained from a fit that assumes sufficiently high $n'_{\max}$, chosen 50 for both the lamellar grating profiles and Ta paraboloidal-wire profiles. Thus, the subfigures depict how the critical dimensions are approaching their approximate-limit values with high $n_{\max}$.

In Fig. 7.13 (a, b, c), the convergences of the relative depth, linewidth, and period are displayed obtained on Samples A, B, C, respectively. The errors of all the critical dimensions of the transparent grating are less than 1 % for $n_{\max} \geq 2$ and are rapidly

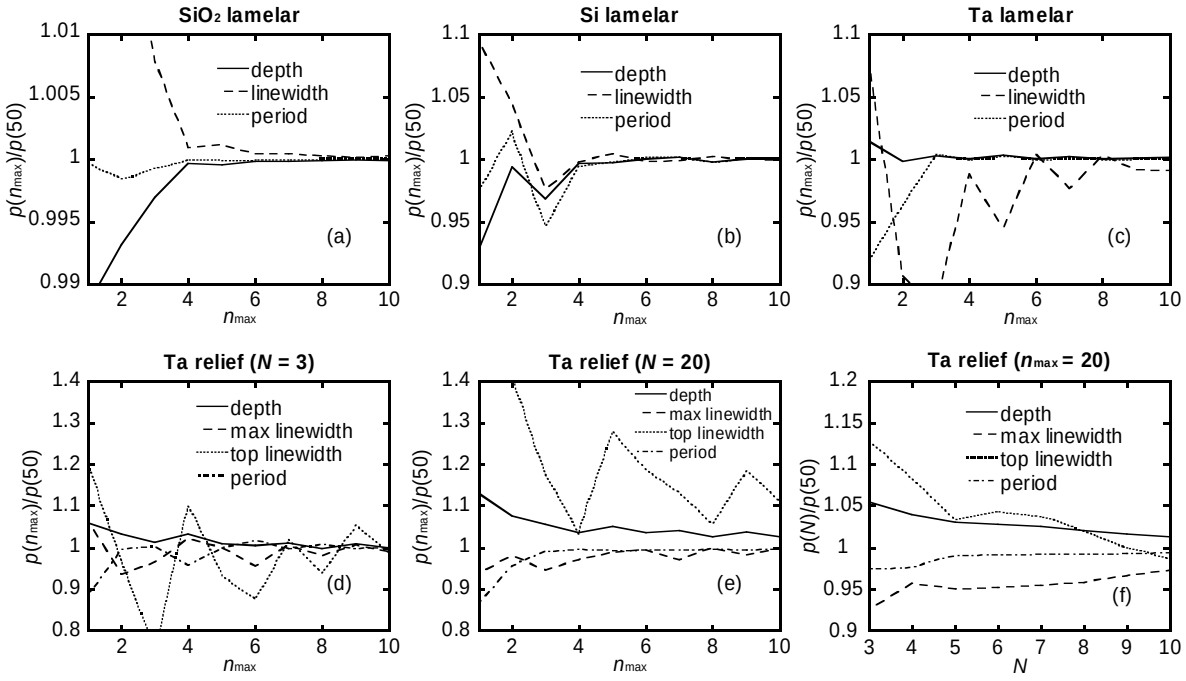

Figure 7.13 Convergence properties of the relative critical dimensions according to increasing $n_{\max}$ **(a–e)** and according to increasing N **(f)**, obtained on the Samples A and B **(a, b)**, on the lamellar-assumed **(c)** Sample C, and on the paraboloidal-wire-assumed Sample C with fixed $N = 3$ **(d)**, with fixed $N = 20$ **(e)**, and with fixed $n_{\max} = 20$ **(f)**.

decreasing for higher $n_{\max}$ [Fig. 7.13 (a)]. Note that the period converges fastest while the linewidth does slowest. Similarly, the errors of all the dimensions of the Si grating are less than 1 % for $n_{\max} \geq 4$ [Fig. 7.13 (b)]. In the case of the Ta grating with its wires assumed lamellar, the errors of the depth and the period are less than 1 % for $n_{\max} \geq 3$, whereas the linewidth converges much slower. This can be explained by the inhomogeneity of the linewidth within depth or, in other words, by the incorrectness of the model applied for fitting which does not take into account all the aspects of the reality.

In Fig. 7.13 (d, e), the convergences of the relative depth, top linewidth, maximum linewidth, and period are displayed obtained on Sample C with the number of slices N assumed 3 and 20, respectively. Here the convergences of all the dimensions are slower than in the case assuming the lamellar profile. The most probable explanation follows from a partial inadequacy of the Fourier factorization rules applied here to wires with slightly curved edges, though the rules have been derived for rectangular-relief gratings. Nevertheless, the slopes of the wires of Sample C are so small that the factorization rules should still be approximately valid.

In Fig. 7.13 (f), the convergences of the relative depth, top linewidth, maximum linewidth, and period according to increasing N are displayed obtained on Sample C with $n_{\max}$ fixed to 20. The relative parameters can now be written as $p(N)/p(N')$ where $p(N)$ is a parameter whose convergence properties according to increasing N are studied, while $p(N')$ represents an approximate-limit value obtained by assuming $N' = 50$. Just as

the ellipsometric parameters do in Fig. 7.12, the relative dimensions gradually converge while the number of slices is increasing. We can conclude from Fig. 7.13 (d, e, f) that the period converges most rapidly whereas the maximum linewidth most slowly in the case of a sliced nonrectangular profile.

Conclusions

In summary, it was demonstrated that applying Li's Fourier factorization rules incredibly enhanced the convergence properties of both the simulated ellipsometric parameters and the extracted critical dimensions, though an improvement based on generalizing the factorization rules would provide better results for wires with curved edges. In the case of the gratings made of transparent quartz and semiconducting Si, the agreement between the experimental data and the fitted parameters was nearly perfect, obviously indicating high relevance of the model assuming a rectangular-relief structure of Samples A and B. In the case of the Ta grating, however, slight discrepancies were observed in the short-wavelength part of the range of interest, even though a top native Ta_2O_5 overlayer and a non-ideal shape of wires with curved edges were considered. The method could be improved by generalizing the model assuming more aspects of the reality, the most important of which are the optical constants of Ta to be monitored more precisely in a broader spectral range with an energy reflectance measurement included, the surface roughness of Ta for which spectroscopic ellipsometry is sensitive, and/or a more general shape of the Ta wires with higher-order parameters of the Taylor series.

7.4 Sine-like relief gratings

Introduction

Periodically modulated sinusoidal surfaces have widely been studied in terms of energy reflectance measurements. Many applications employ transparent or metallic sinusoidal gratings; therefore, many scientific reports on their optical response have been published [96, 87, 88, 97]. Especially, the resonant nature of surface-relief gratings has become the reason for large interest. Various resonation effects appear in the region of Wood anomalies and surface-plasmons observed on sinusoidal metallic gratings [96, 87, 88]. In the case of dielectric relief surfaces, the multi-reflection effects also cause great modulation of the reflectivity vs. wavelength [97].

Those resonance effects are highly sensitive on each parameter of the structure and strongly depend on the polarization of incident light, which can be effectively used to determine the geometrical and/or material parameters of gratings from the ellipsometric measurement. Although scatterometry based on spectroscopic ellipsometry has been successfully used to measure geometrical parameters of various profiles, sine-like profiles have been studied by optical spectroscopy very rarely.

In this section, spectroscopic ellipsometry is applied to study an imperfectly sinusoidal polymer grating situated on a glass plate. The initial inverse problem of determining the parameters of the relief sine function is therefore extended to two additional problems: the problem to find the correct shape of the relief function and the problem coupled with a grating system containing a thick layer, since the interface between the polymer and the glass causes incoherent contributions to the optical response. The solution of both problems can demonstrate the possibility to verify not only the geometrical parameters of the grating, but also the quality of the optical matching between the polymer and the glass intended by the manufacturer.

Samples and experiments

The sample was fabricated as a transparent relief grating with a period of about 10 000 nm. The optically thick epoxy-polymer layer with the sinusoidal surface was situated on a crown glass substrate [Schott B270 with refractive indices $n_{\mathrm{e}} = n(\lambda = 546\ \mathrm{nm}) = 1.525$ and $n_{\mathrm{d}} = n(\lambda = 588\ \mathrm{nm}) = 1.523$ and with the Abbe number being 58.5]. The refractive index of the polymer was optically matched to the index of the glass.

The shape of the grating was investigated by measuring AFM at 16 positions on the surface. The ellipsometric measurement was performed with a Jobin Yvon ellipsometer in the spectral range of 240–850 nm at several angles of incidence. Here we report on measurements near the Brewster angle of incidence, where the ellipsometric response is highly sensitive, i. e., at two incidence angles of 55° and 57.5°.

Modeling and fitting

There are many theoretical approaches capable to calculate the optical response of sinusoidal gratings with different levels of numerical precision. Specially, shallow-relief gratings can be considered as phase gratings with a small perturbation due to the Fresnel reflection coefficients varied by different angles of incidence along the inflexed surfaces. This approach can explain the global dependences of reflection efficiencies, but in the ratio $r_{\mathtt{p}}/r_{\mathtt{s}}$ the main influence of that small perturbation vanishes. Theoretical models based on the Rayleigh approximation [98] can include the multiple-reflection effects and thus explain the effects of the Wood anomalies. Unfortunately, their explanation has just a qualitative character since the Rayleigh approximation is not valid in the case of gratings where those effects become significant. For accurate simulations of the resonance effects observable in ellipsometric spectra we therefore need an accurate physical model.

Like in the case of lamellar-like profiles we have utilized the coupled wave theory implemented as the Airy-like series. To receive acceptable numerical results also for a sine-like profile, we assume $N = 20$ slices and the presence of 81 diffraction orders (from -40 to $+40$).

Since the sizes of the relief profile are smaller than the coherence length of the light

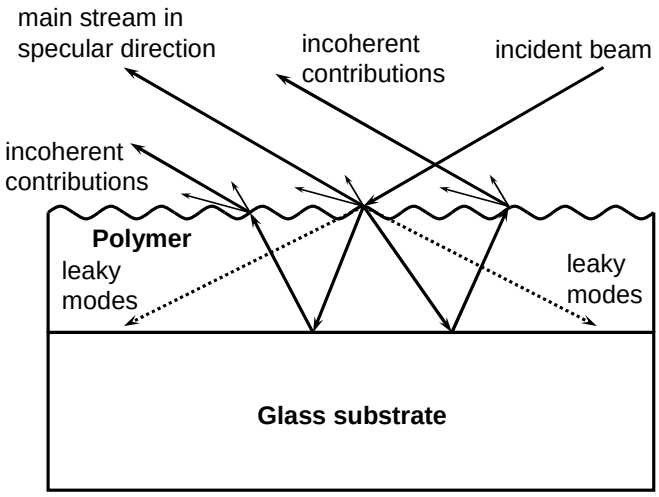

Figure 7.14 Configuration of the diffraction problem.

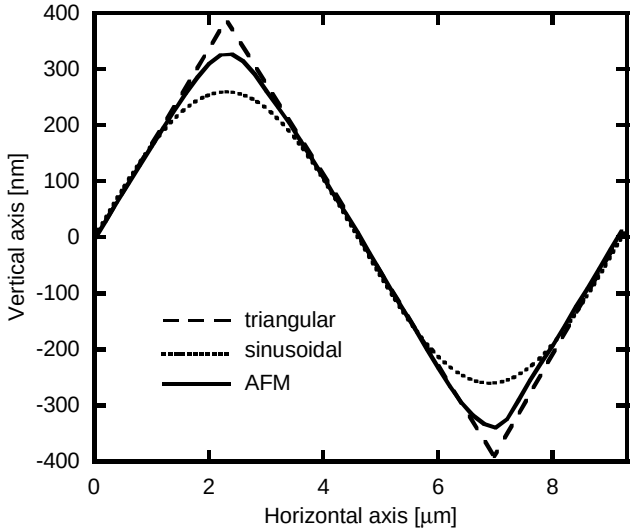

Figure 7.15 Measurement of AFM compared with the ideal sinusoidal and triangular profiles.

source, the standard amplitude matrices for reflected and transmitted light are calculated. On the other hand, the thickness of the polymer layer is considered thicker; incoherent contributions of efficiencies are therefore assumed as a result of backreflections (Fig. 7.14). Those contributions do not depend on the thickness of the polymer because its extinction coefficient is assumed zero. The theoretical model of a grating containing a thick layer is derived in terms of efficiencies as described in Sec. 7.1. However, in this section we present only the analysis of the parameter Ψ, because the Δ-parameter is too sensitive on other unimportant imperfections such as slight random irregularities of the periodicity of the geometrical parameters which were revealed by the systematic AFM analysis.

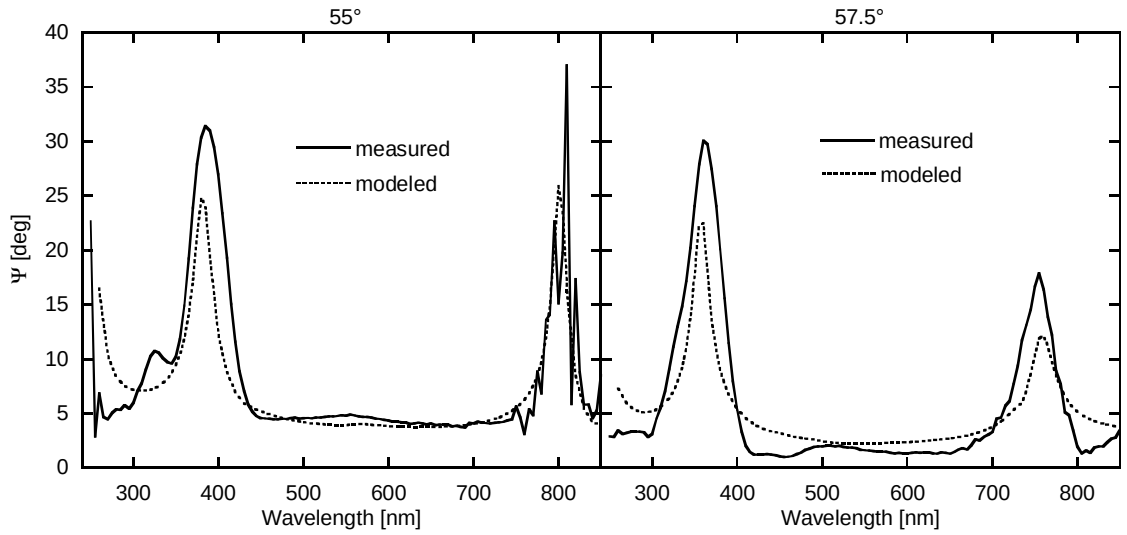

Figure 7.16 Comparison between the measured and modeled Ψ-parameter in two incidences of $55°$ (left) and $57.5°$.

Results and discussion

The measurement of AFM yielded the period of 9 365 nm and the amplitude of about 350 nm. It also evidenced that the surface is not perfectly sinusoidal; its real shape is between a sinusoidal and rectangular profile, as depicted in Fig. 7.15. In order to evaluate the optical response corresponding to the real surface, we have chosen the linear combination between the sinusoidal and the linear function described by Eq. (6.13). The real sine-like surface is then described by the period Λ, the depth d, and the parameter of sharpness σ, the value of which corresponds to the sinusoidal or triangular shape when $\sigma = 0$ or $\sigma = 1$, respectively. The application of the Eq. (6.13) to the AFM measurement yields the value of $\sigma = 0.6$, which is used in the ellipsometric calculations.

Since the grating sample investigated here can be considered shallow, mainly measuring the resonation effects can determine its optical and geometrical features sensitively. The measurements in both angles of incidence yields spectral dependences with two significant features, one high maximum in the near-UV region, and one, lower, in near infrared (Fig. 7.16). Both maxima demonstrate an enhancement of diffraction caused by resonances in the region of Wood anomalies.

Since the parameter of sharpness is determined by AFM and the manufacturer provided the optical constants of the glass, only the depth and the refractive index of the polymer have to be determined by employing spectroscopic ellipsometry. The result of fitting the correct values is displayed in Fig. 7.16. The depth is found to be equal to 620 nm, which is in good accordance with the expectation yielded by AFM. The refractive index of the polymer is found a little higher than the index of the glass. As expected, in the region of visible light the optical matching is performed with better precision than in near-UV. At the spectral point of 700 nm the difference of indices is $\Delta n \approx 0.03$, whereas the value of

$\Delta n \approx 0.1$ corresponds to the point of 300 nm. It is important to point out that the values of Δn are approximations since the backreflections are weaken by leaky modes. Namely, the finite light beam of higher diffraction orders is deflected from the original beam while propagating through the polymer layer. Unfortunately, it was not possible to apply the IBMG method precisely as described in Sec. 7.1 because the experimental diminution function on the commercial Jobin Yvon ellipsometer was not available. Nevertheless, the tendency of the optical matching in spectral distribution is determined reasonably.

The positions and shapes of both spectral anomalies are compared with reasonable correspondence, though the amplitudes and bandwidths of the measured anomalies are higher than those of the modeled ones. A possible inclination of the surface, its irregularity along periodicity or a little absorption of the polymer could affect the measurement of the optical response and thus disable to fit the structural parameters precisely. To improve the reliability of the inverse problem, a theoretical model generalized by considering those features should be applied.

Conclusions

In summary, specular-mode spectroscopic ellipsometry is presented as highly sensitive on both geometrical and material properties of sinusoidal surface-relief gratings. In the case of shallow gratings, this sensitivity is realized via resonation effects in the region of Wood anomalies. The ellipsometric measurement was here applied to extract features of a transparent grating with a sine-like relief located on a structure of polymer/glass, while AFM was used as a complementary technique to minimize the possibility of a mutual correlation between the parameters to be extracted. The shape and amplitude of the relief function, as well as the quality of the optical matching between the polymer and the glass, were determined successfully. Further improvement of theoretical considerations, e. g., a slightly irregular periodicity, the finite beam aperture, or a more suitable profile formula can enhance the reliable solution of the inverse problem of measuring the optical response.

7.5 Binary arrays of holes in silicon

Introduction

As we have seen in Sec. 4.8.3, the simulation of the optical response of a two-dimensional grating requires long-time and large-memory computation, which makes the fitting procedure enormously difficult. Therefore, scatterometry has been applied to other than one-dimensional gratings very rarely. In this section we present an analysis of periodic arrays of circular holes patterned with square periodicity on the top of a silicon wafer.

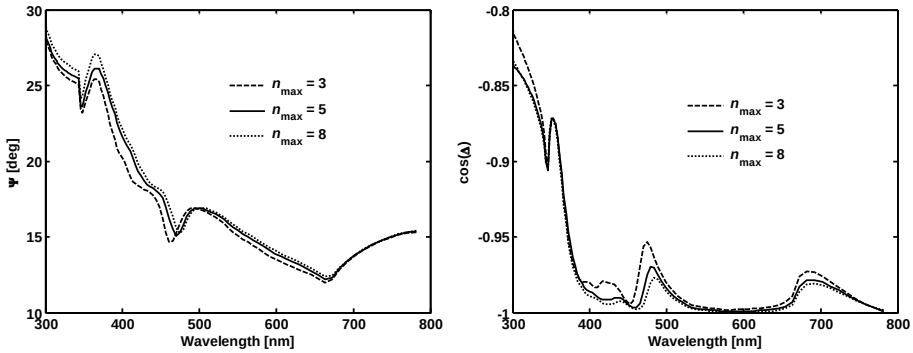

Figure 7.17 Convergence properties of the algorithm applied to simulate the ellipsometric parameters Ψ **(a)** and Δ **(b)** on a binary array of holes patterned on the top of an Si wafer. Three examples of $m_{\max} = n_{\max}$ are calculated in the visible and near-UV range.

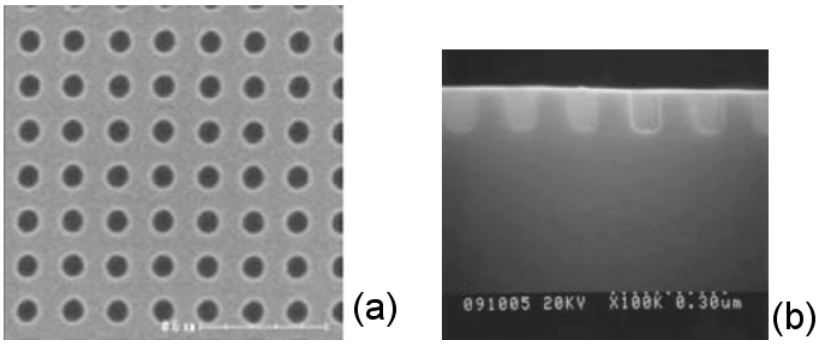

Figure 7.18 Pictures of SEM obtained on the investigated sample, a binary array of circular holes patterned on the top of an Si wafer. The top view **(a)** is accompanied with a cross-section **(b)**.

Numerical example showing the convergence properties

Before proceeding to the scatterometric analysis, we will provide one numerical example of numerical simulation from which the convergence properties of the numerical algorithm for binary gratings will be clearly visible.

We denote $m_{\max}$ and $n_{\max}$ the maximum diffraction orders in the x- and y-axis directions, respectively. The upper and lower limits for summations of the Fourier and pseudo-Fourier series are correspondingly given by $\sum_{m=-m_{\max}}^{+m_{\max}} \sum_{n=-n_{\max}}^{+n_{\max}}$, corresponding to the total matrix dimension of $2(2m_{\max}+1)(2n_{\max}+1)$, where the factor "2" is due to two polarizations.

The convergence properties in a spectral range from 300 to 800 nm is shown in Fig. 7.17 for three examples of $m_{\max} = n_{\max}$. The simulated structure is chosen as a binary array of circular holes on the top of an Si wafer with a square periodicity 180×180 nm^2 and with the diameter and the depth of the holes being 80 and 130 nm, respectively. (These dimensions correspond to the nominal fabrication parameters.) One can see that the value of $n_{\max} = 5$ is sufficient to receive high precision of computation. The same value is therefore chosen for the later analysis of an experimental optical response.

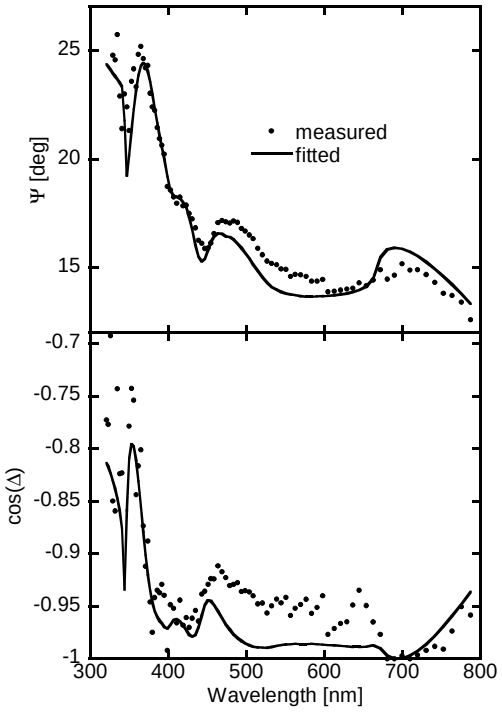

Figure 7.19 Fitted ellipsometric parameters Ψ and $\cos\Delta$. The marks correspond to experimental data, whereas the curves represent the simulations fitting the geometrical values.

Samples and experiments

SEM pictures of the sample investigated here are displayed in Fig. 7.18, both the top-view [Fig. 7.18 (a)] and a cross-section [Fig. 7.18 (b)]. The structure was fabricated as a binary array of circular holes patterned on the top of an Si wafer with the nominal periodicities $\Lambda_x = \Lambda_y = 180$ nm, the holes' nominal diameter being 80 nm, and the nominal depth being 130 nm.

The optical response of the sample was measured by means of microspot spectroscopic ellipsometry with polarizer-sample-analyzer configuration adopting the rotating-analyzer method. Technical details of the ellipsometer are described in Ref. [99].

	depth [nm]	diameter [nm]	error [deg]
nominal	130	80	—
SEM	130.7	93	—
SE	103.5	94.6	3.8

Table 7.7 The extracted geometrical parameters of the binary array of circular holes on the top of an Si wafer with the square periodicity fixed to the nominal value 180×180 nm^2.

Results and discussion

According to our experiences with fabricating laterally patterned structures, the period of the patterning is usually made with high accuracy. In other words, neither SEM nor spectroscopic ellipsometry can detect its error. (Only a high-precision, noise-less experiment can, which is not the case of the measurement presented in this section.) On the other hand, linewidths and depths of the patterning can easily be confirmed by both SEM and ellipsometric analyses. Therefore, we fixed the square period to $\Lambda_x = \Lambda_y =$ 180 nm, and determine the holes' depth and lateral diameter by both methods with the results summarized in Tab. 7.7. The results of the fitting of the ellipsometric parameters are displayed in Fig. 7.19.

As visible from Tab. 7.7, the holes' diameter determined by spectroscopic ellipsometry is in very good agreement with that determined by SEM, but differs considerably from the nominal diameter intended by the manufacturer. On the other hand, the optically determined depth differs considerably from the depth visible on the SEM picture, but the SEM's depth is in very good agreement with the nominal depth. We can conclude our analysis by the following simple explanation. Due to the good agreement in the diameter measured by both methods, its real value can be trusted to be higher than the value intended by the manufacturer. The disagreement in the case of the depth makes one believe that SEM provides better values of depths than ellipsometry does. However, the cross-section in Fig. 7.18 (b) suggests that the bottom surface of the holes is slightly curved, so that the depth actually measured at the central part is larger than that measured at the edges. Since the optical response of the structure is essentially based on the interference effects in small waveguide-like holes, the difference in the fitted value can be understood. If the structure was simulated by a more general geometrical model taking into account the real shape of the bottom surface of the holes, then ellipsometry could provide more general picture of the sample in better agreement with the SEM picture.

It is worth noting at the end of our analysis that, according to our experiences, the ellipsometric response at high angles of incidence is only sensitive to surface properties on the top of the structure, and is much less sensitive to the surface properties on dots' or holes' edges. Moreover, in the case of an Si structure, even the properties of the top surface contribute to the optical response only by a small perturbation, which is highly correlated with the geometrical parameters of the patterning. Therefore, the potential native oxide overlayers neither on the top surface, nor on the holes' edges were taken into account in our analysis.

Conclusions

In summary, remarkably effective convergence properties of the theory were demonstrated on an example configuration corresponding to a real sample of a two-dimensional grating. Microspot spectroscopic ellipsometer was utilized to measure the optical response of a

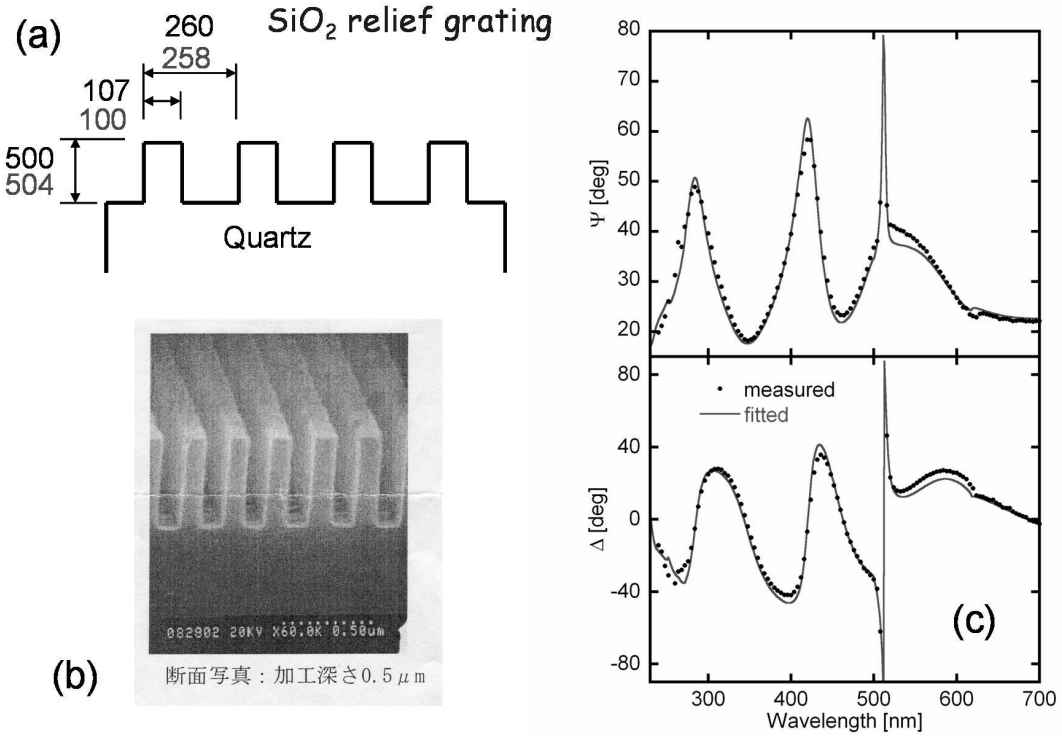

Figure 7.20 Comparison between SEM and scatterometry results obtained on a lamellar quartz grating sample. The values are in nanometers.

binary array of holes patterned on the top of an Si wafer. By means of scatterometry, two geometrical parameters were extracted from the ellipsometric measurement, namely the diameter and the depth of the holes, while the square period of the array was fixed at the value intended by the manufacturer. The values obtained from fitting the ellipsometric values were compared with dimensions visible on a SEM picture with a reasonable agreement. While the holes' diameter is provided by both methods in a very good agreement, the holes' depth seems to be more accurately determined by SEM, because the ellipsometric simulations do not take into account the curved bottom surface of the real holes. This weak point of spectroscopic ellipsometry could be avoided by generalizing the CWT algorithm to two-dimensional surface-relief structures.

7.6 Final comparison between SEM and scatterometry results

The quality of the scatterometric technique presented in this thesis with respect to the comparison with SEM measurements is viewed in Fig. 7.20 for the case of the transparent lamellar gratings, in Fig. 7.21 for the case of the lamellar semiconductive lamellar gratings, in Fig. 7.22 for the case of the incorrectly assumed ideal lamellar profile of metallic wires, in Fig. 7.23 for the case of the correctly assumed metallic wires with curved edges, and in Fig. 7.24 for the case of the two-dimensional gratings. From all the comparisons the

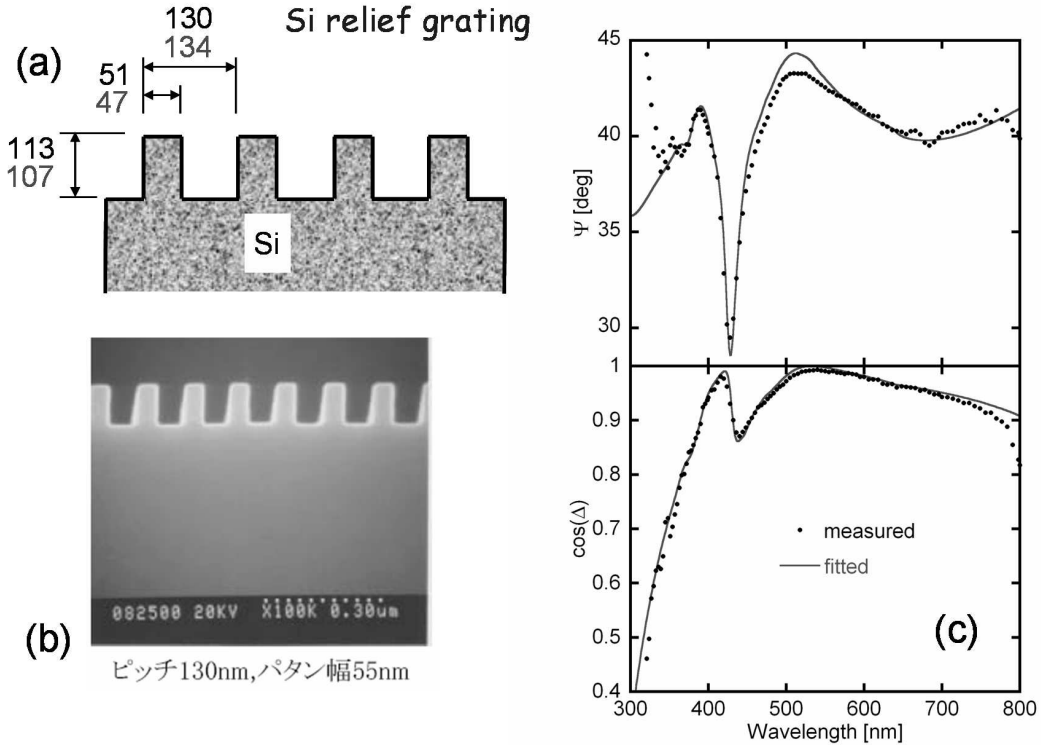

Figure 7.21 Comparison between SEM and scatterometry results obtained on a lamellar silicon grating sample. The values are in nanometers.

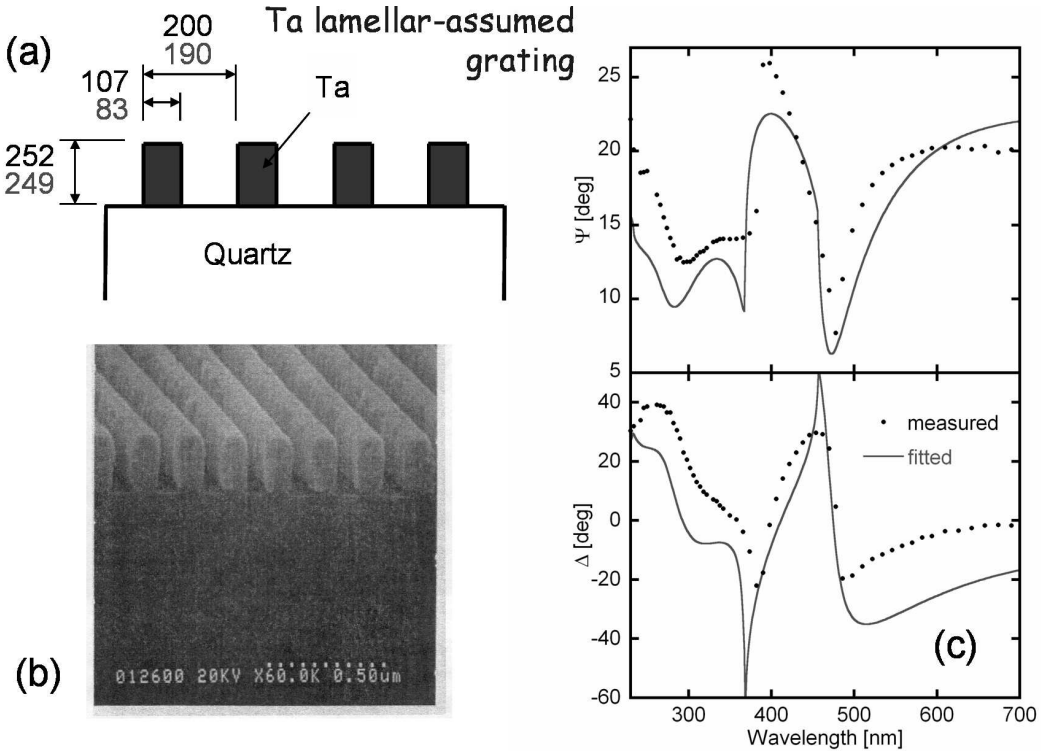

Figure 7.22 Comparison between SEM and scatterometry results obtained on a lamellar-wire-assumed tantalum grating sample. The values are in nanometers.

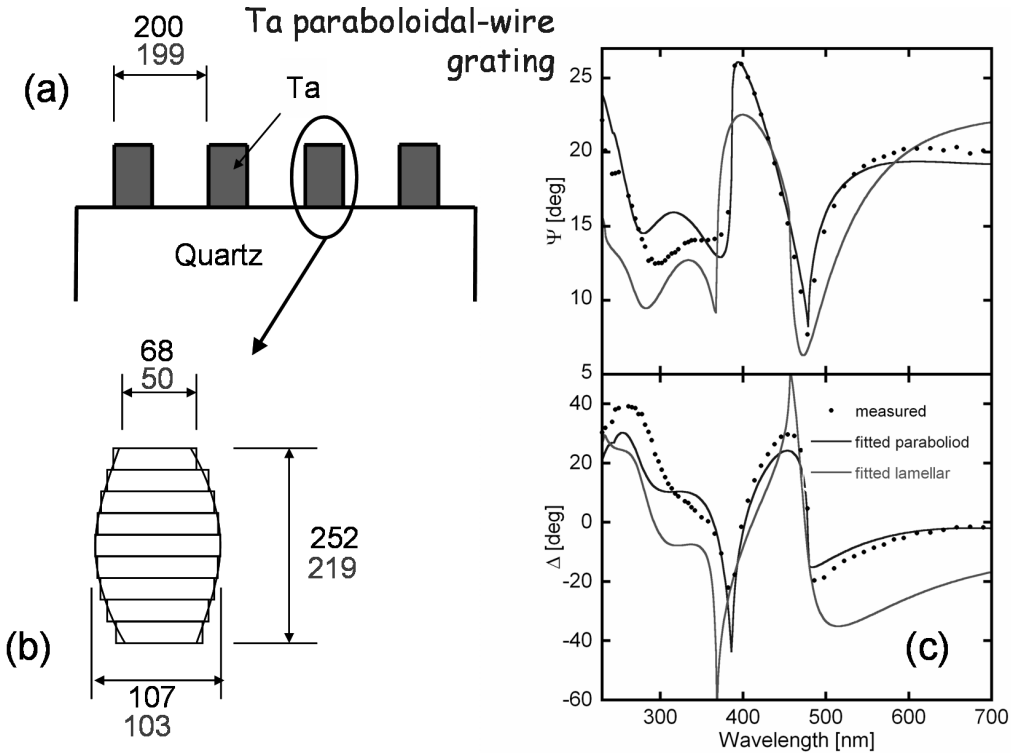

Figure 7.23 Comparison between SEM and scatterometry results obtained on a paraboloid-wire-assumed tantalum grating sample. The values are in nanometers.

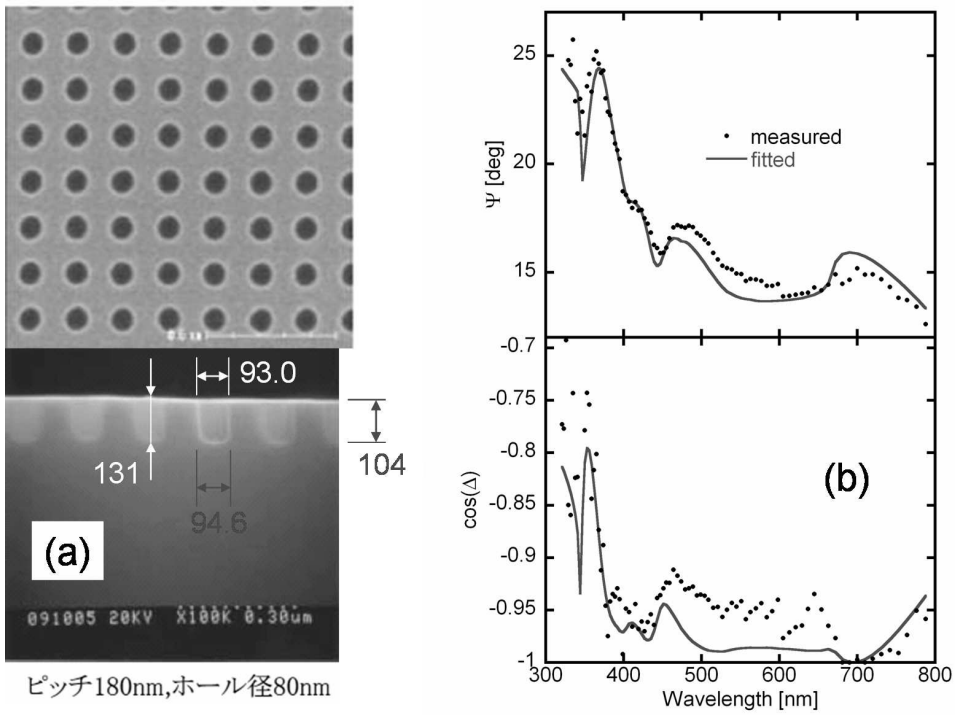

Figure 7.24 Comparison between SEM and scatterometry results obtained on a binary array of holes patterned on the top of an Si wafer. The values are in nanometers.

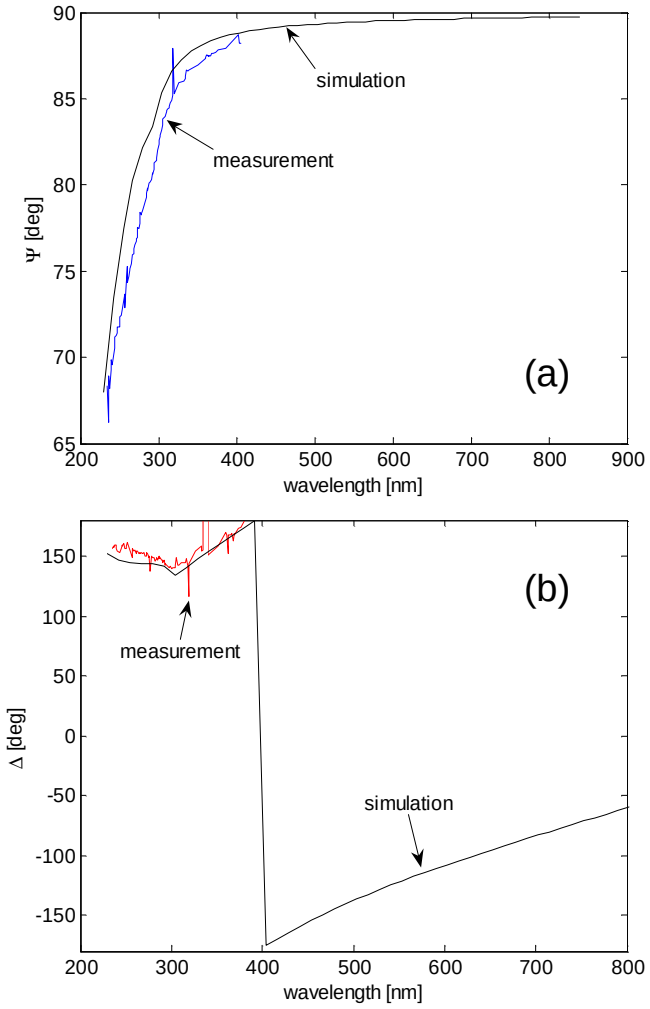

Figure 7.25 Spectro-ellipsometric parameters Ψ and Δ measured and simulated on the Ta-wire grating in the transmitted 0th diffraction order.

high correspondence between the both methods is obvious.

The geometric parameters obtained on the Ta wire gratings were used to simulate the transmitted 0th order of diffraction, whose results are compared with measurement in Fig. 7.25. The measurement was carried out on the four-zone null spectroscopic ellipsometer in the setup for transmission mode. The spectrum of the Ψ-parameter exhibits the attenuation ratio $T_{\mathrm{p}}/T_{\mathrm{s}} = \tan^2 \Psi^{(t)}$ of the Ta-wire grating whose intended to be applied as a wire-grid polarizer (WGP). The spectrum of the Δ-parameter exhibits WGP's phase difference $\phi_{\mathrm{p}}^{(t)} - \phi_{\mathrm{s}}^{(t)} = \Delta^{(t)}$. Unfortunately, the measurement was not possible to perform in the visible spectral range where the WGP becomes of too high quality and hence the four zones are not detectable separately. The spectra also evidence that in the shortest wavelength the disagreement between the model and experiment becomes higher. This is most probably caused by the surface roughness on the edges of the wires, for which the short-wavelength normal-incidence transmission-mode ellipsometry is extremely sensitive.

Chapter 8

Characterization of magnetic gratings by magneto-optic spectroscopy

The magneto-optical (MO) diffraction techniques applied to arrays of submicron magnetic elements have provided valuable information on their fundamental micromagnetic properties [62, 63]. Those techniques are also promising for contactless, nondestructive, and low-cost metrology of magnetic nanostructures such as magnetic and MO recording disks and magnetic random access memory chips. Arrays of magnetic wires [64, 65, 66], dots [67], and antidots [68] have been investigated in the reflection mode by measuring the magneto-optical Kerr effect (MOKE) at polar, longitudinal, and transverse magnetization.

So far, the MO diffraction techniques were restricted to single-wavelength micromagnetic studies with coherent wave sources. Further data were acquired by the extension of experiments to multiple incidence angles and to changing the orientation of the magnetization vector. It was found that lateral magnetization distribution can be deduced from the diffracted MOKE, which makes it an important technique complementary to the magnetic force microscopy, Brillouin light scattering [69], etc. The extension of the single-wavelength MOKE to the multiple-wavelength version, i. e., "diffracted MOKE spectroscopy," should in principle deliver larger volume of information on the optical and MO characteristics of magnetic gratings, which is the aim of this chapter.

Here we demonstrate a joint analysis of a set of shallow Permalloy gratings employing spectroscopic ellipsometry, normal-incidence reflectometry, and (especially) specular-mode and diffracted MOKE spectroscopy. We structure this chapter so that the details of experiment, theory, and particular results are divided into separate sections. Section 8.1 provides the description of the investigated samples and the used experimental techniques. In Sec. 8.2 applied theoretical approaches are briefly introduced, concretely the coupled wave theory described in Chap. 4 as well as two other original ones suitable for this anal-

Sample	Period [nm]	Linewidth [nm]	Filling factor
A	900	536	0.596
B	910	700	0.769
C	970	680	0.701

Table 8.1 Nominal lateral-geometric parameters of the investigated Permalloy gratings.

ysis. In Sec. 8.3 experimental and simulation results of purely optical spectroscopy are shown based on spectroscopic ellipsometry and reflectometry. In Sec. 8.4 the presence and thicknesses of native oxides is determined developed on the capping and substrate of the studied gratings. Section 8.5 demonstrates the evaluation of the sharpness of patterning of the gratings (in literature referred to as *line edge roughness* as mentioned in Chap. 2). Finally, conclusions for this chapter is written in Sec. 8.6.

8.1 Samples and measurements

The experiments were performed on wire gratings prepared from a nominally 10 nm thick Permalloy ($Ni_{81}Fe_{19}$) layer deposited onto a chemically cleaned Si substrate and protected by 2 nm thick Cr capping. The patterning was made by means of electron-beam lithography with subsequent ion milling to produce periodic arrays of wires. The nominal parameters of the lateral geometry are summarized in Tab. 8.1. The method of deposition of the Cr/Permalloy bilayers did not allow us to prepare single-layer reference samples required for determining the precise material parameters of the Permalloy and Cr; therefore, only literature optical parameters were used in modeling. The method of the patterning included thermal processes in air atmosphere which might have changed the thicknesses of both native oxides on the top of wires, $t(Cr_2O_3)$, and between wires, $t(SiO_2)$; therefore, non-patterned reference bilayer structures were not investigated to avoid errors due to that effect.

The ellipsometric experiments were performed on the four-zone null ellipsometer with the PSCA configuration in the spectral range of 1.5–5.4 eV at several angles of incidence. The reflectometry experimental arrangement in the nearly normal incidence of 5° employed a Shimazu^{TM} UV-3100PC spectrophotometer covering approximately the same spectral range.

The MOKE experiments were performed with an MO spectroscopic ellipsometer employing azimuth modulation and compensation technique. The samples were set up with applied out-of-plane magnetic field of 1.4 T, sufficient for the saturated polar magnetization [100]. The MO response in the specular mode was measured at an angle of incidence of 7° in the spectral range of 1.3–5.1 eV for both the `s` and `p` azimuths of a linearly

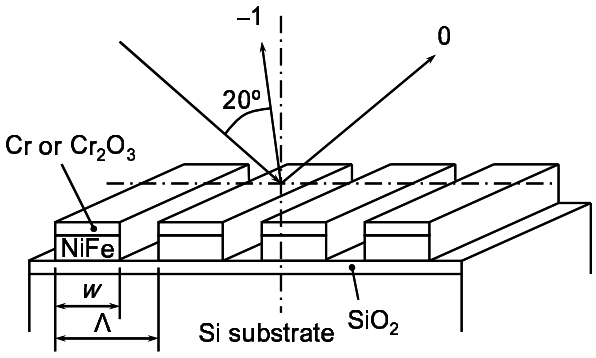

Figure 8.1 Periodic wire array prepared by lithography of a 12 nm thick Permalloy layer covered by 2 nm thick protecting Cr capping deposited on an Si substrate covered by a native SiO_2 layer. The wire width w and the wire period Λ assume the values of $w = 700$ nm and $\Lambda = 910$ nm, respectively. The Cr capping is found completely transformed into a 2 nm thick Cr_2O_3 film due to the aging effect. In the -1st diffraction ordered polar magneto-optical Kerr effect spectroscopic measurements, the sample is free to rotate about an s-oriented axis parallel to the wires axes.

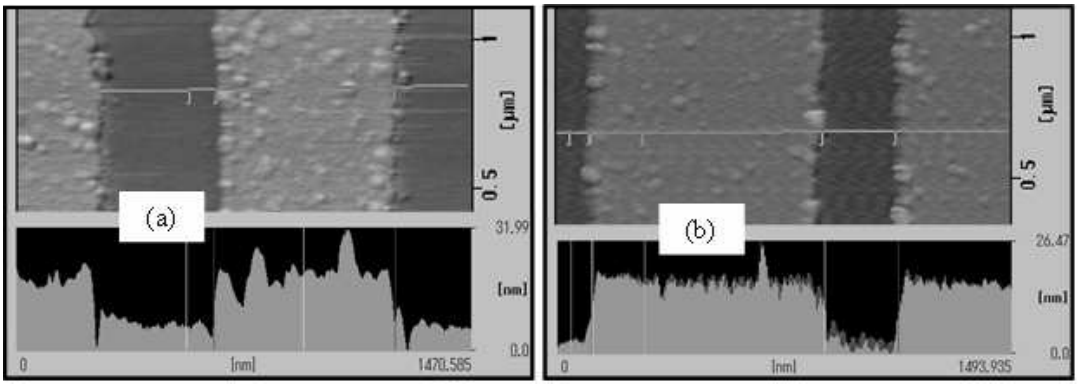

Figure 8.2 Atomic force micrographs of Sample A **(a)** and Sample B whose quality is obviously higher **(b)**. The top view of each sample is accompanied by a cross section.

polarized incident beam, but no azimuth dependence was detected.

The reflection angles of higher diffraction orders are wavelength dependent; therefore, a special arrangement was necessary to measure the polar MOKE in the -1st diffraction order. The angle between the incident and reflected beams was fixed to 20°, with the sample free to rotate about the axis parallel to the wires, while the wavelength was swept (Fig. 8.1). The position of the beam spot on the detector could not be kept completely fixed with the changing wavelength, which produced jumps in the measured spectra.

The AFM measurements on two chosen samples are displayed in Fig. 8.2. For our purposes, the MOKE results obtained on two samples with differently evident irregularities in the set will be reported. An AFM picture of the Sample A is shown in Fig. 8.2 (a) compared with Sample B of better quality [Fig. 8.2 (b)].

8.2 Theoretical approaches

Two different theoretical approaches were used to model the optical and MO spectra of the gratings, i. e., the coupled-wave theory (CWT) described in Chap. 4 and the local-modes method (LMM), which is an approximate analytical method based on the far-field Fourier analysis of the lateral amplitude-reflectance distribution; the details of LMM will be provided here.

In the case of ellipsometry and reflectometry, CWT was implemented as the Airy-like series. In the case of MO spectroscopy, however, the transfer-matrix approach was utilized.

According to the applied magnetic filed, in modeling we assume homogenous saturated magnetization in the Permalloy wires without any domain structure. Since none of both approaches describes correctly the measured spectrum of the -1st diffraction order corresponding to incident p-polarization, a third model will be derived involving both the CWT and LMM calculations and assuming reduced quality of the wire edges.

Here we provide a short description of the LMM including an evaluation of its error. Let x be the coordinate along the wires of the grating and y the coordinate along its periodicity. Any shallow optical element, with all its lateral-texture sizes considerably higher than its depth, can be described by a complex amplitude reflectance $r_{jk}(y)$, which is a function of only the lateral coordinate y for we are working with one-dimensional patterning. The indices j and k denote any of the polarization-basis indices s and p of reflected and incident waves, respectively. According to the LMM, in which the edge effects are considered negligible, the function $r_{jk}(y)$ uses only two parameters, the amplitude reflection coefficients of wires, $r_{\mathrm{w},jk}$, and of the system of air/substrate between wires, $r_{\mathrm{b},jk}$. In accordance with the principles of the far-field Fraunhofer diffraction, the amplitude reflection coefficients in the separate diffracted orders are determined by formulae

$$r_{jk}^{(n=0)} = w r_{\mathrm{w},jk} + (1-w) r_{\mathrm{b},jk} + \Delta r_{jk}^{(n=0)}, \tag{8.1}$$

$$r_{jk}^{(n\neq 0)} = \tfrac{i}{2\pi n} \left(w r_{\mathrm{w},jk} - r_{\mathrm{b},jk}\right) \left(1 - e^{2\pi i n w}\right) + \Delta r_{jk}^{(n\neq 0)}, \tag{8.2}$$

where n corresponds to the nth diffraction order while w denotes the grating's filling factor given by the ratio of the wire linewidth to the period. The term $\Delta r_{jk}^{(n)}$ represents the influence of the internal diffraction at wire edges in the rigorously calculated optical response or, in other words, the error of the LMM with respect to the CWT. According to various numerical experiments, only $r_{\mathtt{pp}}^{(n)}$ at oblique angles of incidence contains a significant amount of $\Delta r_{\mathtt{pp}}^{(n)}$, especially in higher diffraction orders. This effect is demonstrated by two examples of simulated absolute values of the amplitude reflection coefficients $|r_{\mathtt{sp}}|$ and $|r_{\mathtt{pp}}|$ in Fig. 8.3.

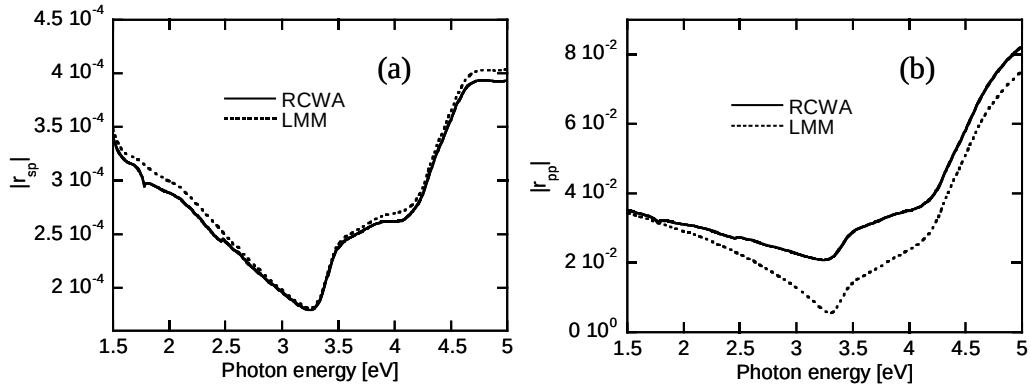

Figure 8.3 Absolute values of two simulated amplitude reflection coefficients, $|r_{\mathrm{sp}}|$ **(a)** and $|r_{\mathrm{pp}}|$ **(b)**, in the -1st diffraction order. Simulations of the CWT (solid curves) are compared with the LMM (dotted curves).

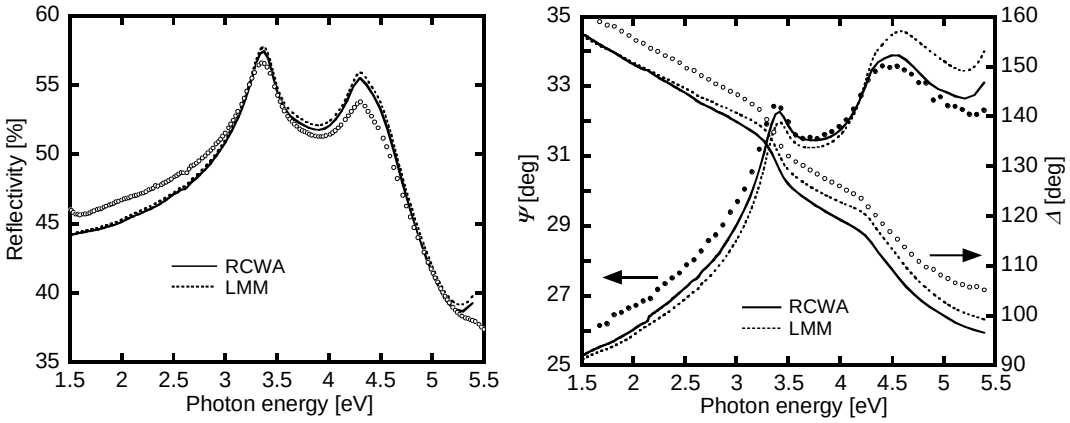

Figure 8.4 The spectroscopic reflectometry **(a)** and ellipsometry **(b)** of Sample B. Circles mark measurement, full and dotted lines represent simulation of the coupled-wave theory and local-modes method, respectively. The reflectometry is in nearly normal incidence, ellipsometry in the incidence of $64°$.

8.3 Spectroscopic reflectometry and ellipsometry

The purely optical response was measured as specular-mode ellipsometric parameters $\Psi^{(0)}$, $\Delta^{(0)}$ and energy reflectance $R^{(0)}_{\mathtt{s(p)}}$. Each of them was modeled with both CWT and LMM, assuming the presence of native oxides. Fig. 8.4 illustrates how the purely optical response is insensitive on the wire edges, which was theoretically suggested by Fig. 8.3. The reflectance curves $R^{(0)}_{\mathtt{pp}} = |r^{(0)}_{\mathtt{pp}}|^2$ calculated with CWT and LMM show identical spectroscopic features and are remarkably close to each other. The ellipsometric parameters, defined by $\tan\Psi^{(0)} \exp i\Delta^{(0)} = r^{(0)}_{\mathtt{pp}}/r^{(0)}_{\mathtt{ss}}$ are in the incidence of $64°$ more sensitive to the choice of the model but both exhibit the same relevant features of the spectra.

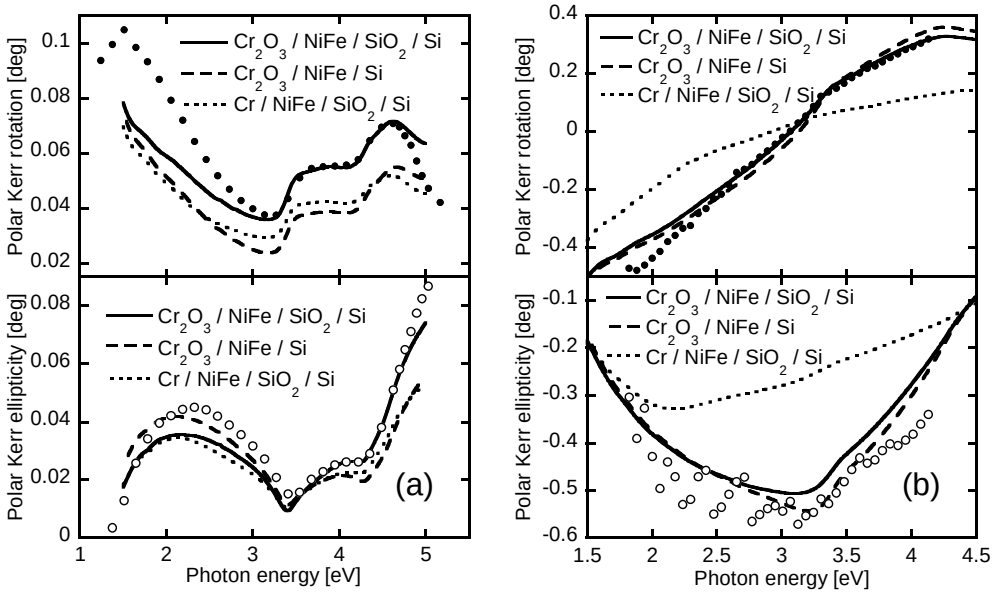

Figure 8.5 The 0th **(a)** and -1st **(b)** diffraction order of polar magneto-optical Kerr effect spectra of Sample B. The full and empty circles indicate the experimental values of the azimuth rotation and ellipticity, respectively. The simulated curves are displayed for t, the thicknesses of the capping and substrate native oxide layers: $t(Cr_2O_3) = 2$ nm and $t(SiO_2) = 3$ nm (full lines), $t(Cr_2O_3) = 2$ nm and $t(SiO_2) = 0$ (dashed lines), and $t(Cr) = 2$ nm and $t(SiO_2) = 3$ nm (dotted lines).

8.4 Evidence of the native oxides

For the purpose of the analysis in this section, we have selected Sample B. The precise Permalloy layer thickness $t(Ni_{81}Fe_{19}) = 12$ nm was determined by means of AFM. As will be demonstrated below, only the MOKE measurements with s-polarized incidence were sufficient to provide the characteristics on native oxides.

The rigorous coupled-wave theory implemented as the transfer-matrix approach for anisotropic gratings served as a basis for justifying the application of LMM. Since the LMM curves closely follow those computed by CWT, here we present only the former ones. Extensive simulations for varying $t(Cr_2O_3)$ and $t(SiO_2)$, using literature values of the optical constants [93, 94, 101, 102, 103], give the following most probable values for the native oxide layers, $t(Cr_2O_3) = 2$ nm and $t(SiO_2) = 3$ nm. The simulations also eliminated the possibility of the capping's oxidation into magnetic CrO_2, as well as the post-patterning increase of $t(SiO_2)$ on the uncovered substrate surface between wires.

Figure 8.5 (a) displays the experimental specular-mode Kerr rotation $\theta_{\mathtt{Ks}}^{(0)}$ and ellipticity $\epsilon_{\mathtt{Ks}}^{(0)}$ as functions of the photon energy determined for small values from the ratio $r_{\mathtt{ps}}^{(0)}/r_{\mathtt{ss}}^{(0)} = \theta_{\mathtt{Ks}}^{(0)} - i\epsilon_{\mathtt{Ks}}^{(0)}$ of the off-diagonal to diagonal elements of the specular-mode Jones reflection matrix. To illustrate the sensitivity of the model to $t(SiO_2)$ and to the conversion $Cr \rightarrow Cr_2O_3$, the simulated curves are displayed for the cases without $[t(SiO_2) = 0]$ and with $[t(SiO_2) = 3$ nm$]$ the native oxide on the top of the Si substrate either for the nominal Cr capping thickness, i. e., $t(Cr) = 2$ nm, or for the capping completely oxidized

with the equal thickness $t(Cr_2O_3) = 2$ nm. The best agreement with the experiment requires $t(SiO_2) = 3$ nm and the completely oxidized capping $t(Cr_2O_3) = 2$ nm. The value of $t(SiO_2) = 3$ nm was subsequently confirmed by an ellipsometric measurement on the Si substrate surface area free of Permalloy and Cr (or Cr_2O_3) layer. However, the calculation ignoring either the conversion $Cr \rightarrow Cr_2O_3$ or the presence of SiO_2 [$t(SiO_2) = 3$ nm] produced the same trend in the simulated spectra and it is only the diffracted MOKE which allows to distinguish between the two effects, as will be discussed below.

On the basis of extensive modeling, we suggest that the deviation of the model from the experiment at low photon energies have their origin in the free-electron (Drude, cf. Tab. 6.1) components of the optical-constant spectra. These are sensitive to the effect of the reduced dimensionality in the nanometer-scale structures (e. g., free-electron scattering at interfaces) and to the residual metallic Cr in the capping. Unfortunately, the appropriate corrections cannot be introduced quantitatively without a simultaneous analysis of the unavailable single-layer reference samples.

Figure 8.5 (b) displays the diffracted Kerr rotation $\theta_{\mathtt{Ks}}^{(-1)}$ and ellipticity $\epsilon_{\mathtt{Ks}}^{(-1)}$ as functions of the photon energy determined from the ratio $r_{\mathtt{ps}}^{(-1)}/r_{\mathtt{ss}}^{(-1)} = \theta_{\mathtt{Ks}}^{(-1)} - i\epsilon_{\mathtt{Ks}}^{(-1)}$ of the off-diagonal to diagonal elements of the diffracted-mode Jones reflection matrix. To illustrate the sensitivity of the model to the capping, the simulated curves are displayed for the same three cases as in Fig. 8.5 (a). The account for the completely oxidized capping layer [$t(Cr_2O_3) = 2$ nm] remarkably improves the agreement with the experiment. However, the diffracted MOKE is less sensitive to $t(SiO_2)$, as seen from the "$t(Cr_2O_3) = 2$ nm" curves displayed for both $t(SiO_2) = 0$ and $t(SiO_2) = 3$ nm. The explanation can be found in Eq. (8.2). The contributions of SiO_2 to both $r_{\mathrm{w},jk}$ and $r_{\mathrm{b},jk}$ are comparable, making the sensitivity of their difference weak to $t(SiO_2)$. This fact is essential for the selective account for the effect of the native oxides and thus manifests the uniqueness of the proposed technique even without simultaneous analyses of reference samples.

8.5 Evaluation of the quality of the sharpness of patterning

The principles of monitoring the quality of surfaces and thin films are suitably established using statistical quantities determined by AFM [104, 105] and by optical techniques [106, 107]. The height deviation and autocorrelation length of surface irregularities measured either by AFM or optically foremost produce a difference due to the convolution of the AFM tip with the surface. To evaluate imperfections of the wire-edge parts of surfaces in laterally textured films using AFM is obviously very difficult even with highest-quality tips. For this reason, the MO method proposed here suggests high advantages over AFM.

For the purpose of the analysis in this section, we have selected Sample A. The precise Permalloy layer thickness $t(Ni_{81}Fe_{19}) = 11$ nm was determined by means of AFM. Ac-

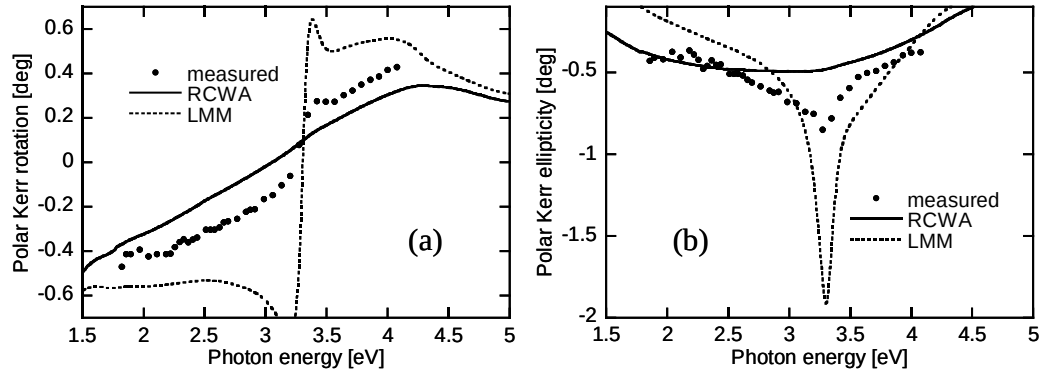

Figure 8.6 Polar Kerr rotation **(a)** and ellipticity **(b)** in the -1st diffraction order for p-polarized incidence. Experimental data (circles) are compared with simulations of CWT (solid curves) and LMM (dotted curves).

cording to the results of Sec. 8.4, the wires are assumed to be deposited on an Si substrate with a 3 nm thick native SiO_2 layer and to be protected by completely oxidized 2 nm thick Cr_2O_3 capping.

As will be demonstrated below, the MOKE measurements with p-polarized incidence contributes by new information from which we will analyze the quality of the sharpness of patterning. Namely, the diffracted MOKE response with p-polarized incidence is strongly affected by random irregularities of the wire-edge parts of the structure's surface, which may cause both the approximate and rigorous models inaccurate. The quality of such magnetic gratings is here evaluated by using one parameter identifying the amount of the edges' internal-diffraction contribution to the diffracted MOKE response in a broad spectral range.

The diffracted MOKE ellipsometric parameters in the -1st diffraction order for p-polarized incidence, the Kerr rotation $\theta_{\mathrm{Kp}}^{(-1)}$ and ellipticity $\epsilon_{\mathrm{Kp}}^{(-1)}$, are determined for small MOKEs as the real and imaginary parts of the ratio of the corresponding amplitude reflection coefficients $r_{\mathrm{sp}}^{(-1)}/r_{\mathrm{pp}}^{(-1)} = \theta_{\mathrm{Kp}}^{(-1)} - i\epsilon_{\mathrm{Kp}}^{(-1)}$. Considering the small values of $r_{\mathrm{pp}}^{(-1)}$

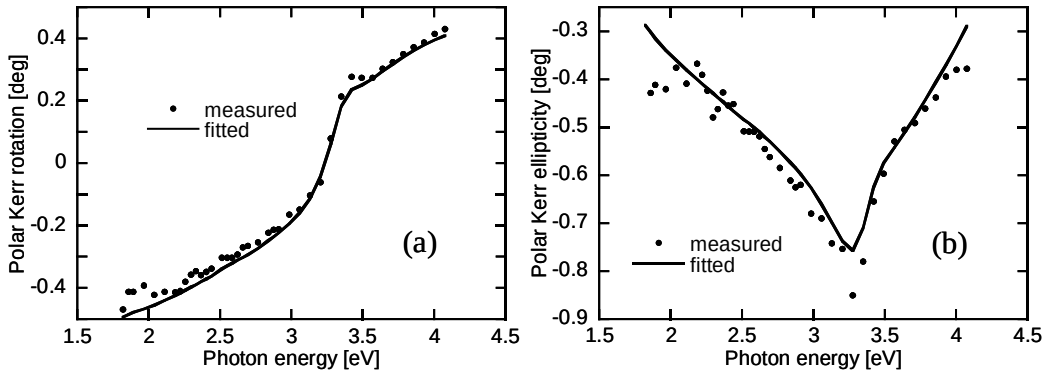

Figure 8.7 Polar Kerr rotation **(a)** and ellipticity **(b)** in the -1st diffraction order for p-polarized incidence. Experimental data (circles) are compared with simulations of the combined CWT–LMM model (solid curves).

in Fig. 8.3, the diffracted MOKE parameters are obviously highly sensitive to $\Delta r_{\mathrm{pp}}^{(-1)}$, or, in other words, both the LMM and CWT produce remarkably different values, as shown in Fig. 8.6 together with the experimental data. Since even the rigorous method does not match the measurement, the most acceptable explanation follows from Fig. 8.2. The AFM picture in Fig. 8.2 (a) indicates considerable irregularities in the wire edges, which naturally reduce the value of $\Delta r_{\mathrm{pp}}^{(-1)}$ in Eq. (8.2) due to diffraction losses. It is straightforward to replace this value by a reduced value

$$\overline{\Delta r_{\mathrm{pp}}^{(-1)}} = \eta(\lambda)\Delta r_{\mathrm{pp}}^{(-1)} \tag{8.3}$$

and to determine the wavelength-dependent function $\eta(\lambda)$ by using real values expected between 0 and 1. In the case of our samples, however, no wavelength dependence was detected. Each sample in the set was successfully characterized with a constant value of η by applying the least-square method in a one-parameter fit of the diffracted MOKE rotation and ellipticity. We refer to this parameter as the "quality factor of the grating with respect to the wire edges," and to the new theoretical approach as the "combined CWT–LMM model." Analogous to the height deviation and autocorrelation length of random irregularities of non-patterned surfaces, which are connected with the reduction of the reflectance due to diffraction losses, the η-factor describes a reduction of the diffracted light according to similar principles. The value of $\eta = 1$ corresponds to ideal periodical smooth edges, whereas $\eta = 0$ implies that no edge effects are observed. The realistic value according to the diffracted MOKE parameters measured on Sample A was found 0.53, with the fitted spectrum displayed in Fig. 8.7. The same procedure applied to Sample B of obviously higher quality, with the AFM picture displayed in Fig. 8.2 (b), yielded the value $\eta = 0.70$.

8.6 Conclusions for Chapter 8

In this chapter, the combined experimental and model optical and magneto-optical spectroscopy in the 0th and -1st diffraction orders was applied to analyze Permalloy wire gratings deposited on Si substrates and protected by Cr capping. The most probable values of the thicknesses of the surface native oxides Cr_2O_3 and SiO_2 were deduced with a demonstration of the high sensitivity and uniqueness of the technique. The simulations employed the simple and efficient local modes method, the adequacy of which had been confirmed by a nearly perfect agreement with the rigorous analysis. The agreement between the model and experiment indicates the consistency of the carefully selected optical constants of the materials involved including those for Permalloy. The approach forms the basis for the extension of the scatterometric techniques to magnetic nanostructures and could be applied to sensitive and non-destructive aging studies of magnetic and MO recording disks and magnetic random access memory chips.

Moreover, diffracted MO spectroscopy with p-polarized incidence was successfully applied to evaluate the quality of periodically patterned magnetic structures with respect to the sharpness of patterning, in literature referred to as line-edge roughness. The method appears to be profitable since the wire edges measured by AFM can hardly be analyzed statistically, as it is conventional in the case of flat surfaces. The principle can be applied for any optical or MO configuration where the edge effects are not negligible compared to the surface or thin-film response. The results also suggest advantageous possibilities in other applications, e. g., analyzing the non-linear MO effect or photo-elastic and magneto-elastic effects, since any effect usually negligible may be enhanced in a particular experimental arrangement.

Chapter 9

Further magneto-optic analyses

In Chapter 8 we have demonstrated a complex analysis of one particular set of one-dimensional gratings formed as imperfect ferromagnetic wires; the imperfection was studied related to the developed native oxides and the line-edge roughness. In this chapter we will focus our attention to the theoretical study of the general magneto-optic spectroscopic properties of ideal one- and two-dimensional gratings (Secs. 9.1 and 9.2, respectively). Finally, in Sec. 9.3 we will conclude our work on magneto-optics by presenting two experimental examples and our try of their theoretical explanation, resulting to suggestions of future perspectives.

9.1 Numerical analysis of magneto-optic spectroscopic response of periodic ferromagnetic wires

In this section we will theoretically analyze the diffraction response of one-dimensional grating made as perriodic array of ferromagnetic wires located on a silicon substrate, without capping and any additional interlayer. We will keep the periodicity and width of wires constant and analyze the sensitivity of magneto-optic (MO) spectroscopy to the increasing depth of the periodic medium. For better understanding of diffraction effects, we will also compare the simulation spectra with calculations performed on a continuous (unpatterned) thin film with properties identical to those of the wires (material and thickness).

First, we will use the energy reflectance coefficients to demonstrate the polarization-sensitive spectrophotometric response of an anisotropic diffraction grating consisting of a single anisotropic periodic layer sandwiched by two uniform isotropic ambient semi-infinite media. For the layer we have chosen an optically isotropic ferromagnetic permalloy ($Ni_{81}Fe_{19}$) whose anisotropy is induced by an externally applied uniform magnetic field. As well as in Chap. 8, we assume the application of magnetic field with sufficient magnitude to saturate magnetization. This constitutes an anisotropic periodic structure characterized by a periodic permittivity tensorial function taking on only two values, one

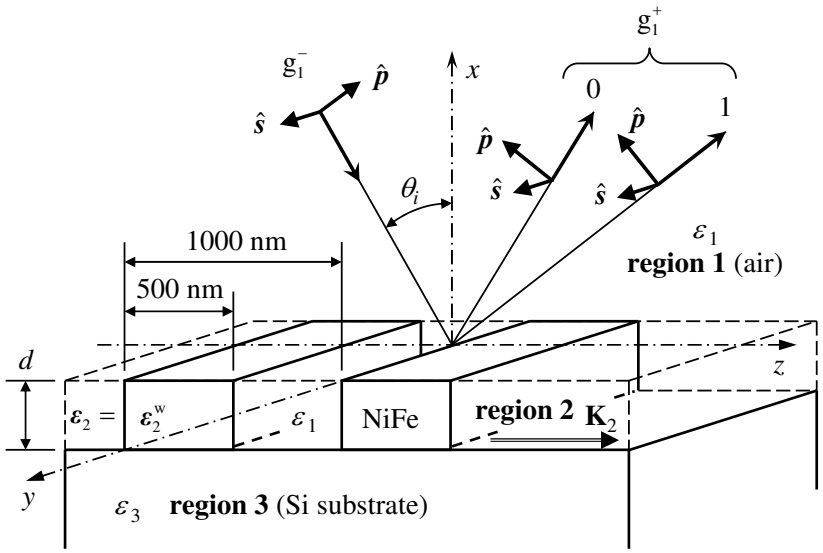

Figure 9.1 The periodic structure in the configuration for planar diffraction according to the numerical example. The permalloy wires are deposited on a Si substrate with the wire periodicity of 1000 nm, wire width of 500 nm, and wire thickness, d, assuming the values of 20, 40, 60, and 100 nm. Two principal polarization modes, s and p, are indicated for the incident wave and for the reflected zeroth and first diffraction orders.

of the patterned periodic ferromagnetic wires,

$$\boldsymbol{\varepsilon}_{\mathrm{w}} = \begin{bmatrix} \varepsilon_1 & i\varepsilon_2 & 0 \\ -i\varepsilon_2 & \varepsilon_1 & 0 \\ 0 & 0 & \varepsilon_1 \end{bmatrix}, \tag{9.1}$$

and second of the gap medium between them. In this manner we apply the polar-oriented saturation field whose permittivity tensor can be split into the symmetric and the antisymmetric part. The symmetric part is due to the optical isotropy represented by a multiple of the unit matrix, while the antisymmetric part represents the effect of magnetization parallel to the z-axis of our Cartesian system and perpendicular to the interfaces.

The periodic structure is shown in Fig. 9.1. The permalloy wires are deposited on a Si substrate with the periodicity of 1000 nm. The lateral width of a wire is set to 500 nm, and the wire thickness, d, assumes the values of 20, 40, 60, and 100 nm. The plane of incidence is chosen normal to the axes of the wires. Note that in the limit of normal incidence the s-polarization remains parallel to the wire axes while the p-polarization becomes parallel to the grating vector. In the absence of magnetization the s- and p-polarizations represent the eigenmodes of the periodic structure in all diffraction orders.

As mentioned above, we will start the analysis with the limiting wire width of 1000 nm corresponding to a continuous film. The reflectance spectra in the continuous film are displayed in Fig. 9.2 (a, c). We observe that the effect of the Si substrate decreases with increasing d of the strongly absorbing metallic film. This is manifested by the absence of the Si characteristic spectral features at higher d. It is remarkable that at higher d

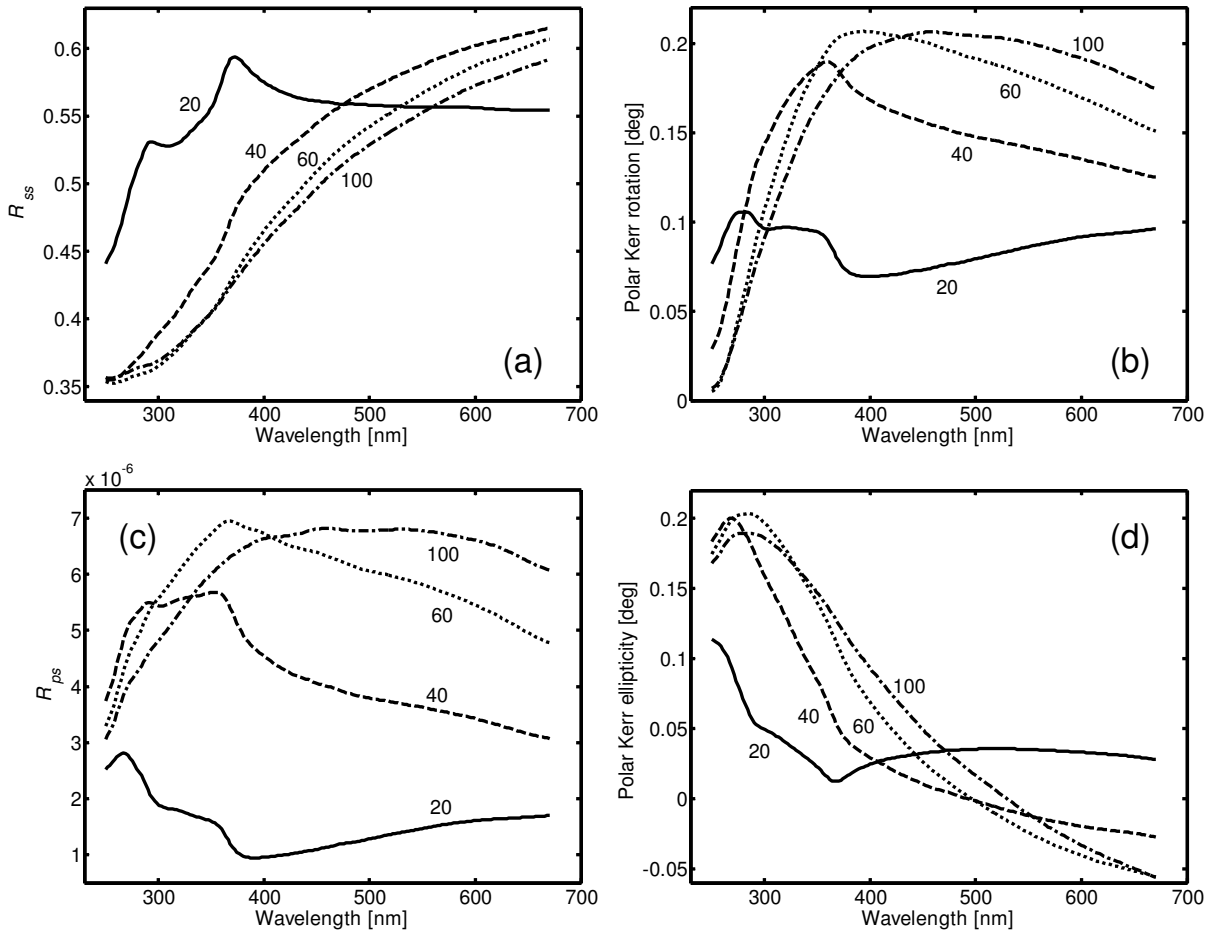

Figure 9.2 The energy reflectance coefficients R_{ss} (a) and R_{ps} (c) and the polar magneto-optical Kerr rotation (b) and ellipticity (d) calculated on the permalloy gratings with a limiting wire width of 1000 nm, corresponding to a continuous film. Solid, dashed, dotted, and dash-dotted curves correspond to the film thicknesses of 20, 40, 60, and 100 nm.

the substrate effect is better preserved in the off-diagonal reflectances, $R_{ps}^{(n)}$, than in the diagonal ones, $R_{ss}^{(n)}$, suggesting that $R_{ps}^{(n)}$ has higher in-depth sensitivity than $R_{ss}^{(n)}$ does.

Next, in Fig. 9.2 (b, d) we show the spectroscopic response in terms of the MO ellipsometric quantities, i. e., MO polar Kerr azimuth rotation, θ_K, and MO polar Kerr ellipticity, ϵ_K, defined for the incident s-polarized wave as

$$\Phi_{Ks}^{(n)} = \frac{r_{ps}^{(n)}}{r_{ss}^{(n)}} = \frac{\tan\theta_K^{(n)} - i\,\tan\epsilon_K^{(n)}}{1 + i\,\tan\theta_K^{(n)}\,\tan\epsilon_K^{(n)}} \approx \theta_K^{(n)} - i\epsilon_K^{(n)}, \tag{9.2}$$

where $\Phi_{Ks}^{(n)}$ denotes the complex polar MO Kerr effect (MOKE) of the nth diffraction order. In the MOKE spectra we again observe the reduction of the substrate contribution with the magnetic film thickness.

Finally we will show the response of the studied ferromagnetic grating displayed in Fig. 9.1 with the varied thickness of its wires. Figure 9.3 displays the reflectance spectra in the zeroth, $R_{ss}^{(0)}$ and $R_{ps}^{(0)}$, and the first, $R_{ss}^{(1)}$ and $R_{ps}^{(1)}$, diffraction orders. The main

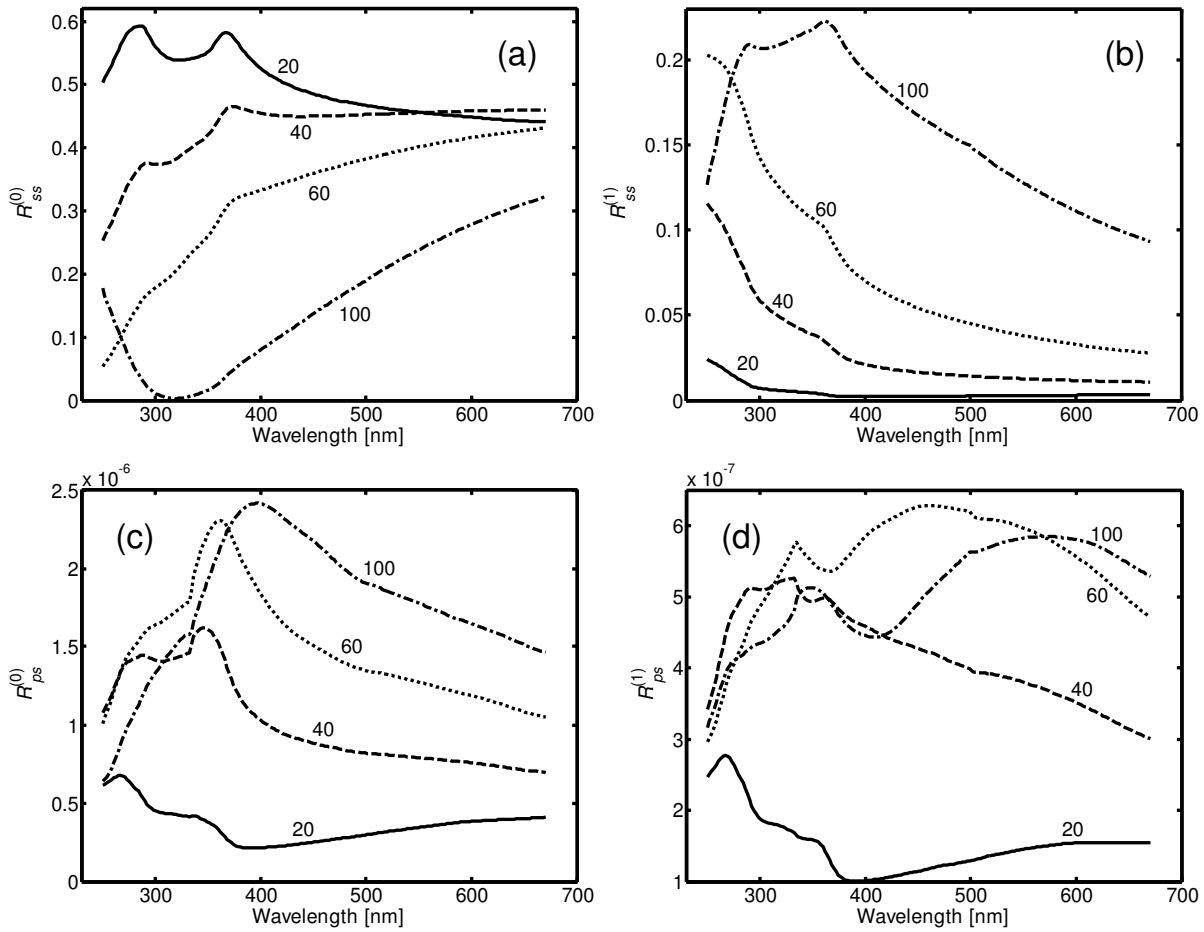

Figure 9.3 The diagonal (a, b) and off-diagonal (c, d) energy reflectance coefficients in the zeroth (a, c) and first (b, d) diffraction orders calculated on the permalloy gratings displayed in Fig. 9.1. Solid, dashed, dotted, and dash-dotted curves correspond to the wire thicknesses of 20, 40, 60, and 100 nm.

effect produced by the transition from the continuous film to the grating consists in the amplitude reduction corresponding to the reduced highly absorbing and consequently highly reflecting area of the metallic surface. Upon the increase of the wire thickness, d, the features originating from the Si substrate do not disappear as in the case of the continuous film. The MOKE response is made of the amplitude superposition of the wire reflection, uncovered substrate reflection, and diffraction on the wire edges. The edge diffraction effect is more pronounced in $R^{(0)}_{ps}$ than in $R^{(0)}_{ss}$. The value of $R^{(0)}_{ss}$ decreases with the film thickness while $R^{(1)}_{ss}$ increases. This indicates the transfer of energy from the zeroth to the first diffraction order. The spectra of the off-diagonal $R^{(0)}_{ps}$ and $R^{(1)}_{ps}$ are less sensitive to the contribution from the uncovered substrate being dominated by the reflection on the wire surface and wire edges. The comparison of $R^{(0)}_{ps}$ with R_{ps} on the continuous film shows the same trends, i. e., we observe an increase with d but instead of the saturation with d due to a small penetration depth observed in the continuous film we have the enhanced effect of the edge diffraction. This effect can also be seen in the

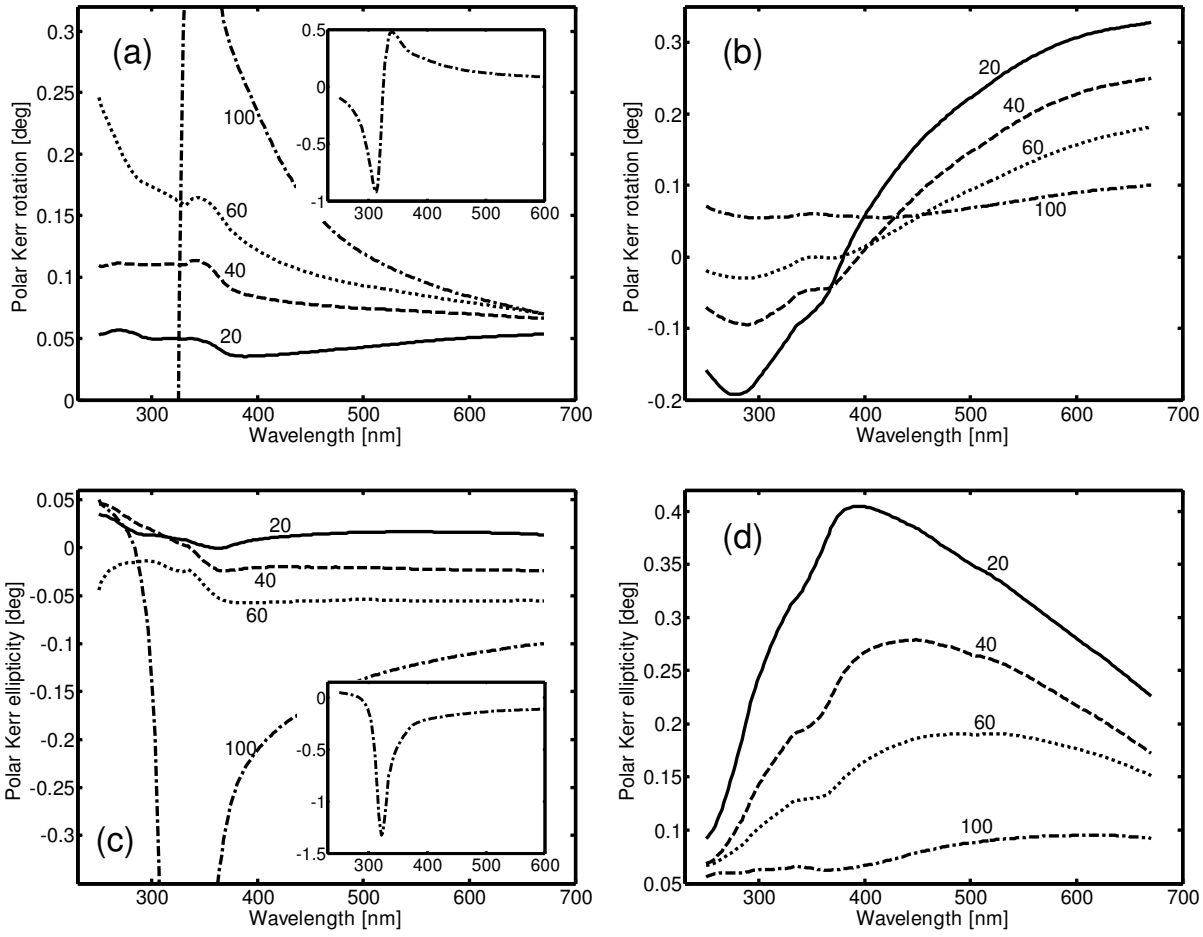

Figure 9.4 The polar magneto-optical Kerr rotation (a, b) and ellipticity (c, d) in the zeroth (a, c) and first (b, d) diffraction orders calculated on the permalloy gratings displayed in Fig. 9.1. Solid, dashed, dotted, and dash-dotted curves correspond to the wire thicknesses of 20, 40, 60, and 100 nm.

first diffraction order, $R_{ps}^{(1)}$, but the explanation is less straightforward.

The corresponding MOKE spectra are displayed in Fig. 9.4. Both the reduction of $R_{ss}^{(0)}$ and the increase of $R_{ps}^{(0)}$ with d demonstrated in Fig. 9.3 result in an increase of $\left|\Phi_{Ks}^{(0)}\right|$ according to the relation

$$\left|\Phi_{Ks}^{(0)}\right| = \left(\frac{R_{ps}^{(0)}}{R_{ss}^{(0)}}\right)^{1/2} . \tag{9.3}$$

This increase is more important in $\theta_K^{(0)}$ than in $\epsilon_K^{(0)}$. The anomalous structure centered near the wavelength of 320 nm observed at $d = 100$ nm originates from the reduced value of $R_{ss}^{(0)}$. On the other hand, the $\theta_K^{(1)}$ amplitude decreases with d due to the enhanced $R_{ss}^{(1)}$ according to

$$\left|\Phi_{Ks}^{(1)}\right| = \left(\frac{R_{ps}^{(1)}}{R_{ss}^{(1)}}\right)^{1/2} . \tag{9.4}$$

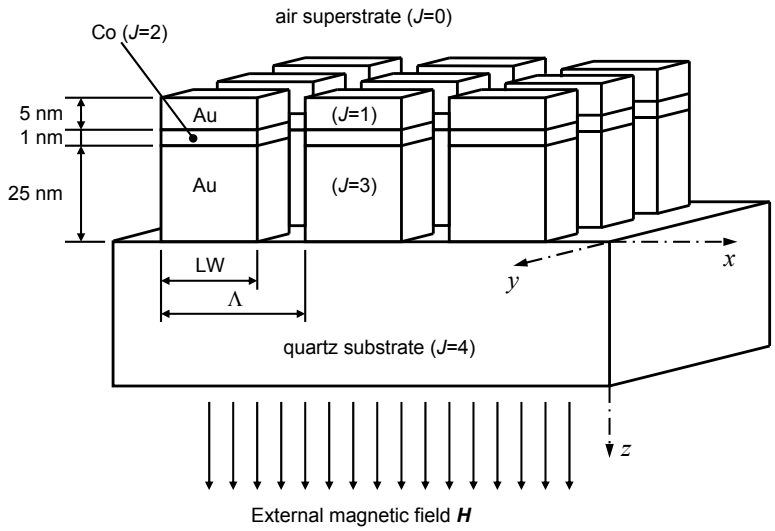

Figure 9.5 Binary magnetic grating patterned from an ultrathin film sandwich Au(5 nm) / Co(1 nm) / Au(25 nm) deposited on a quartz substrate. The magnetization in the Co elements is oriented normal to the grating surface.

9.2 Numerical analysis of magneto-optic spectroscopic response of biperiodic multilayered ferromagnetic dots

In this section we will present polar magneto-optical Kerr effect (MOKE) spectra in the visible and near-UV range on hypothetical biperiodic arrays of square and circular dots patterned in ultra-thin Au/Co/Au sandwiches on quartz substrates. The simulations of the selected model cases will demonstrate high numerical efficiency as well as remarkable sensitivity of MOKE spectroscopy to all the adjusted array parameters and the shape of the array elements. As a realistic model corresponding to the contemporary lithography resolution, we choose a two-dimensional array system with subwavelength dimensions of individual elements. A schematic picture of the studied arrays is displayed in Fig. 9.5. The spectroscopic response will be presented in terms of the MO ellipsometric parameters.

We will apply the modeling algorithm to the numerical analysis of 2D rectangular arrays with square (AS) and circular (AC) dot elements with subwavelength periodicities. For AS, we choose squares with the sides parallel to the x- and y-axes having the dimensions 10×10 nm^2 (AS1) and 20×20 nm^2 (AS2) with the periodicities (also parallel to the x- and y-axes) $\Lambda = 15$ nm (AS1) and 30 nm (AS2), respectively (Fig. 9.5). For AC, the periodicities parallel to the x- and y-axes are same, i.e., $\Lambda = 15$ nm (AC1) and 30 nm (AC2), with the surface area of 100 nm^2 (AC1) and 400 nm^2 corresponding to that of AS1 and AS2, respectively. Each element is a sandwich Au(5 nm)/Co(1 nm)/Au(25 nm) on a fused quartz substrate for all the samples. The uniform saturation magnetization in Co is perpendicular to the interfaces and fixed to the positive z-axis.

For the selected Λ and element shape and area we now compute the polar Kerr rotation (PKR), $\theta_{K\mathtt{s(p)}}$, and polar Kerr ellipticity (PKE), $\theta_{K\mathtt{s(p)}}$, for both the s- and p-polarized incident (i) waves. The plane of incidence is the zx-plane. At the zero angle of incidence the wavevector of the incident wave is parallel to the z-axis. For small MO azimuths and ellipticities of PKR and PKE, we again have

$$\theta_{K\mathtt{s}} \approx -\frac{r_{\mathtt{ps}}^{(00)}}{r_{\mathtt{ss}}^{(00)}}, \tag{9.5}$$

$$\theta_{K\mathtt{p}} \approx \frac{r_{\mathtt{sp}}^{(00)}}{r_{\mathtt{pp}}^{(00)}}, \tag{9.6}$$

where the 00th diffraction order amplitude reflection coefficients $r_{\mathtt{ss}}^{(00)}$, $r_{\mathtt{sp}}^{(00)}$, $r_{\mathtt{ps}}^{(00)}$, and $r_{\mathtt{pp}}^{(00)}$ represent the central elements in proper sub-matrices of the reflection matrix of the three-layered biperiodic structure.

The simulations are performed in the spectral range of 1.6–5.1 eV where the optical and MO constants obtained on the corresponding continuous-film multilayer are available [108], [109]. We have limited ourselves to the 00th diffraction order, which is the only observable order for the chosen subwavelength periodicity.

Partially using Li's Fourier factorization rules, we have achieved very fast convergence of our algorithm. This is of practical importance since the computer time and capacity required for two-dimensional gratings increase rapidly with the required maximum orders of Fourier components, $m_{\max}$ and $n_{\max}$, parallel to x- and y-axes, respectively. The order of the matrices involved then becomes $2(2m_{\max}+1)(2n_{\max}+1)$. To illustrate the convergence speed, Fig. 9.6 shows the spectra for three sets of $m_{\max} = n_{\max}$. For the subsequent simulations we therefore choose $m_{\max} = n_{\max} = 8$, a well justified value.

For the plane of incidence parallel to any of the mutually orthogonal periodicity axes, we have observed no cross-polarization effect in both PKR and PKE at zero magnetization in the whole range of angles of incidence. Therefore, the spectra with saturated magnetization correspond to the pure MO effect. Two components can be distinguished. The first is due to the MO effect of the continuous-film sandwich reduced by the grating filling factor [given by $w = (\text{linewidth})^2/\Lambda^2$ in the case of square dots]. The second can be assigned to MO diffraction. Since all the samples are chosen with their filling factors equal, the second component can be identified by comparing separately AS1 with AS2 and AC1 with AC2, and vice versa.

In normal incidence, PKR and PKE spectra for all the samples are displayed in Fig. 9.7 along with spectra computed for a continuous-film sandwich. The curves exhibit similar spectral dependences, having a steep change in PKR and a corresponding positive peak near the plasma edge region of Au at 2.45 eV. In the range of higher photon energies, the curves mainly depend on the period, whereas the slope of the plasma-edge anomaly in PKR together with its position in PKE only depends on the shape of dots. The differences at low photon energies can be explained by MO phase changes introduced by diffraction

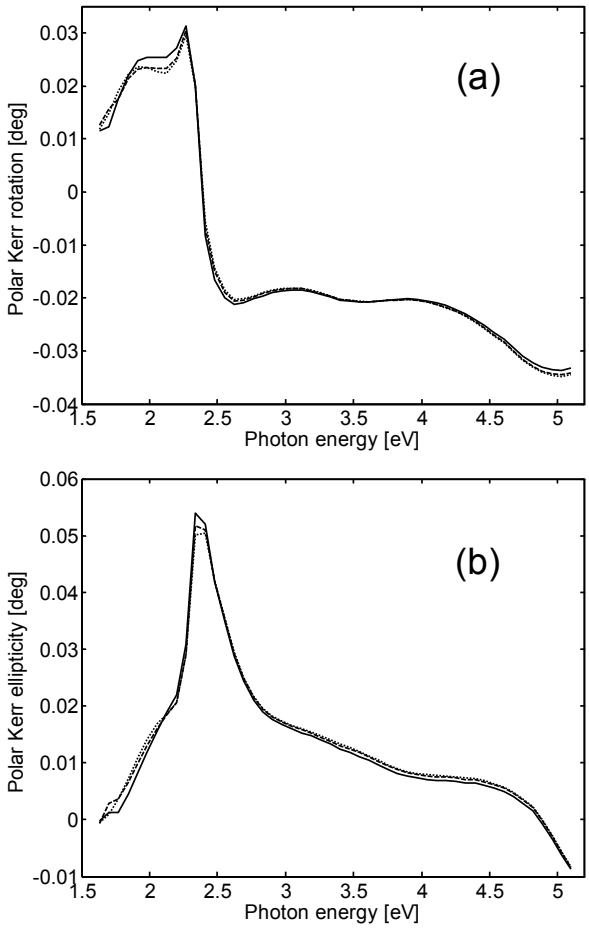

Figure 9.6 Number of Fourier x- and y-components, $m_{\max} = n_{\max}$, included in the simulation procedure of the normal-incidence polar Kerr rotation (a) and ellipticity (b) in a two-dimensional rectangular array of squares of 10×10 nm^2 with x- and y-periodicities of 15 nm patterned in a Au/Co/Au sandwich. The solid, dashed, and dotted curves represent $m_{\max} = n_{\max}$ equal to 4, 8, and 12.

which manifest themselves by a specific transformation of the PKE towards the PKR, and vice versa. In this process the diffracted PKR curve comes near the PKE curve of the continuous film, while the diffracted PKE curve comes near the PKR curve of the continuous film with the opposite sign.

At oblique angles of incidence, the MO response becomes polarization sensitive. The most remarkable changes are observed at an angle of incidence of 60° for a p-polarized incident wave (Fig. 9.8). Similar to the case of normal incidence (Fig. 9.7), the spectra above the photon energy of 2.5 eV are the most sensitive to Λ. At lower energies both PKR and PKE strongly depend on both the profile (circle or square) and Λ. This feature may find use in MO metrology of the lithographic fabrication of magnetic nanostructures. The strongest anomalies are observed on the short-period 2D arrays of circles (AC1).

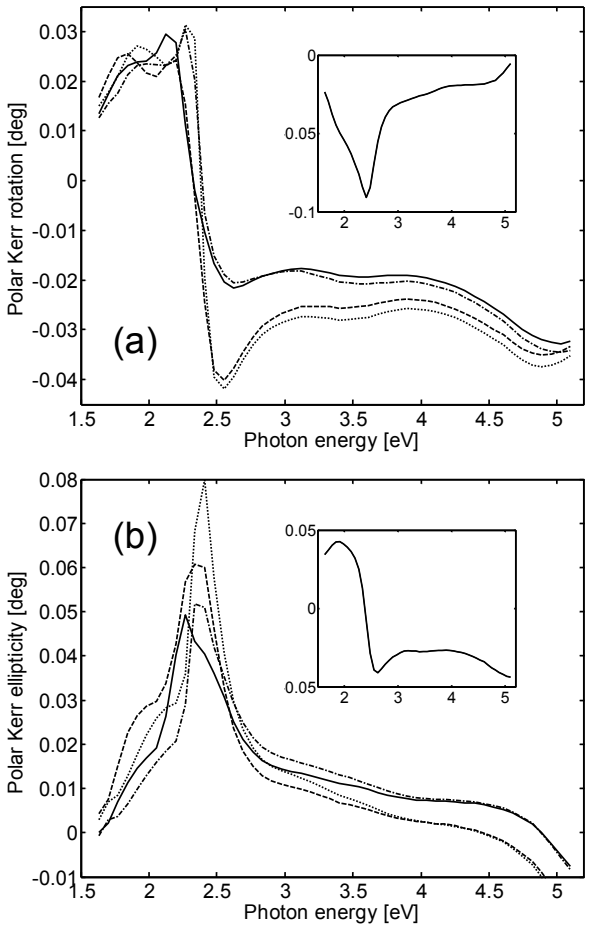

Figure 9.7 Computed normal incidence polar Kerr rotation (a) and ellipticity (b) spectra in two-dimensional periodic arrays of squares AS1 (solid) and AS2 (dash) and circles AC1 (dash-dot) and AC2 (dot). The insets show spectra for the corresponding continuous-film Au(5 nm) / Co(1 nm) / Au(25 nm) sandwich on a quartz substrate.

9.3 Two more experimental examples of applying magneto-optic spectroscopy

In this section we apply MO spectroscopy to two sets of magnetic gratings, slightly different from those presented in Chap. 8. First of them is a partially etched uncovered Permalloy(32 nm)/Si structure with the period of 1000 nm and wire linewidth of 307 nm. The nearly-normal-incidence specular MOKE response of a chosen sample etched up to 24 nm of depth is displayed in Fig. 9.9 (a). Unfortunately, there is not available literature permittivity data of oxide formed from Permalloy, so that a possible native oxide overlayer had to be excluded from calculation. Moreover, this measurement was done with applied out-of-plane magnetic field of only 0.4 T which did not probably saturate the sample completely. Both effects could therefore create the discrepancies visible in parts of the presented spectral dependences.

The second set consists of partially oxidized Ni wires deposited on a thermally oxidized

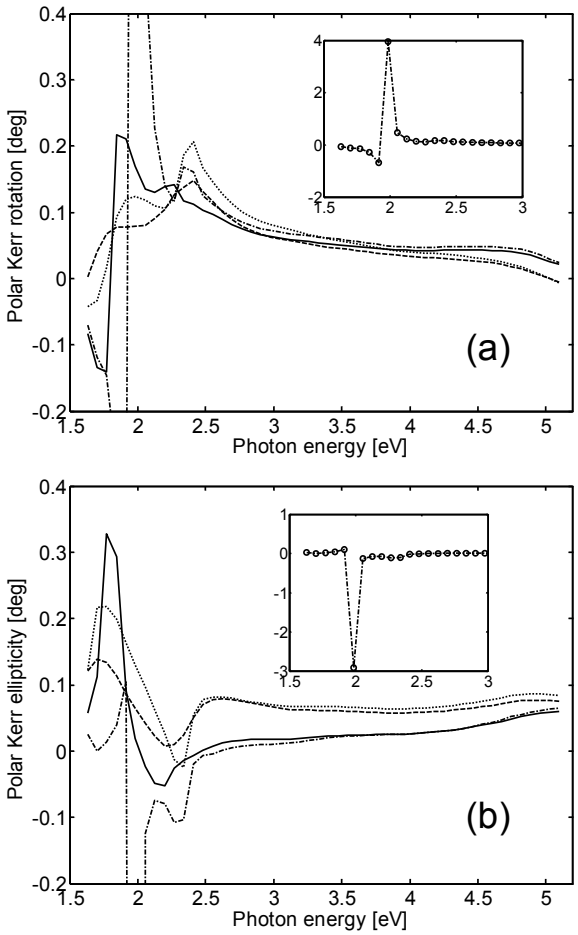

Figure 9.8 Computed polar Kerr rotation (a) and ellipticity (b) spectra for the incidence of a p-wave at 60° on two-dimensional periodic arrays of squares AS1 (solid) and AS2 (dash) and circles AC1(dash-dot) and AC2 (dot) patterned from an Au(5 nm) / Co(1 nm) / Au(25 nm) sandwich. The insets show the spectra of AC1 in reduced scale.

system SiO_2(500 nm)/Si. The nearly-normal specular MOKE response of a sample with the wire thickness of about 40 nm is displayed in Fig. 9.9 (b). Here the deep SiO_2 interlayer entails significant interference effects which considerably increase the sensitivity of the approach. The reasonable correspondence between the simulation and the experiment visible in the figure was achieved by assuming that Ni was partially being oxidized already during the deposition process. The composition of the $Ni_{52}(NiO)_{48}$ structure uniform within depth was determined by a fitting procedure involving both MOKE and purely optical spectro-ellipsometric data. Moreover, the MO effect had to be reduced down to 25 %, which cannot be explained by unsaturated polar magnetization. The most probable explanation assumes that a possible nanocrystalline character of the $Ni_{52}(NiO)_{48}$ structure reduces the MO constants of the system as the whole.

According to the interesting results of the two demonstrative experimental examples presented in this section, we can conclude that MO spectroscopy, though only applied in the specular mode, suggests new, highly advantageous potentialities. We have demon-

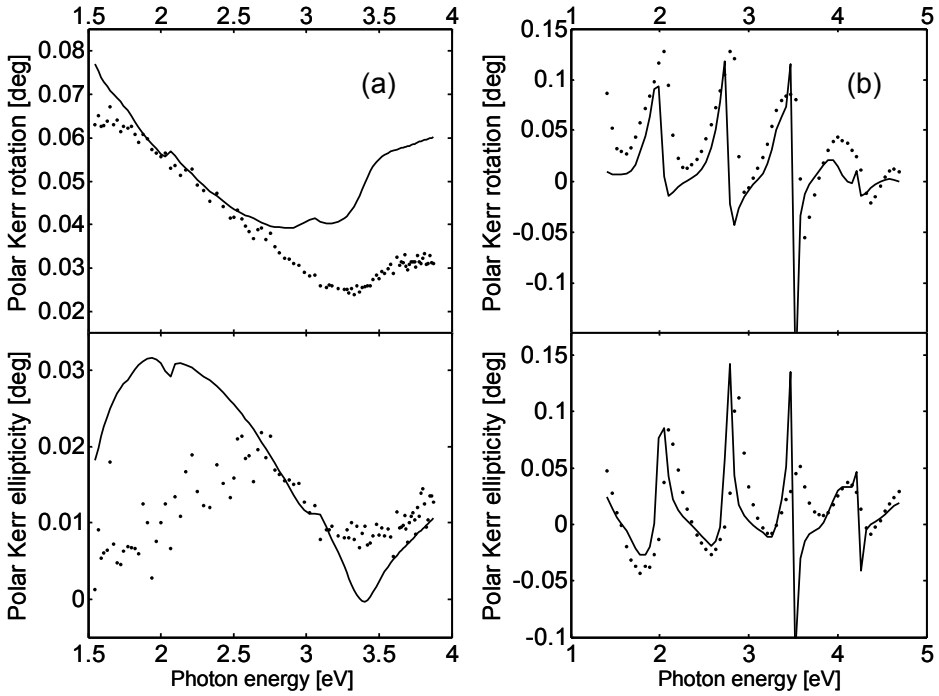

Figure 9.9 Specular MOKE spectra with nearly-normal incidence obtained on a partially etched $\mathrm{Permalloy}(32\ \mathrm{nm})/\mathrm{Si}$ structure (a) and Ni wires on an $\mathrm{SiO_2}(500\ \mathrm{nm})/\mathrm{Si}$ structure (b). Experimental data (points) are compared with coupled-wave simulations (curves).

strated the possibility to employ MO spectroscopy for observing structural features such as unsaturated magnetization, material composition, or particular crystalline properties caused by imperfect deposition processes. The approach can obviously be arranged for investigating arbitrary surface material changes due to aging or thermal treating as well as for line-edge roughness or linewidth roughness control in industrial production. After an appropriate generalization, the theoretical model demonstrated in this thesis could be also applied to binary magnetic gratings with arbitrary magnetization distribution such as arrays of dots with vortex spin structures.

Chapter 10

Conclusions and perspectives

The aim of this thesis was the fundamental description of the optical diffraction on laterally patterned generally anisotropic periodic nanostructures, referred here to as gratings, the creation of an original, numerically highly efficient model, and various theoretical and experimental applications to particular grating systems.

Among the applications, the most important in contemporary industry is the characterization of geometric properties of lithographic patterning. The properties of particular interest are the optical critical dimensions (and how they differ from those intended by the manufacturer or from those measured by other, conventional approaches such as AFM or SEM), the line-edge roughness (which is conventionally measured by AFM, SEM, or optical Fourier transform techniques), and other features due to imperfect fabrication or aging (such as oxidation process, deposited crystalline structure, or just variation in the thicknesses of layers). According to these demanding tasks we have briefly reviewed literature works performed on the both conventional and optical characterization techniques (Chap. 2) with the explanation of their mutual advantages. The review is completed with the reference to our original papers written on this subject; the results published in those papers approximately match the contents of Chaps. 7 and 8.

Besides the applications related to lithographic quality control mentioned above, the theoretical analysis of the optical diffraction response is also of high importance, because various grating systems similar to those studied here are fabricated for particular optical applications or just as new metamaterials based on photonic band-gap structures. Such systems are adjusted by diffraction calculation before they are suggested for production, and hence developing numerically efficient algorithms and studying spectrally resolved optical properties belong to important contributions of this thesis. For this reason, Chaps. 3 and 4 were devoted for the introduction to the optical diffraction response with description of related parameters and the principles of the most used theoretical diffraction approach with our original numerical implementation.

The properties of our theoretical approach such as numerical efficiency were presented jointly with the results of analyses to which the approach was used, i. e., scatterometry

based on spectroscopic ellipsometry combined with magneto-optic spectroscopy on periodical nanostructures made of various materials and with various shapes. The conclusions from this extended field are as follows.

We have described the electromagnetic-coupled-wave implementation referred to as the Airy-like series in detail to increase the clarity of monitoring optogeometric parameters of gratings by means of scatterometry, particularly with respect to the convergence properties of optical critical dimensions (approximation such as the truncation order of Fourier series or the number of slices of a nonrectangular-wire grating). We have demonstrated that the use of Li's Fourier factorization rules considerably enhanced the convergence properties of both the simulated ellipsometric parameters and the extracted dimensions, though an improvement based on generalizing the factorization rules would provide better results for wires with curved edges. In the case of the gratings made of transparent quartz and semiconductive silicon, the agreement between the experimental data and the fitted parameters was nearly perfect, obviously indicating the high relevance of the model assuming a rectangular-relief structure. In the case of the tantalum grating, however, slight discrepancies were observed in the short-wavelength part of the range of interest, even though a top native Ta_2O_5 overlayer and a non-ideal shape of wires with curved edges were considered. The method could be improved by generalizing the model assuming more aspects of the reality, the most important of which are the optical constants of Ta to be monitored more precisely in a broader spectral range with an energy reflectance measurement included, the surface roughness of tantalum for which ellipsometry is sensitive, and/or a more general shape of the tantalum wires with higher-order parameters of the Taylor series.

Specular-mode spectroscopic ellipsometry was also demonstrated as a highly sensitive technique detecting both the geometrical and material properties of sinusoidal surface-relief gratings. In the case of shallow gratings this sensitivity is realized via resonance effects in the region of Wood anomalies. The ellipsometric measurement was applied to extract features of a transparent grating with a sine-like relief located on a structure of polymer/glass. AFM was used as a complementary technique to minimize the possibility of a mutual correlation between the parameters to be extracted. The shape and amplitude of the relief function, as well as the quality of the optical matching between the polymer and the glass, were determined successfully. Further refinement of theoretical considerations, e.g., a slightly irregular periodicity, the finite beam aperture, or an extension of the number of input parameters, will enhance the reliability of the inverse problem solution.

The coupled wave theory with the Airy-like series algorithm was also applied for the case of two-dimensional gratings. Remarkably effective convergence properties of the theory were demonstrated on a sample of a binary array of circular holes in a silicon wafer. Microspot spectroscopic ellipsometer was utilized to measure the optical response. By means of scatterometry, two geometrical parameters were extracted from the ellipsometric measurement, namely the diameter and the depth of the holes, while the square period

of the array was fixed at the value intended by the manufacturer. The values obtained from fitting were compared with dimensions visible on a SEM picture with reasonable agreement. While the holes' diameter is provided by both methods in very good correspondence, the holes' depth seems to be more accurately determined by SEM, because the ellipsometric simulations do not take into account the curved bottom surface of the real holes. This weak point could be avoided by generalizing the coupled-wave algorithm.

Then, results of magneto-optic spectroscopic scatterometry were demonstrated. A set of periodic Permalloy wires deposited on silicon substrates and protected by chromium capping layer was analyzed. Besides examples of measurements and simulations of spectroscopic ellipsometry and reflectometry, two main original results of magneto-optic spectroscopy have been obtained. First, the native oxides existing on the top of wires and substrates were very sensitively monitored by measuring the magneto-optic Kerr effect with `s`-polarized incident light. Different diffraction orders (either 0th or -1st) were shown to be sensitive to different oxides (existing either on the top of capping or below wires). Second, the quality of the sharpness of patterning was monitored by the diffracted Kerr effect with `p`-polarized incident light. For this purpose, a new parameter of quality was defined, whose concrete values received on different samples were successfully compared with an AFM analysis. This parameter can be identified with the line-edge roughness usually monitored only by conventional techniques. Accordingly, the MO spectroscopy is shown to be a proper tool for monitoring aging effects and fabrication imperfections of magnetically ordered patterned nanostructures.

Finally, further magneto-optic results were presented in Chap. 9. From detailed theoretical analyses of the spectroscopic properties of one- and two-dimensional magnetic gratings it is obvious that a great amount of information is present in the diffracted spectrum of a sufficiently broad range. Similarly, two experimental examples of applying magneto-optic spectroscopy revealed high sensitivity to the parameters of gratings with special fabrication geometries (either partial etching or the deposition on a thicker transparent interference-causing interlayer). The high sensitivity of the magneto-optic response to all the geometrical parameters was evidenced. Moreover, the parameters were shown most probably uniquely distinguishable, though they were not exactly determined in the presented examples. New advantageous potentialities of our technique are thus suggested, e. g., the possibility to observe unsaturated magnetization, material composition, or particular crystalline properties (for example caused by imperfect deposition).

According to the results presented in Chaps. 7, 8 and 9, we certify that scatterometry based on the mentioned spectroscopic techniques is a highly sensitive and accurate tool for monitoring metrologic, topographic, and other features of laterally patterned periodic systems. Its main advantages are nondestructivity, independence on contact mechanical elements, and convenience of application for *in situ* monitoring.

Besides our aimed further development of the diffraction theory and future applications in non-destructive diagnostics of newly designed nanostructures, we also assume

usability of our approach to suggest and create novel optical tools (such as better wire-grid polarizers, optical or magneto-optic isolators, or grating-based phase plates) and new artificial metamaterials (such as the photonic crystals with photonic band structures of unlimited complexity and tunability, which is in considerable contrast to the difficult manageability of electronic states). It is also desirable to appreciate the capability of the formalism to deal with generally anisotropic media, e. g., magnetically ordered materials forming magneto-photonic crystals, because they offer further opportunities such as highly efficient optical isolation, unidirectional and time-reversal asymmetry, nonreciprocity causing a broad range of mode group velocities down to frozen modes (usable for signal delay lines or optical buffers for data storage), or magneto-optically induced second- and third-harmonic generation.

References

[1] R. W. Wood, Phil. Mag. **4**, 396 (1902).

[2] F. Abeles, Ann. Phys. Paris **5**, 596 (1950).

[3] J. Lafait, T. Yamaguchi, J. M. Frigerio, A. Bichri, and K. Driss-Khodja, Appl. Opt. **29**, 2460 (1990).

[4] D. Marcuse, *Light Transmission Optics* (Bell Laboratories Series, Van Nostrand Rienhold Company, New York, 1972).

[5] D. Marcuse, *Theory of Dielectric Optical Waveguides* (Academic Press, New York and London, 1974).

[6] P. K. Tien, Rev. Mod. Phys. **49**, 361 (1977).

[7] M. Born and E. Wolf, *Principles of Optics, Electromagnetic Theory of Propagation Interference and Diffraction of Light, Sixth (Corrected) Edition* (Cambridge University Press, Cambridge, New York, Melbourne, 1997).

[8] R. M. A. Azzam and N. M. Bhashara, *Elipsometry and Polarized Light* (North Holland, Amsterdam-New York-Oxford, 1997).

[9] A. K. Zvezdin and V. A. Kotov, *Modern Magnetooptics and Magnetooptical Materials* (Institute of Physics Publishing, Bristol and Philadelphia, 1997).

[10] S. Visnovsky, Czech. J. Phys. B **36**, 1424 (1986).

[11] T. H. P. Chang, M. Mankos, K. Y. Lee, and L. P. Muray, Microelectron. Eng. **57-58**, 117 (2001).

[12] Y. Sohda, H. Ohta, F. Murai, J. Yamamoto, H. Kawano, H. Satoh, and H. Itoh, Microelectron. Eng. **67-68**, 78 (2003).

[13] F. Lehmann, G. Richter, T. Borzenko, V. Hock, G. Schmidt, and L. W. Molenkamp, Microelectron. Eng. **65**, 327 (2003).

[14] J. Stodolka, D. Nau, M. Frommberger, C. Zanke, H. Giessen, and E. Quandt, Microelectron. Eng. **78-79**, 442 (2005).

[15] P. Ferrand, J. Seekamp, M. Egen, R. Zentel, S. G. Romanov, and C. M. Sotomayor Torres, Microelectron. Eng. **73-74**, 362 (2004).

[16] R. Steingruber and M. Mohrle, Microelectron. Eng. **78-79**, 51 (2005).

[17] C.-M. Cheng and R.-H. Chen, Microelectron. Eng. **71**, 335 (2004).

[18] S.-W. Ahn, K.-D. Lee, J.-S. Kim, S. H. Kim, S. H. Lee, J.-D. Park, and P.-W. Yoon, Microelectron. Eng. **78-79**, 314 (2005).

[19] S.-W. Ahn, K.-D. Lee, J.-S. Kim, S. H. Kim, J.-D. Park, S.-H. Lee, and P.-W. Yoon, Nanotechnology **16**, 1874 (2005).

[20] R. Murillo, H. A. van Wolferen, L. Abelmann, and J. C. Lodder, Microelectron. Eng. **78-79**, 260 (2005).

[21] F. Yu, P. Li, H. Shen, S. Mathur, C.-M. Lehr, U. Bakowsky, and F. Mucklich, Biomaterials **26**, 2307 (2005).

[22] S. Asakura, A. Hozumi, T. Yamaguchi, and A. Fuwa, Thin Solid Films **467**, 127 (2004).

[23] M. Zaborowski, P. Grabiec, and I. W. Rangelow, Microelectron. Eng. **76-74**, 588 (2004).

[24] L. A. Files-Sesler, J. N. Randall, and D. Harkness, J. Vac. Sci. Technol. B **9**, 659 (1991).

[25] A. Ali, V. Ukraintsev, H. Sabri, and M. Yang, J. Vac. Sci. Technol. B **20**, 95 (2001).

[26] A. Pasquini, G. B. Picotto, and M. Pisani, Sens. Actuators A **123-124**, 655 (2005).

[27] G. Dahlen, M. Osborn, N. Okulan, W. Foreman, and A. Chand, J. Vac. Sci. Technol. B **23**, 2297 (2005).

[28] H. Liu, M. Klonowski, D. Kneeburg, G. Dahlen, M. Osborn, and T. Bao, J. Vac. Sci. Technol. B **23**, 3090 (2005).

[29] J. Thiault, J. Foucher, J. H. Tortai, O. Joubert, S. Landis, and S. Pauliac, J. Vac. Sci. Technol. B **23**, 3075 (2005).

[30] Y. Ma and F. Cerrina, J. Vac. Sci. Technol. B **23**, 1096 (2005).

[31] N. S. Gluck, H. Sankur, J. Heuer, J. DeNatale, and W. J. Gunning, J. Appl. Phys. **69**, 3037 (1991).

[32] S. S. H. Naqvi, J. R. McNeil, R. H. Krukar, and K. P. Bishop, Microlithogr. World **2**, 5 (1993).

[33] C. J. Raymond, M. R. Murnane, S. L. Prins, S. Sohail, H. Naqvi, and J. R. McNeil, J. Vac. Sci. Technol. B **15**, 361 (1997).

[34] B. K. Minhas, S. A. Coulombe, S. S. H. Naqvi, and J. R. McNeil, Appl. Opt. **37**, 5112 (1998).

[35] N. Blayo, R. A. Cirelli, F. P. Klemens, and J. T. C. Lee, J. Opt. Soc. Am. A **12**, 591 (1995).

[36] H. L. Maynard, N. Layadi, and J. T.-C. Lee, J. Vac. Sci. Technol. B **15**, 109 (1997).

[37] H. L. Maynard, N. Layadi, and J. T. C. Lee, Thin Solid Films **313-314**, 398 (1998).

[38] L. Desvoivres, L. Vallier, and O. Joubert, J. Vac. Sci. Technol. B **18**, 156 (2000).

[39] X. Niu, N. Jakatdar, J. Bao, and C. J. Spanos, IEEE Trans. Semicond. Man. **14**, 97 (2001).

[40] B. S. Stutzman, H.-T. Huang, and F. L. Terry Jr., J. Vac. Sci. Technol. B **18**, 2785 (2000).

[41] H.-T. Huang, W. Kong, and F. L. Terry Jr., Appl. Phys. Lett. **78**, 3983 (2001).

[42] H.-T. Huang and F. L. Terry Jr., Thin Solid Films **455-456**, 828 (2004).

[43] D. Jucius, V. Grigaliunas, and A. Guobiene, Microelectron. Eng. **71**, 190 (2004).

[44] C. A. Mack, Proc. SPIE **5037**, 1 (2003).

[45] P. C. Logofatu, Proc. SPIE **5038**, 208 (2003).

[46] J. Perlich, F.-M. Kamm, J. Rau, F. Scholze, and G. Ulm, J. Vac. Sci. Technol. B **22**, 3059 (2004).

[47] R. L. Jones, T. Hu, E. K. Lin, W.-l. Wu, D. M. Casa, N. G. Orji, T. V. Vorburger, P. J. Bolton, and G. G. Barclay, Proc. SPIE **5038**, 191 (2003).

[48] D.-M. Shyu and M.-H. Lu, Rev. Sci. Instrum. **76**, 085103 (2005).

[49] A. De Martino, T. Novikova, S. BenHatit, B. Drevillon, and D. Cattelan, Proc. SPIE **5752**, 217 (2005).

[50] B. Kaplan, T. Novikova, A. De Martino, and B. Drevillon, Appl. Opt. **43**, 1233 (2004).

[51] F. L. Terry Jr. and J. J. Bendik, Proc. SPIE **5752**, 237 (2005).

[52] J. Pistora, J. Vlcek, K. Watanabe, K. Postava, S. Visnovsky, R. Antos, and T. Yamaguchi, International Journal of Microwave and Optical Technology **1**, 63 (2005).

[53] P. Reinig, R. Dost, M. Moert, T. Hingst, U. Mantz, J. Moffitt, S. Shakya, C. J. Raymond, and M. Littau, Proc. SPIE **5752**, 559 (2005).

[54] R. Quintanilha, J. Hazart, P. Thony, and D. Henry, Proc. SPIE **5752**, 204 (2005).

[55] M. Foldyna, D. Ciprian, J. Pistora, K. Postava, and R. Antos, Proc. SPIE **5445**, 226 (2004).

[56] R. Antos, J. Pistora, I. Ohlidal, K. Postava, J. Mistrik, T. Yamaguchi, S. Visnovsky, and M. Horie, J. Appl. Phys. **97**, 053107 (2005).

[57] R. Antos, J. Mistrik, M. Aoyama, S. Visnovsky, and T. Yamaguchi, Rep. Graduate School Electron. Sci. Technol., Shizuoka Univ. **26**, 55 (2005).

[58] R. Antos, I. Ohlidal, D. Franta, P. Klapetek, J. Mistrik, T. Yamaguchi, and S. Visnovsky, Appl. Surf. Sci. **244**, 221 (2005).

[59] R. Antos, I. Ohlidal, J. Mistrik, K. Murakami, T. Yamaguchi, J. Pistora, M. Horie, and S. Visnovsky, Appl. Surf. Sci. **244**, 225 (2005).

[60] R. Antos, J. Mistrik, T. Yamaguchi, M. Horie, and S. Visnovsky, Proc. SPIE **5858**, 58580Y (2005).

[61] R. Antos, I. Ohlidal, J. Mistrik, T. Yamaguchi, S. Visnovsky, S. Yamaguchi, and M. Horie, Proc. SPIE **5965**, 59652B (2005).

[62] M. Grimsditch and P. Vavassori, J. Phys.: Condens. Matter **16**, R275 (2004).

[63] J. I. Martin, J. Nogues, K. Liu, J. L. Vicent, and I. K. Schuller, J. Magn. Magn. Mater. **256**, 449 (2003).

[64] Y. Souche, V. Novosad, B. Pannetier, and O. Geoffroy, J. Magn. Magn. Mater. **177-181**, 1277 (1998).

[65] Y. T. Shen, Y. H. Wu, T. C. Chong, H. Xie, Z. B. Guo, K. B. Li, and J. J. Qiu, Appl. Phys. Lett. **79**, 2034 (2001).

[66] T. Schmitte, K. Westerholt, and H. Zabel, J. Appl. Phys. **92**, 4524 (2002).

[67] P. Garcia-Mochales, J. L. Costa-Kramer, G. Armelles, F. Briones, D. Jaque, J. I. Martin, and J. L. Vicent, Appl. Phys. Lett. **81**, 3206 (2002).

[68] I. Guedes, N. J. Zaluzec, M. Grimsditch, V. Metlushko, P. Vavassori, B. Ilic, P. Neuzil, and R. Kumar, Phys. Rev. B **62**, 11719 (2000).

[69] J. Jorzick, S. O. Demokritov, C. Mathieu, B. Hillebrands, B. Bartenlian, C. Chappert, F. Rousseaux, and A. N. Slavin, Phys. Rev. B **60**, 15194 (1999).

[70] R. Antos, J. Mistrik, M. Aoyama, T. Yamaguchi, S. Visnovsky, and B. Hillebrands, J. Magn. Magn. Mater. **272-276**, 1670 (2004).

[71] R. Antos, J. Mistrik, S. Visnovsky, M. Aoyama, T. Yamaguchi, and B. Hillebrands, Trans. Magn. Soc. Japan **4**, 282 (2004).

[72] R. Antos, M. Veis, E. Liskova, M. Aoyama, J. Hamrle, T. Kimura, P. Gustafik, M. Horie, J. Mistrik, T. Yamaguchi, S. Visnovsky, and N. Okamoto, Proc. SPIE **5752**, 1050 (2005).

[73] R. Antos, J. Mistrik, T. Yamaguchi, S. Visnovsky, S. O. Demokritov, and B. Hillebrands, Opt. Express **13**, 4651 (2005).

[74] R. Antos, S. Visnovsky, J. Mistrik, and T. Yamaguchi, International Journal of Microwave and Optical Technology **1**, 511 (2005).

[75] L. Li, J. Opt. Soc. Am. **13**, 1870 (1996).

[76] M. Nyvlt, Ph. D. thesis, Charles University in Prague, 1996.

[77] G. Bader, P. V. Ashrit, F. E. Girouard, and V.-V. Truong, Appl. Opt. **34**, 1684 (1995).

[78] G. Bader, P. V. Ashrit, and V.-V. Truong, Appl. Opt. **37**, 1146 (1998).

[79] R. Joerger, K. Forcht, A. Gombert, M. Kohl, and G. W., Appl. Opt. **36**, 319 (1997).

[80] M. Kildemo, P. Bulkin, B. Drevillon, and O. Hunderi, Appl. Opt. **36**, 6352 (1997).

[81] K. Postava, T. Yamaguchi, and R. Kantor, Appl. Opt. **41**, 2521 (2002).

[82] K. Postava, O. Zivotsky, J. Pistora, and T. Yamaguchi, Thin Solid Films **455-456**, 615 (2004).

[83] S. Visnovsky, V. Prosser, and R. Krishnan, J. Appl. Phys. **49**, 403 (1978).

[84] S. Visnovsky and R. Krishnan, J. Opt. Soc. Am. **71**, 315 (1981).

[85] N. Chateau, J. P. Hugonin, B. Guldimann, and P. Chavel, Opt. Commun. **103**, 444 (1993).

[86] L. Li, Opt. Commun. **160**, 15 (1999).

[87] M. C. Huttley and V. M. Bird, Opt. Acta **20**, 771 (1973).

[88] R. C. McPhedran and D. Maystre, Opt. Acta **21**, 413 (1974).

[89] H. Kikuta, H. Yoshida, and K. Iwata, Opt. Rev. **2**, 92 (1995).

[90] E. Popov and M. Neviere, J. Opt. Soc. Am. A **17**, 1773 (2000).

[91] M. G. Moharam and T. K. Gaylord, J. Opt. Soc. Am. **71**, 811 (1981).

[92] M. G. Moharam, D. A. Pommet, E. B. Grann, and T. K. Gaylord, J. Opt. Soc. Am. A **12**, 1077 (1995).

[93] D. F. Edwards, *Handbook of Optical Constants of Solids* (ed. E. D. Palik, Academic Press, Inc., Tokyo, 1998).

[94] H. R. Philipp, *Handbook of Optical Constants of Solids* (ed. E. D. Palik, Academic Press, Inc., Tokyo, 1998).

[95] E. Franke, C. L. Trimble, M. J. DeVries, J. A. Woollam, M. Schubert, and F. Frost, J. Appl. Phys. **88**, 5166 (2000).

[96] R. C. McPhedran and M. D. Waterworth, Opt. Acta **19**, 877 (1972).

[97] D. Maystre and M. Nieto-Vesperinas, J. Opt. Soc. Am. A **9**, 2218 (1992).

[98] A. Wirgin, Opt. Acta **28**, 1377 (1981).

[99] A. Kinoshita, F. Kitamura, M. Horie, and T. Yoshida, Proc. SPIE **5752**, 874 (2005).

[100] S. Ingvarsson, PhD. thesis, Brown University, 2001.

[101] D. W. Lynch and W. R. Hunter, *Handbook of Optical Constants of Solids* (ed. E. D. Palik, Academic Press, Inc., Tokyo, 1998).

[102] G. Neuber, R. Rauer, J. Kunze, T. Korn, C. Pels, G. Meier, U. Merkt, J. Backstrom, and M. Rubhausen, Appl. Phys. Lett. **83**, 4509 (2003).

[103] P. Hones, M. Diserens, and F. Levy, Surf. Coat. Tech. **120-121**, 277 (1999).

[104] P. Klapetek, I. Ohlidal, D. Franta, and P. Pokorny, Surf. Interface Anal. **33**, 559 (2002).

[105] P. Klapetek, I. Ohlidal, D. Franta, A. Montaigne-Ramil, A. Bonanni, D. Stifter, and H. Sitter, Acta Phys. Slov. **53**, 223 (2003).

[106] D. Franta and I. Ohlidal, J. Mod. Opt. **45**, 903 (1998).

[107] I. Ohlidal and D. Franta, Progress in Optics **41**, 181 (2000).

[108] E. D. Palik, *Handbook of Optical Constants of Solids* (Academic Press, Inc., Tokyo, 1998).

[109] S. Visnovsky, M. Nyvlt, V. Parizek, P. Kielar, V. Prosser, and R. Krishnan, IEEE Trans. Magn. **29**, 3390 (1993).

List of the Author's Publications

Original refereed journal papers

1. **R. Antos**, J. Mistrik, M. Aoyama, T. Yamaguchi, S. Visnovsky, and B. Hillebrands, "Magneto-optical spectroscopy on permalloy wires in 0th and 1st diffraction orders," *J. Magn. Magn. Mater.*, Vol. 272-276, pp. 1670–1671 (May 2004).
2. J. Mistrik, K. Takahashi, **R. Antos**, M. Aoyama, T. Yamaguchi, Y. Anma, Y. Fukuda, et al., "Spectroscopic ellipsometry of TaN_x and VN films," *Thin Solid Films*, Vol. 455-456, pp. 473-477 (May 2004).
3. J. Mistrik, **R. Antos**, K. Murakami, M. Aoyama, T. Yamaguchi, Y. Anma, Y. Fukuda, A. Medvid', and A. Michko, "Spectroscopic ellipsometry of pulsed laser irradiated c-Ge surfaces," *Thin Solid Films*, Vol. 455-456, pp. 478-481 (May 2004).
4. **R. Antos**, J. Mistrik, S. Visnovsky, M. Aoyama, T. Yamaguchi, and B. Hillebrands, "Characterization of permalloy wires by optical and magneto-optical spectroscopy," *Trans. Magn. Soc. Japan*, Vol. 4., pp. 282–285 (November 2004).
5. **R. Antos**, J. Pistora, I. Ohlidal, K. Postava, J. Mistrik, T. Yamaguchi, S. Visnovsky, and M. Horie, "Specular spectroscopic ellipsometry for the critical dimension monitoring of gratings fabricated on a thick transparent plate," *J. Appl. Phys.*, Vol. 97, 053107 (March 2005).
6. **R. Antos**, J. Mistrik, M. Aoyama, S. Visnovsky, and T. Yamaguchi, "Generalized scatterometry of laterally patterned periodic nanostructures based on spectroscopic ellipsometry," *Rep. Graduate School Electron. Sci. Technol.*, Shizuoka Univ., Vol. 26, pp. 55–61, (March 2005).
7. **R. Antos**, I. Ohlidal, D. Franta, P. Klapetek, J. Mistrik, T. Yamaguchi, and S. Visnovsky, "Spectroscopic ellipsometry on sinusoidal surface-relief gratings," *Appl. Surf. Sci.*, Vol. 244, No. 1–4, pp. 221–224 (May 2005).
8. **R. Antos**, I. Ohlidal, J. Mistrik, K. Murakami, T. Yamaguchi, J. Pistora, M. Horie, and S. Visnovsky, "Spectroscopic ellipsometry on lamellar gratings," *Appl. Surf. Sci.*, Vol. 244, No. 1–4, pp. 225–229 (May 2005).
9. J. Mistrik, I. Ohlidal, **R. Antos**, M. Aoyama, and T. Yamaguchi, "Evidence of refractive index change in glass substrates induced by high-density reactive ion plating deposition of SiO_2 films," *Appl. Surf. Sci.*, Vol. 224, pp. 51-54 (May 2005).
10. **R. Antos**, J. Mistrik, T. Yamaguchi, S. Visnovsky, S.O. Demokritov, and B. Hillebrands, "Evidence of native oxides on the capping and substrate of Permalloy gratings by magneto-optical spectroscopy in the zeroth- and first-diffraction orders," *Appl. Phys. Lett.*, Vol. 86, 231101 (June 2005).

11. **R. Antos**, J. Mistrik, T. Yamaguchi, S. Visnovsky, S.O. Demokritov, and B. Hillebrands, “Evaluation of the quality of Permalloy gratings by diffracted magneto-optical spectroscopy,” *Opt. Express*, Vol. 13, pp. 4651-4656 (June 2005).
12. K. Rokushima, **R. Antos**, J. Mistrik, S. Visnovsky, and T. Yamaguchi, “Optics of anisotropic nanostructures,” *Czech. J. Phys.*, Vol. 56, No. 7, pp. 665-764 (July 2006).
13. **R. Antos**, S. Visnovsky, J. Mistrik, and T. Yamaguchi, “Magneto-optical polar Kerr effect spectroscopy on 2D-periodic subwavelength arrays of magnetic dots,” *International Journal of Microwave and Optical Technology*, Vol. 1, No. 2, Man. Id: IJMOT-2006-6-157 (August 2006).
14. **R. Antos**, J. Pistora, J. Mistrik, T. Yamaguchi, S. Yamaguchi, M. Horie, S. Visnovsky, and Y. Otani, “Convergence properties of critical dimension measurements by spectroscopic ellipsometry on gratings made of various materials,” *J. Appl. Phys.*, Vol. 100, 054906 (September 2006).
15. **R. Antos**, J. Mistrik, T. Yamaguchi, M. Veis, E. Liskova, S. Visnovsky, J. Pistora, B. Hillebrands, S. O. Demokritov, T. Kimura, and Y. Otani, “Magneto-optical spectroscopic scatterometry for analyzing patterned magnetic nanostructures (*invited*),” *J. Magn. Soc. Japan*, Vol. 30 (November 2006), to be published.

Papers from proceedings of conferences

16. J. Mistrik, K. Postava, **R. Antos**, T. Yamaguchi, M. Takeyama, and A. Noya, “Spectro-ellipsometric study of thin films for ULSI process – Optical properties of transition metal nitride barrier layers,” *Tech. Report of IEICE*, CPM 2003-65, pp. 25-30 (August 2003).
17. M. Foldyna, D. Ciprian, J. Pistora, K. Postava, and **R. Antos**, “Reconstruction of grating parameters from ellipsometric data,” *Proc. SPIE*, Vol. 5445, pp. 226-229 (April 2004).
18. **R. Antos**, M. Veis, E. Liskova, M. Aoyama, J. Hamrle, T. Kimura, P. Gustafik, M. Horie, J. Mistrik, T. Yamaguchi, S. Visnovsky, and N. Okamoto, “Optical metrology of patterned magnetic structures: deep versus shallow gratings,” *Proc. SPIE*, Vol. 5752, pp. 1050–1059 (May 2005).
19. **R. Antos**, J. Mistrik, T. Yamaguchi, M. Horie, and S. Visnovsky, “Airy-like internal reflection series applied in scatterometry and simulations of gratings,” *Proc. SPIE*, Vol. 5858, 58580Y (August 2005).
20. **R. Antos**, I. Ohlidal, J. Mistrik, T. Yamaguchi, S. Visnovsky, S. Yamaguchi, and M. Horie, “Optical metrology of binary arrays of holes in semiconductor media using

microspot spectroscopic ellipsometry," *Proc. SPIE*, Vol. 5965, 59652B (October 2005).

Conference presentations

21. **R. Antos**, J. Mistrik, T. Yamaguchi, S. Visnovsky, S. Demokritov, and B. Hillebrands, "Magneto-optic spectroscopy on permalloy nano-wires in 0th and 1st diffraction orders," The 50th Spring Meeting of the Society of Applied Physics of Japan (第 50 回応用物理学関係連合会), 30aZH12/I,III (March 2003).
22. **R. Antos**, J. Pistora, J. Vlcek, J. Mistrik, M. Aoyama, T. Yamaguchi and M. Horie, "Spectro-ellipsometric investigation of Si_3N_4 2D periodic dots by local modes method," The 50th Spring Meeting of the Society of Applied Physics of Japan (第 50 回応用物理学関係連合会), 30aZH11/I,III (March 2003).
23. J. Pistora, J. Vlcek, K. Postava, T. Yamaguchi, M. Horie, **R. Antos**, M. Foldyna, and M. Aoyama, "Monitoring of 2D long periodicity gratings by spectral ellipsometry," 3rd ICSE, Vienna, ThP F4.9 (July 2003).
24. J. Pistora, **R. Antos**, J. Vlcek, T. Yamaguchi, and M. Lesnak, "2D long period gratings," 9th ISMOT, Ostrava, Reg. number: 111 (August 2003).
25. **R. Antos**, J. Mistrik, K. Murakami, M. Aoyama, T. Yamaguchi and A. Medvid, "Spectro-ellipsometric investigation of Ge surfaces irradiated by Nd:YAG pulsed laser," The 64th Annual Meeting of the Society of Applied Physics of Japan (第 64 回応用物理学会), 1pW13/III (September 2003).
26. J. Mistrik, **R. Antos**, M. Aoyama and T. Yamaguchi, "Change in refractive index of glass substrates by EB assisted plasma deposition of SiO_2 layer," The 64th Annual Meeting of the Society of Applied Physics of Japan (第 64 回応用物理学会), 1pW12/III (September 2003).
27. J. Mistrik, T. Yamaguchi, **R. Antos**, Z.-T. Jiang, I. Ohlidal, and M. Aoyama, "Spectroscopic ellipsometry: its accuracy and potentiality (*invited*)," 10th ISMOT, Fukuoka, Aug. 23, D-11 (August 2005).
28. J. Pistora, J. Vlcek, K. Watanabe, K. Postava, S. Visnovsky, **R. Antos**, and T. Yamaguchi, "Total reflection ellipsometry of lamellar gratings (*invited*)," 10th ISMOT, Fukuoka, Aug. 23, B-05 (August 2005).